INFORMATION TO USERS

This manuscript has been reproduced from the microfilm master. UMI films the text directly from the original or copy submitted. Thus, some thesis and dissertation copies are in typewriter face, while others may be from any type of computer printer.

The quality of this reproduction is dependent upon the quality of the copy submitted. Broken or indistinct print, colored or poor quality illustrations and photographs, print bleedthrough, substandard margins, and improper alignment can adversely affect reproduction.

In the unlikely event that the author did not send UMI a complete manuscript and there are missing pages, these will be noted. Also, if unauthorized copyright material had to be removed, a note will indicate the deletion.

Oversize materials (e.g., maps, drawings, charts) are reproduced by sectioning the original, beginning at the upper left-hand corner and continuing from left to right in equal sections with small overlaps. Each original is also photographed in one exposure and is included in reduced form at the back of the book.

Photographs included in the original manuscript have been reproduced xerographically in this copy. Higher quality 6" x 9" black and white photographic prints are available for any photographs or illustrations appearing in this copy for an additional charge. Contact UMI directly to order.

UMI

A Bell & Howell Information Company
300 North Zeeb Road, Ann Arbor MI 48106-1346 USA
313/761-4700 800/521-0600

ON-LINE MONITORING AND PET IMAGING OF THE POSITRON-EMITTING ACTIVITY CREATED IN TISSUE BY PROTON RADIOTHERAPY BEAMS

by

Dale William Litzenberg

A dissertation in partial fulfillment
of the requirements for the degree of
Doctor of Philosophy
(Department of Physics)
in The University of Michigan
1997

Doctoral Committee:

Professor Frederick Becchetti, Jr.
Associate Professor Fred Adams
Professor Joachim Jänecke
Professor Lawrence Jones
Professor W Leslie Rogers
Professor Randall Ten Haken

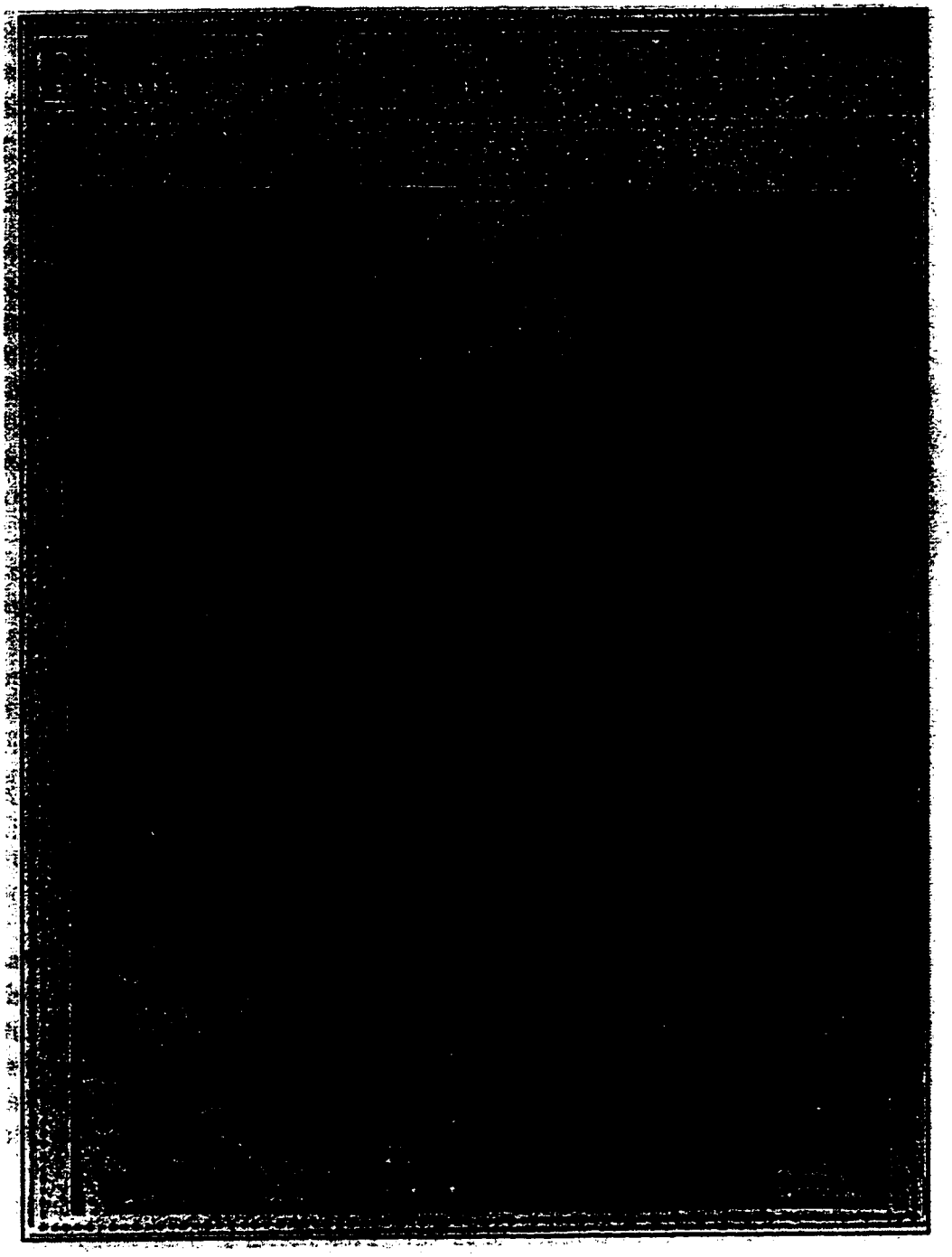

For those who have lost a loved one to cancer

and those who have suffered under its affliction

ACKNOWLEDGMENTS

I would like to first thank my advisor, Professor Fred Becchetti, for his generous support and guidance. I would also like to thank the present and past members of the nuclear physics research group from whom I have learned so much: Professor Janecke, Dr. Don Roberts, Dr. Jim Brown, Khai Pham, Mu Young Lee and John Bajema. I also owe many thanks to my committee members: Fred Adams, Quin Jänecke, Larry Jones, Les Rogers, and Randy Ten Haken, for all their guidance and advice. Special thanks go to my early mentor Dr. Koltick for his guidance and patient tutelage. Other professors who provided valued guidance and significantly influenced my education include Professors Jim Gaidos and Homer Neal.

Special thanks go to all the staff at the National Superconducting Cyclotron Laboratory. I would like to mention Reg Ronnigen and Raman for their technical and logistical support, Ron Fox for software assistance and especially Skip Vander Molen for his guidance and assistance with the data acquisition system.

To my parents, Jack and Charlotte Litzenberg, and my sister Leslie, and my love, Tracey Rapp, for all their love, support and encouragement. I can't thank you enough for all you've done for me.

And finally, to all my friends who have made graduate school a fun and rewarding experience: Miriam Allersma, Dennis Allen, John Bajema(Indian Pass), Don Crandell and Jean Garland, Brian Davis(it only feels like you're crawling to Cincinnati), Mike Gowin(what do you mean the Soviet hockey team couldn't make it?), Dave Graff(she was *supposed* to be watching my car), Dan Jacques(isn't Bimini supposed to be around here somewhere?), Ben Mathiesen, Missi (luck) Mercer, Chris Metzler, (General) Ed Nam

(Gettysburg), Tom Nelson(I thought *you* had the key), "Betsy" Elizabeth Schuler Smith and Todd Smith(scoring at the net!), Eric and Ines Storhock (Pasadena!), and the Friday night volleyball crew(point!).

This work was supported by grants PHY 9512104 and PHY 9208468 from The National Science Foundation and by grants from the following groups within the University of Michigan: The Office of the Vice President for Research, The John Munn Foundation through The Comprehensive Cancer Center, The College of Literature, Science and Art, The Rackham School of Graduate Studies, and The Department of Physics.

TABLE OF CONTENTS

LIST OF TABLES

Table

LIST OF FIGURES

Figures

LIST OF APPENDICES

INTRODUCTION

In 1946 Dr. Robert Wilson proposed using recently developed charged particle beams for the treatment of cancer. Previous experience with X-ray radiotherapy and radioactive implants had shown that local control of cancerous tumors would be maximized if the lethal dose of radiation could be confined to the tumor volume. In addition, the side effects of radiation treatment on the patient would be minimized if the dose to the surrounding healthy tissue could be reduced. This has historically presented a challenge using X-rays which deposit most of their dose near the surface of the body. As the X-ray beam penetrates the body less dose is delivered at increasing depths where most of the tumor volume is located.

The motivation for Dr. Wilson's proposal was based on the phenomenon know as the Bragg peak which had been placed on a firm theoretical footing by Bethe and Bloch in 1937. As charged particles pass through matter they lose energy primarily through ionizing the material. This ionization is the main source of the dose deposited in the material. Through the ionization process the particles continually lose energy and eventually stops at a well-defined range. Near the end of the particles range its velocity is comparable to the classical velocity of the electrons orbiting around the nucleus. This gives the charged particles in the beam the most time to interact with the electrons in the material through the electromagnetic force. Consequently, most of the ionization produced by the protons is located at the end of the beams range and relatively little dose is deposited at the surface of the body where the particles are traveling faster. This is the Bragg peak phenomenon. Another characteristic of charged particle beams which made them attractive for radiotherapy was that they are scattered less than X-rays in the body.

Therefore a well-defined beam of charged particles would maintain its shape comparatively well. The use of charged particle beams potentially enabled the high dose volume to be shaped and controlled much more precisely.

Until the mid-1980's charged particle radiotherapy was primarily conducted at physics research institutions which could afford the accelerators necessary to produce the beams. However, by this time advances in technology made the cost of dedicated proton radiotherapy accelerators justifiable at large medical research hospitals. As of this writing there are eighteen operating proton radiotherapy facilities around the world and another sixteen which have been proposed or are under construction. In addition, there are five existing or proposed facilities for heavy-ion radiotherapy.

While proton radiotherapy has proven to be an effective tool in the local control of cancer, there are several practical difficulties which prevent its full potential from being realized. The range of the beam depends on its energy and the composition, density and thickness of the tissue. The human body contains many different types of tissue, all with varying compositions and densities. These may include bone, soft tissues or even air spaces. In addition, the proton beam will typically traverse layers of different tissues with varying thicknesses before reaching the tumor. These variations in composition, density and thickness from layer to layer make it very difficult to predict the range of the beam and may lead to significant errors in delivering the desired dose to the prescribed treatment volume. In addition to these complications, internal organs may shift several centimeters from day to day between treatments. These complications conspire to significantly diminish the potential benefits of delivering a highly localized lethal dose. If these factors are not taken into consideration during each treatment, large fractions of the prescribed treatment volume may receive non-lethal doses while adjacent healthy tissue may be severely damaged. The possibility of realizing the full potential offered by the Bragg peak lies in making every reasonable effort to accurately identify the

tumor volume and deliver a highly localized lethal dose to this volume during each treatment.

In the interest of realizing this potential we have investigated the possibility of monitoring the positron-emitting activity created by proton radiotherapy beams. This technique may be used to verify the range of the treatment beam and to determine the composition of the tissue traversed by the beam. In large tumors this technique may potentially be used to determine the oxygen content of the tumor by measuring the rate of blood flow at different depths.

Chapters 1 and 2 of this dissertation have already been published in refereed journals and are often cited within this dissertation. To make it clear that the cited material may also be found in this dissertation, references to the paper containing the information in Chapter 1 will be will be in the form [DWL1], and so on for Chapters 2 and 3. Other papers on this work have appeared in unrefereed conference proceedings. These will be referenced as [Lit#], as given the following list of references.

Chapter 1 presents the design considerations of a PET imaging system suitable for monitoring positron-emitting activity between pulses of a proton radiotherapy beam. The results of Monte Carlo simulations are presented and compared with experimental results obtained during calibrations of the imaging system. The algorithms used for image reconstruction are also presented. Possible improvements on the design of the prototype imaging system are discussed based on the simulation results and our experience with the system. Chapter 2 discusses the architecture and implementation of the data acquisition system. Chapter 3 presents the theory of calculating the expected positron-emitting activity distributions produced by proton radiotherapy beams and the algorithm for reconstructing radioisotopic decay distributions. This is followed by results of experiments designed to examine range verification and tissue composition determination. Chapter 3 concludes with a discussion of the results and the potential benefits anticipated with this type of imaging system.

References to Introduction

DWL1 D. W. Litzenberg, F. D. Becchetti, and D. A. Roberts, "On-Line PET Monitoring of Radiotherapy Beams: Image Reconstruction and Monte Carlo Simulations of Detector Geometries," *IEEE Trans. Nucl. Sci.*, vol. 44, no. 4, August, 1997.

DWL2 D. W. Litzenberg, F. D. Becchetti, D. A. Roberts, "A Parallel, Transputer-Based Data Acquisition System for On-Line PET Imaging of Proton and Gamma-Ray Radiotherapy Beams," IEEE Trans. Nucl. Sci., vol. NS-43, no. 1, pp. 154-158, Feb. 1996.

DWL3 D. W. Litzenberg, F. D. Becchetti, D. A. Roberts, et al., "On-Line PET Monitoring of Radiotherapy Beams: Experimental Results with Proton Beams," to be submitted for publication.

Lit1 D.W. Litzenberg, et al., "Positron Emission Tomography of Implanted Radioactive Analog Radiotherapy Beams," in *Second International Conference on Radioactive Nuclear Beams*, Louvain-la-Neuve, Belgium, 1991.

Lit2 D. W. Litzenberg, J. F. Bajema, F. D. Becchetti, et al., "On-Line Monitoring and P.E.T. Imaging of Proton Radiotherapy Beams," IEEE Med. Imag. Conf. Rec., 954-956, Orlando, FL, pp. 25-31, Oct. 1992.

Lit3 D. W. Litzenberg, J. F. Bajema, F. D. Becchetti, et al., "On-Line Monitoring and P.E.T. Imaging of Proton Radiotherapy Beams," IEEE Med. Imag. Conf. Rec., pp. 1672-1676, Norfolk, VA, Oct. 30-Nov. 5, 1994.

CHAPTER 1

ON-LINE PET MONITORING OF RADIOTHERAPY BEAMS: IMAGE RECONSTRUCTION AND MONTE CARLO SIMULATIONS OF DETECTOR GEOMETRIES

Radiotherapy has long been an effective tool in the treatment of cancer. Survival rates have continually increased as advances are made in the field. The difficulties associated with this treatment modality and the complexity of the apparatus used to produce the treatment beams have lead to the development of sophisticated systems to plan treatments and to monitor the beams as they are administered to the patient. However, systems designed to directly monitor the effects on the patient during therapy are still limited. Treatment verification and patient safety have primarily been inferred from the beam monitoring devices, calculations of beam interactions in phantoms and on the previous results of clinical trials. The development of systems to directly monitor the effect on a patient is an attractive concept but difficult to implement due to the harsh radiation environment and a lack of immediately measurable biological conditions which would have an impact on the treatment plan.

The post-treatment technique of detecting 511 keV, coincident gamma-ray pairs emitted from positron-emitting isotopes produced in tissue by radiotherapy beams has been investigated by many researchers [1-5]. Most of these studies employed a commercial Positron Emission Tomography (PET) imaging system or a coincidence counting system located at a nearby hospital or research facility requiring a lengthy transportation and setup time. The resulting images predominantly show activity from isotopes whose half-life is comparable to or longer than the transportation and setup time.

While these studies lend valuable insight, the images obtained are mainly of ^{11}C which is of limited physiological value for subsequent treatment planning. However, ^{15}O is the most active positron-emitting isotope produced during proton and gamma-ray radiotherapy due to the abundance of oxygen in the body, its short 2 minute half-life and the relatively large cross-section of the $^{16}O(p, pn)^{15}O$ and $^{16}O(\gamma, n)^{15}O$ [4,6] reactions. A system which measures the distribution of ^{15}O during or immediately after the treatment could provide information on the range of charged particles, total dose delivered, and the oxygen content of the tumor on a much shorter time scale.

This paper presents Monte Carlo design simulations and the image reconstruction technique for a prototype on-line positron-emission monitoring system. This prototype on-line camera was designed, constructed and evaluated to monitor the positron-emitting nuclei produced by radiotherapy beams. The primary design considerations focus on the feasibility of imaging between beam pulses rather than achieving optimal spatial resolution or implementing sophisticated imaging algorithms. The detector requirements and constraints are discussed first, followed by how the detector configuration effects image reconstruction. The output of the imaging system is mapped into a discrete representation of the activity distribution using a two-dimensional system matrix. This matrix is determined during a calibration experiment and contains all information about the system including position-to-detector-pair mapping, solid angle, intrinsic detector efficiency, penetration of shielding and detectors by gamma-rays, and determines the bandwidth limit for image reconstruction. The detector configuration, therefore, determines the characteristics of this matrix which in turn affects image reconstruction. The method for analyzing the system matrix is presented next so that various detector configurations may be compared. A computer program was written to simulate various detector arrangements and to generate the system matrix for each configuration. This code is described and the results compared to measured system matrices obtained during experiments. On- and off-line experiments were conducted using proton and ^{12}C beams

produced at the National Superconducting Cyclotron Laboratory at Michigan State University. Off-line gamma-ray experiments were conducted using the University of Michigan's 50 MV racetrack microtron. The results of these experiments will be presented in [DWL3].

Design Analysis and Image Reconstruction

Detector Configuration

The administration of radiotherapy requires the use and specific placement of many pieces of apparatus to safely and effectively deliver the treatment. Among these are bulky patient support and immobilization systems, ionization chambers, energy modulation devices, collimators, filters, scatterers, boluses, monitoring cameras and the support structures for each of these devices. While many of these devices are relatively compactly contained in the gantry system, the range of positions the gantry may occupy is very large in most facilities. Given these spatial constraints, it is difficult if not impossible to use conventional, annular, PET imaging devices for on-line monitoring. In addition, detectors placed at forward angles may become damaged or activated from nuclear reaction products produced in tissue during beam pulses or they may also experience a drift in gain due to high background rates. On-line imaging systems are therefore limited to relatively low solid angle detector configurations consisting of parallel rows or planes of detectors placed on either side of the patient in such a way as to avoid the beam and other hardware.

We have designed a prototype, low solid angle, detector system using Bismuth Germanate Oxide(BGO) scintillation crystals. The system consists of two rows of detectors encased in a custom-made lead shield. This prototype detector system is illustrated in Figure 1.1. The two rows of detectors are typically separated by $2d$ which is 60 cm for our on-line measurements but may be adjusted for maximum efficiency. A schematic representation

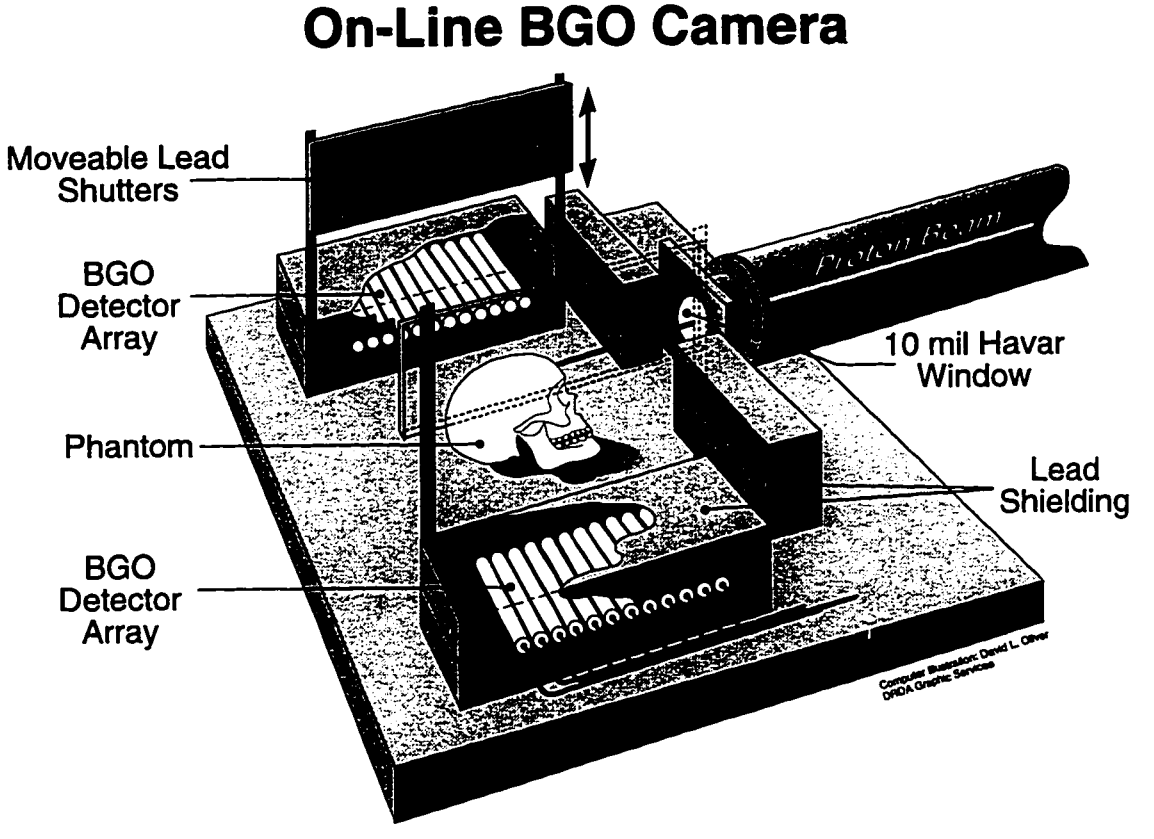

Figure 1.1. Schematic representation of the low solid angle BGO detection system. The two rows of twelve BGO detectors encased in lead shielding are typically separated by 60 cm. The lead shutters are closed during beam pulses to prevent activation of the crystals.

of the detector arrangement shows the parameters used for the Monte Carlo simulations in Figure 1.2. Each row of our prototype contains twelve cylindrical BGO crystals. Each crystal is 5.08 cm long and has a radius, r_d, of 0.95 cm. This is illustrated by Figure 1.3. These crystals are placed into a 2.22 cm diameter hole in the lead shielding. The space between adjacent crystals, s, is 0.50 cm. This produces a minimum septa thickness of 0.18 cm between adjacent detectors for Compton suppression. Each crystal is optically coupled to a high-gain version of the Hamamatsu R1166 photomultiplier tube. A LeCroy high voltage mainframe is used to match the gains of all detectors by independently adjusting the voltage applied to each phototube. Each detector produces one analog signal. These 24 signals constitute the physics-related input to the data acquisition system [DWL2, 7].

Image Reconstruction and The System Matrix

A complete set of projections through the imaging space in the desired plane is required to obtain axial tomographic imaging capabilities. This is generally not feasible while delivering the beam for the reasons cited above. Axial tomograms may be obtained while the beam is off by rotating the imaging system about the patient. However, the patient support and immobilization systems may obscure the view of the imaging plane or volume making it difficult to produce axial tomograms with minimal image reconstruction artifacts. For these reasons, on-line beam monitoring systems are usually only capable of producing images which are projections of the activity present in the cameras' field of view (FOV). Tomograms parallel to planes of detectors may be produced using a coded aperture, or electronic collimation in the case of PET. While this does allow several planes or lines of the FOV to be imaged, it has the disadvantage of lowering the efficiency to achieve a spatially invariant point response function (PRF) over the FOV for Fourier-based reconstruction algorithms [8]. Algorithms not requiring

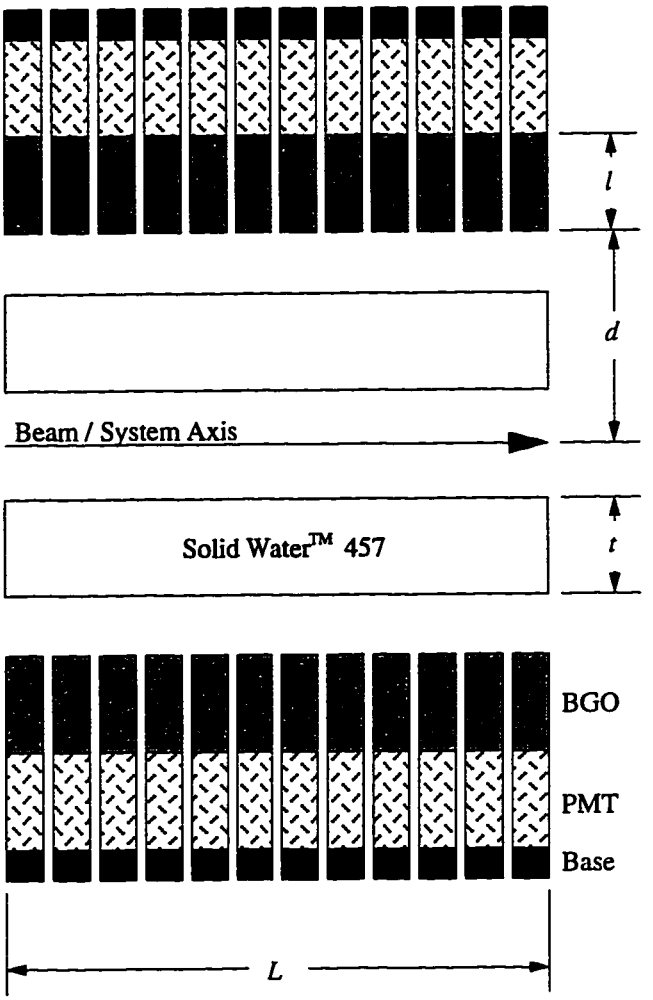

Figure 1.2. Relative orientation and dimensions of array, radiotherapy beam, and attenuating material.

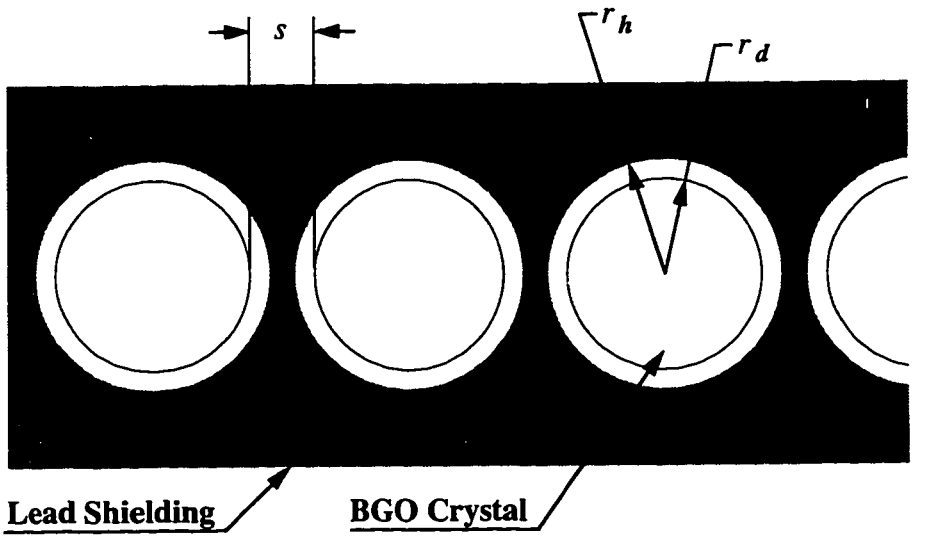

Figure 1.3. Geometry and dimensions of BGO crystals in lead shielding.

a shift-invariant PRF have been implemented [9] but are not suitable for real-time, on-line image reconstruction due to their time-consuming iterative nature.

Due to budgetary restrictions we were limited to a single row of detectors on each side. However, the charged particle beams used were selected to be pencil-like in size, so that only a one-dimensional reconstruction algorithm was required. A simple, non-iterative, matrix inversion algorithm using a shift variant PRF was implemented to obtain the highest possible detection efficiency and provide real-time, on-line image reconstruction. The pencil-width radiotherapy beam creates a positron-emitting activity distribution, $\mathcal{A}(\mathbf{r},t)$, parallel to, and equidistant between, the two rows of detectors. This vector of activity produces a vector response, $\mathcal{R}$, from the imaging system after imaging for a time, $T_I = t_2 - t_1$. The distribution of decays producing the response is given by

$$\mathcal{D}(\mathbf{r}) = \int_{t_1}^{t_2} \mathcal{A}(\mathbf{r},t)\, dt. \tag{1.1}$$

The mapping between the two representations is provided by the system matrix, $\mathcal{S}$. The response of the imaging system is then

$$\mathcal{R} = \mathcal{S}\mathcal{D}, \tag{1.2}$$

where $\mathcal{D}$ is a discrete representation of the continuous decay distribution, $\mathcal{D}(\mathbf{r})$.

The system matrix is formed by moving a calibrated positron-emitting source along the system axis and recording the response vector, $\mathcal{R}$, at n system points. In practice, the system points were chosen at local maxima of the coincidence detection efficiency (CDE) along the axis which will be discussed later. The response vector for each system point is a histogram of all events, binned by detector pair, that occur in the peak corresponding to this maxima. These response vectors are then placed beside each other in columns to form the system matrix. The dimension, m, of the response vector, $\mathcal{R}$, and therefore the system matrix, is less than or equal to the maximum number of possible

detector pairs which are in electronic coincidence. An algorithm for solving this m x n system of equations has been presented in [10].

For the apparatus discussed here, the dimensions of the system matrix and vectors were chosen based upon the detection efficiency characteristics as a function of distance along the system axis. These characteristics result primarily from the detection geometry, and the crystal's size and shape. If there are N_d detectors in each row, then the dimension of $\mathcal{R}$ may be as large as N_d^2, if each detector is in coincidence with all detectors in the opposite bank. However, this would result in a system matrix with linearly dependent rows since many of the detector pairs observe the same segment of the system axis. Therefore, all detector pairs which observe the same segment of the system axis are grouped together and their response added. This results in $\mathcal{R}$ and $\mathcal{A}$ having a reduced dimension m, and $\mathcal{S}$ having dimensions m x m, where $m = 2N_d - 1$. The system of equations is therefore completely determined and solvable using standard techniques. The decay distribution, relative to the decay distribution used during calibration, is then given by

$$\mathcal{D} = \mathcal{S}^{-1} \mathcal{R}. \tag{1.3}$$

In practice the system matrix is determined by translating a calibrated ^{22}Na source along the system axis at a constant velocity. Events occurring within a specific time interval are incremented in the appropriate column of the system matrix. The surface plot of a typical system matrix is shown in Figure 1.4. This matrix was generated during a 90 minute calibration run using a 10.4 μCi calibration source and contains over 1.7 x 10^6 coincidence events. The detector banks were separated by 20 cm. If the distance between the rows of detectors is changed, the system matrix must be redetermined. The system matrix and response vector from a calibration run are produced from the same data set and are related by the set of linear equations

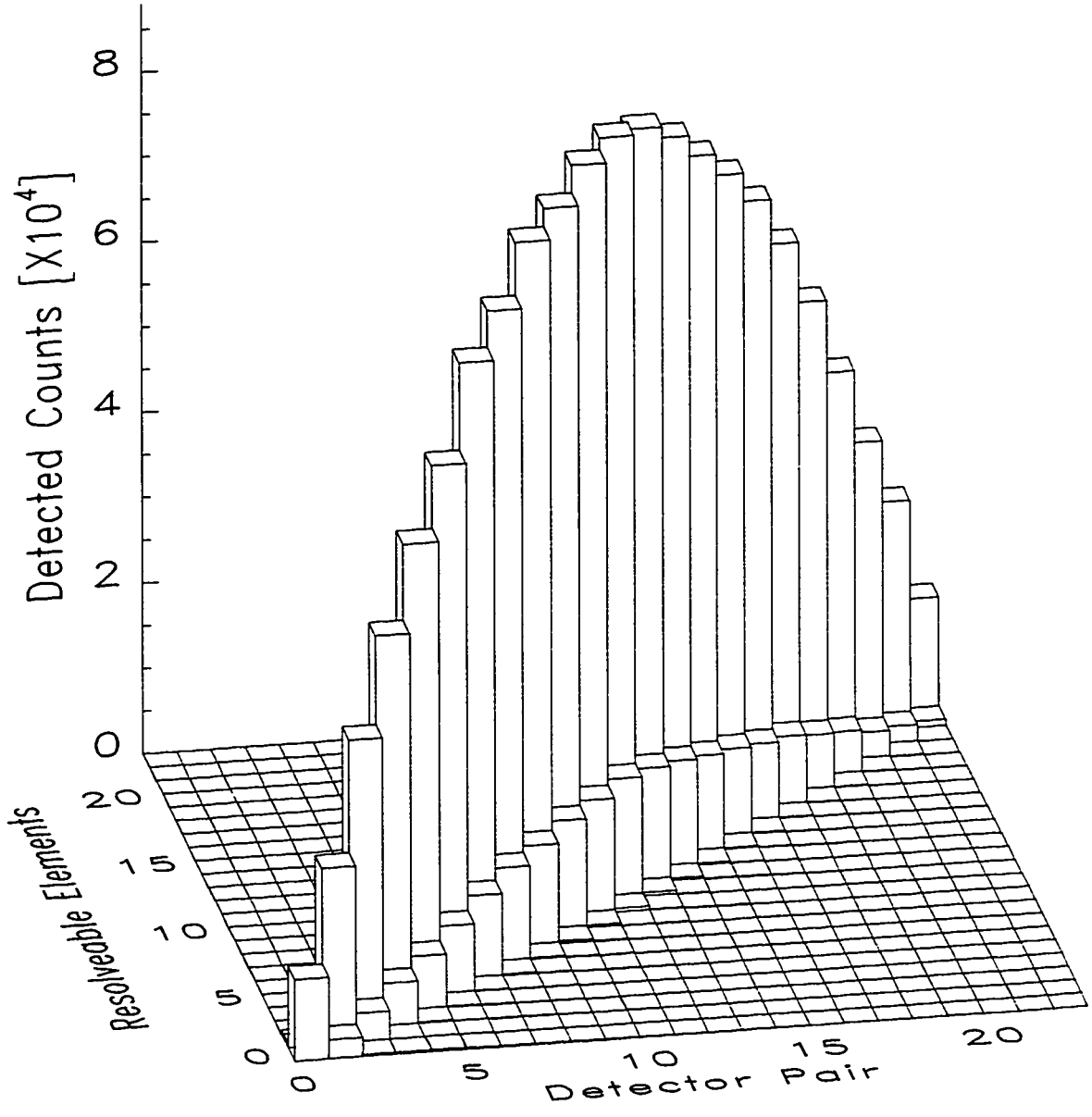

Figure 1.4. Surface plot of a system matrix generated during a typical calibration run. Note that the plot has been rotated 90 degrees counter-clockwise for illustrative purposes.

$$\mathcal{R} = \mathcal{S}\mathbf{1}. \tag{1.4}$$

Here $\mathbf{1}$, is a column vector with m elements, all of which contain the value, one. Substituting (1.3) into (1.2) we find that the decay distribution along the system axis during a calibration run has a value of one, in all elements of the reconstructed distribution. The decay distribution, expressed in the absolute number of decays during the imaging time, $\mathcal{D}_{abs}$, is obtained by normalizing by the number of decays from the calibration source per resolvable element during the calibration run as

$$\mathcal{D}_{abs} = \frac{1}{m}\left(\frac{A_{cal}\, L}{v_s}\right)\mathcal{S}^{-1}\,\mathcal{R}. \tag{1.5}$$

Here, A_{cal}, is the activity of the calibration source in decays per second, L is the length of the imaging array, v_s is the velocity of the calibration source, and m is the number of elements in the decay distribution.

System Matrix Evaluation

The method of eigenvector and eigenvalue analysis [10] was used in the design of the experimental apparatus and will be applied to the Monte Carlo simulation results to be presented in later sections. This method stipulates that the condition number, ζ, of the system matrix will be minimized as a more favorable detector configuration is approached for a specific number of system points. The condition number is defined as

$$\zeta \equiv \frac{\lambda_{max}}{\lambda_{min}} \tag{1.6}$$

where λ_{max} and λ_{min} are the largest and smallest eigenvalues, λ, of the system matrix. As this ratio becomes large the matrix becomes more singular and is said to be ill-conditioned. If the observed segments along the system axis do not overlap and

$$\lambda_i = S_{ii}. \tag{1.7}$$

In this case, the matrix is purely diagonal and the eigenvalues equal the number of counts observed around the corresponding system point. In this case, the condition number is a measure of the relative variance of the magnitude of the point response function over the FOV. If adjacent detectors are placed within a detector's width of each other, the observed segments along the system axis begin to overlap and (1.7) is no longer valid. If detectors are placed irregularly, segments of the system axis will be under- or over-sampled which will cause the eigenvalues to vary greatly.

In more conventional imaging problems involving PET or X-ray CT, the condition number of the system matrix may be quite large. Condition numbers in the thousands are common and in many cases they may be infinite if the system matrices have a nonzero nullspace. However, the system matrix under consideration is of full rank and very well conditioned, with $\zeta < 20$ in all the geometries considered in this work. Because the condition number is a measure of the uniformity of the counting efficiency in the FOV, it is best to minimize this number so that Poisson error does not dominate part of the reconstructed image. Acceptable limits on the condition number vary depending on the intended imaging application. For on-line imaging where the total number of counts acquired is low, the condition number should be roughly 25 or less. While for more prolonged imaging studies acquiring hundreds of thousands of counts, a condition number in the hundreds may be acceptable.

The System Model

A computer simulation using Monte Carlo techniques was written to study the efficiency and imaging characteristics of variations on the detector arrangement shown in Figure 1.1. The detector array and crystal dimensions are shown in Figures 1.2 and 1.3. All experimental and Monte Carlo simulation studies were conducted with twelve detector pairs. This model simulates the calibration of the imaging system and gives the

system matrix and the *CDE* along the system axis for a given detector arrangement. The *CDE* is defined as the number of detected coincidences divided by the total number of positron annihilations at a given location along the system axis during a fixed time interval. The *CDE* and system matrix are obtained from the same data but the *CDE* contains no detector pair information. The *CDE* is vector whose elements contain the sum of the columns of an arbitrarily over-determined system matrix as given by (1.4).

Calibrations were performed prior to conducting imaging experiments using an Isotope Products Laboratories type-D standardized ^{22}Na source which was translated along the system axis with a constant velocity. The disk-shaped source was placed on edge in a Lucite holder with the flat sides parallel to the detector faces. The active area of the circular ^{22}Na deposit had a radius of 0.25 cm and was of negligible thickness. The energy spectrum of the positrons emitted by ^{22}Na peaks just below 0.2 MeV with an endpoint energy of 0.546 MeV. The maximum range of the positrons in Lucite is 0.15 cm.

The system model generates a random location for the position of the center of the ^{22}Na disk along the system axis from a uniform distribution for each event. A random location on the disk is then chosen for the emission of a positron. The positron's energy is randomly sampled from the inverse of the known cumulative energy distribution and linearly scaled to find its maximum range. A random range between zero and the maximum range is uniformly chosen neglecting backscatter. The positron is emitted isotropically and its final annihilation position is calculated. The direction of one of the annihilation 511 keV gamma-rays is generated isotropically. If attenuating material is present between the activity and the detectors, the pathlength, l, of the gamma-ray through the material is calculated and the transmission determined by sampling the distribution $I(l) / I_o = \exp(-(\mu / \rho) \cdot \rho \cdot l)$, where (μ/ρ) is the mass attenuation coefficient of the material and ρ is its density. If the gamma-ray is scattered, a new decay is initiated. Likewise, if the path of the gamma-ray does not intersect a cylindrical volume

defined by a crystal, a new decay event is generated. If the gamma-ray does intersect one or more crystals, the pathlengths in the successive layers of lead and BGO are calculated and the location and material of interaction determined. This process continues until the gamma-ray interacts or passes out of the detector array. If the gamma-ray interacts in a crystal the direction of the second, collinear, 511 keV gamma-ray is then calculated. The small, non-collinear effects due to positronium center-of-mass motion are not considered. The second gamma-ray is then followed until it interacts or passes out of the array.

The mass attenuation coefficients of all materials in the system model were calculated [11] using

$$\mu/\rho = \sum_i w_i \cdot (\mu/\rho)_i, \tag{1.8}$$

where, w_i, is the mass fraction of the atomic constituents. The values at 511 keV were calculated by linear interpolation between the values given at 500 keV and 600 keV. While the linear interpolation will introduce a small error, the bulk of the error in the mass attenuation coefficients arises from the uncertainties in the calculated mass attenuation coefficients for each element. In the energy range between 10 keV and 10 MeV, the quoted uncertainty is ±2% for all elements [11]. For compounds and mixtures, the error in the mass attenuation coefficient is then given by the square root of the weighted error for each element when added in quadrature. Uncertainties are also present in the densities of the lead and Solid Water™ [12] due to impurities and methods of preparation. Density variation for Lucite and BGO are assumed to be less than 1%. Table 1.1 lists the physical values of the mass attenuation coefficients and densities of all materials simulated in the code and their estimated uncertainty.

Due to the large volume and high density of the BGO crystals, no attempt is made to follow the Compton scattered secondaries. The maximum range of Compton scattered

Material	Mass Attenuation, $(\mu/\rho)_{511}$ (cm^2/g)	Density, ρ (g/cm^3)
Lead	0.1577 ± 0.0032	11.25 ± 0.15
Lucite	0.0933 ± 0.0012	1.19
Solid Water™ 457	0.0934 ± 0.0012	1.035 ± 0.005
BGO	0.1362 ± 0.0020	7.13

Table 1.1. Physical values of the mass attenuation coefficients and densities used to simulated materials in the model of the detection system.

electrons from 511 keV gamma-rays in BGO is less than 0.2 mm and the probability of them escaping a crystal is roughly 1%. However, the Compton scattered gammas are more likely to escape the crystal. These are handled statistically by multiplying the *CDE* by the experimentally determined photopeak efficiency. This was measured by setting the discrimination threshold just above the background and recording the singles spectrum as the calibration source was translated along the system axis. The photopeak efficiency was found to be 51% using the same energy window used during imaging experiments.

Validation of the System Model

Simulation results were compared with results from calibration runs performed during previous experiments to confirm the validity of the system model. The values of the mass attenuation coefficients used for all comparisons are shown in Table 1.1. The spacing between adjacent crystals, s, is 0.50 cm, the crystal length, l, is 5.08 cm, and attenuation due to the Lucite source holder is included. Figure 1.5 shows the experimental and simulated *CDE*, for detector separations, $2d$, of 20 cm and 60 cm.

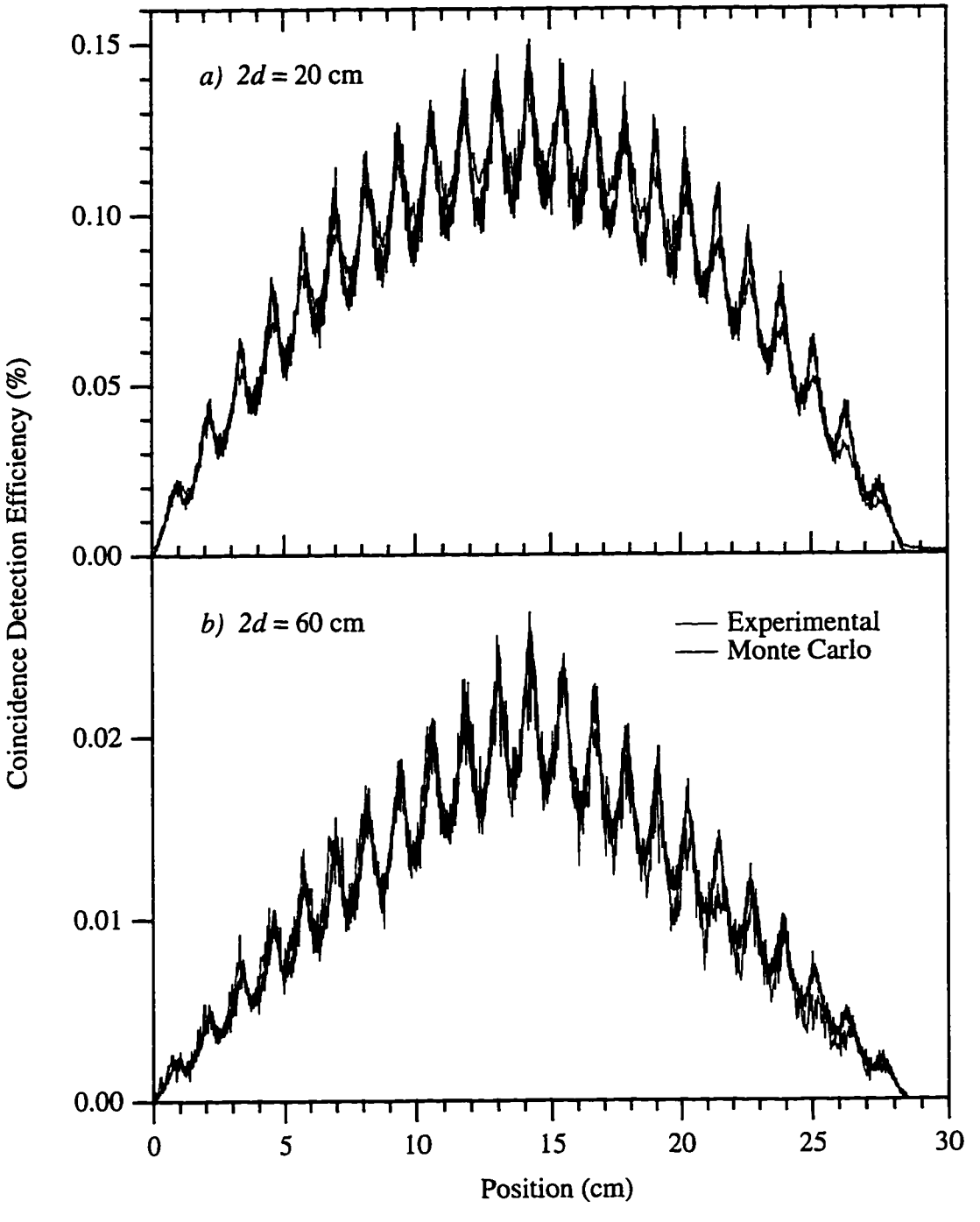

Figure 1.5. Comparison of Monte Carlo simulation and experimentally measured *CDE*'s with no attenuating material. (*s = 0.5 cm, 2d = 20 and 60 cm, l = 5.08 cm, t = 0 cm + 0.5 cm Lucite*)

The functional form of the experimental *CDE* is well described by the system model. The average *CDE*, $\overline{CDE}$, when the detector separation, *2d*, was 20 cm, was experimentally found to be 7.80 x 10^{-2}% while the value obtained from the simulated results was 7.74 x 10^{-2}%. When the detector separation was 60 cm the experimental and simulated $\overline{CDE}$ were found to be 1.10 x 10^{-2}% and 1.12 x 10^{-2}%, respectively. The experimental results agree with those simulated by the system model to within ±2%.

Results

The following sections present the simulation results of variations in the spacing, *s*, between adjacent crystals, the distance, *d*, from the beam to the front surface of a row of detectors, the length, *l*, of the crystals, and the mass attenuation coefficient $(\mu/\rho)_{511}$ of the intercrystal shielding. We then show that the depth-of-interaction blurring caused by crystal penetration is removed by the calibration and image reconstruction techniques and discuss the practical limitations of the technique. Finally, the effects of extended activity distributions and the presence of varying thicknesses, *t*, of Solid Water™ [12] attenuation are described. The values of dimensions held constant in a study were determined by the properties of the experimental apparatus. No attenuating material is included in the system model except during attenuation studies. In all studies, the crystal radius, r_d, and the radius, r_h, of the hole in the shielding remained constant at 1.90 cm and 2.22 cm, respectively.

Monte Carlo Results for Variations in Crystal Spacing:

There are several tradeoffs to be considered when choosing the spacing between adjacent crystals. The FWHM resolution of the system, R, is roughly, (r_d + s/2) and worsens as the spacing, s, increases. As mentioned earlier, if the space between the detectors is more than a detector's width or diameter then the observed segments along the system axis will not overlap, leaving intermediate positions unsampled. However, to monitor the longest

possible portion of the beam path with a fixed number of detectors it is not cost efficient to place the crystals immediately next to each other. Figure 1.6 shows the *CDE* for detector spacings, s, of 0.2, 0.4, 0.8 and 1.6 cm. As the spacing between adjacent detectors increases the system points or peaks of coincidence detection efficiency decouple and the $\overline{CDE}$ decreases. These simulations were performed with a detector separation, *2d*, of 20 cm and 5.08 cm long crystals. Figure 1.7 shows the condition number and resolution for crystal spacings, *s*, from 0.2 cm to 2.9 cm. As the space between adjacent crystals decreases, the resolution improves and the system matrix becomes less well-conditioned. The overlap in observed segments along the system axis increases the off-diagonal elements of the system matrix and increases the correlation between resolvable elements along the system axis. As the correlation increases, the error in a given element of the resulting image depends more on the value of adjacent elements. The resolution then approaches the physical limit determined by the positron range, detector size, and the attenuation length of 511 keV gamma-rays in BGO regardless of how closely spaced the system points are chosen. If the best possible resolution is required, the space between the detectors should be made as small as possible. The effects of removing the intercrystal shielding, and consequently reducing the spacing, will be discussed in sections II. F. 4 and 5. For a discussion of the effects on crystal spacing for a series of rectangular crystals see [13].

Monte Carlo Results for Variations in Detector Separation:

It is desirable to have as high a coincidence detection rate as possible while imaging between beam pulses to perform on-line imaging. Figure 1.8 shows the $\overline{CDE}$ and condition number for detector separations, *2d*, from 10 cm to 65 cm. As the separation increases and efficiency decreases, the condition number increases. At larger detector separations the *CDE* as a function of position along the axis is more peaked in the center as shown in Figure 1.9. The center element along the system axis is observed

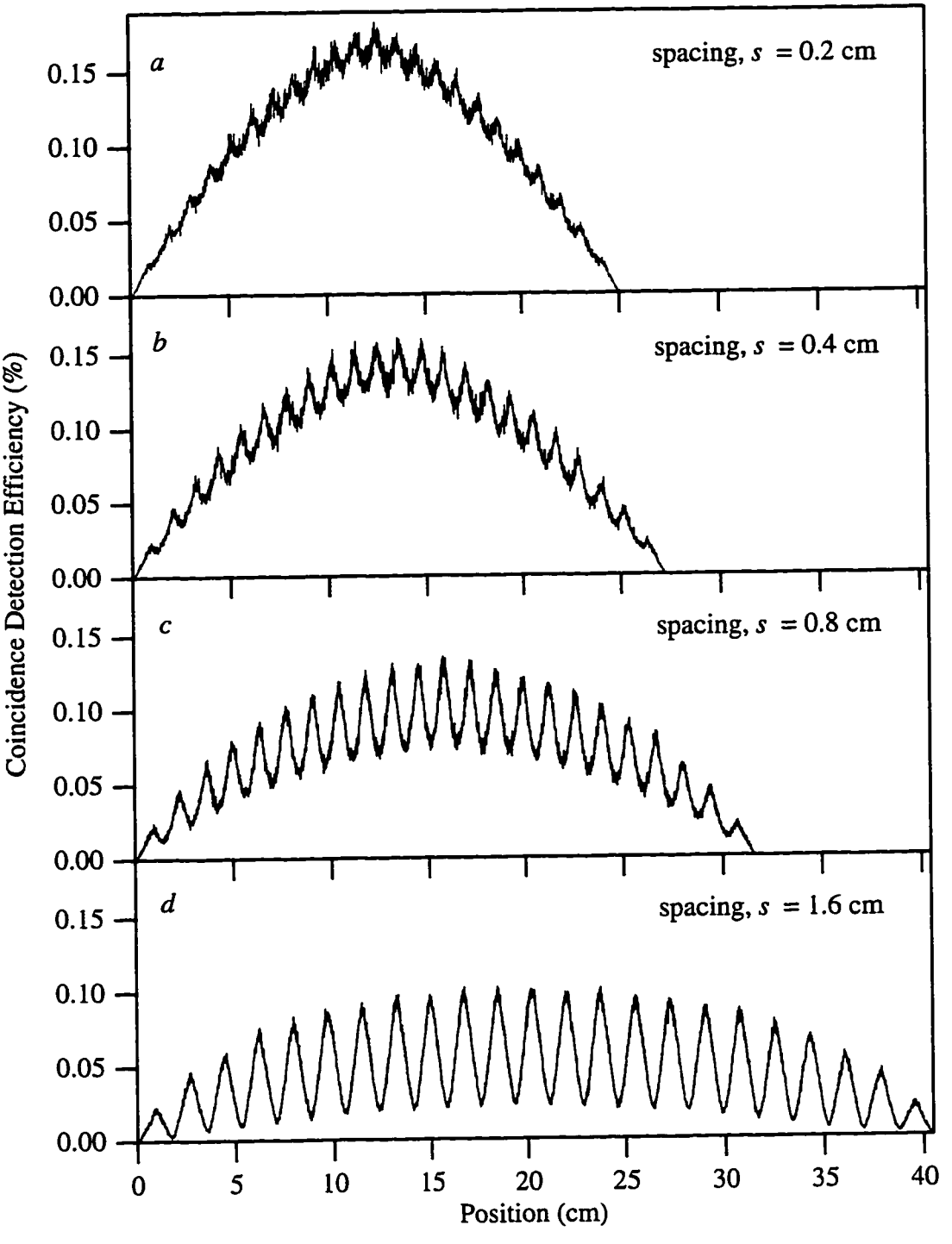

Figure 1.6. Simulated *CDE* versus detector spacing, *s*. (s = 0.2, 0.4, 0.8 and 1.6 cm, l = 5.08 cm, $2d$ = 20 cm, t = 0 cm)

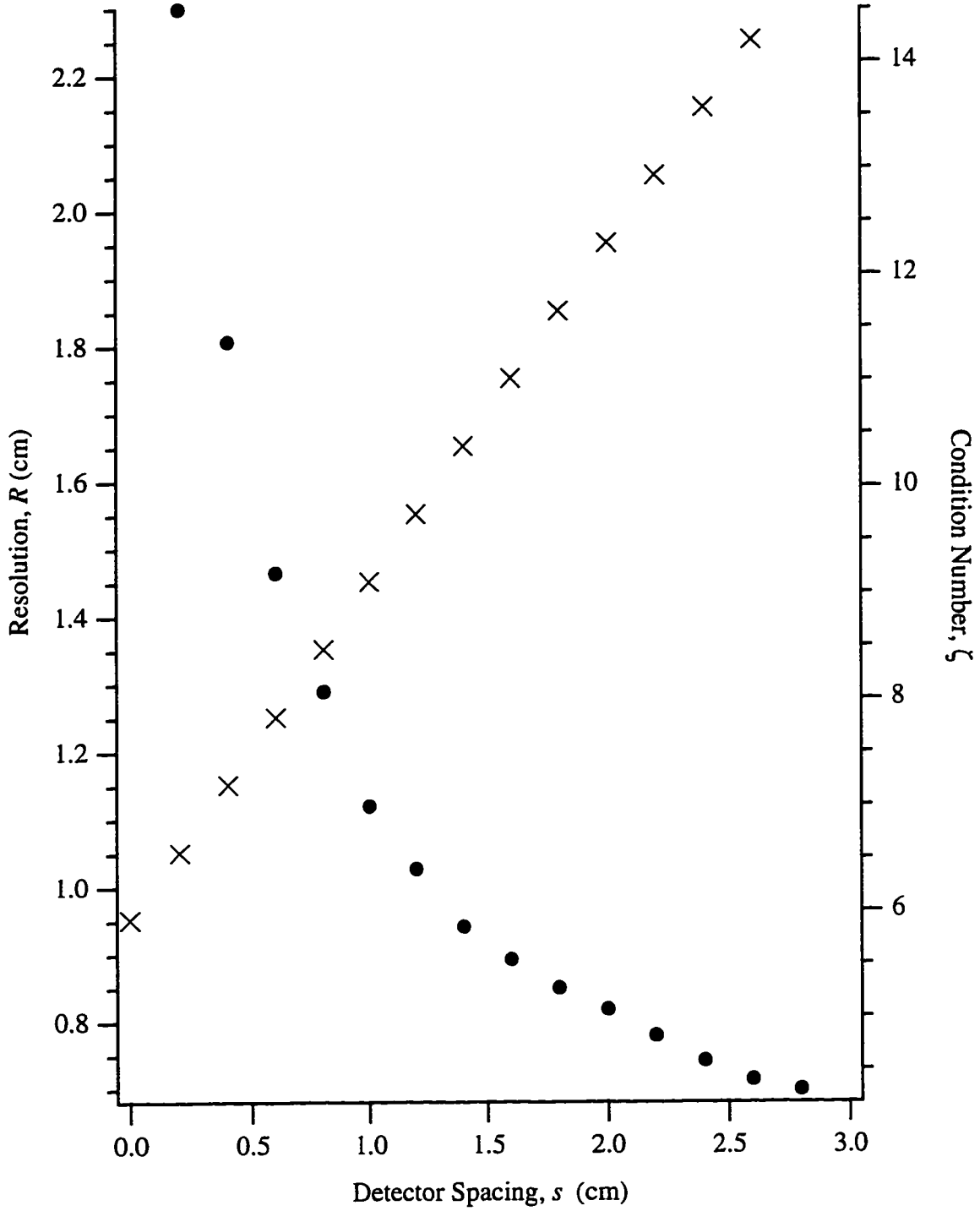

Figure 1.7. Simulated condition number, ζ, (•) and resolution versus detector spacing, s, (x) for a lead shielded, BGO array. (l = *5.08 cm*, $2d$ = *20 cm*, t = *0 cm*)

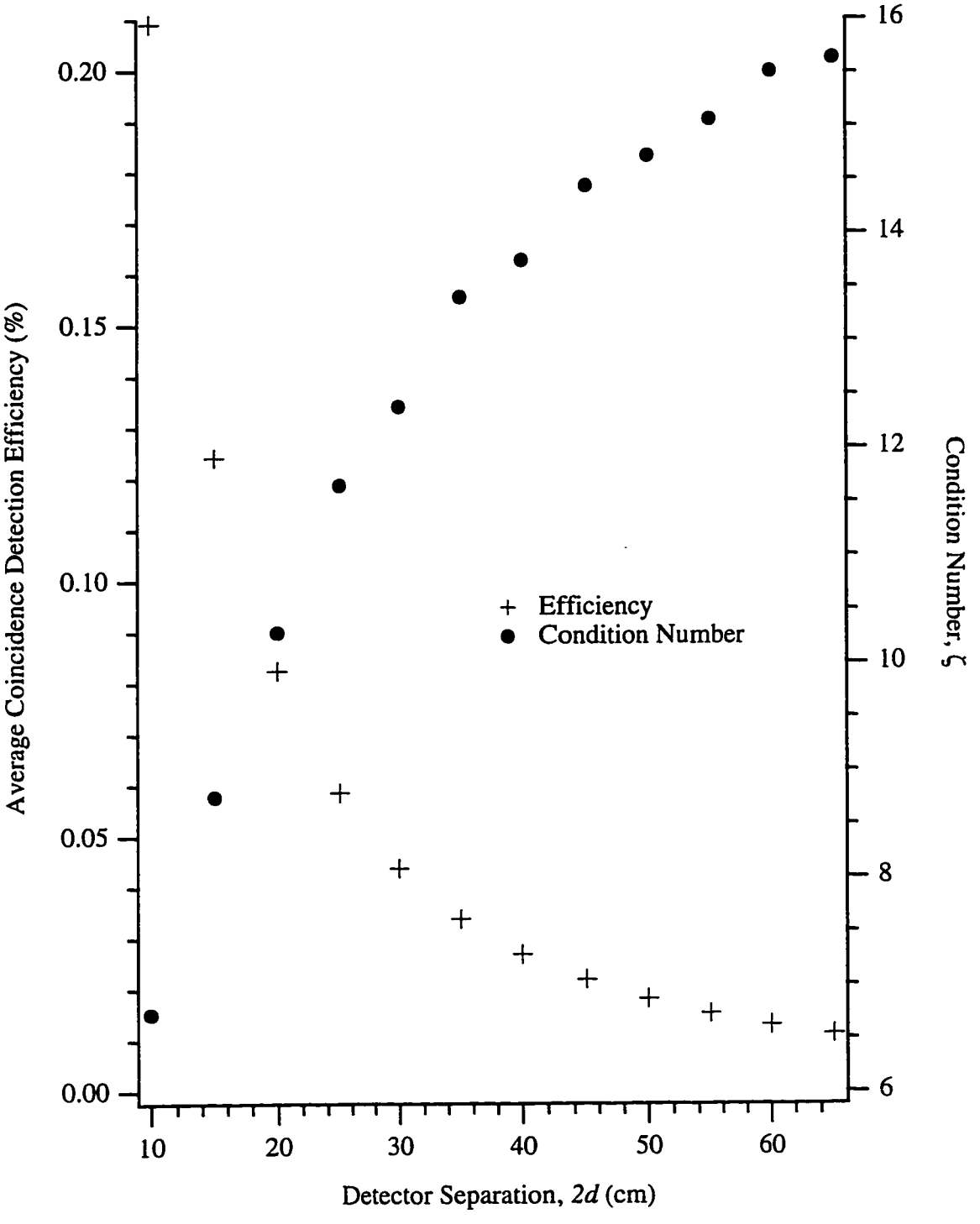

Figure 1.8. Simulated $\overline{CDE}$ and condition number versus detector separation, $2d$, for a lead shielded, BGO array. ($s = 0.5$ *cm*, $l = 5.08$, $t = 0$ *cm*)

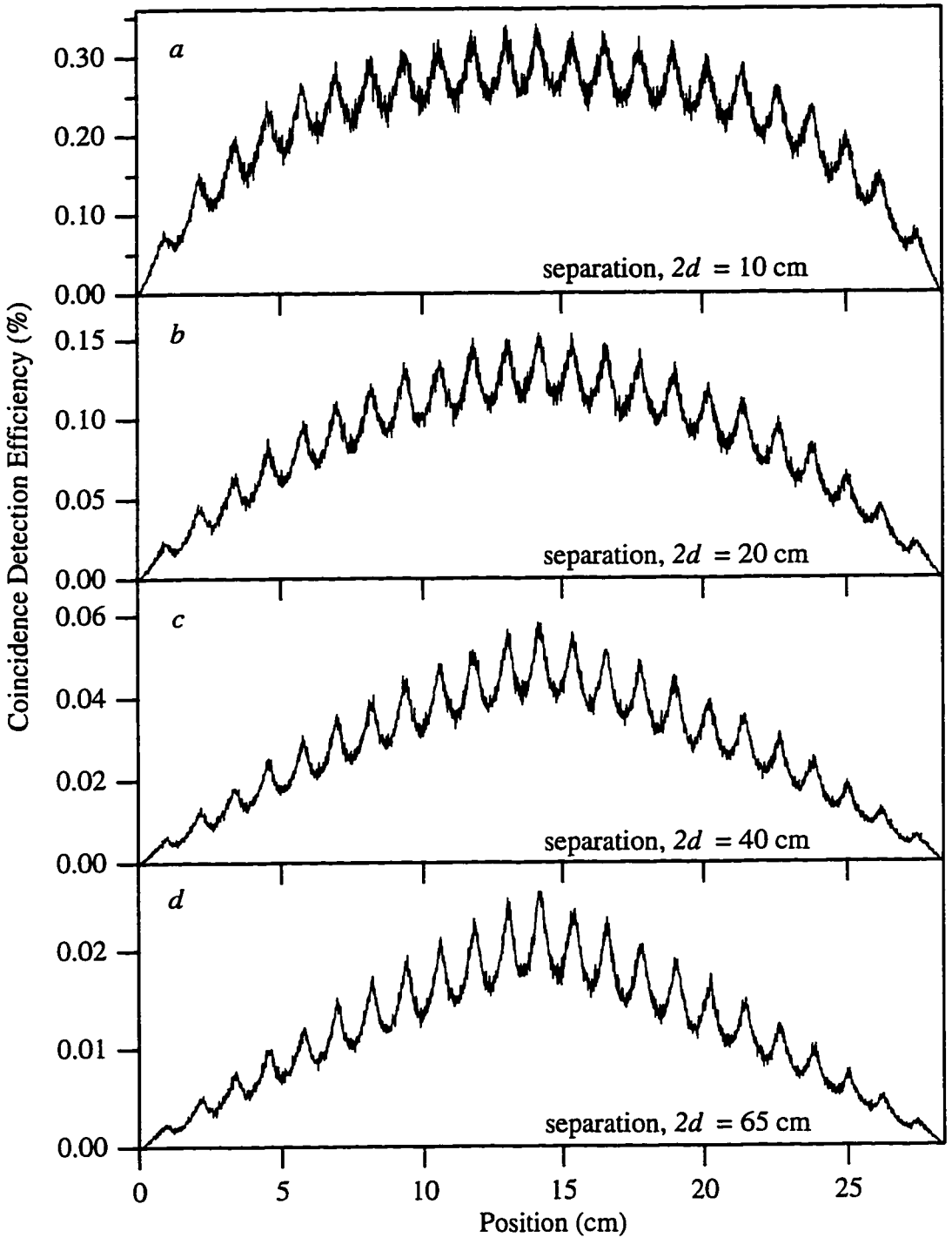

Figure 1.9. Simulated *CDE* versus detector separation, *2d*. (*s = 0.5 cm, l = 5.08 cm, t = 0 cm*)

by N_d, detector pairs. As the detector separation increases the solid angle for each of the detector pairs approaches the same value. In addition, the maximum possible pathlength in the BGO increases as the gamma-rays detected in coincidence become more parallel to the cylindrical axis of the crystal. Thus at separations large compared to the length of the array each detector pair contributes roughly the same detection efficiency. At smaller detector separations, more oblique detector pairs contribute less to the detection efficiency than detector pairs at $\theta = 90^\circ$ to the system axis. This produces a less peaked overall coincidence detection efficiency at the center of the array. The system axis is more uniformly sampled at smaller detector separations resulting in a lower condition number. However, even at a separation of 65 cm the system matrix is very well conditioned, $\zeta < 16$, and easily inverted. Therefore, it is best to minimize the separation of the two detector banks to increase the detection efficiency as long as the data acquisition system's deadtime does not become excessive for the deadtime correction techniques used in image reconstruction. However, as the separation decreases the image may become blurred if the activity distribution is extended in the plane of the detectors. This will be discussed in greater detail in a later section.

Similar effects to those discussed above are observed if the length of the detection array is increased by adding detector pairs. Once the length of the array is roughly the same as the detector separation the solid angle for the most oblique coincidences becomes relatively small. Consequently these added detector pairs do not contribute significantly to the CDE and the condition number doesn't increase significantly. However, if the separation of the detectors is large compared to the length of the array, each detector pair contributes roughly the same solid angle for detecting coincidences and the condition number and $\overline{CDE}$ increases almost linearly with the number of detector pairs.

Monte Carlo Results for the Effects of Crystal Length

It is important to select a scintillation crystal of the appropriate length to maximize the detection efficiency relative to the detector cost. While the optimum crystal length is generally considered to be three attenuation lengths, cameras which accept coincidence events at large angles to the crystal axis may use shorter crystals to obtain the same average efficiency. Simulations of the *CDE* at detector separations, *2d*, of 20 cm and 60 cm were performed with BGO crystal lengths of one through five centimeters. The $\overline{CDE}$ are shown in Figure 1.10 and have been plotted on the left and right axes, for detector separations of 20 cm and 60 cm respectively. The data points for the five centimeter crystal lengths were graphically normalized to 100% efficiency. The five centimeter crystals will be 99.9% efficient regardless of the detector separations due to the 1.1 cm attenuation length of 511 keV gamma-rays in BGO. Smaller detector separations with more oblique coincidence acceptance angles are slightly more efficient due to the longer possible pathlength. However, unless the detector separation is expected to be fixed, the optimum detector length remains three attenuation lengths. The impact of this effect would be more significant in a block detector design which has no intercrystal shielding. The five centimeter long BGO crystals used in this array will also be used in other physics experiments and were chosen to accommodate the present and future requirements.

Monte Carlo Results on the Effects of Intercrystal Shielding on Efficiency

The radiation environment in which the imaging system operates includes high and low energy background produced by the radiotherapy beam in addition to the positron-emitting activity being imaged. The lead shielding which encapsulates each of the detectors therefore serves to reduce background rates and as intercrystal shielding to suppress Compton scattered secondaries. However, the presence of shielding significantly reduces the detection efficiency along the system axis. Simulation results of

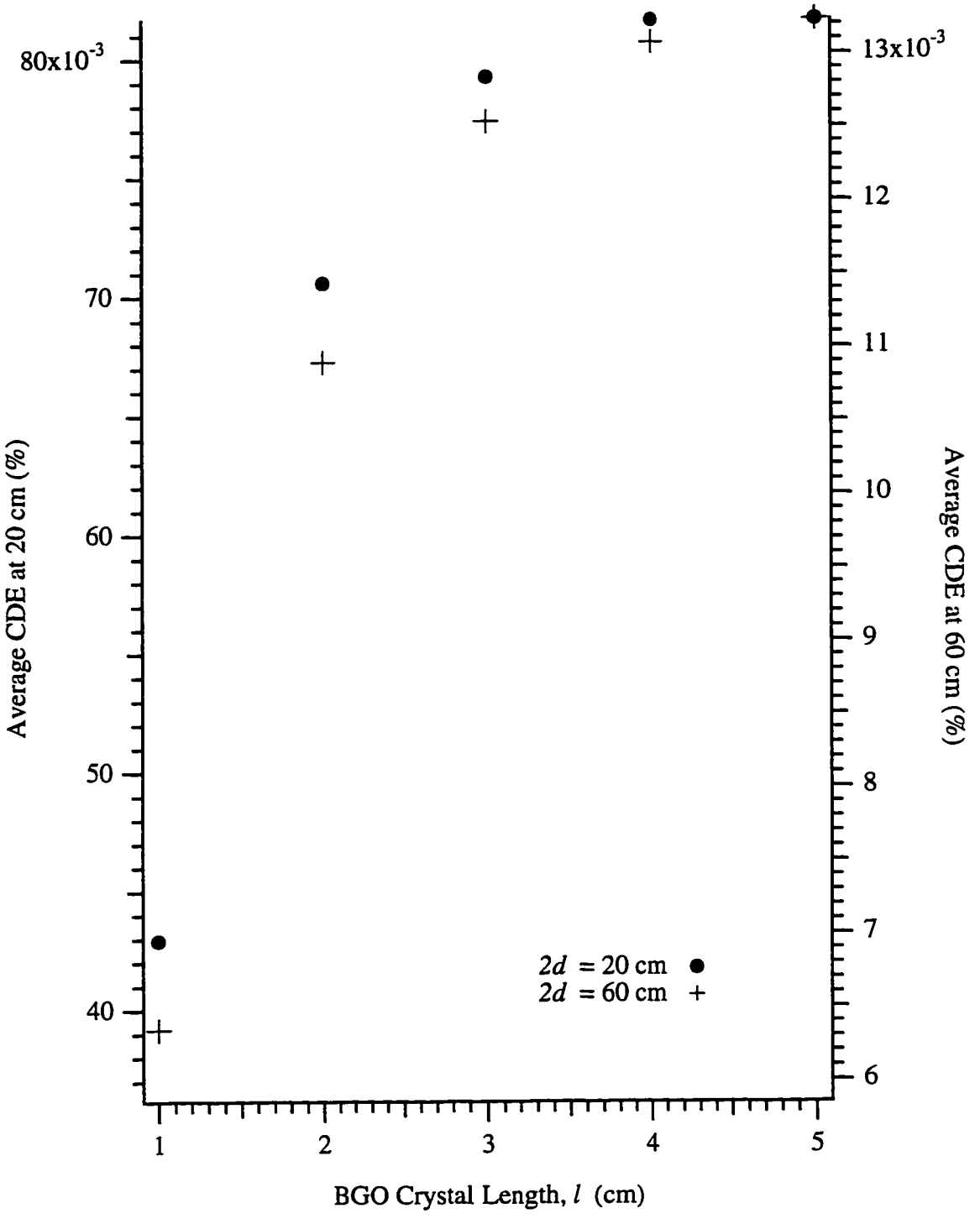

Figure 1.10. Simulated $\overline{CDE}$ versus crystal length, l, for detector separations, $2d$, of 20 cm and 60 cm. The plots have been graphically normalized at crystal lengths, $l = 5$ *cm*, for comparison. ($s = 0.5$ *cm*, $t = 0$ *cm*)

the detection efficiency with no intercrystal shielding, lead shielding and impenetrable shielding are shown in Figure 1.11. Comparing Figure 1.11*b* and 1.11*c* shows that the $\overline{CDE}$ increases by 28% for lead shielding over ideal, impenetrable shielding. If the lead is removed the $\overline{CDE}$ increases by 63%. The local efficiency peaks of the *CDE* become less defined as the intercrystal shielding material becomes less attenuating, due to the detection of gamma-rays entering through the sides of the crystals.

Intercrystal shielding is typically used in high-resolution imaging systems to reduce the detection of Compton scattered secondaries in adjacent crystals. The PRF of these systems is decreased resulting in less blurred images. However, to obtain the highest *CDE* possible for on-line imaging, the intercrystal shielding should be omitted. The calibration technique used in this system records the crystal penetration probabilities in the system matrix. The effects are then removed in the reconstructed image as further explained in the next section.

Removal of Depth of Interaction (DOI) Blurring

Until recently most image reconstruction algorithms used in PET imaging assumed that the positron annihilation event occurred between the faces of the two crystals which detected the 511 keV gamma-rays. This is not always true since one or both of the annihilation gamma-rays may penetrate one or more detection crystals and the intercrystal shielding. This gives the appearance that the annihilation event occurred at a slightly different location causing images to become blurred due to a shifted, broadened and skewed PRF. The use of flood phantoms for calibrating these systems prevents the true coordinates of the annihilation event from being otherwise determined and corrected.

Prior to our experiments the on-line imaging system was calibrated using a translated source, whose position is known at all times, instead of using a line source of constant activity. The known location of the source is used to determine the correct column of the system matrix to index when a detected event is binned. The probability of

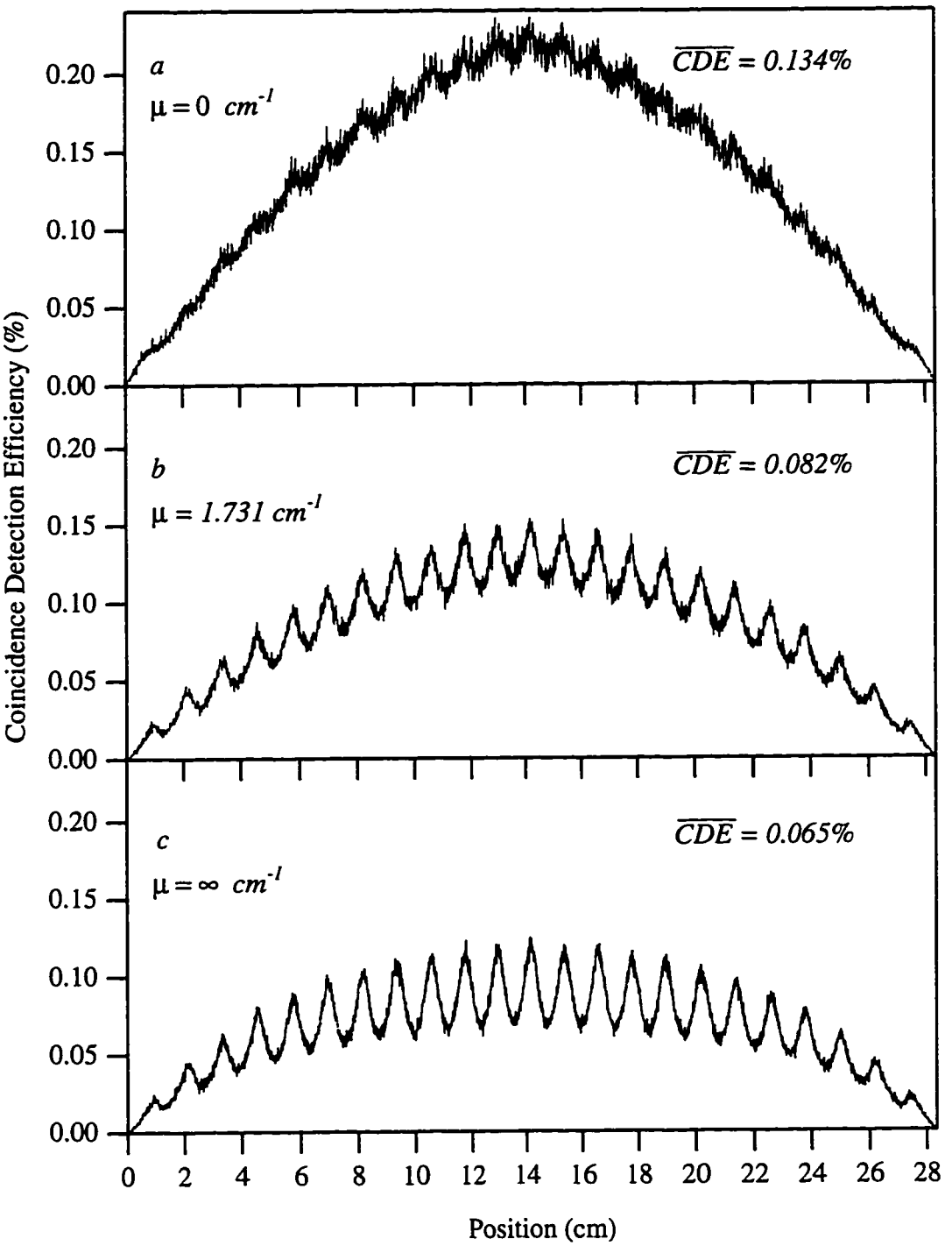

Figure 1.11 Simulated *CDE* versus intercrystal shielding attenuation coefficient, μ. Plot *a* shows the *CDE* with no shielding. Plots *b* and *c* are the *CDE* for lead and ideal shielding, respectively. ($s = 0.5$ *cm*, $l = 5.08$ *cm*, $t = 0$ *cm*)

crystal penetration and scatter is contained in the off-axis elements of the appropriate column in the system matrix. The DOI blurring effect associated with axial tomography is therefore corrected by means of the calibration process and image reconstruction algorithm in this system.

To verify this correction, we imaged the calibration source at several different locations along the system axis and examined the response vectors, $\mathcal{R}$, and the corresponding reconstructed image vectors, $\mathcal{A}$. Two of these vector pairs are shown in Figure 1.12. The lead shielding was in place between the detectors and the detector separation, $2d$, was 20 cm during these experiments. This small separation greatly increases the probability of detector and shielding penetration for oblique detector pairs monitoring activity at the center of the array. Conversely, gamma-rays originating near the end of the array are less likely to penetrate the crystals because they are nearly parallel to the crystal axis due to the coincidence requirement. We therefore expect the largest number of misregistrations to occur for activity near the center of the array, as seen in Figure 1.12*a*. Activity centered in a given "pixel" is expected to give a symmetrical peak in the response vector due to the coincidence requirement and the short attenuation length of the BGO and lead. Some asymmetry is observed in the last two to three centimeters of the response vector due to gamma-rays passing out the ends of the array. However, this end effect is also contained within the system matrix. Figure 1.12*b* shows that the image of a small source is the same in the center of the array as it is near the ends and that the DOI blurring and end effects are corrected. Simulations of the experiments above, but with no intercrystal shielding, show a three-fold increase in the number of crystal penetrations. Using a system matrix generated with no shielding in the simulation yields corrected images similar to those found experimentally.

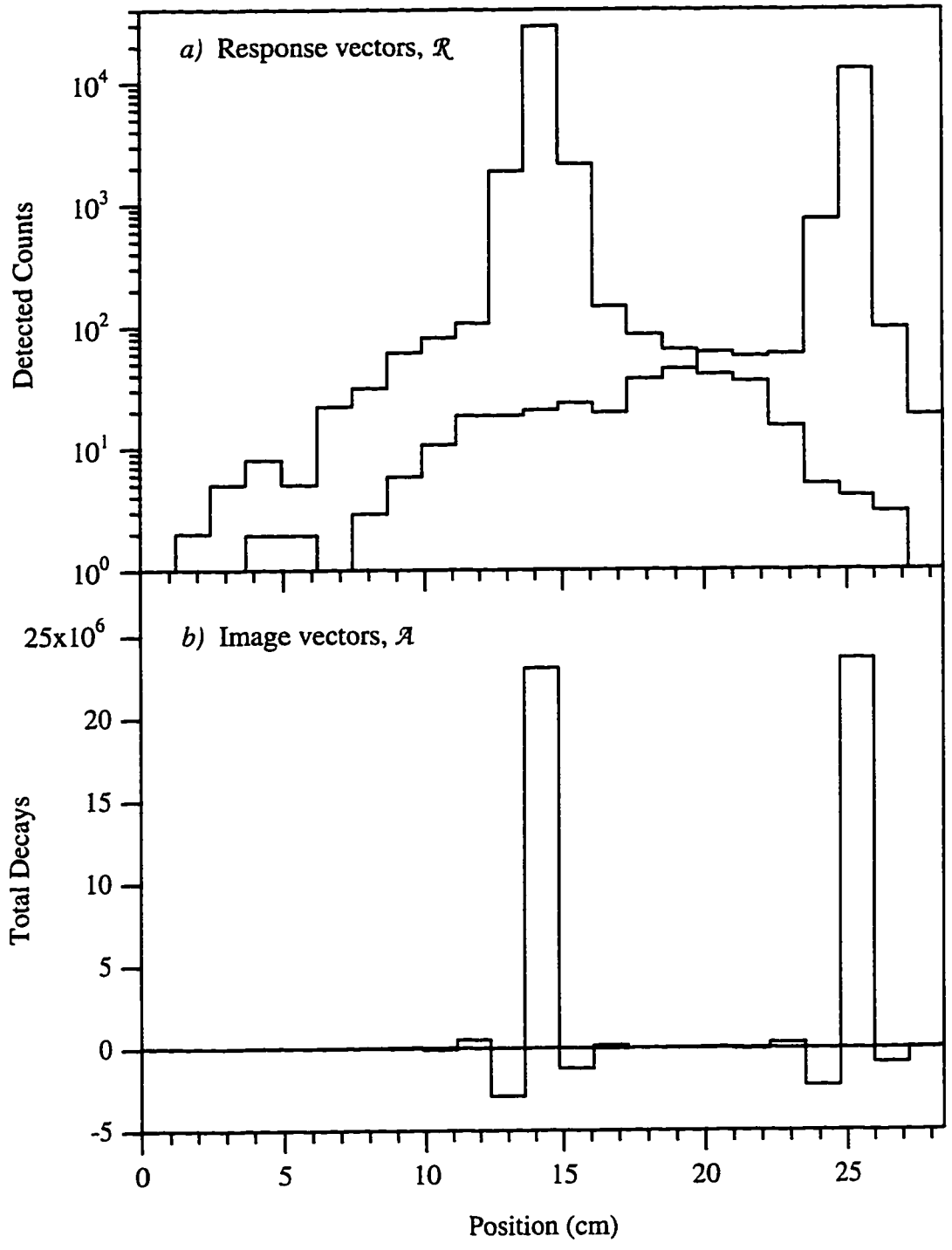

Figure 1.12. Response and image vectors of the calibration source placed near the center and end of the array. Effects of crystal penetration and gamma-rays escaping from the ends of the array are evident in bins adjacent to the primary bins.

This implies that the spatial resolution limits of future systems employing this calibration technique and reconstruction algorithm are limited primarily by the crystal width, positron range and, for strongly coupled detection systems, crystal identification error. In Figure 1.12 it can be seen that the FWHM resolution of the 0.5 cm diameter calibration source is less than or equal to the resolution limit, $(r_d + s/2)$, imposed by the detector dimensions. There are two primary practical limitations to this technique. If the calibration source is spatially extended along the system axis, the origin of the emitted positron is uncertain within half the width of the source, $\pm(w_s / 2)$. Additionally, the positrons range will also add to the uncertainty in the location of the annihilation event. Since the columns of the system matrix are binning according to the location of the center of the calibration source this causes a small correlation between adjacent pixels and consequently, a degradation to the spatial resolution of the reconstructed images. This effect is the primary cause of the negative values which arise in the reconstructed image vectors. These uncertainties may be reduced by using a calibration source whose spatial extent along the system axis is small and by wrapping the source in a thin layer of high-Z material to reduce the range of the positrons.

Effects of Off-Axis Activity

As the activity distribution created by the radiotherapy beam becomes more extended, image quality and detection efficiency decrease. A vertical spread in the activity distribution out of the plane of the detectors quickly decreases the solid angle available for coincidence detection. If a line source on the axis of the system is replaced by a vertical planar source of the same activity with dimensions, $(L) \times (2r_d)$, the number of detected events decreases by roughly a factor of two. The detection efficiency in the plane of the detectors is not significantly reduced for activity not located on the system axis. Figure 1.13 shows a simulation of the *CDE* for the calibration activity distribution

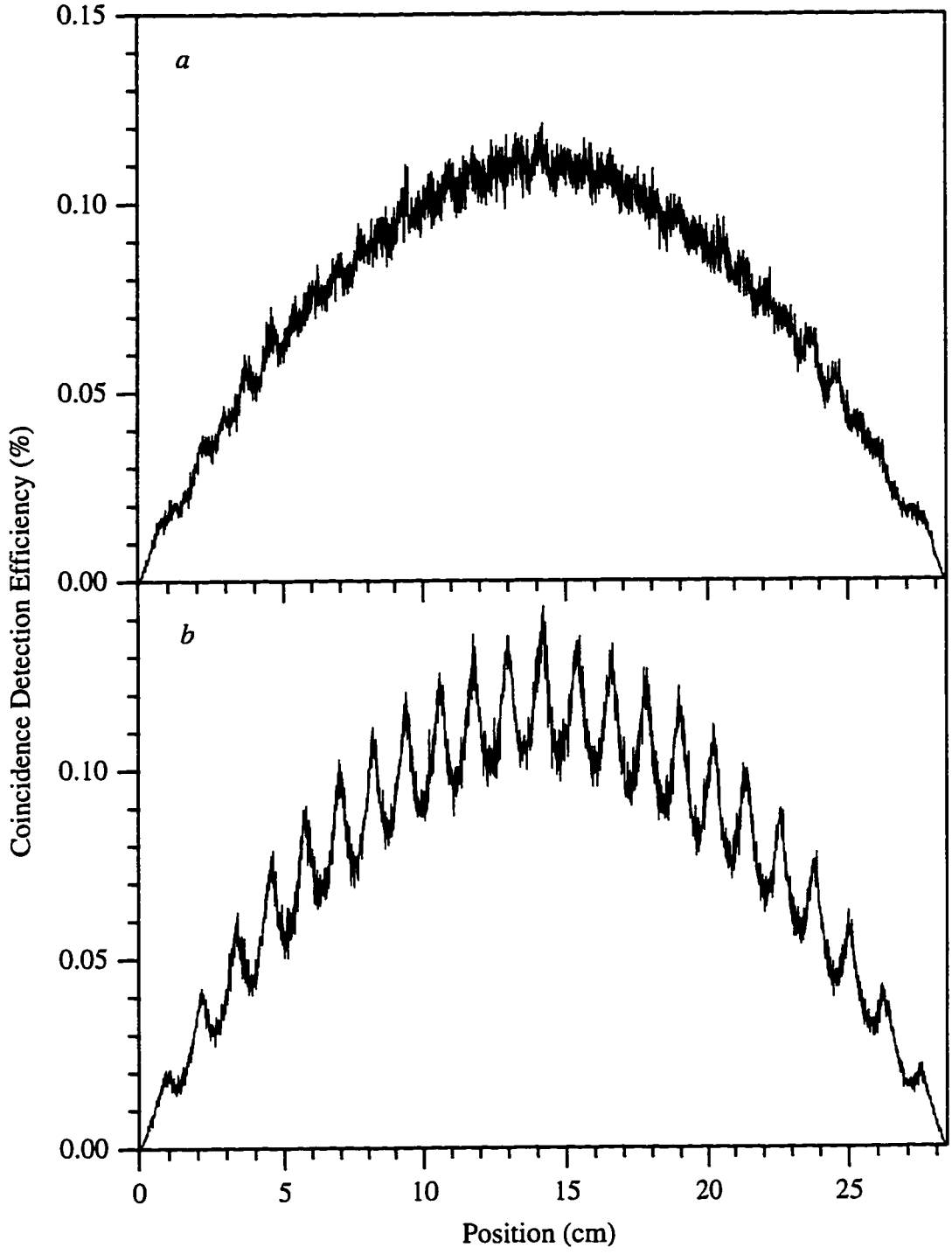

Figure 1.13. Simulated *CDE* for a calibration source translated parallel and 3 cm away from the system axis in the plane of the detectors. ($s = 0.5$ *cm*, $l = 5.08$ *cm*, $2d = 20$ *cm*, $t = 0$ *cm*)

described earlier which has been placed parallel to and three centimeters off the system axis in the plane of the detectors. On average this exhibits the same efficiency as when placed on axis, Figure 1.13*b*, but lacks the same structure due to a magnified PRF for off-axis activity. Figure 1.14 shows the PRF at the center of the axis for a point of activity 0, 1, 2, and 3 cm off axis. These PRF were generated from an experimentally determined system matrix, $\mathcal{S}$, and simulated response vectors, $\mathcal{R}$. The detector banks were separated by 20 cm and adjacent crystals were spaced 0.5 cm apart. The system matrix contained over 1.7 x 10^6 events and each of the response vectors contained 10^4 events.

The following geometrical argument may be used to roughly determine the maximum acceptable width of the activity distribution for a given detector configuration. Consider the detector configuration shown in Figure 1.15. Suppose a line of activity, $\overline{AB}$, occurs a distance, $w/2$, away from and parallel to the system axis such that the back projection of a point on $\overline{AB}$ gives the line segment $\overline{CD}$. To minimize the blurring effects of the off-axis activity the length of the line segment, $\overline{CD}$, should be no larger than the resolution limit, R, imposed by the detector dimensions, which is roughly $(r_d + s/2)$. The maximum acceptable width, w, of the activity distribution is estimated to be

$$w = \frac{2dR}{L - R}, \tag{1.9}$$

using similar triangles. For activity distributions significantly wider than w, substantial errors will be introduced in the final image by the blurring effect of the outlying activity. Ideally, (1.9) could be used to determine the detector separation, $2d$, from the desired width of the treatment beam. This, however, leads to very large detector separations even for systems with poor resolution. As shown in an earlier section, the $\overline{CDE}$ decreases quickly with increasing detector separation making on-line imaging more difficult. If the activity distribution exceeds the width given by (1.9) it is generally best to maximize the detector separation based on the maximum time available and minimum number of counts required to obtain an image. For this system a detector separation, $2d$, of 60 cm

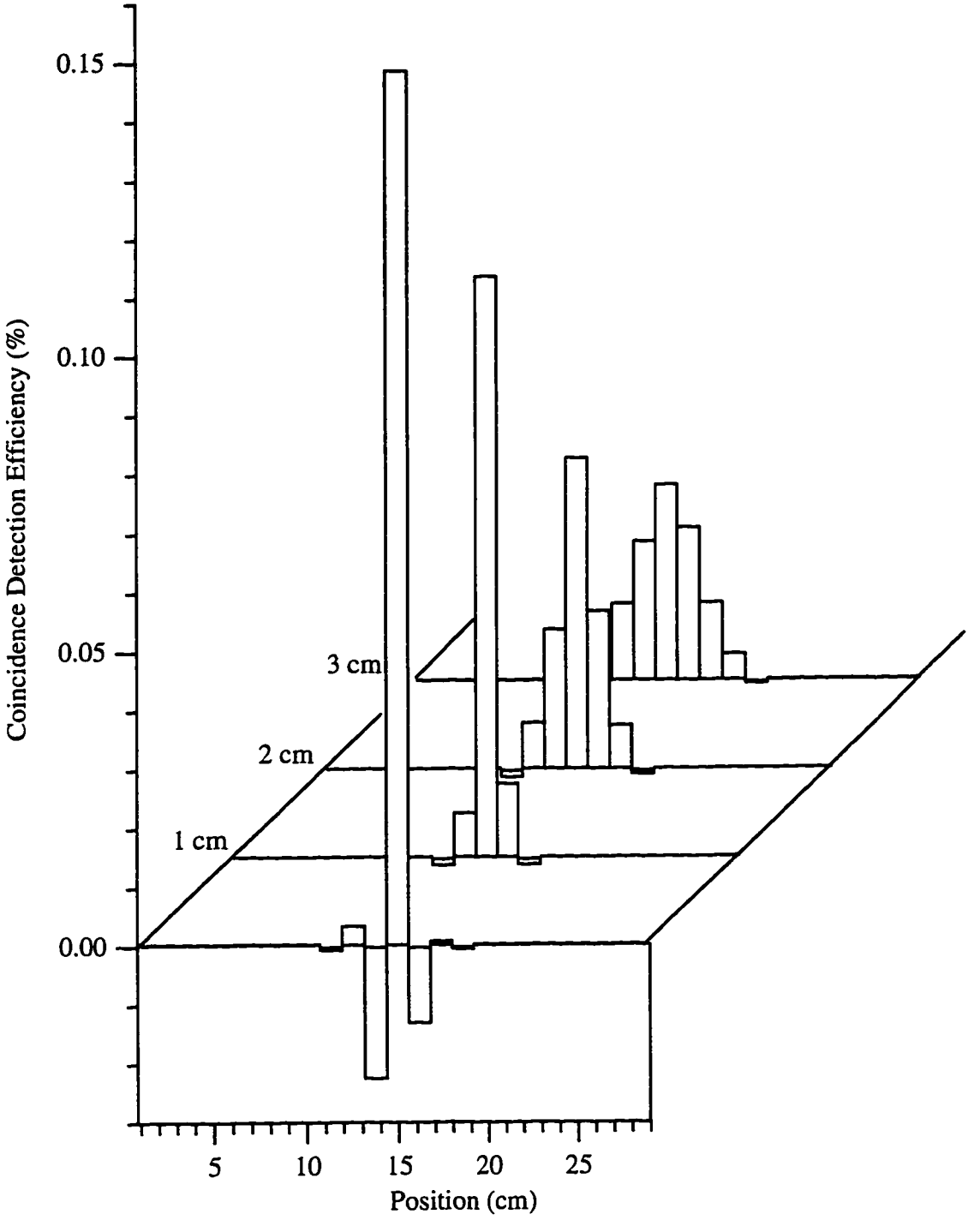

Figure 1.14. Reconstructed point response functions for point sources placed 0, 1, 2, and 3 cm from the system axis in the plane of the detectors at the center of the array. (*s = 0.5 cm, l = 5.08 cm, 2d = 20 cm, t = 0 cm*)

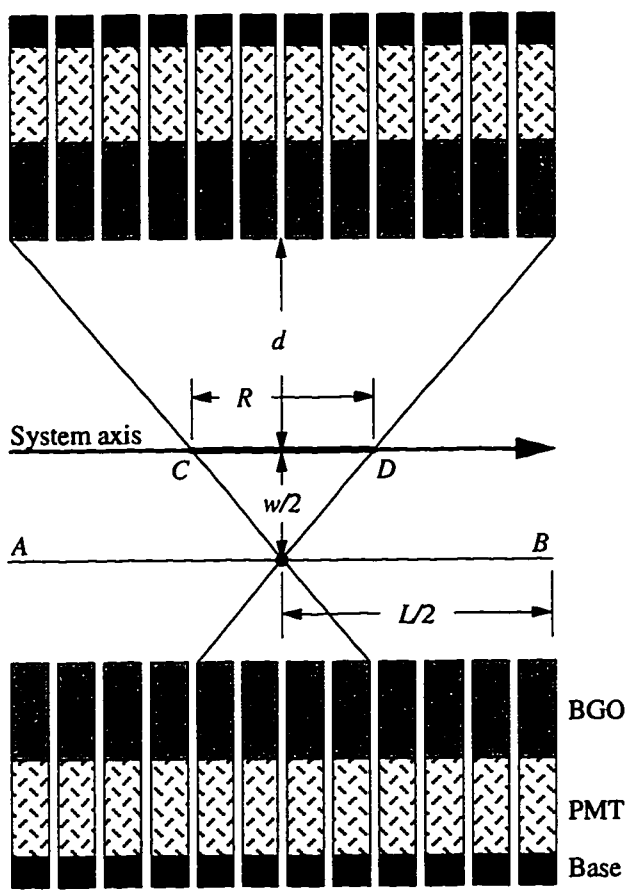

Figure 1.15. Geometrical derivation of maximum acceptable width of activity distribution. The dimensions, R, and $w/2$, have been exaggerated for illustration.

allows beam widths of approximately 2.7 cm to be used without significant blurring. This makes the system best suited for many head and neck tumors and some small abdominal tumors. Details on producing parallel tomograms of extended activity distributions from projections have been discussed by other authors [8, 14].

Loss of Efficiency Due to Attenuation

The attenuation length of 511 keV gamma-rays in tissue is roughly 11 cm. In adult-size phantoms and patients this causes a significant decrease in the coincidence detection rate and blurs the image due to the detection of Compton scattered gamma-rays. In addition, a quantitative reconstruction of the activity distribution becomes much more difficult without a detailed knowledge of the geometry and attenuation characteristics of the phantom or patient. However, given that this information may be obtained directly from the treatment planning process or from transmission attenuation studies, we will assume for the time that these obstacles may be overcome if sufficient statistics may be obtained for imaging.

Varying thicknesses of Solid Water™, model 457 [12], were introduced between the source and detectors during the calibration process, as shown in Figure 1.2, to study the effects of attenuation on count rate and efficiency. This simple geometry was added to the system model to simulate the effects of attenuation on the *CDE* for comparison to the experimentally measured efficiencies. The calibration source holder acted as additional converter material for positrons and introduced some attenuation which was also included in the system model.

Compton scattered gamma-rays are not followed by the code. The experimental *CDE*'s should therefore be slightly larger than those predicted by the simulation since gammas may be scattered into the detectors from angles or positions not otherwise allowed by true coincidence events. This is especially true for attenuating materials whose thickness is less than the attenuation length of the material since the gamma-rays

are much more likely to be scattered only once. Scattered gamma-rays, which have lower energies, are more strongly attenuated and less likely to have an energy above the detectors threshold energy if scattered multiple times. Consequently, if the thickness of the material is about one attenuation length or greater it is self-shielding against Compton scattered coincidences. The results of our model should therefore approach the experimental results for thickness of Solid Water™ equivalent to the calculated attenuation length of 10.3 cm or greater.

Due to the poor energy resolution of BGO it is necessary to set a rather large window on the 511 keV energy peak. In this system, the FWHM energy resolution was measured to be 30% and the full width at ten percent of the maximum (FWTM) was 55%. Upper and lower energy cuts were placed at FWTM in the software which allowed annihilation gamma-rays Compton scattered through angles as large as 52° to make the energy cut.

Figure 1.16 shows the experimental and simulated $\overline{CDE}$ for attenuation with Solid Water™ thicknesses, t, of 0, 1, 5, and 9 cm at a detector separation, $2d$, of 20 cm. The experimental and simulated CDE are shown in Figure 1.17. When the only attenuating material present is the Lucite holder, the magnitude of the experimental and simulated $\overline{CDE}$ were found to agree within 1%, $t = 0$ cm in Figure 1.16. Comparing the results for one centimeter of Solid Water™ we find that the experimental $\overline{CDE}$ is higher than that predicted by the system model as expected due to scattering. However, the experimental results for five and nine centimeters are significantly lower than expected. The uncertainties in the mass attenuation coefficient and density of Solid Water™ shown in Table 1.1 result in an uncertainty of only about 1% in the simulated $\overline{CDE}$ shown in Figure 1.16. This suggests that the value of the mass attenuation coefficient calculated for Solid Water™ in Table 1.1 is higher than the true value, or that the density is higher than the manufacturer's stated value. Consequently, the false coincidences caused by

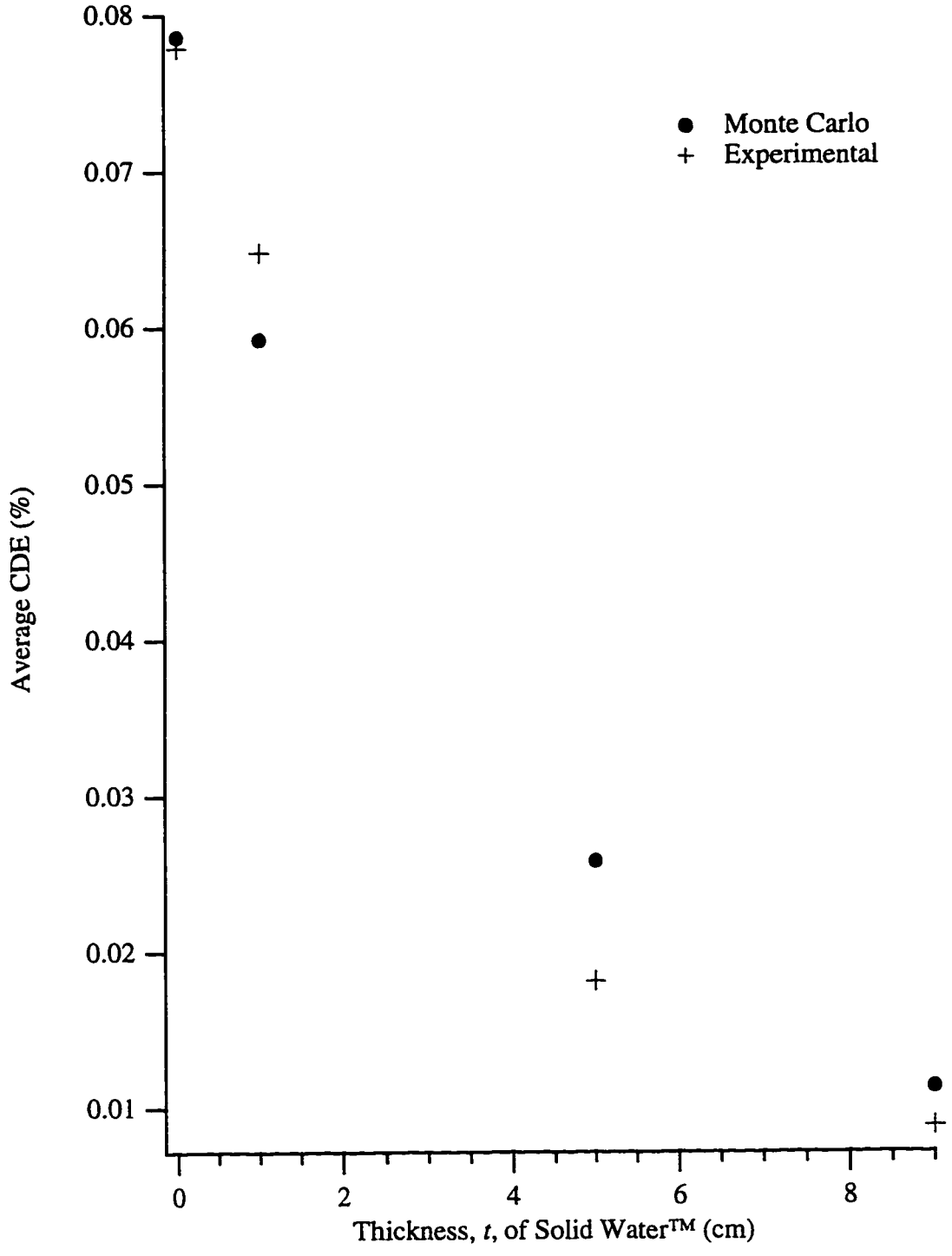

Figure 1.16. Simulated and experimentally determined $\overline{CDE}$ versus attenuation thickness, t.

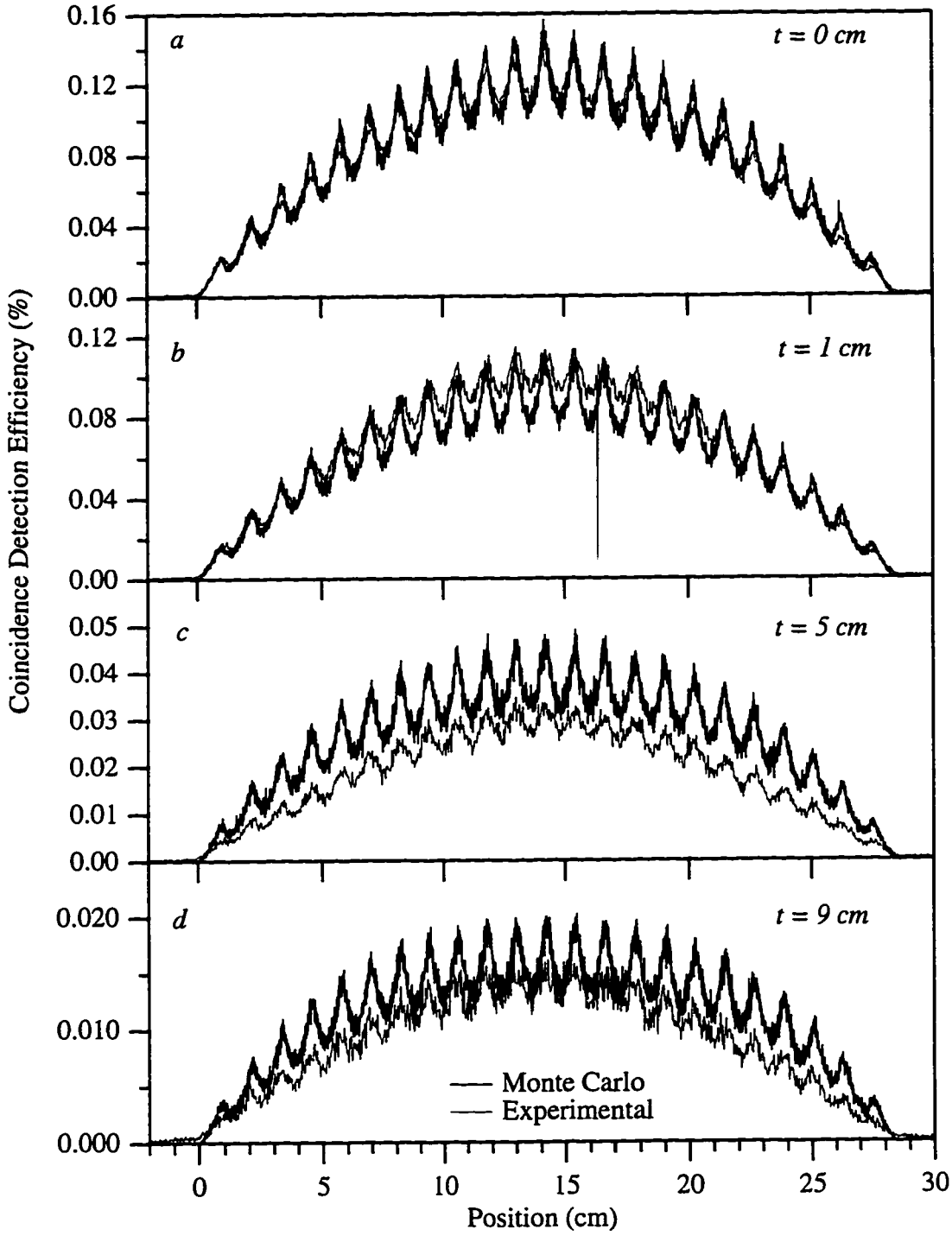

Figure 1.17. The experimentally measured and the simulated CDE for thickness of Solid Water attenuation for $t = 0$, 1, 5, and 9 cm.

scattered gamma-rays would be more abundant than suggested by the data point at $t = 1$ cm in Figure 1.16. Aside from the apparent discrepancy between the true and calculated attenuation length of Solid Water™ the results agree with our expectations. For one centimeter of Solid Water™ the $\overline{CDE}$ is greater than predicted by our model yet the $\overline{CDE}$ approaches our prediction for $t \approx 1/\mu_{SW}^{511}$.

The presence of roughly 10 g/cm^2 of attenuating material on both sides to the source is fairly representative of most head tumors and some abdominal tumors. The presence of this material will lead to a factor of eight decrease in the count rate and therefore, a corresponding increase in the minimum image acquisition time. While such a loss will not seriously impair the ability to perform off-line isotopic imaging studies, it may limit the present system for clinical on-line imaging in many situations. As discussed below, this may be overcome in the design of future systems by increasing the solid angle.

Conclusions

The presented results can be used to determine the best PET detection geometry based on the imaging conditions, the object being imaged, the desired resolution, the permissible image acquisition time and budgetary considerations. The prototype system presented here may be further optimized for on-line imaging of radiotherapy beams. The highest detection efficiency may be achieved by removing the intercrystal shielding and minimizing the spacing between adjacent detection crystals. The detection efficiency may also be improved by minimizing the separation between the detector banks. However, the distance between the detector banks should not be less that given by (1.9) or blurring from outlying activity may degrade the resolution. Alternatively, the effective length may be reduced by omitting coincidences from oblique detector pairs. Thus the optimum configuration for on-line imaging is a compromise between detection efficiency and blurring due to extended activity distributions.

Based on these simulation results and experienced gained with this prototype imaging system several improvements may be suggested for next-generation systems. While planar detection arrays [9] are an attractive improvement for providing 3D imaging of the treatment volume the iterative algorithms needed prohibit their use for fast, on-line image reconstruction. Possible improvements which retain the present imaging capabilities include the use of rectangular [13] instead of cylindrical crystals and the omission of the intercrystal shielding. This would provide a significant increase in detection efficiency by increasing the solid angle and packing efficiency, and by allowing the detection of gammas which entered through adjacent crystal faces. Rectangular crystals having dimensions 0.5 cm along the system axis, 2 cm, perpendicular to the plane of the detectors, and 3 cm deep would provide a resolution along the system axis of about three millimeters, and increase the solid angle by 50% while using the same volume of scintillator in the present system. Ideally each crystal would be readout by a single PMT. However, for the detector dimensions given above, individual crystal readout would quadruple the number of PMT's and electronic channels needed to process the signals. Alternatively, a block of scintillator may be partially cut perpendicular to its length every few millimeters producing an optically coupled block design which could be readout with fewer PMT's or using fast position-sensitive PMT's [15]. Depth-of-interaction blurring could still be prevented by using the same calibration technique with a point-like source or a line source perpendicular to the plane of the detectors.

Currently the best scintillator for use in PET applications is BGO due to its high stopping power and its adequate coincidence timing characteristics. It does however have the disadvantages of having a long decay constant, low light output, and hence poor energy resolution. The long time constant limits the count rate capabilities due to pulse pileup. The poor energy resolution makes the system susceptible to the detection of photons scattered by the overlying material in the object containing the activity. While not yet economical, the use of cerium-doped lutetium oxyorthosilicate (LSO) would

significantly reduce these effects [16]. LSO has a marginally lower stopping power and effective atomic number than BGO resulting in a photopeak efficiency 20% to 25% lower than that in BGO. However, LSO has better energy resolution since its light output is about five times larger than that of BGO. LSO is also capable of higher rates since it has decay constants of 12 ns (30%) and 42 ns (70%) compared to a 300 ns time constant for BGO.

While medical applications tend to require the best spatial resolution possible [17], other applications with less demanding needs may use larger spaces between the adjacent crystals. Simulations show that even with intercrystal shielding, spaces as large as half the detector width provide a reasonable detection efficiency at all points along the system axis. If the intercrystal shielding is removed the detection efficiency will likely increase by more than 50% and provide a more uniform *CDE* along the axis. In this case, detector separations of a detectors width would provide resolution of approximately the detector size with good efficiency and at a significantly lower cost.

Acknowledgments

We would like to thank Dr. J. Fessler, University of Michigan, for advice and guidance received during several discussions on image reconstruction. This work was supported by grants PHY 9512104 and PHY 9208468 from The National Science Foundation and by grants from the following groups within the University of Michigan: The Office of the Vice President for Research, The John Munn Foundation through The Comprehensive Cancer Center, The College of Literature, Science and Art, The Rackham School of Graduate Studies, and The Department of Physics.

References to Chapter 1

[1] H. D. Maccabee, U. Madhvanath, and M. R. Raju, "Tissue Activation Studies with Alpha-Particle Beams," Phys. Med. Biol., vol. 14, no. 2, pp. 213-224, 1969.

[2] G.W. Bennett, A. C. Goldberg, G. S. Levine, J. Guthy, and J. Balsamo, "Beam Localization Via ^{15}O Activation in Proton-Radiation Therapy," Nucl. Instr. Meth., vol. 125, pp. 333-338, 1975.

[3] L. G. Strauss, J. H. Clorius, B. Kimmig, et al., "Imaging Positron Emitting Radionuclides Generated during Radiation Therapy," Europ. J. Radiol., vol. 9, pp. 200-202, 1989.

[4] S. Vynckier, S. Derreumaux, F. Richard, et al., "Is it possible to verify directly a proton-treatment plan using positron emission tomography," Radiotherapy and Oncology, vol. 26, pp. 275-277, 1993.

[5] U. Oelfke, G. K. Y. Lam, M. S. Atkins, "Proton dose monitoring with PET: quantitative studies in Lucite," Phys. Med. Biol., vol. 41, pp. 177-196, 1996.

[6] R. K. Ten Haken, G. H. Nussbaum, B. Emani, W. L. Hughes, "Photon activation - ^{15}O decay studies of tumor blood flow," Med. Phys., vol. 8, no. 3, pp. 324-336, 1981.

[7] D. W. Litzenberg, F. D. Becchetti, D. A. Roberts, "A Parallel, Transputer-Based Data Acquisition System for On-Line PET Imaging of Proton and Gamma-Ray Radiotherapy Beams," IEEE Trans. Nucl. Sci., vol. NS-43, no. 1, pp. 154-158, Feb. 1996.

[8] L. T. Chang, B. Macdonald, and V. Perez-Mendez, "Axial Tomography and Three Dimensional Image Reconstruction," IEEE Trans. Nucl. Sci., vol. NS-23, no. 1, pp. 568-572, Feb. 1976.

[9] W. Enghardt, W. D. Fromm, P. Manfrass, and D. Schardt, "Limited-angle 3D reconstruction of PET images for dose localization in light ion tumor therapy," Phys. Med. Biol., vol. 37, no. 3, pp. 791-798, 1992.

[10] J. Llacer, "Theory of Imaging with a Very Limited Number of Projections," IEEE Trans. Nucl. Sci., vol. NS-26, no. 1, pp. 596-602, Feb. 1979.

[11] J. H. Hubbell and S. M. Seltzer, "Tables of X-Ray Mass Attenuation Coefficients and Mass Energy Absorption coefficients 1 keV to 20 MeV for Elements Z = 1 to 92 and 48 Additional Substances of Dosimetric Interest," National Institute of Standards and Technology, Gaithersburg, MD, Tech. Rep. NISTIR 5632, May 1995.

[12] A. K. Ho and B. R. Paliwal, "Stopping-power and mass energy-absorption coefficient ratios for Solid Water," Med. Phys. vol. 13(3), pp. 403-404, May/Jun 1986.

[13] S. E. Derenzo, "Monte Carlo Calculations of the Detection Efficiency of Arrays of NaI(Tl), BGO, CsF, Ge and Plastic Detectors for 511 keV Photons," IEEE Trans. Nucl. Sci., vol. NS-28, no. 1, pp. 131-136, Feb. 1981.

[14] J. Llacer, A. Chatterjee, E. K. Batho, and J. A. Poskanzer, "Design Analysis and Performance Evaluation of a Two Dimensional Camera for Accelerated Positron Emitter Beam Injection by Computer Simulation," IEEE Trans. Nucl. Sci., vol. NS-30, no. 1, pp. 617-625, Feb. 1983.

[15] M. E. Casey and R. Nutt, "A Multicrystal Two Dimensional BGO Detector System for Positron Emission Tomography," IEEE Trans. Nucl. Sci., vol. NS-33, no. 1, pp. 460-463, Feb. 1986.

[16] F. Daghighian, P. Shenderov, K. S. Pentlow, M. C. Graham, and B. Eshaghian, "Evaluation of Cerium Doped Lutetium Oxyorthosilicate (LSO) Scintillation Crystal for PET," IEEE Trans. Nucl. Sci., vol. NS-40, no. 4, pp. 1045-1047, Aug. 1993.

[17] S. Cherry, Y. Shao, S. Siegel, and R. W. Silverman, "Optical Fiber Readout of Scintillator Arrays using a Multi-Channel PMT: A High Resolution PET Detector for Animal Imaging," IEEE Trans. Nucl. Sci., vol. NS-43, no. 3, pp. 1932-1937, June 1996.

CHAPTER 2

A PARALLEL, TRANSPUTER-BASED DATA ACQUISITION SYSTEM FOR ON-LINE PET IMAGING OF PROTON AND GAMMA-RAY RADIOTHERAPY BEAMS

On-line imaging of the positron-emitting activity created by heavy ion [Lit1, 1], proton [Lit3, 2,3] and γ-ray [4] radiotherapy beams presents several challenges. A typical proton radiotherapy treatment will create up to three milliCuries of positron-emitting isotopes, including ^{15}O, ^{14}O, ^{13}N, and ^{11}C. Due to the abundance of oxygen in the body, the high cross section of the $^{16}O(p,pn)^{15}O$ reaction, and the short, 2 minute, half-life of ^{15}O, roughly 90% of all positron-emitting activity is from the decay of ^{15}O. While it is possible to image this activity using a conventional PET imaging system, this requires such a system be very close to the radiotherapy treatment room. Even if a PET scanner is near, patient transport and setup may take five to ten minutes in which time most of the ^{15}O will decay, resulting in an image of the induced ^{11}C which is of limited value. To gain useful information from the decay data it is therefore necessary to use an on-line imaging system.

Due to the spatial constraints required for patient setup and beam delivery it is impossible to use the standard ring configuration of conventional PET imaging devices. We are therefore limited to low solid angle detector configurations, and high efficiency detectors, such as Bismuth Germanate Oxide(BGO). For example, our system, which is shown in Figure 2.1, has two rows of BGO detectors. For 511 keV γ-rays, the coincidence detection efficiency is roughly 0.1% at the center of the array. Despite this low efficiency, if 2 mCi of ^{15}O is created, event rates are roughly 75 kHz. Future

upgrades to the detectors could increase the coincidence detection efficiency by a factor of two, resulting in event rates up to 150 kHz.

These restrictions make a fast, and easily expandable data acquisition system with filtering capabilities a necessity. With this in mind, we have implemented a parallel, transputer-based data acquisition system, developed at the Michigan State University, National Superconducting Cyclotron Lab(MSU NSCL), for use with the 4π detector array [5]. This system will easily accommodate future detector upgrades, has the capability to filter raw data in real-time, and can route data to any number of consumers for on-line analysis, display, or storage [6]. This paper discusses the requirements placed on the data acquisition system by this imaging device, the performance of the system, and presents some of the initial experimental results.

System Parameters and Design

Detection System

The γ-ray detection system, shown in Figure 1.1, consists of two rows of detectors. Each row contains twelve BGO detectors. Each BGO detector measures 1.9 cm in diameter by five centimeters long and is separated from its neighbor by 0.5 cm. Additional detectors may be added to each row and additional rows may be added. The front surfaces of the detectors between the two rows are typically separated by 60 cm but may be adjusted for maximum efficiency. Each detector produces one signal which is 900 ns long due primarily to the 300 ns decay constant of BGO. These 24 signals constitute the physics related input to the electronics and the data acquisition system.

Electronics

The electronics circuit is shown in the block diagram in Figure 2.1. Each of the 24 signals is split. One copy is used for energy discrimination, timing and logic, and the

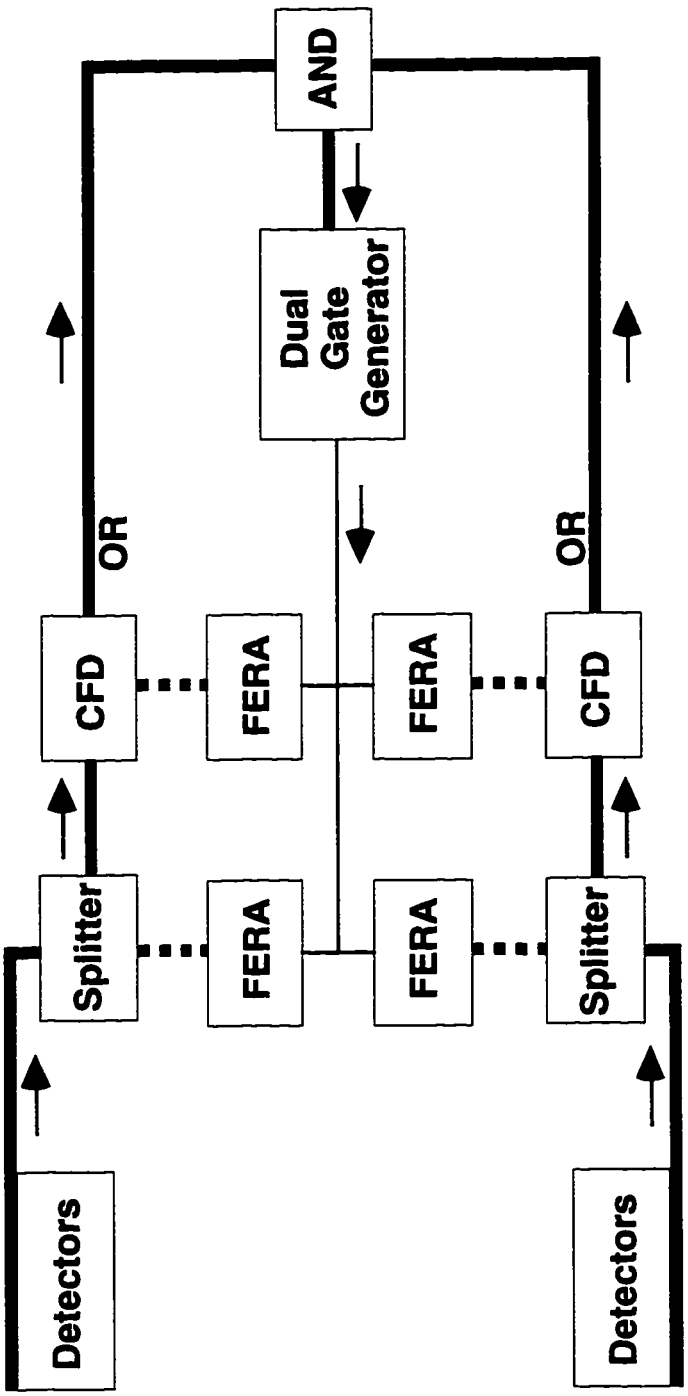

Figure 2.1. Block diagram of electronics circuit.

other copy goes to a 16 channel, Fast Encoding Readout ADC (FERA). Copies of all signals from one row of detectors go to one, 16 channel, CFD which provides a logical OR output and constant current output pulses for timing. The logical OR from each row are used to generate a master gate when a coincidence occurs between the two rows. The timing pulses are integrated by a gated FERA which serves as a time-to-amplitude converter(TAC). For each detector over threshold, time is measured relative to the formation of the master gate. In addition to the four FERA's, two 32 channel scalers record information such as the number of single hits and the number of coincidences.

An event is defined as a coincidence between the two rows of detectors. With zero suppression enabled on the FERA's, the minimum size of an event is eight words: two energy words, two timing words, and four header words. Each header word tells which FERA the following information is from and how many words of data from that FERA follow the header word. Each timing and energy data word consists of eleven bits of data and four bits for channel, or detector, identification. Experimental results show that up to 5% of all events may have events sizes from nine to fourteen words, due to noise in other detectors. This percentage will increase with the number of detectors added and with increased amounts of activity, making real-time data filtering an important capability of the data acquisition system. With the initial detector configuration, typical proton radiotherapy treatments generate event rates as high as 75 kHz, giving data rates of 1.2 Mbytes/sec. Detector upgrades will lead to data rates of roughly 2.4 Mbytes/sec.

Data Acquisition

The VME and CAMAC crates for the data acquisition system, shown in Figure 2.2, are mounted in a standard 19 inch rack along with a NIM bin for the electronics. The system is very portable and future upgrades will easily fit in the existing crates.

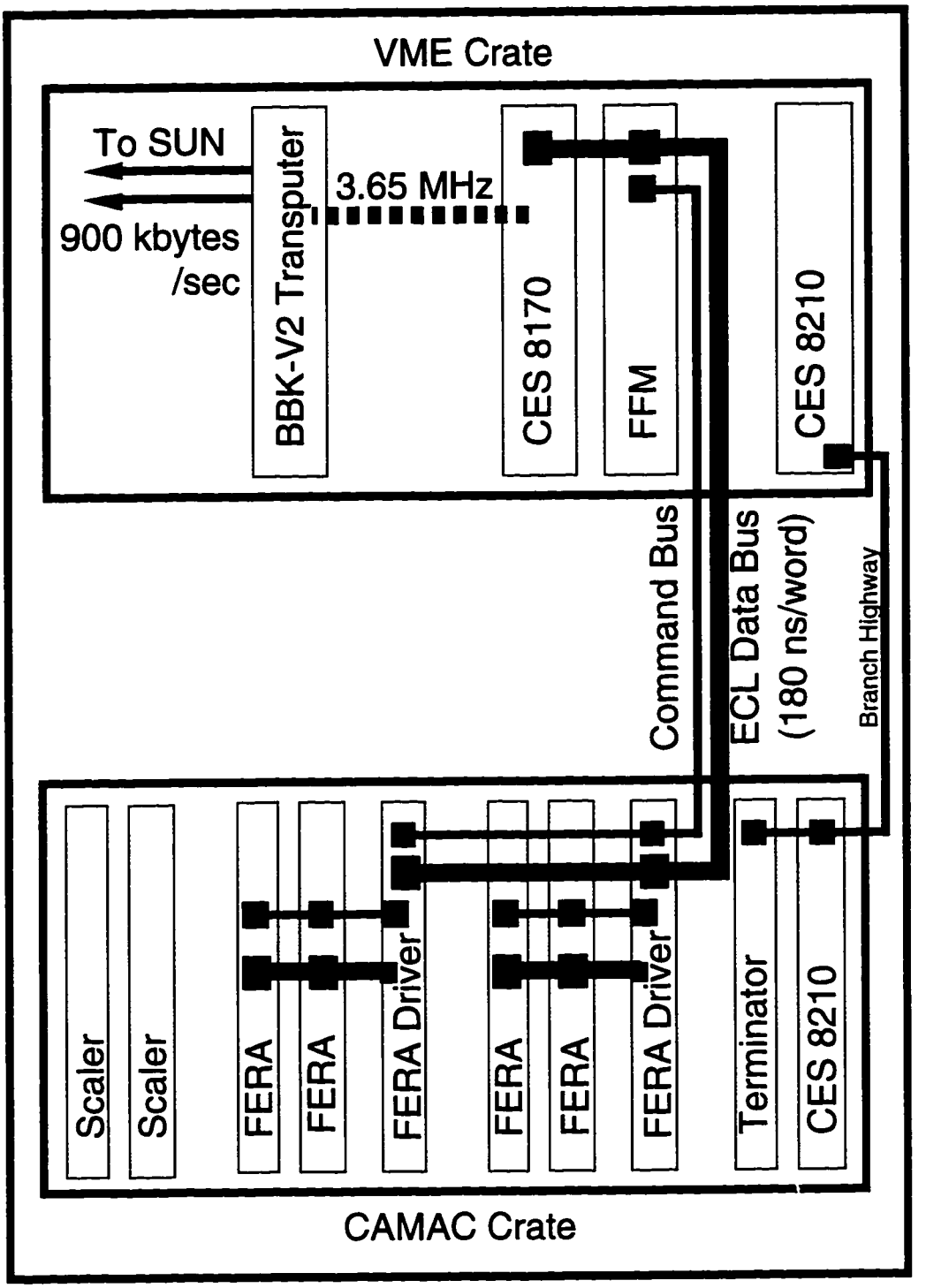

Figure 2.2. Rack mounted VME and CAMAC crates house data acquisition system.

The 11-bit FERA has an analog to digital conversion time of 8.5 μs and a readout time of 180 ns/word over an ECLine data bus. The data is stored in a 512 kbyte, CES 8170, memory board. The memory fill rate depends mainly on the event rate and to a small degree on the event size. When full, the board will hold roughly 5.6×10^4 events. The memory board is read when full, or when a scaler dump is requested after a specified time interval.

The memory board is read by the VME-based transputer at 3.65 Mbytes/sec. However the data rate from the transputer to the SUN host is only 900 kbytes/sec due to a 20 Mbit/sec baud rate and deadtime due to cable delay [5]. The SUN then routes the data to any number of consumers, each of which may present other bottlenecks to the flow of data. For example, 8 mm tape drives typically record data at 500 kbytes/sec. Likewise, on-line data analysis may present a bottleneck if the available RAM for storing data buffers fills up faster than the buffers can be analyzed.

System Efficiency

The coincidence detection efficiency of the system is measured by translating a ^{22}Na calibration source along the axis with a constant velocity. During this calibration run, scalers are dumped at constant time intervals which may be set by the user. The experimental efficiency is calculated as the number of 511 keV coincidences per time interval divided by the number of positron decays per time interval. The simulated and experimental measurement of the coincidence detection efficiency are shown in Figure 1.5, for detector separations, $2d$, of 20 cm and 60 cm.

Although there are 144 possible detector pairs, there are only 23 unique segments of the system axis which are observed by these detector pairs. The 23 peaks in the efficiency curve shown in Figure 1.5 correspond to points with high solid angle for coincidence detection. These points are located on the axis between the centers of the 12 opposite detectors and halfway between these points on the axis. As expected, the

efficiency is highest at the center of the array axis which is monitored by the most detector pairs.

To be useful as an on-line range monitor for proton radiotherapy it is essential that the time to generate an image be reasonably short compared to the time for a typical treatment fraction. Therefore, it is necessary to have the highest possible detection efficiency to minimize the dose per image. For example, a typical proton treatment at Loma Linda University Medical Center lasts 2 minutes and uses a 150 MeV beam pulsed 27 times per minute with an intensity of $3x10^{10}$ protons per pulse [7]. After four pulses, there is roughly 50 μCi of induced positron-emitting activity. The acquisition time required to generate an image with 5% counting statistics is just under three seconds.

Energy and Timing

Coincidences are determined by two criteria: there must be an event in each row of detectors with an energy of 511 keV and, these events must occur in a very short time period. For this system the BGO crystals are the predominant factor limiting the energy and timing resolution. Timing and energy information is collected during the calibration run which is performed before acquiring images. From energy spectra generated for each detector, Figure 2.3, lower and upper energy cuts are determined from the position and width of the 511 keV peak. Coincidence time difference spectra, Figure 2.4, are produced for each of the 144 possible detector pairs by subtracting their TAC values for each event. From these spectra, lower and upper timing cuts are determined and estimates of the accidental coincidence rate for each detector pair are made. These timing and energy cuts maybe downloaded to the transputer for real time data filtering and analysis. Experimentally, the energy resolution was determined to be 30% and the timing resolution 5.5 ns.

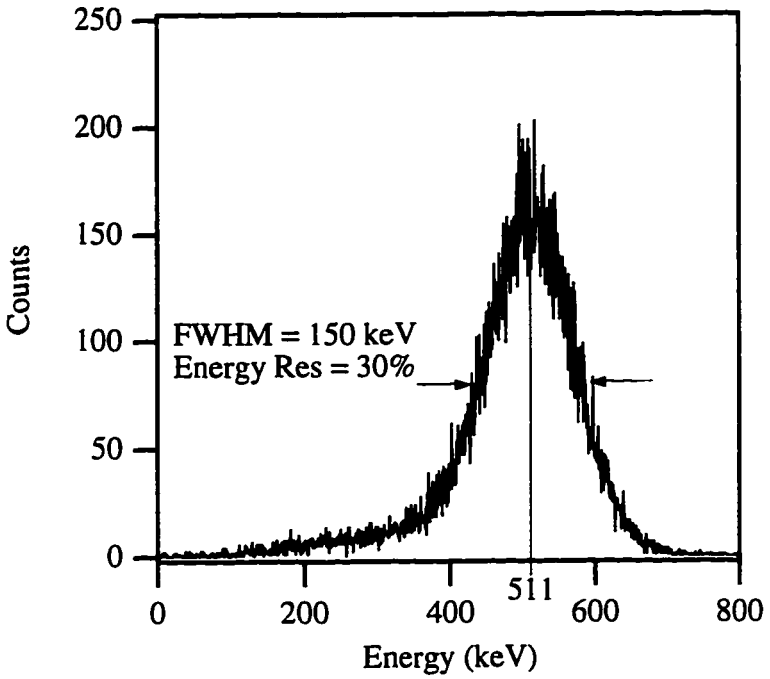

Figure 2.3. The FWHM energy resolution was experimentally found to be 30%.

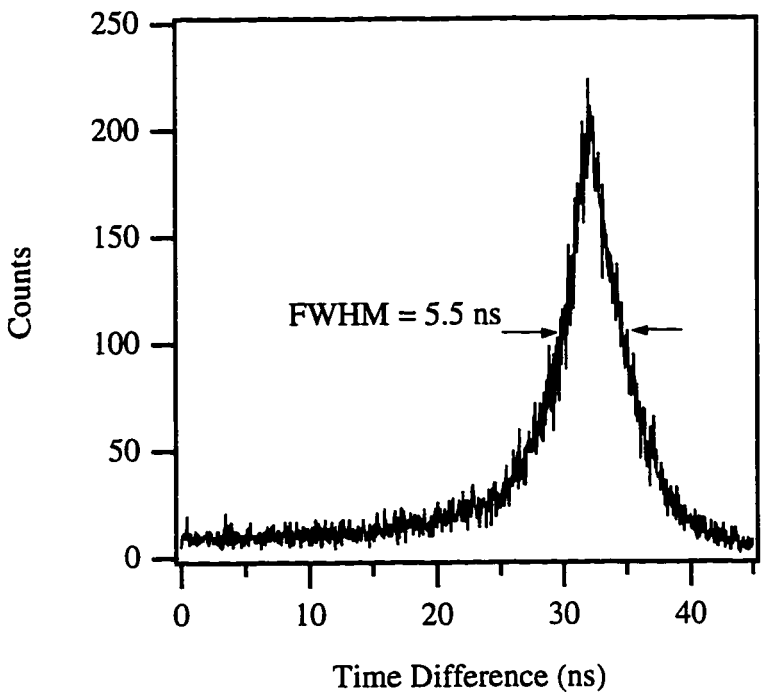

Figure 2.4. The FWHM timing resolution was experimentally found to be 5.5 ns.

Initial Experimental Results

Image Reconstruction

From the data obtained during a calibration run, a system matrix, $\mathcal{S}$, is generated which relates physical position along the system axis to detector pairs. During image acquisition the response, $\mathcal{R}$, of the imaging system to the physical distribution of positron-emitting activity, $\mathcal{A}$, is measured. These are related by the system of equations

$$\mathcal{S}\mathcal{A} = \mathcal{R} \tag{2.1}$$

The system matrix is inverted using a singular value decomposition(SVD) routine. The physical distribution of activity is then given by

$$\mathcal{A} = \mathcal{S}^{-1}\mathcal{R} \tag{2.2}$$

The inverted system matrix may also be downloaded to the transputer. With data filtering enabled, the distribution of positron-emitting activity can be calculated and displayed after every scaler dump. In some cases, such as for total dose monitoring, it may be desirable to perform these calculation on the total accumulated dataset. For charged particle range monitoring or tumor blood flow studies it is possible to generate a sequence of images using sequential subsets of the dataset. Further details on image reconstruction, the error associated with a reconstructed image and of how detector geometry effects image reconstruction will be discussed in Chapter 3.

Point Source

A 2.335 μCi, Isotopes Products Laboratories, type MF-2, ^{22}Na calibration source was wrapped in aluminum foil and place near the center of the array. The effective

spatial extent of the ^{22}Na activity was three millimeters along the axis of the imaging system. Data was acquired for 1.82 hr. Figure 2.5 shows the reconstructed linear image of the point source. The FWHM resolution is measured to be 1.3 cm.

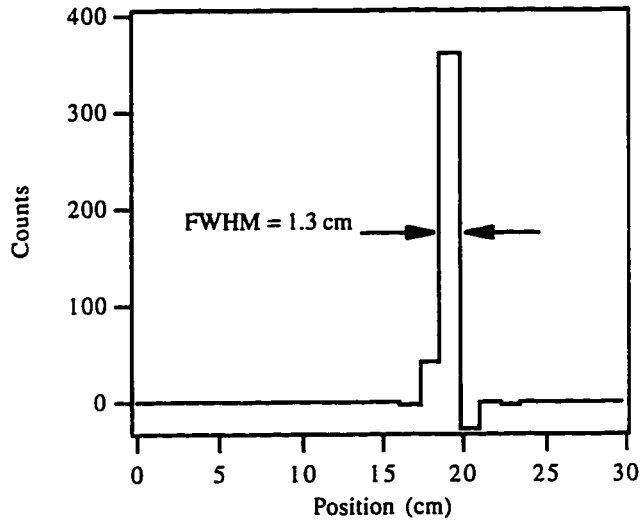

Figure 2.5. Reconstructed image of a point source.

150 MeV Proton Beam in Water

The NSCL, K1200 cyclotron was used to produce a 150 MeV, 25 pA, proton beam, pulsed with a 10 second period. This beam was implanted in a water phantom for 32 minutes. Data was collected for 20 minutes immediately following irradiation. The calculated activity distribution is shown in Figure 2.6 and the measured distribution is shown in Figure 2.7. The spike of activity on the left in the reconstructed image is activity created in the plastic container holding the water. It should also be noted that the relative amount of activity created at higher energies compared to the lower energies, is lower than expected [3]. Additional data obtained with tissue phantoms shows similar results. The distribution of activity in water and tissue phantoms will be discussed in more detail in Chapter 3.

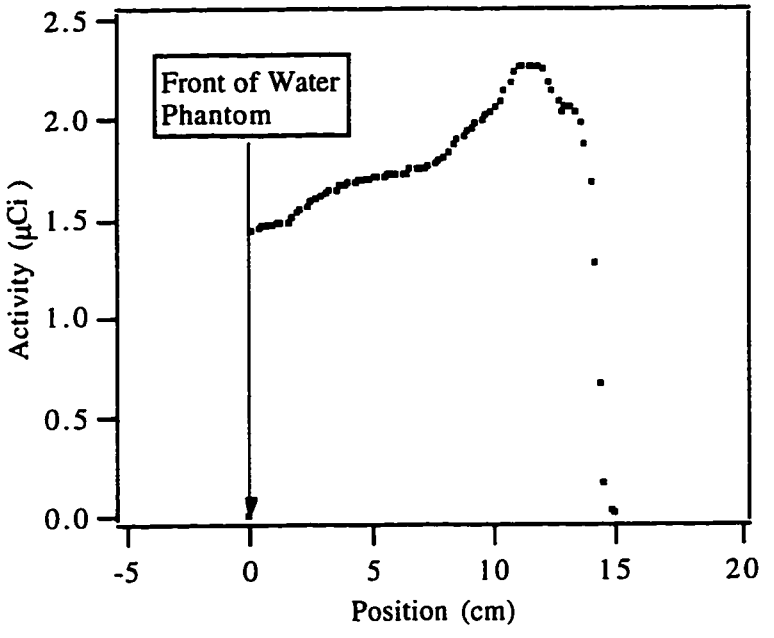

Figure 2.6. Calculated activity distribution of a 150 MeV proton beam in water.

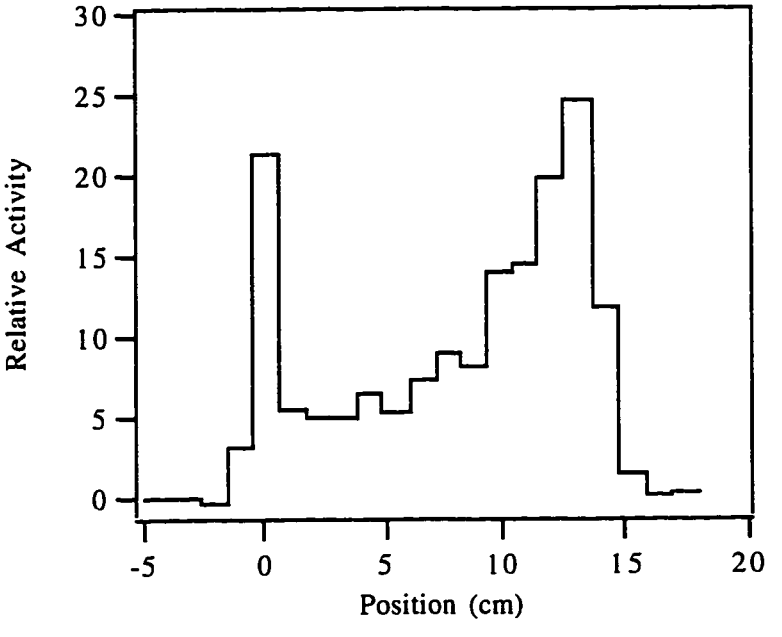

Figure 2.7. Reconstructed image of the activity created by a 150 MeV proton beam in a water phantom.

Discussion

As the detection system is upgraded and the event rate increases, the bottlenecks in the flow of data will become a more serious problem. Upgrades in the data acquisition system will also be required. The addition of VME-based transputers operating in parallel, will allow most of the data manipulation and reduction to be done in real-time before the most severe bottleneck, which occurs between the SUN host and the transputer. Once the system has been calibrated, timing and energy cuts may be down loaded to the transputers. Multiple transputers will filter the energy data for 511 keV interactions, and the time data for events that did not occur within the coincidence timing resolution of the given detector pair.

Conclusions

In vivo dose localization is considered essential for the advancement of proton, and light-ion radiotherapy as a treatment modality for cancer. To be clinically useful the methods that accomplish this must be fast, non-invasive, and have subcentimeter resolution. While the current system described above may not achieve the desired resolution, the technology exists for it to be attained [8,9]. In addition, this system and subsequent generations will be able to analyze and display range information in real-time making it well suited for on-line treatment verification.

References to Chapter 2

[1] D.W. Litzenberg, et al., "Positron Emission Tomography of Implanted Radioactive Analog Radiotherapy Beams," in *Second International Conference on Radioactive Nuclear Beams*, Louvain-la-Neuve, Belgium, 1991.

[2] D. W. Litzenberg, J. F. Bajema, F. D. Becchetti, et al., "On-Line Monitoring and P.E.T. Imaging of Proton Radiotherapy Beams," IEEE Med. Imag. Conf. Rec., pp. 1672-1676, Norfolk, VA, Oct. 30-Nov. 5, 1994.

[3] G.W. Bennett, et al., "Beam Localization Via ^{15}O Activation in Proton-Radiation Therapy," *Nucl. Instr. and Meth.* , vol. 125, pp. 333-338, 1975.

[4] R.K. Ten Haken, et al., "Photon activation- ^{15}O decay studies of tumor blood flow," Med. Phys., vol. 8, no. 3, May/June 1981.

[5] A. Vander Molen, et al., "A Transputer Based Parallel Frontend Data Acquisition System," *IEEE Trans. Nucl. Sci.*, vol. 41, no. 1, pp. 80-82, February 1994.

[6] Ron Fox, et al., "Portable Data Flow in Unix," *IEEE Trans. Nucl. Sci.*, vol. 41, no. 1, pp. 161-164, February 1994.

[7] G. Coutrakon, et al., "A performance study of the Loma Linda proton medical accelerator," Med. Phys. vol. 21, no. 11, pp. 1691-1701, November 1994.

[8] T.J. Llewellyn, et al., "High Resolution and Efficiency Annihilation Photon Detection with a Multi-Element BGO Converter and Two Dimensional Optical Readout," Nucl. Instr. and Meth. in Phys. Res., vol. A273, pp. 869-873, 1988.

[9] A.H. Cho and S.C. Juh, "High Resolution Brain PET with large detectors - II Performance Study," *IEEE Trans. Nucl. Sci.*, vol. 38, no. 2, pp. 726-731, April 1991.

CHAPTER 3

ON-LINE PET MONITORING OF RADIOTHERAPY BEAMS: EXPERIMENTAL RESULTS WITH PROTON BEAMS

Proton and light-ion radiotherapy are increasingly important tools for treating tumors due to the sharp rise and fall of dose at the end of the ions range. For example, typical dose falloff rates along the beam axis for protons are 90% to 50% in 2 mm and 50% to 20% in 3 mm while laterally the dose falls from 90% to 50% in 4.5 mm and from 50% to 20% in 3 mm [1]. This advantage over other radiotherapy modalities is limited by the inability to directly monitor the dose delivered to the tumor volume. The depth of the maximum dose is dependent on the beam energy, tissue composition, multiple Coulomb scattering [2], and in particular the inhomogeneities along the beam path [3-5]. This makes it very difficult to determine the precise range of the treatment beam. The introduction of X-ray CT in treatment planning greatly improved dose localization. However, it has been shown that in the presence of bone or air gaps along the beam path, CT range estimates may be in error by as much as 11% [6,7]. Thus it is desirable to develop on-line, *in vivo* techniques for imaging induced activity, to help ensure that the lethal dose is localized within the prescribed tumor volume.

Tissue activation was first discussed in detail by Tobias in 1949 [8] and was first reported in gamma-ray experiments by Mayneord et al. later that year [9]. Since then the radioactivity induced in tissues by photon [9-11], proton [12,13], neutron [14], pion [15-17], and heavy-ion radiotherapy beams [18-20] has been investigated. This induced activity has been studied as a source of patient dose [12, 21, 22], as a means of determining elemental tissue composition [11, 12, 14], and for determining dose

distributions [15, 16, 18, Lit2, Lit3, 23-31]. *In vivo* dose localization by imaging positron-emitting nuclei is considered essential for light-ion, and radioactive-ion beam therapy [31]. Investigations of PET as a monitor for proton radiotherapy beams generally indicate that it is capable of measuring useful dosimetric, compositional, and range information [12, 13, 23, Lit2, Lit3, 26-30, 32]. However, many of these experiments were conducted off-line by detection systems in the vicinity of the treatment beam requiring that the phantoms or subjects under study be moved. The resulting images predominantly show activity from radioisotopes whose half-life is comparable to or longer than the transportation and setup time. While these studies lend valuable insight, the images obtained are mainly of ^{11}C which is of limited physiological value for subsequent treatment planning. However, ^{15}O is the most active positron-emitting isotope produced during proton radiotherapy due to the abundance of oxygen in the body, its short 2 minute half-life, and the relatively large cross section of the $^{16}O(p,pn)^{15}O$ reaction [33].

In this work we present the results of experiments which imaged the distribution of positron-emitting isotopes on-line, *in vivo*, with a prototype imaging system [DWL1, 34]. We first discuss the nuclear reactions which produce the observed positron-emitting isotopes. The spatial and temporal nature of the activity distributions are then presented when produced by continuous, pulsed and energy-modulated proton radiotherapy beams. These distributions are primarily determined by the distribution of nuclei along the beam path, the energy-dependent reaction cross sections and the flux of the beam as a function of depth. These factors are discussed next, along with a brief description of how they are used to calculate the expected activity distribution. In the following section we describe the proton beam used during the experiments, and several aspects of the imaging system such as its dimensions, construction, shielding characteristics, efficiency, and timing and energy resolution characteristics. We then present the algorithms used to separate and reconstruct depth-distributions for each of the major positron-emitting isotopes produced

in experiments where decay data was collected. This is followed by a discussion of the techniques used to assess the uncertainties and correlation's present in the reconstructed decay distributions.

The results from several experiments are then presented. The first experiment was conducted off-line using a commercial PET imaging system to image and quantify the distribution of the long-lived radioisotopes produced. The second experiment examined the spatial and temporal distributions of the decaying activity produced by a continuous 150 MeV proton beam in tissue. The data was collected *in situ* starting immediately after the beam ended. During the third and fourth experiments, data was collected on-line between beam pulses. From these experiments it is shown that on-line range verification may be performed after a single beam pulse, and that the total dose may be monitored on-line by monitoring the number of counts acquired between successive beam pulses. In addition, the presence of an adipose(fat) deposit in one of the tissue phantoms demonstrates the sensitivity of the images to compositional variations along the beam path. Finally, the calculated activity distribution of an energy-modulated beam are presented and compared to those produced by a mono-energetic beam. The experimental results are followed by discussions on the influence of secondary reactions, the effects of washout by metabolic processes on isotopic imaging, the correlation's between the dose and the activity, the use of anatomical features with different elemental compositions as range markers, possible improvements to the detection geometry, and the advantages and disadvantages of reconstructing two- and three-dimensional images. The results of experiments using ^{12}C and gamma-ray radiotherapy beams will be presented in subsequent papers.

Production of Positron-Emitting Nuclei

Nuclear Reactions in Tissue Which Produce Positron-Emitting Isotopes

A small percentage of the particles in a charged-particle radiotherapy beam will undergo nuclear reactions with elements in the tissue during treatment. The positron-emitting isotopes which are produced during proton radiotherapy are determined by the nuclear isotopic composition of the treated tissue. The elemental composition of the swine-tissue phantoms used for these experiments are shown in Table 3.1, along with the composition of human muscle and adipose tissue. The most abundant elements in tissue from which positron-emitting isotopes may be produced are oxygen, carbon, and nitrogen. While positron-emitting isotopes may be produced from other elements, they are inconsequential due to their low number density.

The production of positron-emitting isotopes in tissue arises through reactions with specific isotopes of the constituent elements. Nuclear reactions induced by protons often produce neutron-deficient nuclei which decay toward stability by positron emission. The energy spectrum of the emitted positrons is continuous with an endpoint energy, ${}^{A}E_{m_i}^{\beta^+}$. The most important reactions in tissue which produce positron-emitting isotopes are shown in Table 3.2, along with their threshold energy, E_i^T, and their Q-value. Also shown is the residual range of the proton in tissue for proton energies less than the various reaction threshold energies. While the production of ^{10}C and ^{18}F are not significant processes, both radioisotopes were observed in our experiments and are included for completeness. Other reactions will be discussed later. The positron-emitting isotopes which may be produced by protons from the isotopes of oxygen, carbon, and nitrogen are shown in Table 3.3 along with their half-lives, $t_{1/2i}$, their endpoint energies and the maximum range of the emitted positrons in tissue [35].

Element	Swine	Muscle	Adipose
Oxygen	74.61	72.893	27.8
Hydrogen	9.80	10.2	11.4
Carbon	11.32	12.3	59.8
Nitrogen	2.52	3.5	0.7
Sulfur	< 0.5	0.5	0.1
Chlorine	-	-	0.1
Potassium	0.29	0.3	
Phosphorus	0.27	0.2	
Sodium	0.21	0.08	0.1
Magnesium	0.065	0.02	
Calcium	0.022	0.007	
Iron	0.0034	-	

Table 3.1. Elemental tissue compositions by percent mass.

Reaction	Threshold Energy, (MeV)	Q-value (MeV)	Proton Range in Tissue, Below Threshold (cm)
$^{16}O(p,3p4n)^{10}C$	39.1	-36.8	1.5
$^{12}C(p,pn)^{11}C$	20.3	-18.7	0.4
$^{14}N(p,\alpha)^{11}C$	3.1	-2.9	0.02
$^{16}O(p,\alpha pn)^{11}C$	27.5	-25.9	0.8
$^{14}N(p,pn)^{13}N$	11.3	-10.6	0.2
$^{16}O(p,\alpha)^{13}N$	5.5	-5.2	0.04
$^{14}N(p,n)^{14}O$	6.6	-5.9	0.06
$^{16}O(p,p2n)^{14}O$	30.7	-28.9	0.9
$^{16}O(p,pn)^{15}O$	16.6	-15.7	0.3
$^{18}O(p,n)^{18}F$	2.6	-2.4	0.01

Table 3.2. The primary proton-induced reactions in tissue which produce positron-emitting isotopes.

Isotope	Half-life (sec)	β^+ Endpoint Energy (MeV)	Maximum β^+ Range (cm)
^{10}C	19.3	1.87	0.9
^{11}C	1218	0.96	0.4
^{13}N	598.2	1.19	0.5
^{14}O	70.6	1.81	0.9
^{15}O	122.2	1.72	0.8
^{18}F	6588	0.64	0.3

Table 3.3. Characteristics of the positron-emitting isotopes produced by protons incident on isotopes of oxygen, carbon, and nitrogen.

Continuous Beams

A general treatment of the production and decay of positron-emitting isotopes by proton radiotherapy beams has been presented in [30]. Here, a detailed formulation is presented for analysis of our specific experimental results. The most important factors in the production of the so-called PET isotopes are the number of target nuclei per cubic centimeter, $n_i(\mathbf{r})$, the particle flux in particles per second per square centimeter, $\Phi(\mathbf{r},t)$, the beam energy, $E(\mathbf{r})$, at all points in the treatment volume, and the energy-dependent cross sections of the target nuclei for the various PET reaction processes, $\sigma_{ip}(E)$. The energy is expressed in units of MeV and the cross section is expressed in units of barns(1b = 10^{-24} cm^2).

For a small volume in the treatment field, the time rate of change in the number, N_i, of positron-emitting nuclei of type, i, depends on the production rate, by a process, p, and the decay rate. This is given by

$$\frac{dN_{ip}(\mathbf{r},t)}{dt} = \sigma_{ip}(E(\mathbf{r}))\ \Phi(\mathbf{r},t)\ n_i(\mathbf{r})\ A\ dz - \lambda_i N_i(\mathbf{r},t) \tag{3.1}$$

where the decay constant of the isotope is $\lambda_i = \ln(2) / t_{1/2_i}$ and the cross sectional area of the beam is A.. If the beam flux is constant over time, $\Phi(\mathbf{r},t) = \Phi(\mathbf{r})$, with a beam-pulse duration of T_{on} seconds, the resultant number of nuclei from the process is

$$N_{ip}(\mathbf{r},t) = \frac{\mathcal{A}_{ip}^{max}(\mathbf{r},t)}{\lambda_i}\begin{cases}(1-e^{-\lambda_i t}) & if\ t \le T_{on} \\ (1-e^{-\lambda_i T_{on}})e^{-\lambda_i (t-T_{on})} & if\ t \ge T_{on}\end{cases} \tag{3.2}$$

where $\mathcal{A}_{ip}^{max}(\mathbf{r},t) = \sigma_{ip}(E(\mathbf{r}))\ \Phi(\mathbf{r})\ n_i(\mathbf{r})\ A\ dz$, is the maximum activity of isotope, i, that can be produced in a differential volume through the process, p. The activity, $\mathcal{A}_{ip}(\mathbf{r},t)$, is then given by

$$\begin{aligned}\mathcal{A}_{ip}(\mathbf{r},t) &= \lambda_i N_{ip}(\mathbf{r},t) \\ &= \mathcal{A}_{ip}^{max}(\mathbf{r},t)\begin{cases}(1-e^{-\lambda_i t}) & if\ t \le T_{on} \\ (1-e^{-\lambda_i T_{on}})e^{-\lambda_i (t-T_{on})} & if\ t \ge T_{on}\end{cases}\end{aligned} \tag{3.3}$$

where time is measured from the moment the beam is turned on. Equation (3.3) may be used to find the distribution of activity, due to isotope, i, which was created through process, p, by a radiotherapy beam have a constant flux over a period of time, T_{on}.

Pulsed Beams

Many of the accelerators used for proton radiotherapy are synchrotrons which deliver macroscopic pulsed beams due to the ramp time of the magnets. (In this treatment we ignore the microscopic, sub-microsecond pulse structure of the beam due to the RF system.) In these cases the equations above are only applicable for one macro-pulse of the beam. If the accelerator has a period, $T = T_{on} + T_{off}$, then the activity present at any time is the sum of the activity remaining from each of the previous pulses. Suppose there are N pulses delivered during a treatment. The amount of activity created through a given process, p, for each pulse is constant as given in (3.3), when $t = T_{on}$. Accounting for the decay of the activity created by each pulse and summing, the activity present after the last beam pulse is

$$\begin{aligned} \mathcal{A}_{ip}(\mathbf{r},t) &= \mathcal{A}_{ip}^{max}(\mathbf{r},t)\left(1-e^{-\lambda_i T_{on}}\right)\left[e^{-\lambda_i T(N-1))}+e^{-\lambda_i T(N-2))}+\ldots+e^{-\lambda_i T(N-N))}\right] \\ &= \mathcal{A}_{ip}^{max}(\mathbf{r},t)\left(1-e^{-\lambda_i T_{on}}\right)\begin{cases} \sum_{j=0}^{n-1} e^{-j\lambda_i T} & \text{after } n \text{ pulses} \\ \left[\sum_{j=0}^{N-1} e^{-j\lambda_i T}\right] e^{-\lambda_i (t-TN+T_{off})} & \text{if } t \geq (TN - T_{off}). \end{cases} \end{aligned} \tag{3.4}$$

In the simplest case, PET activity is created by a continuous beam in a homogenous material of uniform density through one of the reactions shown in Table 3.2. Generally, however, the PET activity distribution produced will be the result of many of these reactions, several of which may produce the same radioisotope through different reaction processes. The final PET activity distribution produced during the treatment is then the sum of these activity distributions and is given by

$$\mathcal{A}(\mathbf{r},t) = \sum_i \sum_p \mathcal{A}_{ip}(\mathbf{r},t). \tag{3.5}$$

The Particle Flux Throughout the Treatment Volume

The particle flux term, $\Phi(\mathbf{r})$, in the equations above describes the particle flux, energy, and energy distribution at all points in the treatment volume. The model of the energy and flux distributions is similar to other models [30]. The energy distribution is primarily determined by the loss of energy through elastic collisions between the protons in the beam and the electrons in the tissue, the energy distribution of the incident beam and energy straggling. The net flux through a small area perpendicular to the beam axis depends primarily on the initial beam flux, absorptive nonelastic nuclear interactions, such as those leading to the production of PET isotopes, and multiple Coulombic nuclear scattering.

To calculate the distribution of positron-emitting activity, the energy as a function of depth must be determined for the material of interest. This is accomplished by numerically integrating the inverse of the total stopping power [36] as follows

$$z = \int_{E}^{E_o} \left(\frac{dE}{dx}\right)_T^{-1} dE. \tag{3.6}$$

Including the energy distribution of the beam and the energy straggling effects due to electronic elastic interactions significantly complicates the calculation of the activity distribution [30]. However, the energy straggling in human tissues at typical treatment energies is expected to be about one percent of the overall energy [36]. Likewise, the acceptable energy distribution of the treatment beam results in range variations of one to two percent [37]. Adding these effects in quadrature results in FWHM range variations in uniform tissue of under 0.5 cm for a 250 MeV proton beam, which has a 38.5 cm range, and under 0.3 cm for a 150 MeV proton beam, which has a 16.0 cm range. The reaction cross sections vary slowly with energy for the most important PET isotopes. Consequently the resulting variations in the PET activity distribution, due to the typical energy spread of a proton radiotherapy beam, would only be resolvable near the end of

the range, where the cross sections quickly decrease with increasing range. This would require using state-of-the-art PET imaging systems with a resolution of about 0.2 cm[38].

In addition to knowing the range-energy relationship it is also necessary to know the range number-distance curve. Particle flux is primarily lost through nonelastic nuclear interactions. At 250 MeV and 150 MeV approximately 31% and 17%, respectively, of the protons passing through tissue are removed from the beam by nuclear processes [36]. By comparison, our calculations for 150 MeV protons in tissue show that about 3.5% of the beam flux produces positron-emitting isotopes through the reactions shown in Table 3.2. It has been shown [30] that if $P_{abs}(E)$, is the probability that a particle is absorbed and undergoes a nuclear reaction before the end of its range, the fraction of the initial flux, $r_{abs}^{E_o}(z)$, remaining at a given depth is

$$r_{abs}^{E_o}(z) = \frac{\left[1 - P_{abs}(E_o)\right]}{\left[1 - P_{abs}(E(z))\right]}. \tag{3.7}$$

The resulting proton flux drops off with increasing depth is then

$$\Phi(z) = \Phi_o \, r_{abs}^{E_o}(z). \tag{3.8}$$

Like energy straggling, the small-angle scattering caused by multiple Coulombic interactions would likewise complicate the calculation of the activity distribution. The angular distributions arising from such small-angle scattering in mixtures and compounds have been adequately parameterized [39, 40] for the purposes of calculating PET activity distributions. These depth-dependent angular distributions may be convolved with the geometrical cross section of the treatment beam to parameterize the beam flux at any given point in the treatment volume. However, the net flux will remain unchanged at a given depth for uniform fields in homogenous targets since the net flux scattered into or out of a given region will be zero. This assumption is not valid near the edge of the treatment field or near inhomogeneities such as bone which have a significant component of their interface parallel to the beam.

Cross Sections for Producing Positron-Emitting Isotopes

Cross sections for the reactions listed in Table 3.2 are presented in Figures 3.1a and 3.1b [33, 41-47]. Due to the high number density of oxygen in tissue and the relatively high cross section for the $^{16}O(p,pn)^{15}O$ reaction, ^{15}O is the most active isotope at the end of a typical treatment. Despite the relatively low number density of ^{12}C in tissue, a significant amount of ^{11}C activity is also produced due to the high production cross section on ^{12}C and the abundance of ^{16}O. As noted earlier the threshold energies, as measured in the reference frame of the lab, vary from 2.6 to 39.1 MeV, below which the production goes to zero. The endpoint of the proton's range is therefore slightly beyond the distal end of the activity distribution as given in Table 3.2. Consequently, the end of the activity distribution and the end of the proton's range will not occur at the same depth. It will be shown that over 80% of the positron-emitting activity occurring on short time scales is due to ^{15}O. The range of the treatment beam below the reaction threshold for the $^{16}O(p,pn)^{15}O$ reaction is only 0.3 cm. Thus for on-line imaging the end of the activity distribution is a rather good marker for the range of the treatment beam in homogenous materials.

Correlation Between Total Dose and Total Activity

The possibility of discerning the dose distribution from the decay distribution of long-lived positron-emitting activity created by the treatment beam has previously been explored by other investigators [28, 30]. Because the physical mechanisms by which nuclear and atomic interactions occur are not related, it is very difficult to extract the dose distribution from the decay distribution. This has been demonstrated with ^{11}C decay distributions produced by proton beams in Lucite [30]. It is possible however, to monitor the total dose delivered by monitoring the total number of annihilation events detected as a function of time. The total dose delivered after n pulses is given by

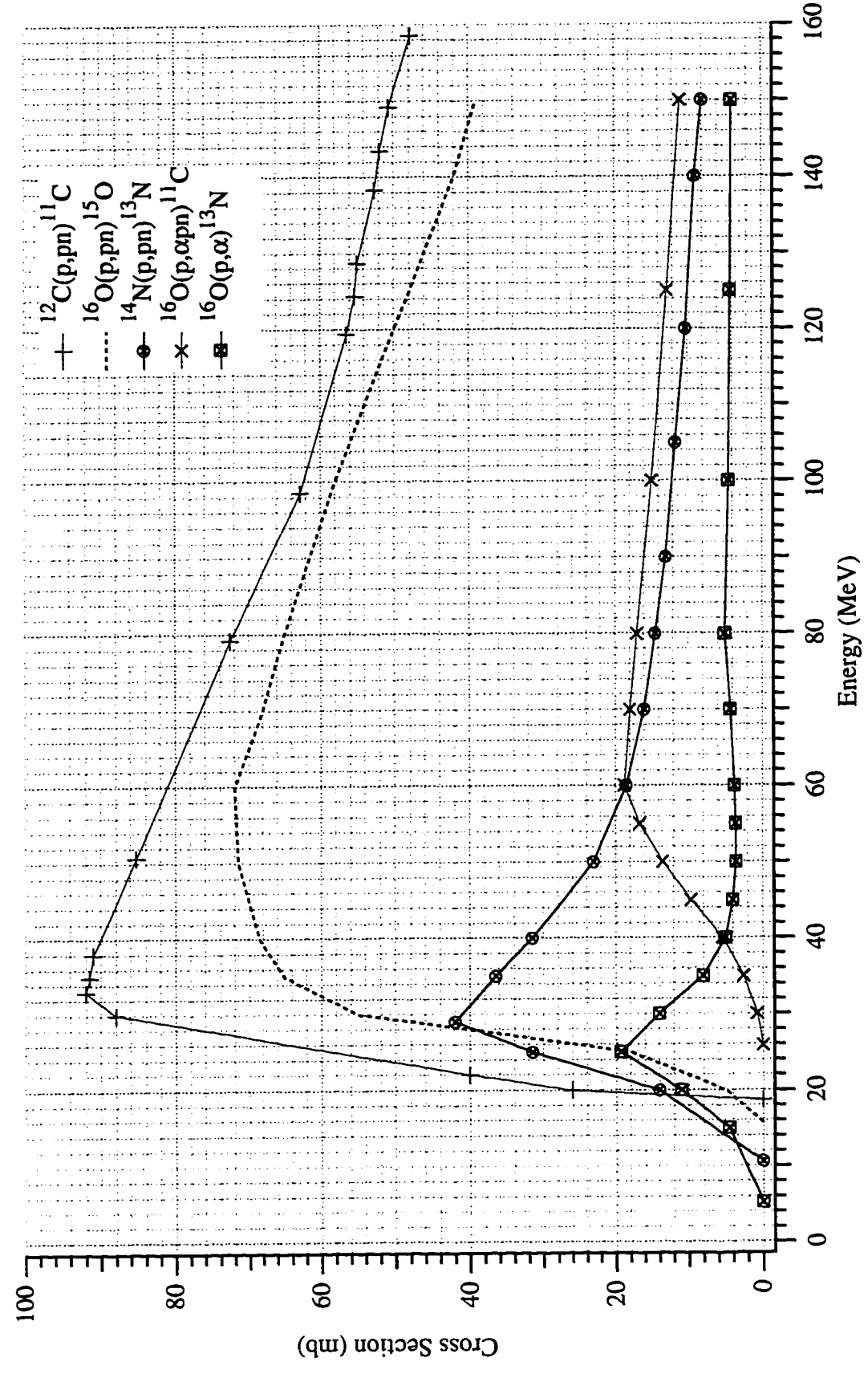

Figure 3.1a. Cross sections for the production of positron-emitting nuclei from the elements commonly found in tissue.

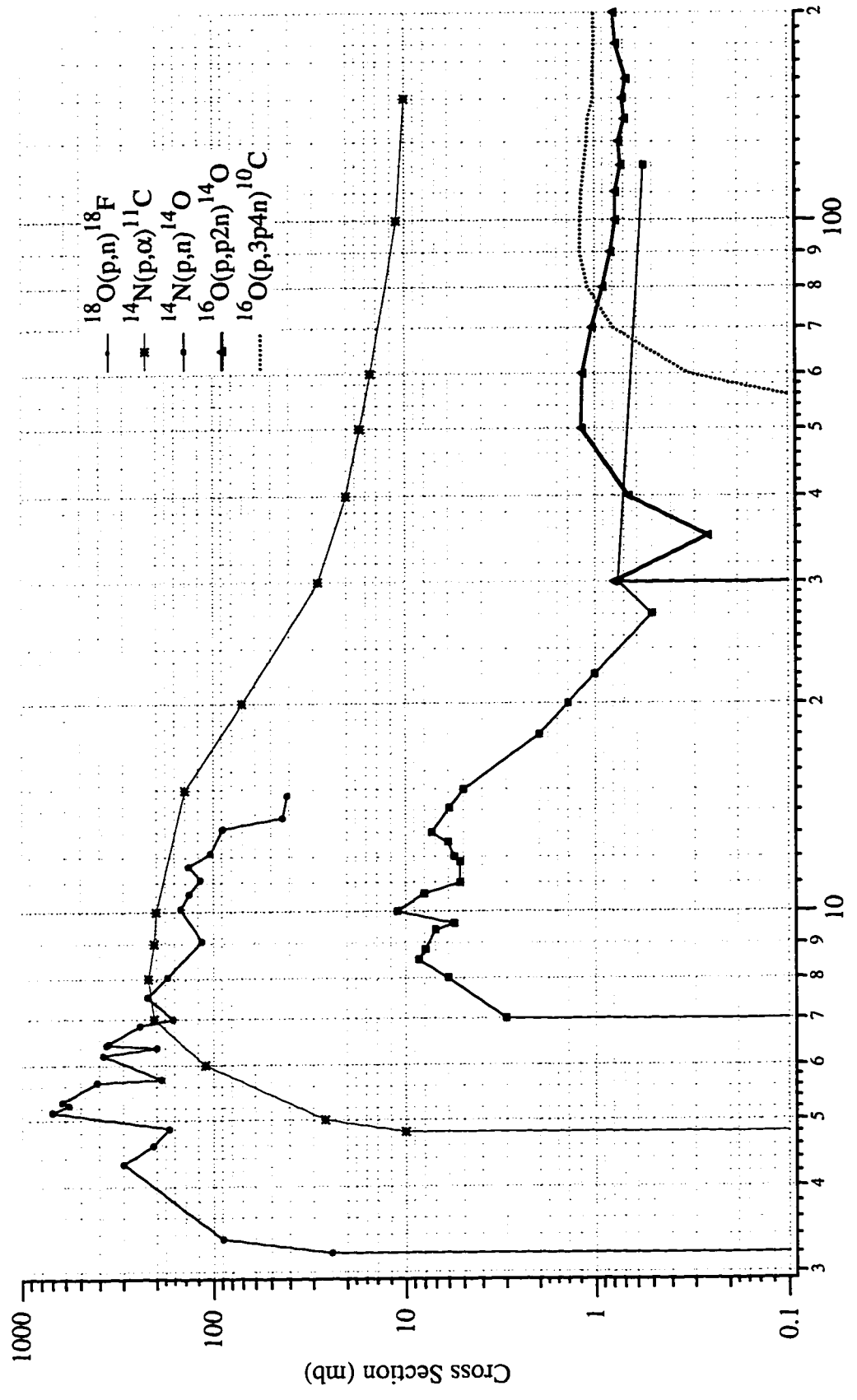

Figure 3.1b. Cross sections for the production of positron-emitting nuclei from the elements commonly found in tissue.

$$D = \frac{energy}{mass} = \frac{P_{beam}\, t}{\rho_T V} = \frac{E_o \Phi_o (nT_{on})}{\rho_T V}, \tag{3.9}$$

where $P_{beam} = E_o \Phi_o$. The units of the dose are in Gray if the beam energy is in MeV, the beam current is in microamps, T_{on} is in seconds, and the mass of the treated volume is in kilograms. The total activity present after n pulses is given by integrating (3.5) over the treatment volume. After performing the integral and solving for the initial beam current the total dose after n pulses, $D(n)$ is found to be related to the activity by the relationship

$$D(n) = \frac{E_o n}{\rho_T V} \frac{N_n}{\sum_i \sum_p \left[Y_{ip} \sum_{j=0}^{n-1} e^{-j\lambda_i T} \right]}. \tag{3.10}$$

Here, $N_n = \mathcal{A}(t)\, T_{on} = \mathcal{A}(t)\, T_{off}$, is the number of decays between pulses n and $(n+1)$, and

$$Y_{ip} = \left(1 - e^{-\lambda_i T_{on}}\right) \int_0^R \sigma_{ip}(E(z))\, r_{abs}^{E_o}(z)\, n_i(z)\, A\, dz \tag{3.11}$$

is the yield of radioisotope, i, by the process, p, per (proton/cm^2) per pulse.

The number of decays between successive beam pulses will eventually become constant if the treatment time is long compared to the half-life of the longest-lived isotope, which is typically ^{11}C. However, if the treatment time is less than or comparable to the half-life of the shortest-lived isotope, the number of decays detected between each beam pulse will be approximately linear. Treatment times are typically less than two minutes, or less than one half-life of ^{15}O which is the shortest-lived isotope produced in abundance. In later sections it will be shown that on short time scales the number of decay events detected between beam pulses increases roughly linearly with the treatment time for macro-pulsed beams.

Activity and Dose Calculations

A simulation code was written to estimate the depth-distribution of PET isotopes produced by proton beams in materials of varying composition. Several layers of materials of differing composition may be placed in series. The stopping power of the material is

$$\frac{1}{\rho_T}\left(\frac{dE}{dz}\right)_T = \sum_i \frac{1}{\rho_i}\left(\frac{dE}{dz}\right)_i, \tag{3.12}$$

where $(dE/dz)_i$ is the stopping power of the individual elements. Stopping power values are obtained from spline fits to the values given in relevant data compilations [36]. The dose and energy as a function of depth are then found by numerically integrating (3.12). Once the energy as a function of depth, $E(z)$, is known the energy-dependent PET-isotope production cross sections may be mapped into depth-dependent cross sections. The depth-dependent particle flux is calculated from (3.7). Range straggling and scattering have not been implemented in the code for the reasons stated previously. The isotopic distribution of PET activity is then calculated in 0.2 cm increments with (3.5) using (3.3) for continuous beams and (3.4) for pulsed beams. The total and isotopic activity distributions may be compared directly with experimental results by integrating the appropriate calculated activity distributions over the experimental imaging time.

Experimental

Characteristics of the Macro-Pulsed Proton Beam

A variable-pulsed beam of protons was produced at the National Superconducting Cyclotron Laboratory at Michigan State University (NSCL) by passing a primary beam of ionized molecular hydrogen through a stripping foil. After passing through the stripping foil the beam passed through a 0.010 inch (0.0254 cm) thick Havar vacuum

window and into air before entering the phantom. In separate experiments conducted on different occasions the beam energies at the surface of the phantom were 145 MeV and 150 MeV. These beams had a micro-pulse structure due to the RF accelerating frequencies of 23.2015 MHz and 24.1036 MHz, respectively. The beam was focused to an average FWHM diameter of one centimeter and one millimeter at these energies respectively. Typical beam currents used ranged from 0.1 to 5 nanoamps. Variable macro-pulsing periods were achieved by phasing and dephasing the RF to the cyclotron dees as described in the next section.

Gamma-Ray Detectors, Beam-Pulsing and Data Acquisition

The gamma-ray detection system consists of two rows of detectors, Figure 3.2, encased in a custom made lead shield. The latter provided a minimum shielding thickness of 116 g/cm^2 on the top and bottom and 30 g/cm^2 on the ends of the array. Each row contains twelve cylindrical BGO crystals. The cylindrical surface and one end of each crystal was ground to provide optimal light collection properties while the other end of the crystal was polished. The ground surfaces were wrapped in a high-purity Teflon tape and then wrapped with aluminum foil. The polished end of the crystal was left unwrapped and coupled to a high-gain version of the Hamamatsu R1166 photomultiplier tube (PMT) with optical grease. The unit was then wrapped with electrical tape, high-permeability, mu-metal for magnetic shielding, and finally more electrical tape. Each crystal is 1.90 cm in diameter and 5.08 cm long and slides into a 2.22 cm diameter hole in the lead shielding. Adjacent crystals are separated by 0.50 cm. This produces a minimum septa thickness of 0.18 cm between adjacent detectors providing a minimum of 1.8 g/cm^2 of shielding between detectors to suppress the detection of Compton-scattered γ's and electrons. The front surfaces of the detectors between the two rows were separated by 60 cm for these experiments. In addition, lead shutters provided 58 g/cm^2 of shielding to the front of the detectors while the beam was

on to reduce activation of the crystals. Further details on the design and efficiency of the detection system may be found in [DWL1, 34]. The shutters were operated by a pneumatic cylinder which was controlled by a time-delay relay switch. Typical periods, T, for a shutter cycle were 10 and 20 seconds with the shutters being opened for half the cycle.

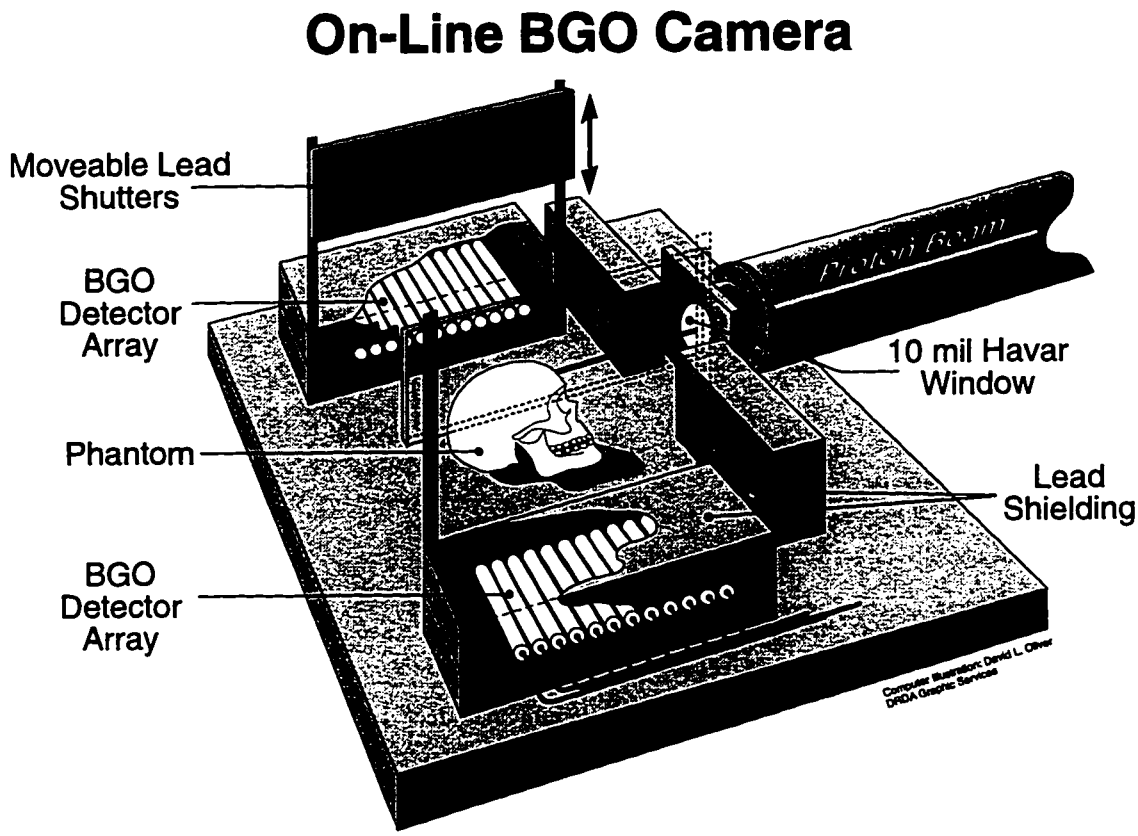

Figure 3.2. Schematic representation of the low solid angle BGO detection system. The two rows of twelve BGO detectors encased in lead shielding are typically separated by 60 cm. The lead shutters are closed during beam pulses to prevent activation of the crystals.

A photogate mounted on the shutters controlled the phase of the RF to the cyclotron. When the shutters were open the cyclotron RF was dephased, quickly turning off the beam, and data acquisition was enabled. After half a period the shutters closed, disabling data acquisition and restoring the phase of the RF for beam acceleration.

Details of the electronics and data acquisition system are described in [DWL2, 48]. This system used fast-encoding readout ADC's (FERA's) to obtain energy and timing information for each event. The data was digitized and readout over an ECL data bus with a deadtime of 25 microseconds. The system allowed the data to be either filtered in realtime, with timing and energy cuts downloaded to VME-based transputers, or stored in a memory board for periodic transferal to the SUN host computer. During pulsed-beam experiments data accumulation intervals were set to match the beams pulse period or half the pulse period. The SUN host could then route the data buffers to other devices for further analysis, display and storage.

System Efficiency

The efficiency of the system was measured during calibration runs when the system matrix, S, was determined. Calibrations were performed prior to conducting imaging experiments by translating a standardized ^{22}Na source along the system axis with a constant velocity. The coincidence detection efficiency(*CDE*) is defined as the number of 511 keV gamma-ray pairs detected in coincidence divided by the total number of positron annihilations at a given location along the system axis during a fixed time interval. The *CDE* as a function of position along the system axis is shown in Figure 3.3. The average *CDE* over the length of the axis was found to be $1.10 \times 10^{-2}\%$. This efficiency results in total event rates of approximately 1000 counts per second if 250 μCi is uniformly distributed along the axis of the imaging system. Further details on how the *CDE* is effected by the detection geometry may be found in [DWL1, 34].

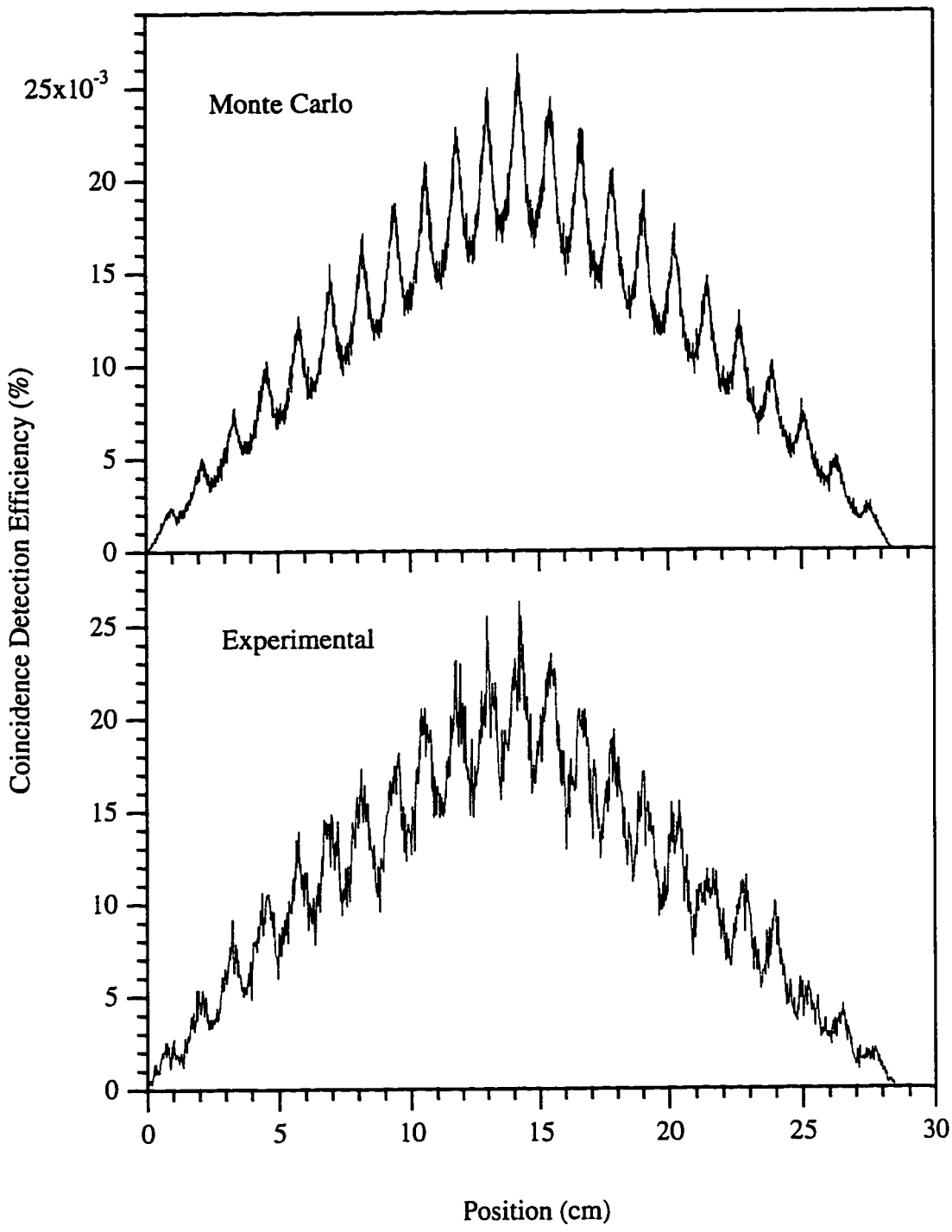

Figure 3.3. Comparison of Monte Carlo simulation and experimentally measured CDE's for a detector separation of 60 cm.

Gamma-Ray Energy and Coincidence Timing Requirements

A valid annihilation event is determined by two primary conditions: 1) there must be an event in at least one detector in each of the opposing rows which has an energy of 511 keV, and 2) these events must occur within the coincidence timing resolution of the given detector pair. Again, the criteria for meeting these conditions are determined during the calibration of the imaging system prior to performing experiments. Figure 3.4 shows a typical coincidence energy spectrum obtained during a calibration run. The full width at half the maximum value(FWHM) is about 30%. The dashed lines show the 55% energy window used for determining if the detected gamma-ray had the required energy of 511 keV. Figure 5 shows a typical coincidence-delay curve obtained during a calibration run. The typical coincidence resolving time for any given detector pair, τ_{ij}, was measured to be about 4 nanoseconds for the experiments presented in this work. Random coincidences are corrected during on-line imaging using a count-rate based method for each detector pair. The total number of coincidences detected per time interval is the sum of the chance and true coincidences, $N_d = N_c + N_t$. The rate at which randoms occur is taken to be $r_c = 2\tau_{ij} r_i r_j$, where τ_{ij}, is the coincidence resolving time, r_i is the singles rate in detector i, and r_j is the singles rate in detector j. After imaging for T seconds the number of singles in detectors i and j are N_i and N_j, respectively. An estimate of the number of true coincidences detected by any given detector pair after acquiring data for T seconds is given by

$$N_t = N_d - \frac{2\tau_{ij} N_i N_j}{T}. \tag{3.13}$$

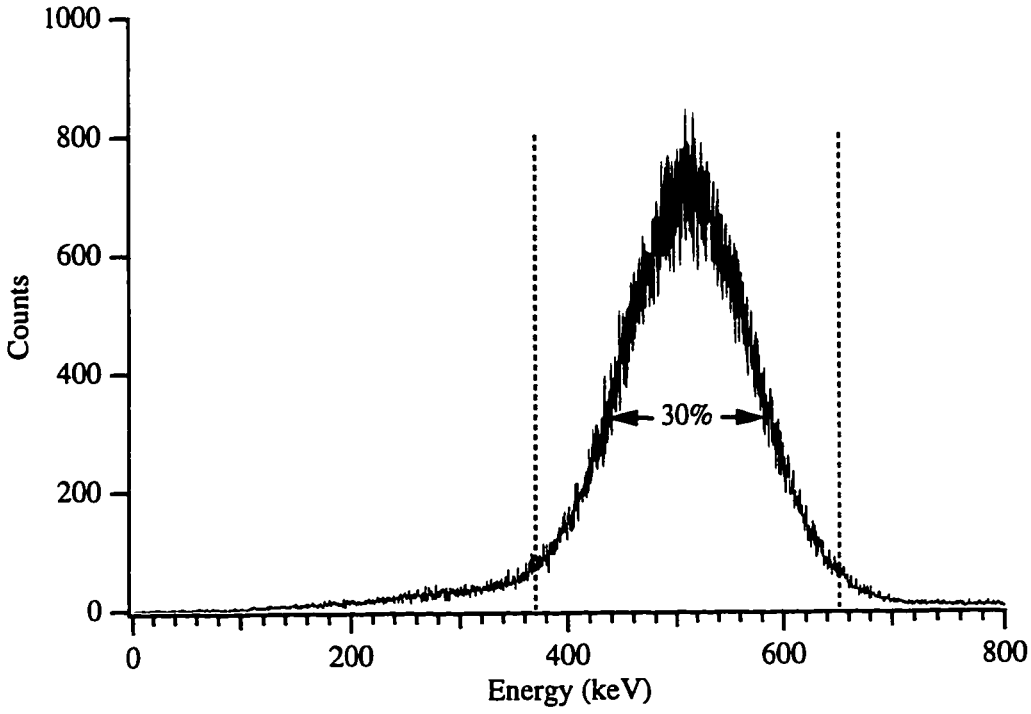

Figure 3.4. A typical coincidence energy spectrum obtained during a calibration run. The FWHM energy resolution is 30%. The energy window is shown by the dashed lines and is at the FWTH or 55%.

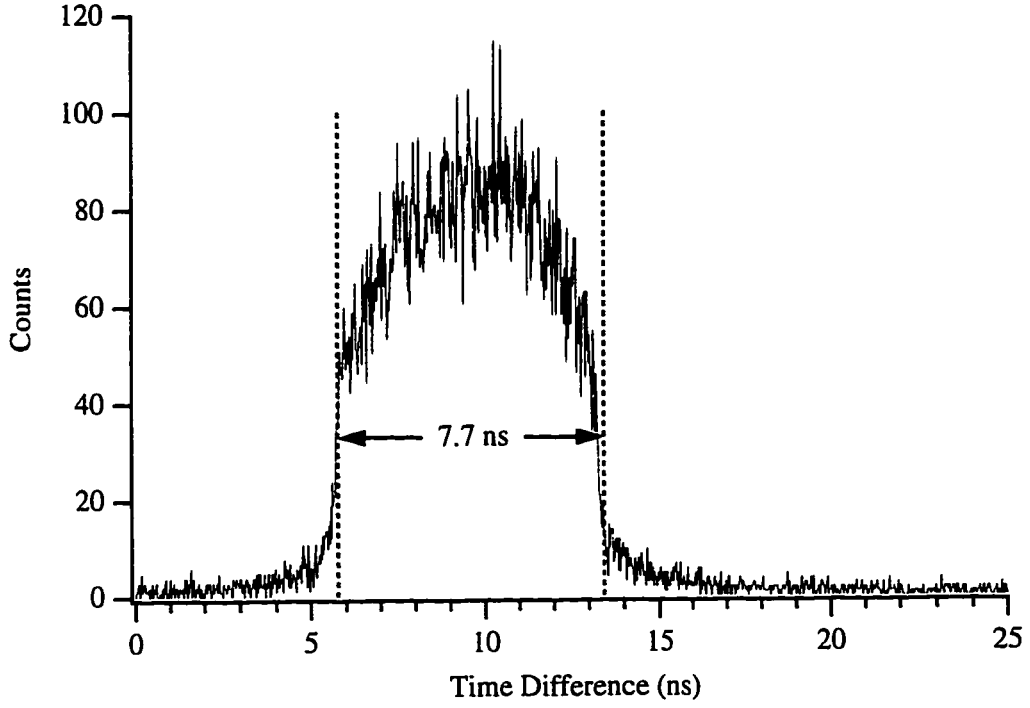

Figure 3.5. A typical coincidence-delay curve obtained during a calibration run. The coincidence resolving time, τ, is about 4 nanoseconds.

The corrections are largest immediately after the treatment is finished as that is when the maximum amount of activity is present. However, even at this time the number of random coincidences is less than 1% of the total coincidences detected primarily due to the short, 4 ns, coincidence resolving time.

Image Reconstruction and Isotopic Imaging

The image reconstruction algorithm for this system has been discussed in [DWL1, 34]. The proton beam creates a distribution of PET activity, $\mathcal{A}(\mathbf{r},t)$, as given by (3.5) with the appropriate substitution of (3.3) or (3.4). Over the image acquisition time, $T_I = t_2 - t_1$, the spatial distribution of decays is

$$\mathcal{D}(\mathbf{r}) = \int_{t_1}^{t_2} \mathcal{A}(\mathbf{r},t)\, dt. \tag{3.14}$$

This vector distribution of decays produces a vector response, $\mathcal{R}$, from the imaging system. The mapping between the vector response and the spatial decay distribution is given by the system matrix, S [DWL1, 34]. The spatial decay distribution is given by

$$\mathcal{D}_{abs} = \frac{1}{m}\left(\frac{A_{cal}\, L}{v_s}\right) S^{-1}\, \mathcal{R}, \tag{3.15}$$

where, A_{cal}, is the activity of the calibration source in decays per second, L is the length of the imaging array, v_S, is the velocity of the calibration source, m is the number of elements in the reconstructed decay distribution and S^{-1} is the inverse of the system matrix. During on-line imaging, data was acquired between beam pulses. In these experiments the image acquisition time was typically five seconds which is half the beam period, $T_I = T/2$. After each beam pulse the expected decay distribution based on (3.4) and (3.5) may be compared with that found by (3.15).

Radioisotopic imaging may be performed if a series of datasets are acquired during the decay of the activity distribution. This is particularly useful for determining

the distribution of oxygen along the beam path since the $^{16}O(p,n)^{15}O$ reaction is the only significant source of ^{15}O in soft tissues and bone. The total imaging time should be about three times the half-life of the radioisotopes being examined, or five to six minutes in the case of ^{15}O.

Suppose the decaying activity distribution is continuously sampled by recording the number of counts occurring in a series of time increments of length, $T_I = t_2 - t_1$. In any given element of one of the response vectors, the number of counts is proportional to the sum of the isotopic activities and has the form

$$\begin{aligned} \mathcal{D}_j &\propto \int_{t_1}^{t_2} \left[\sum_i \mathcal{A}_i^{max} e^{-\lambda_i t} \right] dt \\ \mathcal{D}_j &\propto \sum_i \mathcal{A}_i^{max} \left(\frac{e^{-\lambda_i T_I} - 1}{\lambda_i} \right) e^{-\lambda_i t_2}. \end{aligned} \tag{3.16}$$

The decay data for each element of the response vector may be fit to a decay model to find the initial distribution of activity, $\mathcal{A}_i^{max}$, for each isotope in response-space. Statistical tests for determining the presence of trace radioisotopes in the decay data are presented in the next section. Once the initial activity of each radioisotope has been determined, the total number of counts occurring in that element of the response vector due to a specific radioisotope may be found by integrating the decay curve with the appropriate constants. In this way isotopic response vectors may be obtained for each radioisotope occurring in the field of view of the imaging system. Radioisotopic images may then be found by using (3.15) with each of the radioisotopic response vectors.

Error Analysis and Statistical Tests

The uncertainty in a reconstructed image may be found using the following theorem [49].

> "Let $\mathcal{D}$ be an n-dimensional normal random vector with positive definite covariance matrix K and mean vector μ. Let S be a nonsingular linear

transformation in n dimensions. Then $\mathcal{R} = \mathcal{S}\mathcal{D}$ is an n-dimensional normal random vector with covariance matrix $Q = \mathcal{S}K\mathcal{S}^T$ and mean vector $\beta = A\mu$."

The covariance matrix, Q, of the response vector, $\mathcal{R}$, contains the variance of the elements of $\mathcal{R}$ on its diagonal with all other elements of Q being zero. The uncertainty in the elements of $\mathcal{R}$ is Poisson so that $Q_{jj} = \mathcal{R}_j$. The decay of radioactive isotopes is also a Poisson process, therefore the variance in the elements of the reconstructed image is given by the diagonal elements of the covariance matrix, K, where K is given by

$$K = \mathcal{S}^{-1} Q\left(\mathcal{S}^T\right)^{-1}. \tag{3.17}$$

The uncertainties in radioisotopic images are compounded by the uncertainty in determining the initial activity coefficients while fitting the decay data. The decay curves are fit using the Levenberg-Marquardt method with Poisson weighting. While this non-linear fitting algorithm may be used to determine the half-lives of unknown radioisotopes, the half-lives of the isotopes produced are well known. In all cases presented only the linear activity coefficients are included in the decay model while the half-lives are fixed. This algorithm calculates the covariance matrix for the fit parameters, giving an estimate of the uncertainty in each of the initial isotopic activities for each element of the response vector. The calculated variance is larger than the variance expected from Poisson counting statistics alone and also includes the variance in the fit. It is thus possible to form response variance vectors, $\mathcal{V}$, for each decaying radioisotope by integrating the decay curve with the appropriate constants. As described above, the covariance matrix for a given isotopic response vector is then $Q_{jj} = \mathcal{V}_j$.

In addition to the uncertainties discussed above, there are negative correlations between the values of adjacent pixels. This can be seen in the reconstructed image of the calibration source, shown in Figure 3.6, which shows elements with negative magnitude adjacent to the source. The 10.36 μCi, ^{22}Na calibration source was placed near the center

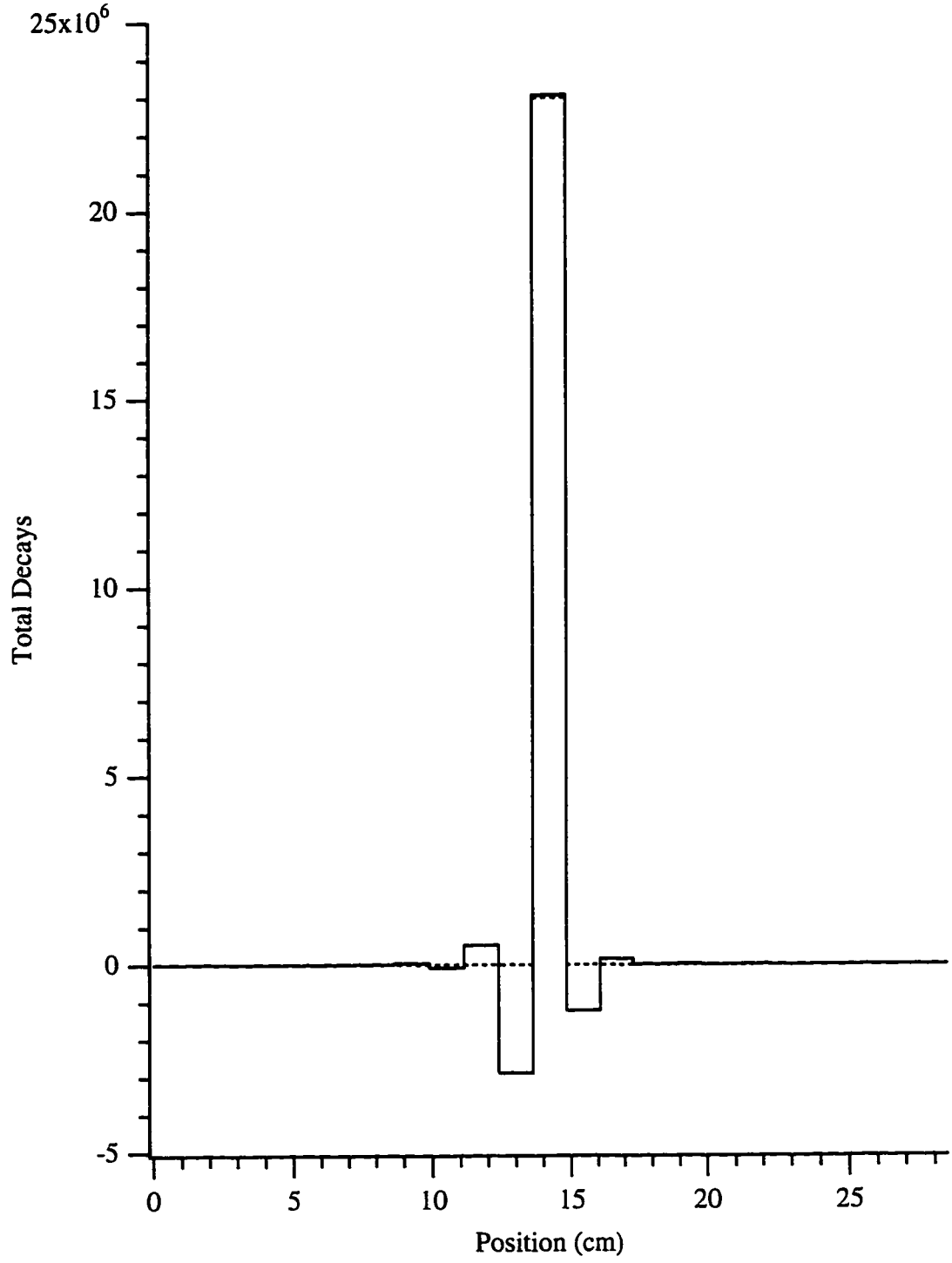

Figure 3.6. Reconstructed image vector of the calibration source placed near the center of the array. The solid line shows the measured image of the calibration source while the dashed line shows the ideal image of a point source of the same magnitude in the same location. The negative correlations in the adjacent bins arises from the uncertainty in the positron's position when annihilated while generating a system matrix during a calibration run.

of the resolvable element and imaged for 60 seconds. The magnitude of the image has been corrected for the attenuation of the Lucite source holder and agrees with the expected magnitude to within 0.3%. As discussed in previous works [DWL1, 34] the spatial extent of the calibration source is one of the limiting factors in the spatial resolution achievable with this type of system. When the system matrix is determined there is an uncertainty in the location of the annihilation arising from the finite size of the calibration source and the range of the positrons. Since the columns of the system matrix are binning according to the location of the center of the calibration source this causes a small correlation between adjacent pixels and consequently, a degradation to the spatial resolution of the reconstructed images due to the calibration. On average the magnitude of the overshoot in reconstructed images is about 9% and is expected anywhere there is a discontinuity in the activity distribution. While this effect is still present for continuous activity distributions it is smaller and varies as the first derivative of the decay distribution, with respect to depth, at that location. These correlations are not reflected by the error bars shown in Figures of the image vectors. This effect may be reduced by using a calibration source whose spatial extent along the system axis is small and by wrapping the source in a thin layer of high-Z material to reduce the range of the positrons. The decay data from an experiment using a tissue phantom will predominately contain ^{11}C, ^{13}N, and ^{15}O but other positron-emitting isotopes such as ^{10}C and ^{14}O may be produced in smaller quantities. If the decay data from each of the 23 resolvable elements is summed, the statistics may be sufficient to estimate the abundances of these radioisotopes by including them in the fit to the summed decay data. Two statistical tests, based on the F-distribution, are used to validate the inclusion of trace radioisotopes in the decay model during a fit [50]. The first is an F test of the multiple-correlation coefficient, R, and verifies that the fit coefficients are positive and tests the minimum square deviation of the data from the decay model. The second F test compares two decay models which differ by one term, that of the trace radioisotope in question. The latter test

is based on the difference in the chi-squares of the two decay models. The presence of the trace radioisotope in question may then be verified to the desired level of confidence, which in this work is set at 99%. More details on these tests may be found in [50].

When the decay data from each of the resolvable elements are not summed the statistics may not be sufficient to identify the trace radioisotopes present in any one of the observed segments along the system axis. The above tests are applied to obtain the optimal fit for each position. If the presence of the trace radioisotopes cannot be confirmed by the *F* tests at the 99% confidence level, the trace radioisotope activity coefficients are set to zero. Measurements of the background rates in the imaging system resulted in vanishingly small rates. *F* tests on the inclusion of a background term in the decay model indicate that it generally does not improve the fit of the data to the model. Including terms for background or trace radioisotopes in the decay model at significantly lower confidence levels introduces additional linear correlations among the isotopic activity coefficients which degrades the quality of the isotopic images.

Results

The following sections contain the results of several imaging experiments carried out using continuous and pulsed protons beams implanted into tissue phantoms. The composition of these phantoms is given in Table 3.1. Decay data was collected for the three experiments presented. In each case, images are presented based on the cumulative dataset and based on the isotopic imaging technique described earlier. In the case of macro-pulsed beams, images acquired between beam pulses are presented. These are compared with the expected decay distributions as calculated using the reaction cross sections shown in Figures 3.1a and 3.1b and the composition shown in Table 3.1 which is assumed to be uniform. No experiments were performed using energy-modulated beams but the expected decay distributions are presented and are compared and contrasted with the expected and measured results obtained using nearly mono-energetic beams.

Off-Line PET Imaging

The production of long-lived positron-emitting isotopes was investigated off-line using a plastic skull phantom filled with swine tissue. This phantom was irradiated with a 125 MeV proton beam having a FWHM diameter of one centimeter. The beam was implanted continuously for ten minutes and had a current of five nanoamps. Due to the limited volume of the cranial cavity it was necessary to use an aluminum energy degrader to reduce the energy of the beam from 145 MeV to 125 MeV resulting in a range in tissue of 12.0 cm. The phantom was then transported ninety minutes by auto to the University of Michigan PET Facility where images of the ^{11}C activity distribution were obtained in a Cyclotron Corporation Model PC 4600 Neuro-PET head scanner [50].

Imaging in the PET scanner began 146 minutes after the beam ended and continued for over three hours. Figure 3.7a shows the PET image of the ^{11}C and ^{18}F activity remaining in the phantom. This image was obtained with the Neuro-PET head scanner in high-resolution mode using a Hanning-weighted ramp filter with a cutoff frequency of 1.75 cm^{-1}. In this mode the resolution is 1.14 cm FWHM. Figure 3.7b shows the profile of the decay distribution along the beam axis as measured by the PET scanner. The zero of the range measurement is located at the beginning of the tissue sample and the calculated proton range, which is just over 10 cm in the tissue, is indicated.

The high activity near the depth of -3 cm was produced by the carbon-rich skull phantom which was made of Lucite. The large decrease in activity from -2 to 0 cm is due to a two centimeter air gap between the plastic phantom and the tissue. The expected total decay distribution is shown in Figure 3.8. This distribution was calculated from the expected activity distribution by integrating over the imaging time which was from 8760 to 20760 seconds after the beam ended. The amount of ^{11}C produced by the $^{12}C(p,pn)^{11}C$ and the $^{16}O(p,\alpha pn)^{11}C$ reactions is nearly equal in this case and accounts for over 99% of the observed activity. During this decay interval the expected number of

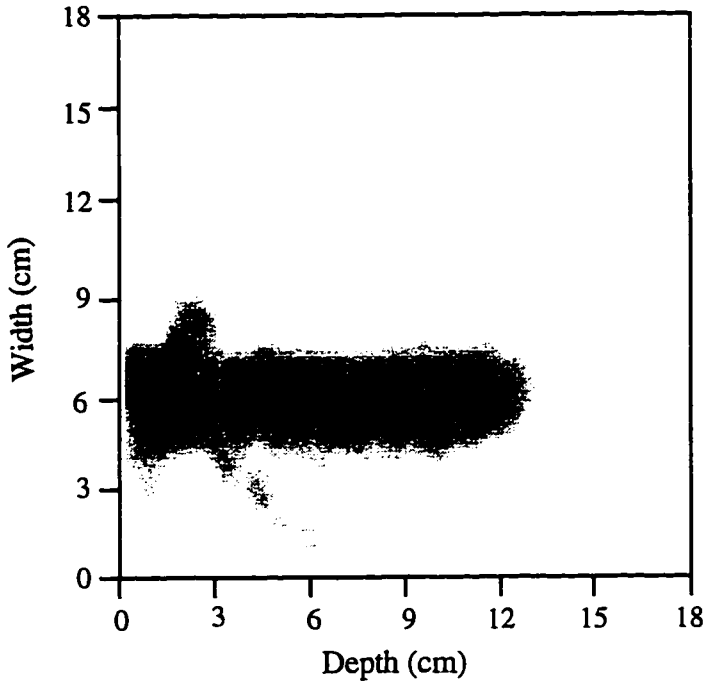

Figure 3.7a. PET image of skull phantom showing ^{11}C activity created by a 117 MeV proton beam.

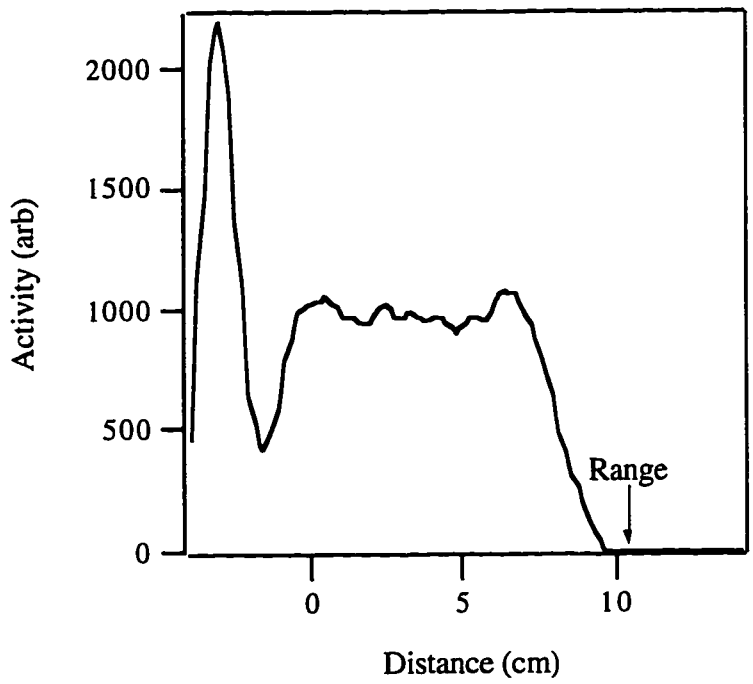

Figure 3.7b. Profile of decay distribution by PET scan in a tissue-filled skull phantom.

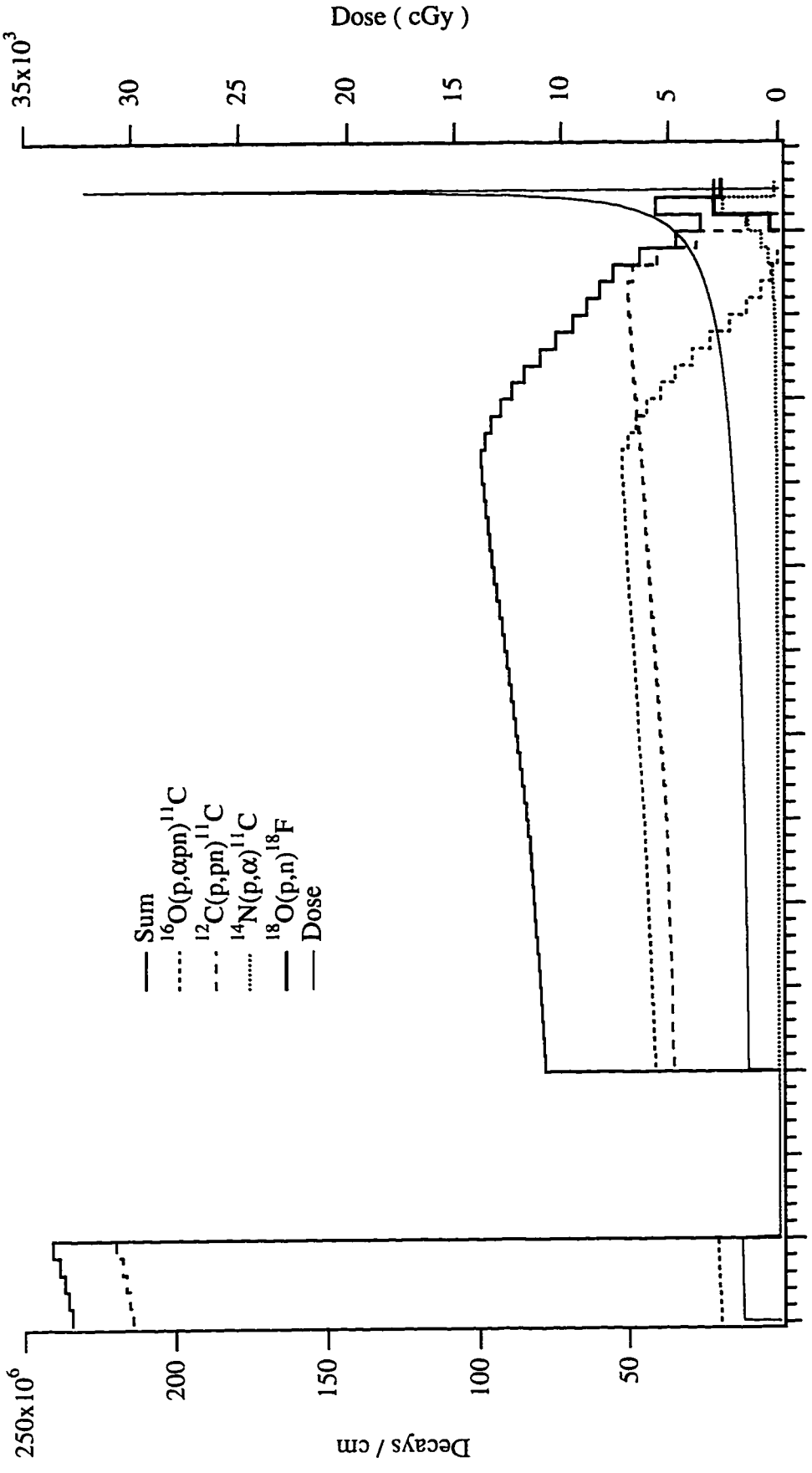

Figure 3.8. The decay and dose distributions expected from the PET scan of the skull phantom. Over 99% of the remaining activity is ^{11}C with traces of ^{18}F.

decays from ^{11}C and ^{18}F are 2.05 x 10^8 and 1.60 x 10^6, respectively. The image in Figure 3.7a was reconstructed from 3 x 10^6 events with no attenuation correction. The qualitative agreement between the measured decay distribution and the expected decay distribution is very good. The carbon-rich plastic skull phantom followed by the air gap is quite pronounced and the distribution of carbon in the tissue is uniform up to seven centimeters were it starts to drop off as expected. The small spike of ^{18}F activity which is expected at the end of the proton range is not observed due to the comparatively large, 1.14 cm FWHM, spatial resolution of the Neuro-PET imaging system.

The activity decay curve obtained while imaging is shown in Figure 3.9. The decay of activity was modeled as the sum of two exponentials, representing ^{11}C and ^{18}F. Background and ^{13}N were not found to be present at the 95% confidence level using the *F* tests described above. Using this data, the total activity at the end of the treatment was found to be 1.8±0.5 mCi of ^{11}C and 2.4±0.7 μCi of ^{18}F. The uncertainty in the activity arises from the uncertainty in the fit to the decay model, the uncertainty in the detection efficiency of the off-line PET imaging system, and from the estimated 20% uncertainty in the beam current. The expected activity from ^{11}C is 2.37 mCi. The amount of ^{11}C produced is about one standard deviation smaller than expected. This discrepancy is largely attributable to attenuation losses in the phantom. Uncertainties in the tissue's composition and variations in its homogeneity may also be a contributing factor. Measured cross sections for the $^{18}O(p,n)^{18}F$ reaction seem to only be available below 15 MeV [46]. Based on these cross sections the activity from ^{18}F, in the last 0.3 cm of the treatment beams range, is expected to be 0.07 μCi when the beam is turned off. This assumes that 0.2% of naturally-occurring oxygen is ^{18}O by mass. The activity of ^{18}F produced, however, is 40 times larger. This suggests that the average cross section of this reaction between threshold and 125 MeV is approximately 83 millibarns if a tissue density of 1 g/cm^3 is assumed. The cross section at 14.7 MeV has been measured to be

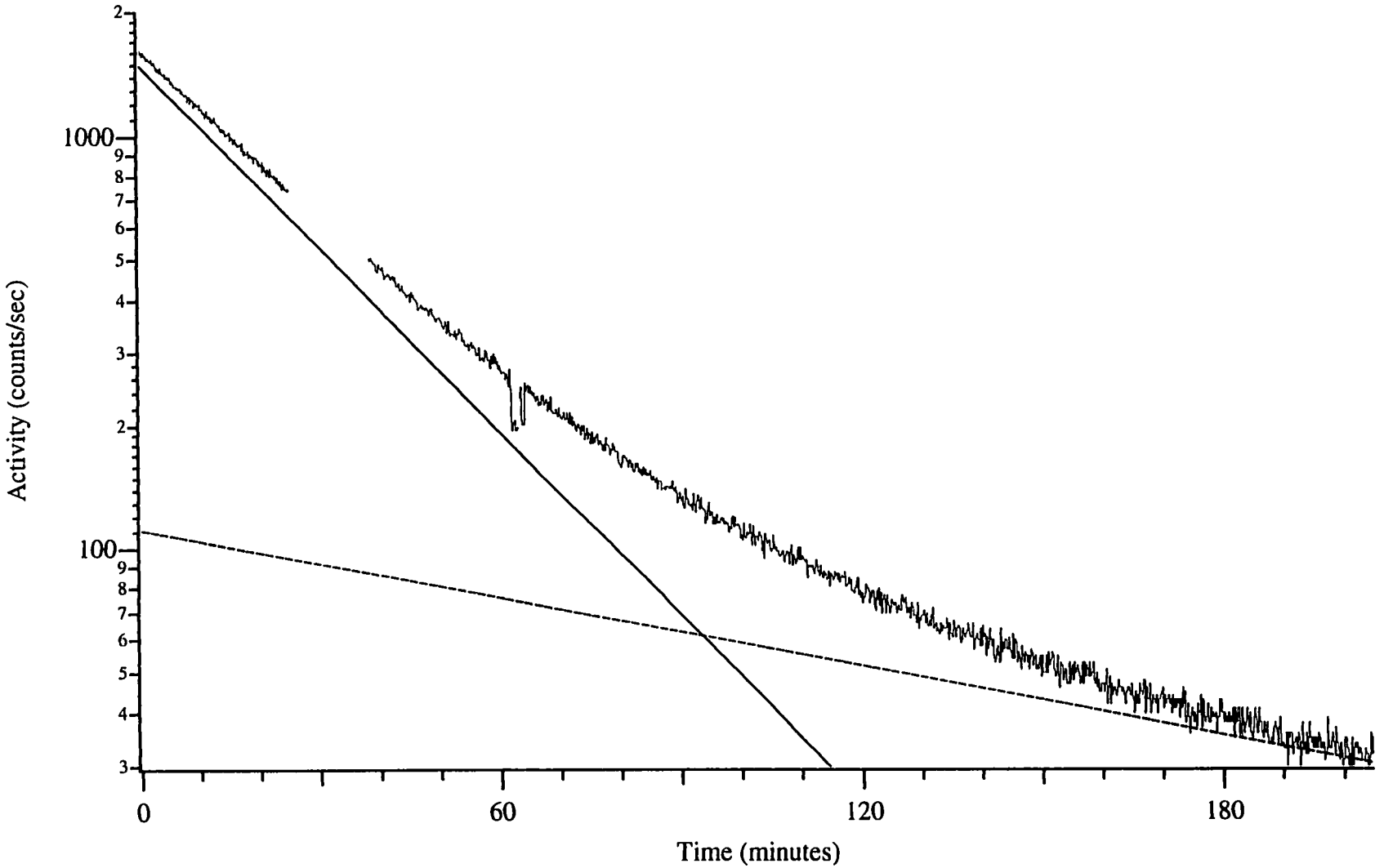

Figure 3.9. Decay data from the PET scan of the skull phantom showing the contributions of ^{11}C (solid line) and ^{18}F (dashed line).

41 mb [46] and would likely continue to decrease slowly with increased energy. This suggests that the amount of ^{18}F activity observed is still several times larger than expected.

Continuous Proton Beams into a Tissue Phantom

Range Verification and Isotopic Imaging

The production and distribution of short-lived isotopes was studied using the prototype on-line imaging system. The activity was created by a 150 MeV proton beam with a current of 1.75 nA and an expected range of 16.0 cm. This beam was implanted continuously for one minute into a swine-tissue phantom. The spatial and temporal decay distributions were measured beginning immediately after the beam was turned off. The surface of the 27 cm x 5 cm x 5 cm phantom was placed 2.0±0.3 cm from the front end of the detector array, inside the imaging system on the systems axis. The beam was terminated by opening the shutters, which dephased the accelerating RF and enabled data acquisition. Decay data was collected for 57 minutes in ten second bins. The initial coincidence rate was 2322 Hz with the computer being live for 2308 of these events giving a livetime of 99.40%. The total number of coincidence events recorded was 9.07×10^5 with 7.92×10^5 of these meeting the required timing and energy window cuts. The initial singles rates in the 24 detectors, after the beam was turned off, ranged from 3500 Hz to 6700 Hz.

Figure 3.10 shows the sum of the decay data from the 23 positions, the fit to the decay data, and the residuals which are shown at the top with the Poisson uncertainty. The best fit to the decay data is obtained by including ^{15}O, ^{14}O, ^{13}N, ^{11}C, and ^{10}C. The *F* tests for a decay model including ^{14}O and ^{10}C, indicate both are present at a 99% confidence level in the summed decay data. However, including a background term is not justified by these tests and this coefficient was set to zero. Isotopic response vectors

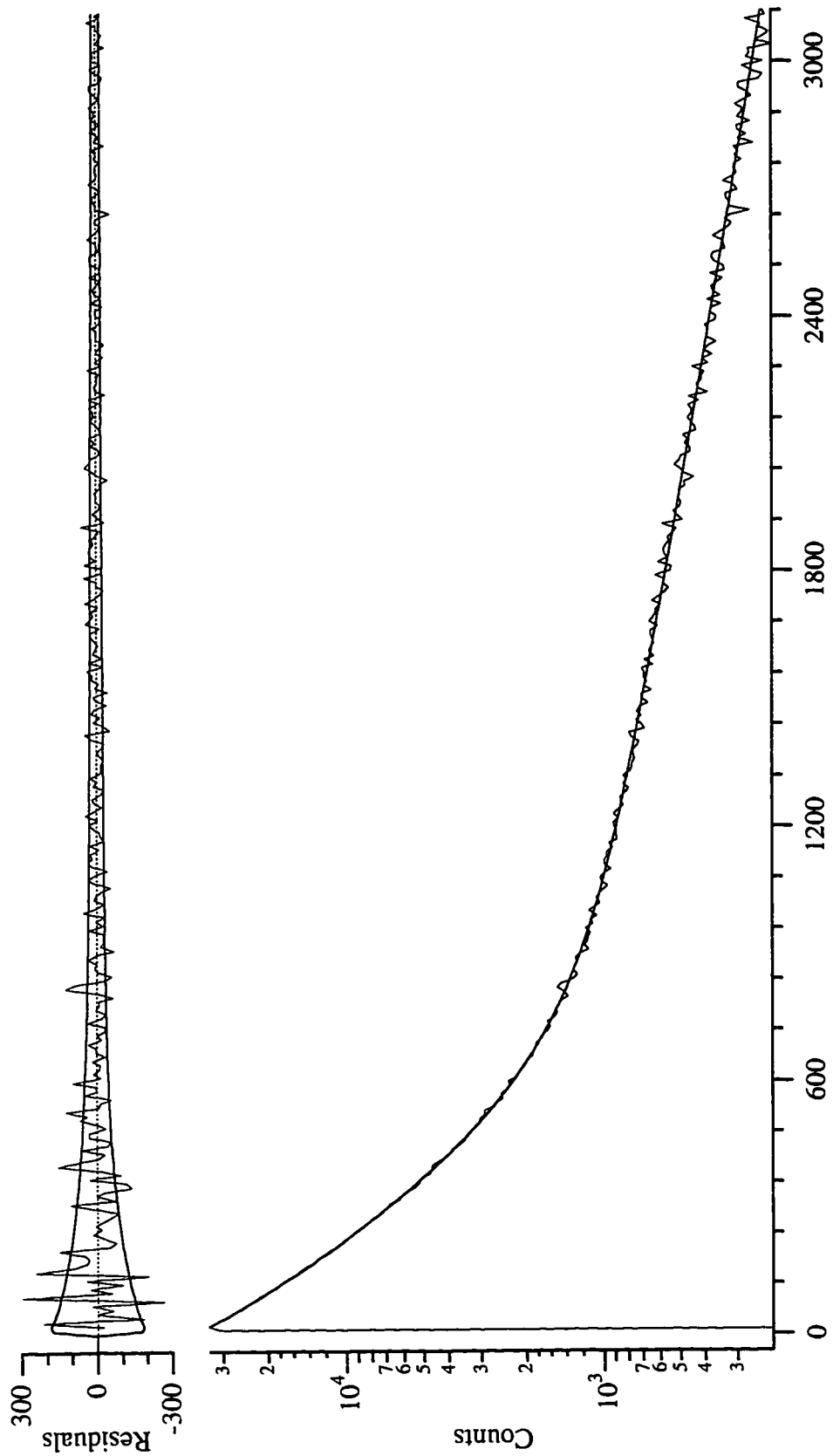

Figure 3.10. The total decay data collected while imaging after a 1.75 nA, 150 MeV proton beam was implanted for 60 seconds. The fit to the data shows that ^{15}O, ^{14}O, ^{13}N, ^{11}C and ^{10}C are present at the 99% confidence level. The residuals of this fit are shown at the top with the Poisson uncertainty.

were produced by first fitting the decay data to the above decay model for the individual pixels. The validity of including the ^{10}C term in the decay model was tested for each set of decay data but was not justified at the 99% confidence level for any of the pixels. Figure 3.11 shows the cumulative and radioisotopic response vectors integrated over the imaging time but before image reconstruction. The error bars shown are the square root of the elements of the variance vectors, $\sqrt{\mathcal{V}_j}$, described above. The error bars were omitted for the ^{14}O and ^{13}N response vectors for illustrative purposes but are comparable to those shown. Figure 3.12 shows the expected activity distribution where different reactions leading to the same radioisotope have been added. The radioisotopic image vectors, shown in Figure 3.13a, were calculated using (3.15). The range of the 150 MeV proton beam is 16.0 cm in tissue and is well determined within the resolution of the imaging system. The distribution of activity drops abruptly near the end of the proton beams range as the proton energy falls below the threshold energies of the various nuclear reactions. But, as noted, some slight ^{14}O activity is observed beyond this range.

Table 3.4 gives the activity expected for each reaction, the expected total activity and number of decays, while imaging, by radioisotope, and the total number of decays as determined from the reconstructed isotopic images. The uncertainties given with the experimentally determined values only reflect the uncertainties due to counting statistics and fitting the data to the decay model. The uncertainty in the beam current during the experiments was about 20%. During an actual treatment the beam current would be monitored to a much higher precision using a transmission ionization chamber. Given these uncertainties, the abundance and distribution of ^{11}C of ^{15}O agree well with the expected distributions. However, based on the known tissue composition, the amount of ^{13}N observed is almost twice as large as expected and the observed amount of ^{14}O is over seventeen times the expected amount.

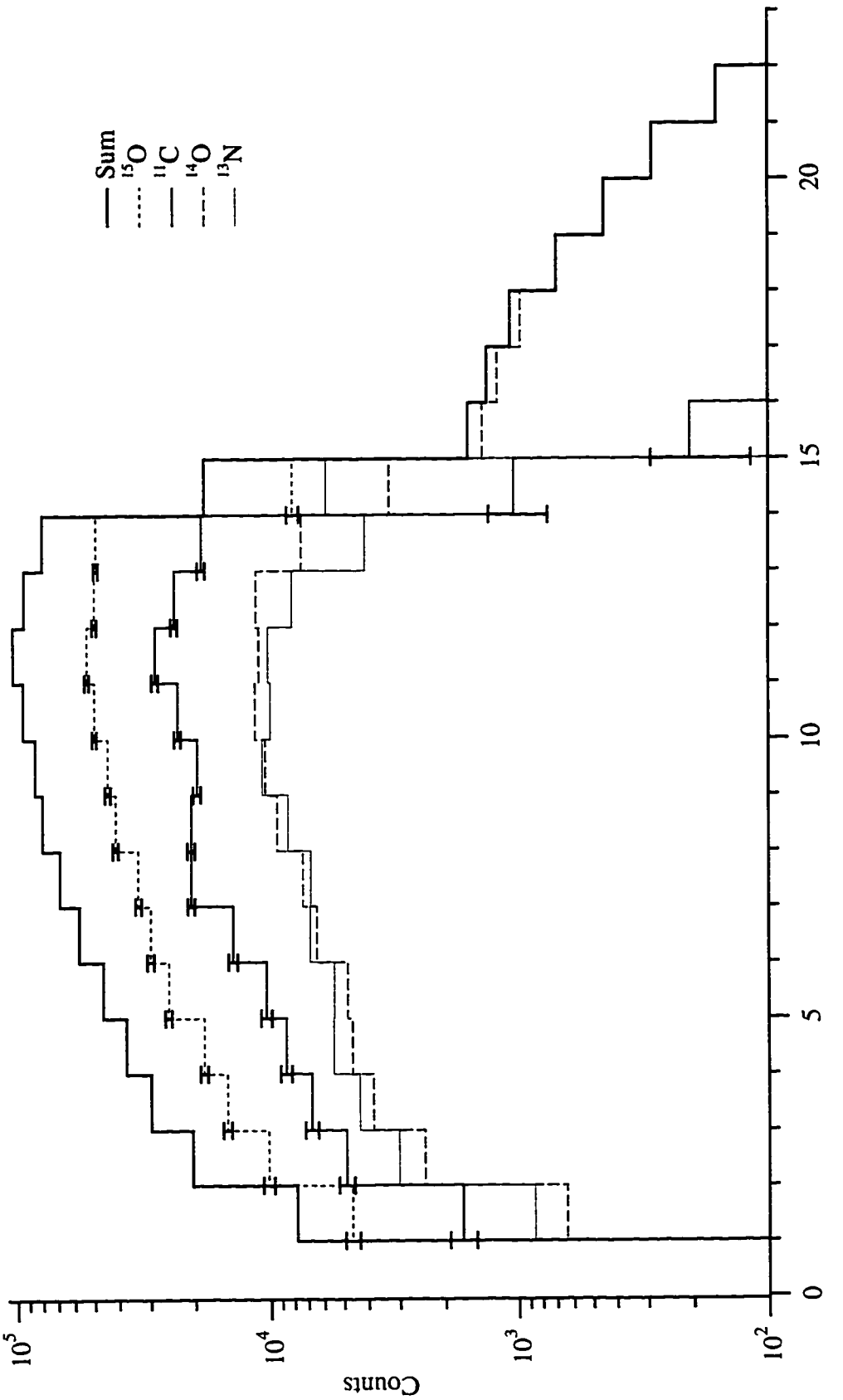

Figure 3.11. Radioisotopic response vectors generated from decay data.

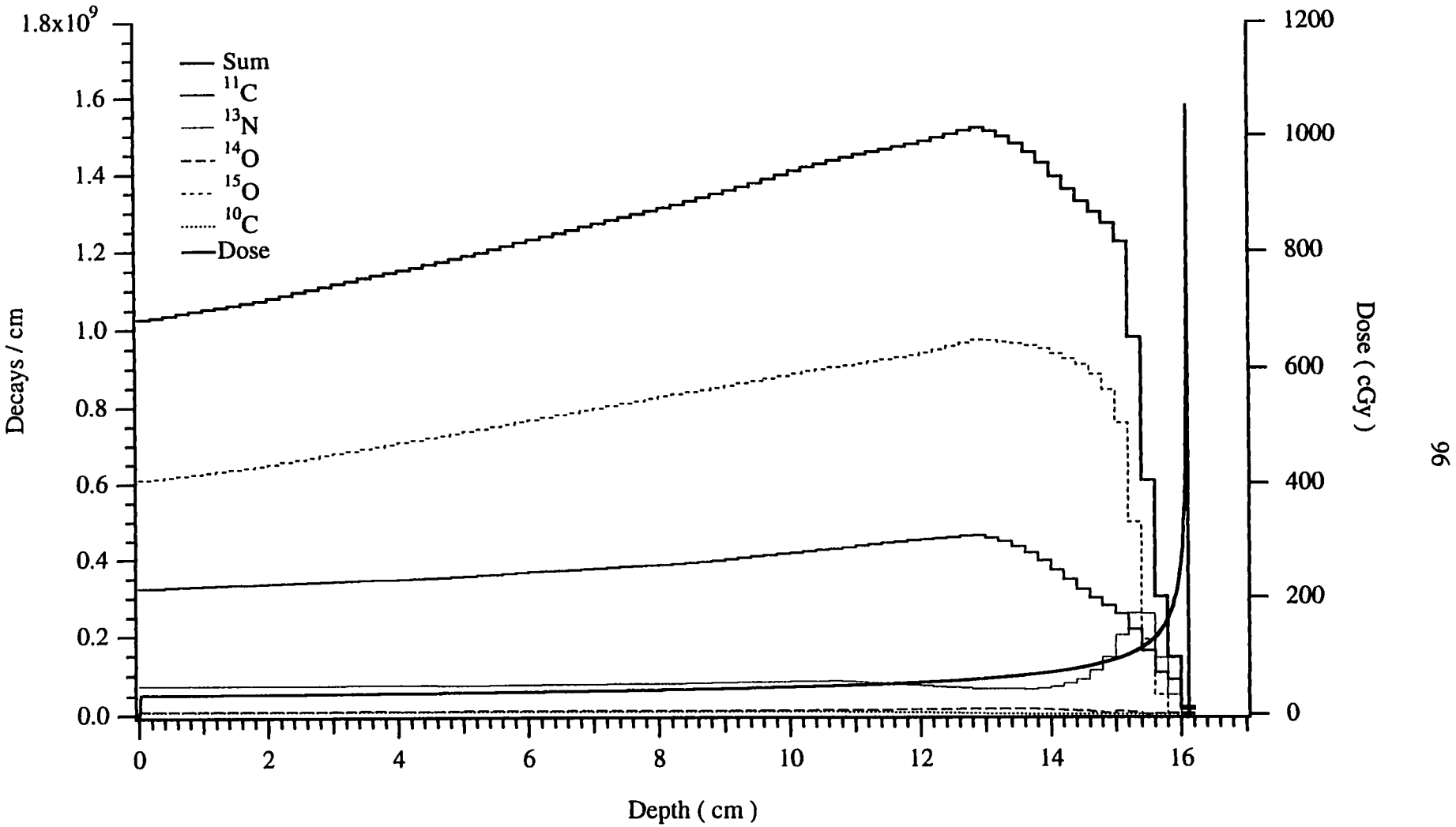

Figure 3.12. Radioisotopic response vectors generated from decay data. Expected isotopic decay distribution for a 1.75 nA, 150 MeV proton beam implanted in tissue for 60 seconds.

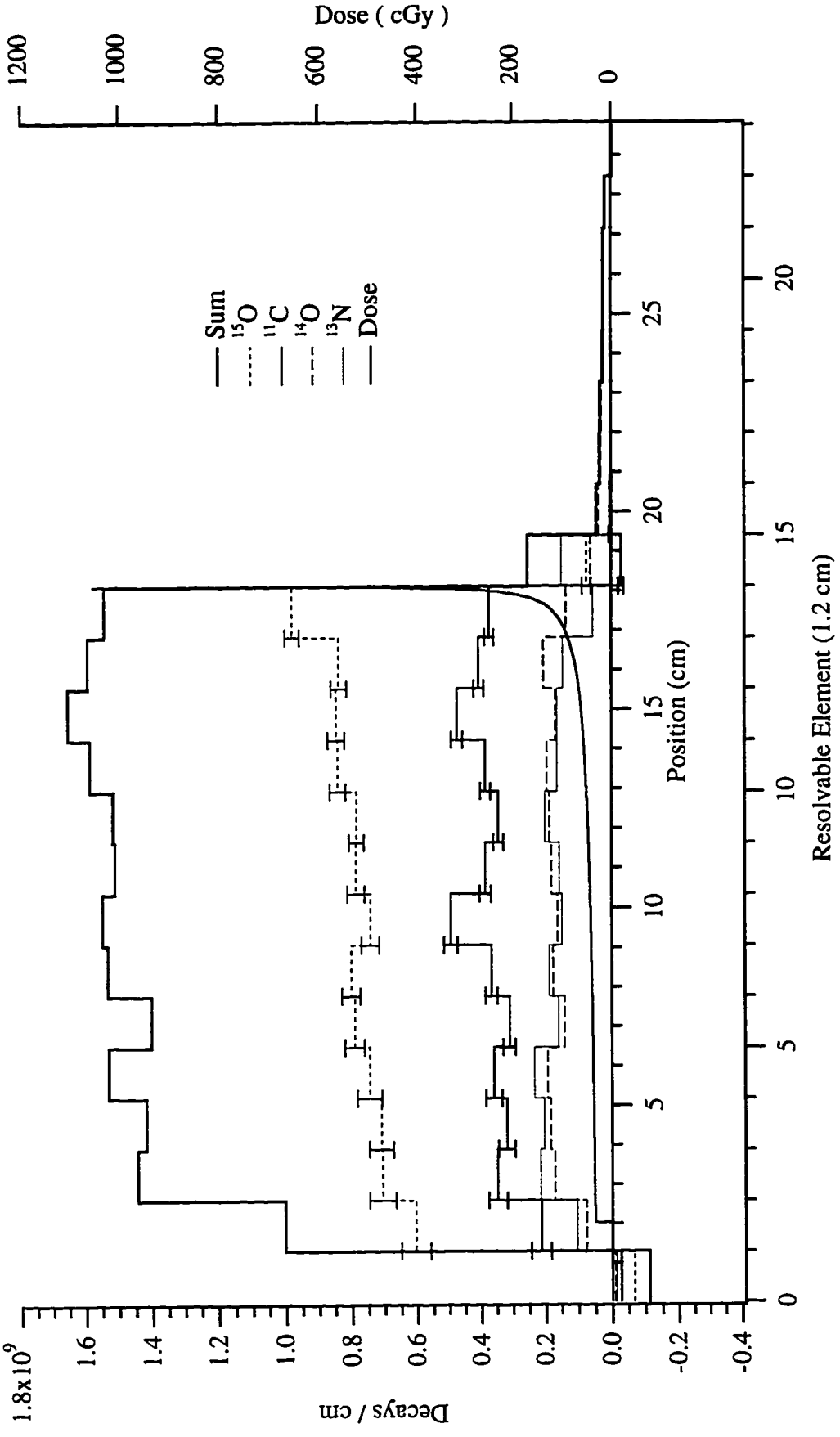

Figure 3.13a. Radioisotopic images of the decay distributions of activity created by a 1.75 nA, 150 MeV proton beam implanted in tissue for 60 seconds.

Reaction	Expected Activity (μCi) by Reaction	Expected Activity (μCi) by Isotope	Expected Counts (x10^9) by Isotope	Measured Counts (x10^9) by Isotope
$^{16}O(p,3p4n)^{10}C$	94.0	94.0	0.097	
$^{12}C(p,pn)^{11}C$	52.0			
$^{14}N(p,\alpha)^{11}C$	2.6	107.8	5.8	5.74±0.08
$^{16}O(p,\alpha pn)^{11}C$	53.2			
$^{14}N(p,pn)^{13}N$	4.4			
$^{16}O(p,\alpha)^{13}N$	38.9	43.3	1.3	2.74±0.09
$^{14}N(p,n)^{14}O$	1.1			
$^{16}O(p,p2n)^{14}O$	41.8	42.9	0.162	2.91±0.09
$^{16}O(p,pn)^{15}O$	1877.5	1877.5	12.25	12.31±0.11
$^{18}O(p,n)^{18}F$	0.0023	0.0023		
Totals		2248.8	19.61	23.70±0.19

Table 3.4. Summary of the isotopic activities produced and the expected and measured number of total coincidence events. This activity was produced by a 1.75 nA, 150 MeV proton beam which was implanted into a swine-tissue phantom continuously for 60 seconds.

Nuclear Secondaries and the Production of ^{14}O

The above discrepancies may arise from at least two different sources. The calculated and experimental cross sections used to calculate the production of ^{14}O have some uncertainty [44, 47] and ^{14}O may be produced in nuclear reactions induced by secondary particles such as neutrons. The cross sections used to calculate the amount of ^{14}O created by the $^{16}O(p,p2n)^{14}O$ reaction were calculated using the GNASH code system [52]. These calculated cross sections are about a factor of two smaller than experimental values which have been reported [53]. In addition, a significant number of

neutrons and other light, charged secondary particles are created which may induce nuclear reactions [21]. The production of positron-emitting isotopes by neutrons is evident beyond the protons range in Figure 3.11. This activity is almost entirely ^{14}O and is most likely produced by the $^{16}O(n,3n)^{14}O$ reaction which has threshold energy of 30.7 MeV. Figure 3.13b shows the decay distribution beyond the protons range. To minimize calibration-induced correlations with the primary proton-induced decay distribution, this image was generated by zeroing elements zero through fourteen of the radioisotopic response vectors, shown in Figure 3.11, before reconstruction. As previously noted the decay distributions have been corrected for attenuation of the 511 keV gamma-rays in the swine-tissue phantom.

The number of secondary neutrons, protons and alpha-particles created per second in the production of the positron-emitting isotopes is easily calculated from the equilibrium radioisotopic activity distributions. The activity distribution reaches an equilibrium state when all the radioisotopes are being produced as quickly as they are decaying. This will occur after the beam has been on for about five half-lives of the longest-lived isotope. The production distribution of the secondaries is then the weighted sum of the radioisotope distributions which produce the appropriate secondaries. The individual distributions are weighted by the number of the appropriate secondaries emitted by the reaction before summing them. Neglecting the trace amount of ^{18}F created, the longest-lived radioisotope created in significant amounts in tissue is ^{11}C with a 20.3 minute half-life. Calculating the activity distribution for each of the radioisotopes after a 100 minute irradiation with a 1.75 nA, 150 MeV proton beam and summing the weighted distributions, yields the distribution of secondaries produced per second. These distributions are shown in Figure 3.14a for neutrons, protons and alpha-particles. Figure 3.14b shows the cumulative secondary distributions with beam depth. It should be kept in mind that while 17% of the initial proton beam flux is lost to nuclear interactions, only about 3.5% of the flux is lost to nuclear reactions which produce positron-emitting

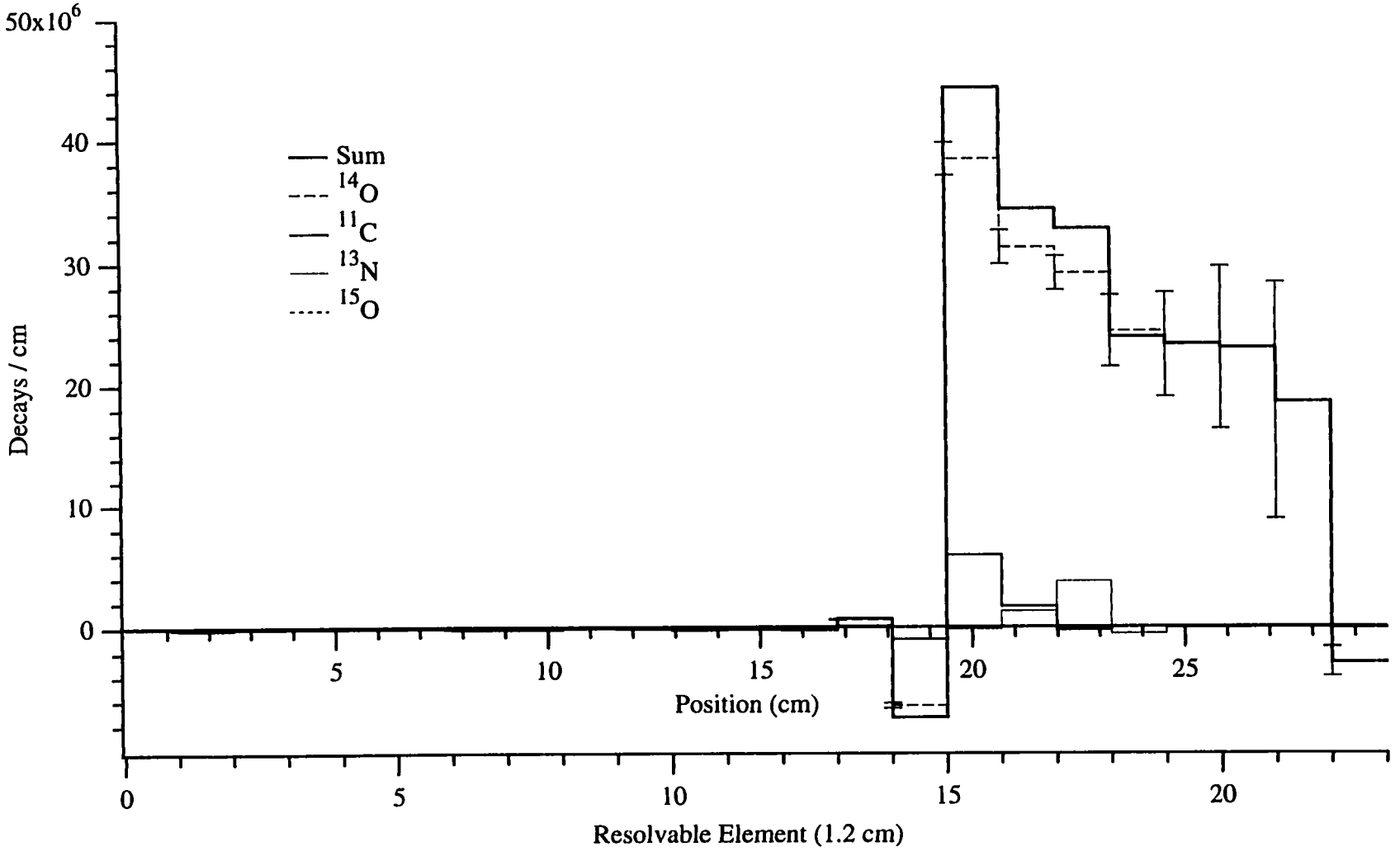

Figure 3.13b. Enlargement of the radioisotopic images beyond the Bragg peak. Reactions induced by secondary neutrons produce ^{14}O for many centimeters beyond the treatment beams range.

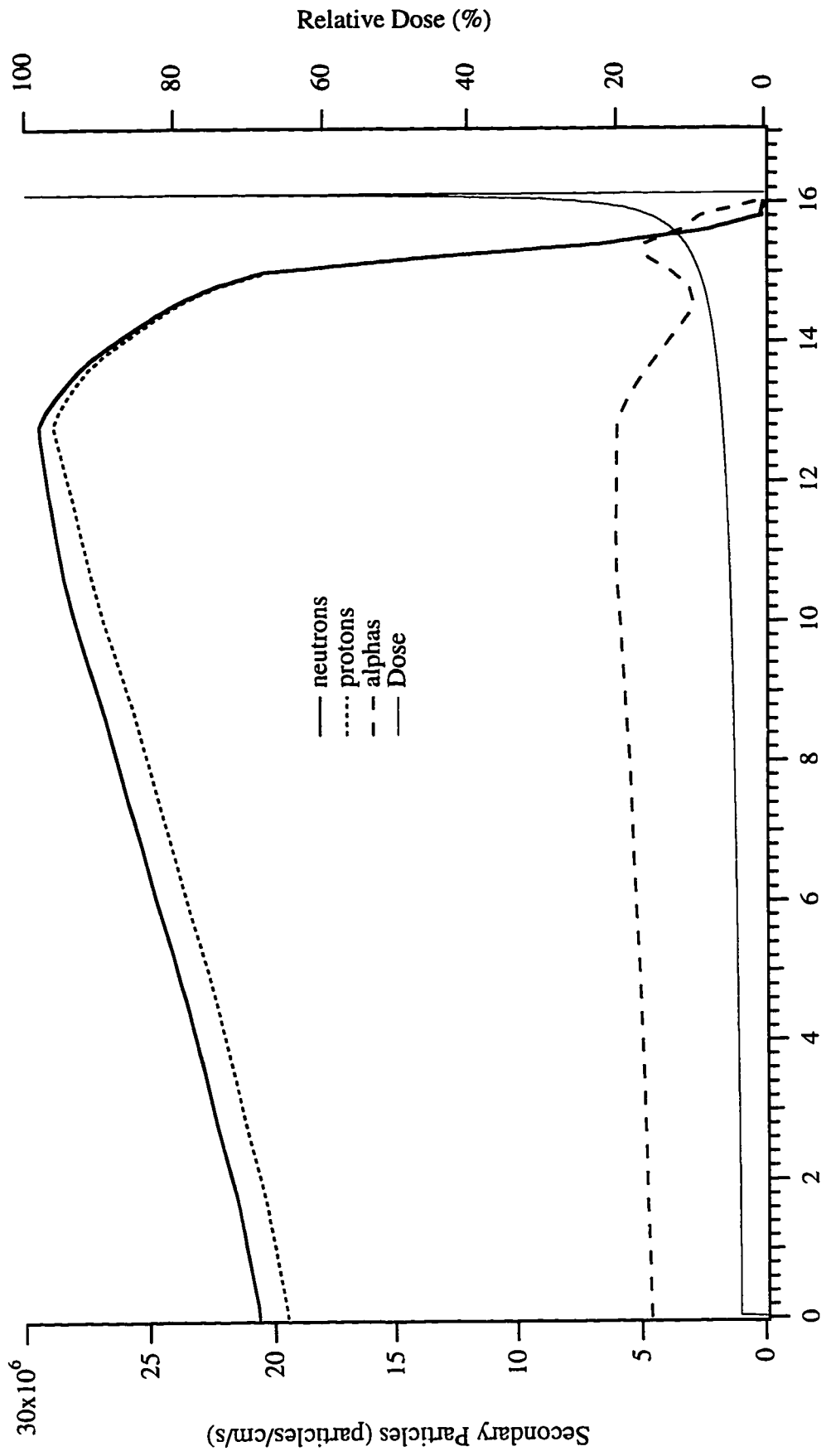

Figure 3.14a. Number of secondary particles produced by reactions creating positron-emitting isotopes per centimeter per second for a 1.75 nA, 150 MeV proton beam in tissue.

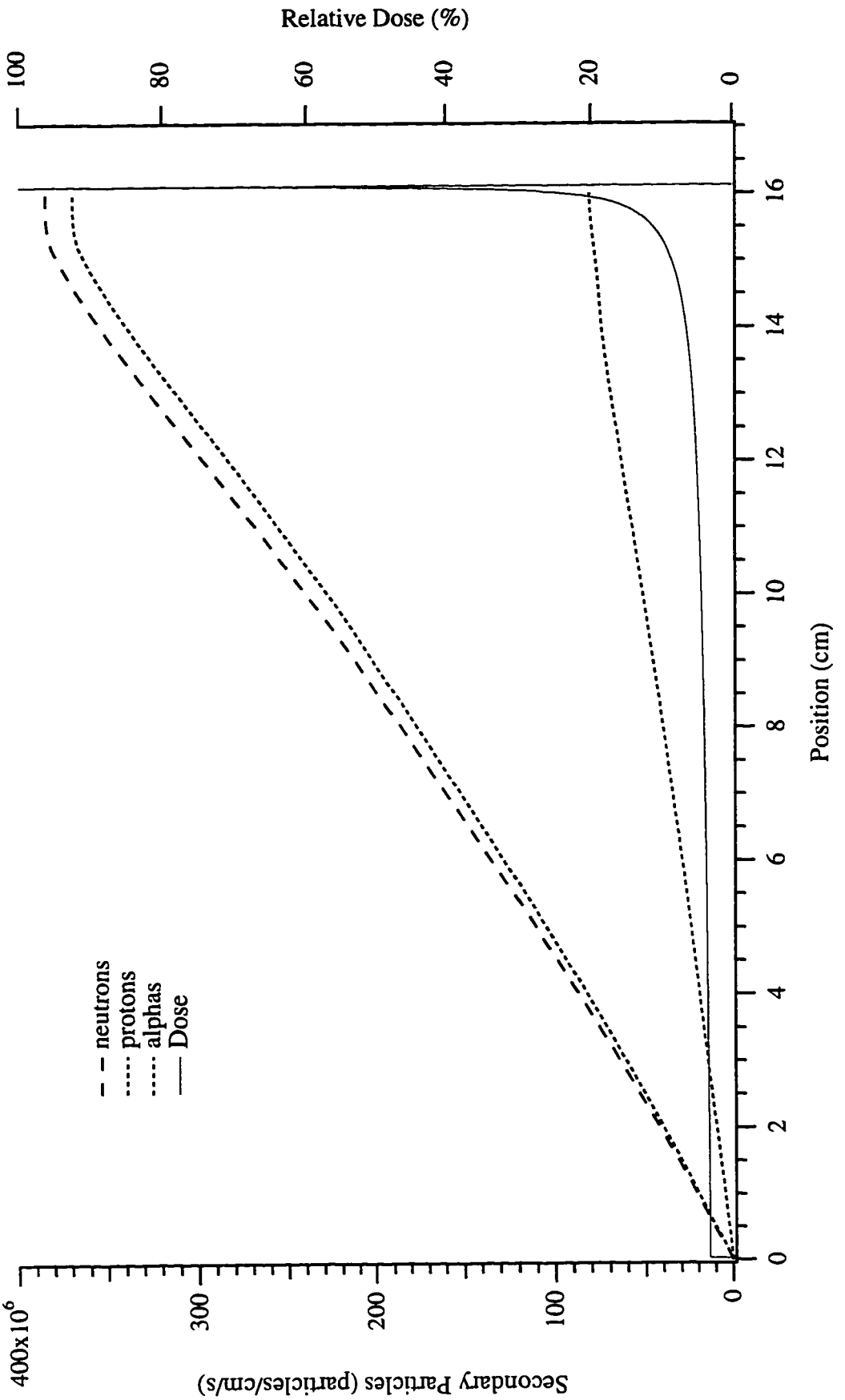

Figure 3.14b. Cumulative number of secondary particles produced by reactions creating positron-emitting isotopes per second for a 1.75 nA, 150 MeV proton beam in tissue.

nuclei. The distributions shown in Figures 3.14a and 3.14b are therefore only lower limit estimates and are likely to have magnitudes which may be several times larger and may have different shapes when including secondary production form reactions which do not produce positron-emitting isotopes. The energy distribution of secondary particles created by proton beams in tissue should be nearly the same as that produced in water. These distributions may be found in [21]. The cumulative distributions shown in Figure 3.14b serve to estimate the total secondary particle production and do not necessarily indicate the secondary particle fluence with depth. For example, the alpha-particles created at any depth have a short range, less than 0.2 or 0.3 centimeters. And neutrons and protons created in compound nucleus reactions below about 20 MeV will be emitted isotropically at relatively low energies and should contribute very little to the fluence in the forward direction.

If the activity after the proton beams range is produced by the $^{16}O(n,3n)^{14}O$ reaction, then a significant portion of the secondary neutron flux is above 30.7 MeV. This indicates that these neutrons originated from small beam penetration depths where the proton beam energy is significantly above about 60 MeV [21]. Even after this high-energy portion of the neutron fluence has been attenuated by many centimeters of tissue, the activity per centimeter beyond the protons range is present in nearly the same quantity expected for the $^{16}O(p,p2n)^{14}O$ reaction. This suggests that ^{14}O production by neutron-induced reactions is even larger within the protons range where the neutron fluence is greater.

Pulsed Proton Beams into a Tissue Phantom

The feasibility of imaging between beam macro pulses was investigated by performing experiments using the same beam described above but the beam was macro-pulsed with a ten second period. This beam was implanted into a tissue phantom for two minutes resulting in twelve, five second beam pulses being delivered to the phantom.

Data was acquired for five seconds between each of the beam pulses and in ten second bins for 56 minutes after beam delivery. A swine-tissue phantom was placed with its front surface 6.0±0.3 cm inside the imaging system. The production and decay of the resulting activity is shown in Figure 3.15a. The production of positron-emitting activity is shown in more detail in Figure 3.15b. As expected, the number of coincidences detected between beam pulses increases approximately linear with total irradiation time on short time scales. During a patient treatment, verifying the range of the beam early in the treatment is of primary importance. Ideally, using a macro-pulsed beam, the range could be measured after one pulse with the continuation of the treatment being contingent upon verification of the proper range. Figure 3.16 shows the reconstructed image after one macro beam-pulse. This image was reconstructed from 1431 coincidence events. The expected dose distribution is shown for comparison. The uncertainties in the image produced after one pulse are large, nonetheless the number of events is adequate for range verification. Images produced from the cumulative dataset after one, two, three, and six macro-pulses are shown in Figure 3.17. Note that all images show the activity distribution beginning and ending at the same location relative to the phantoms surface and the proton range.

Inspection of the inside of the swine-tissue phantom revealed a small adipose deposit beginning 11.2±0.1 cm from the surface of the phantom. Its spatial extent along the beam path was 0.4±0.1 cm. The elemental composition of this material was assumed to be similar to that given in [54] and is shown in Table 3.1. The decay distribution of positron-emitting activity given this phantom geometry and composition is shown in Figure 3.18. The presence of the adipose tissue changes the range of the beam by a small amount which is well below the resolution of the imaging system. Consequently, we do not experimentally observe a deviation in the proton range as might be expected. The decay distribution in Figure 3.18 shows a slightly larger number of decays from the adipose region. This is due to the long half-life of ^{11}C and the long, 56 minute, imaging

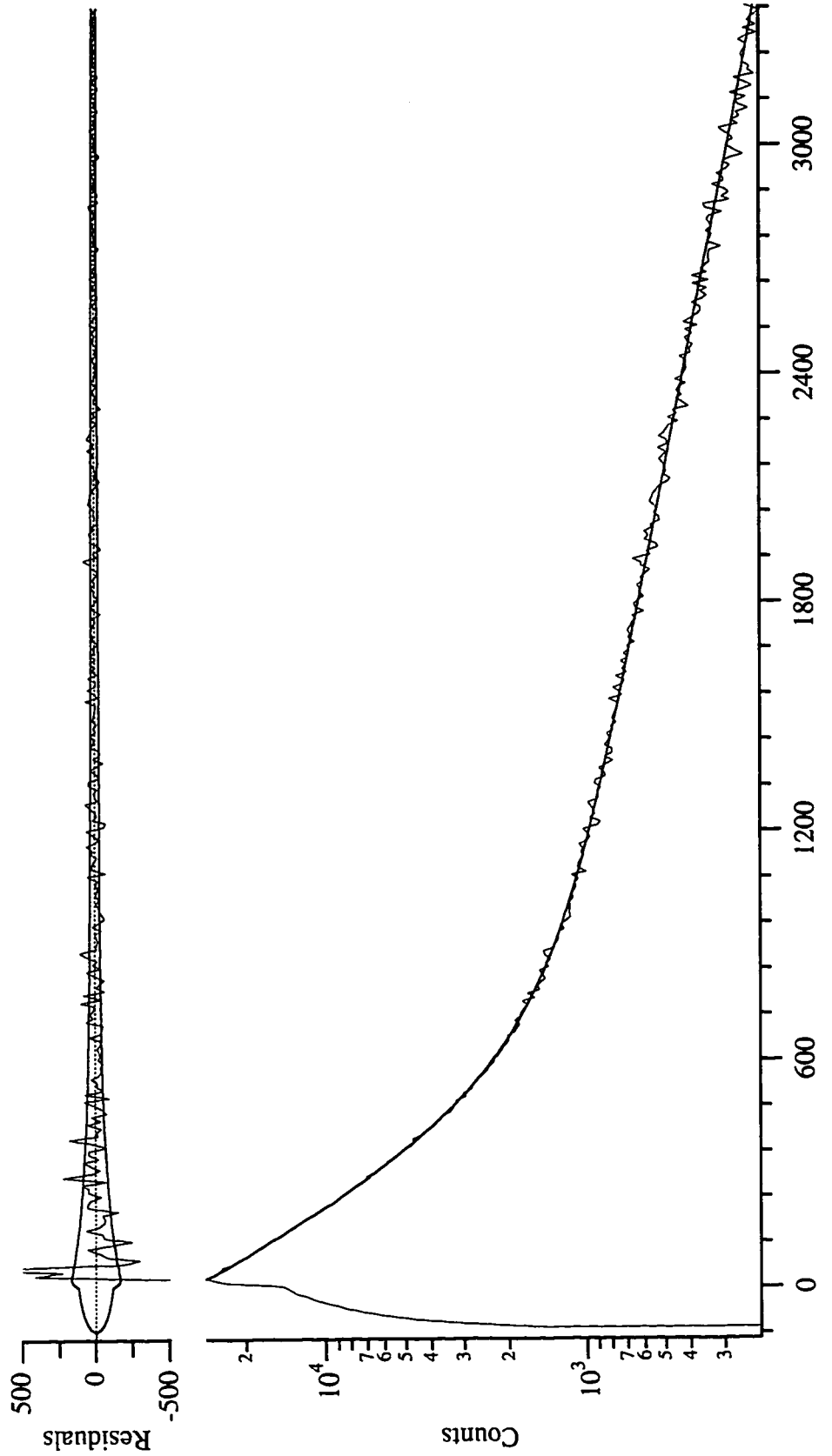

Figure 3.15a. The total decay data collected while imaging after a 1.75 nA, 150 MeV proton beam with a 10 second pulse period was implanted in tissue for 120 seconds. Statistical tests of the decay model shows that ^{15}O, ^{14}O, ^{13}N, ^{11}C, and ^{10}C are present at the 99% confidence level. The residuals of this fit are shown at the top with the Poisson uncertainty.

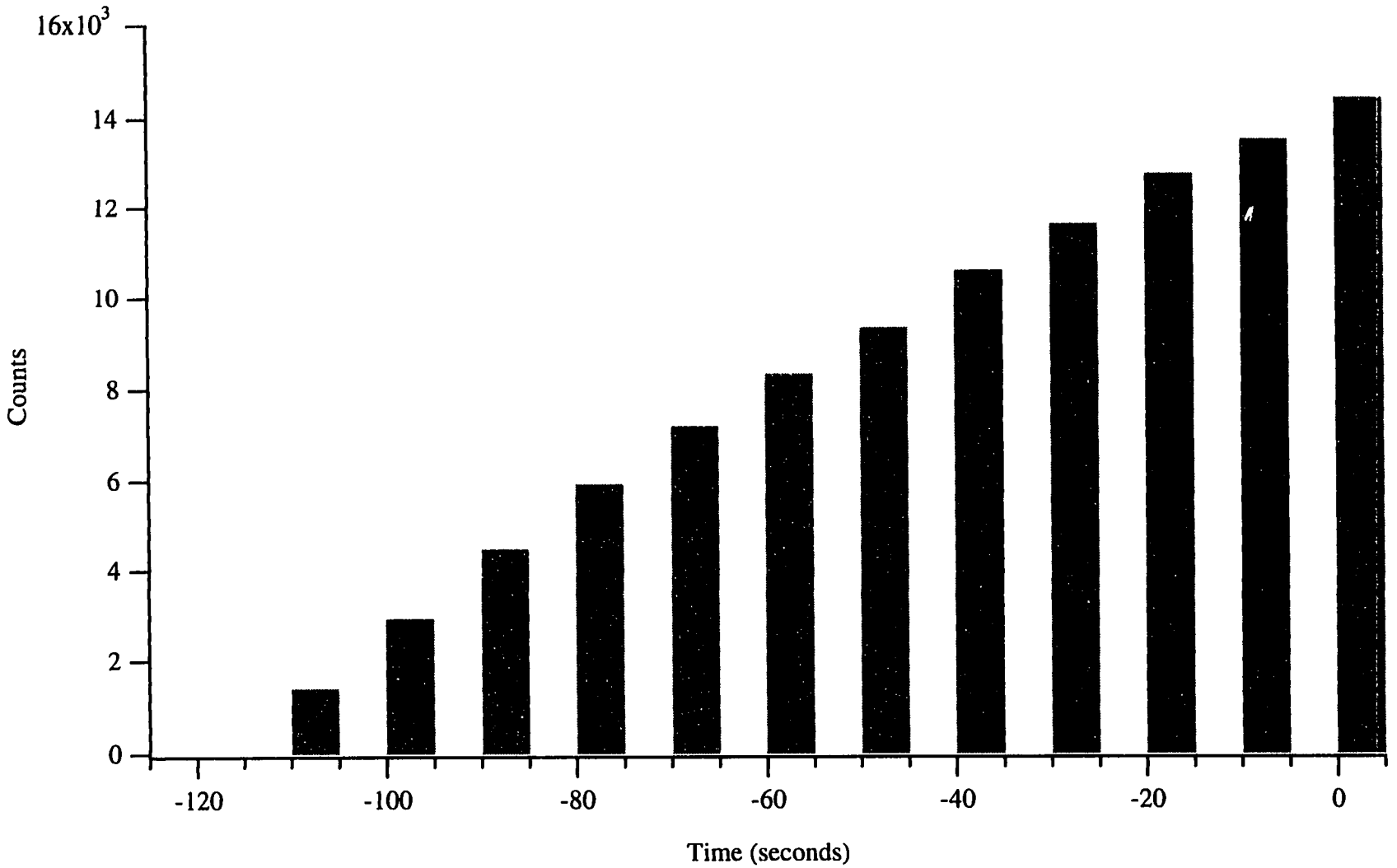

Figure 3.15b. Enlargement of the activity production shown in Figure 3.15a. The activity produced by beams with a duration of about two minutes or less increases approximately linearly.

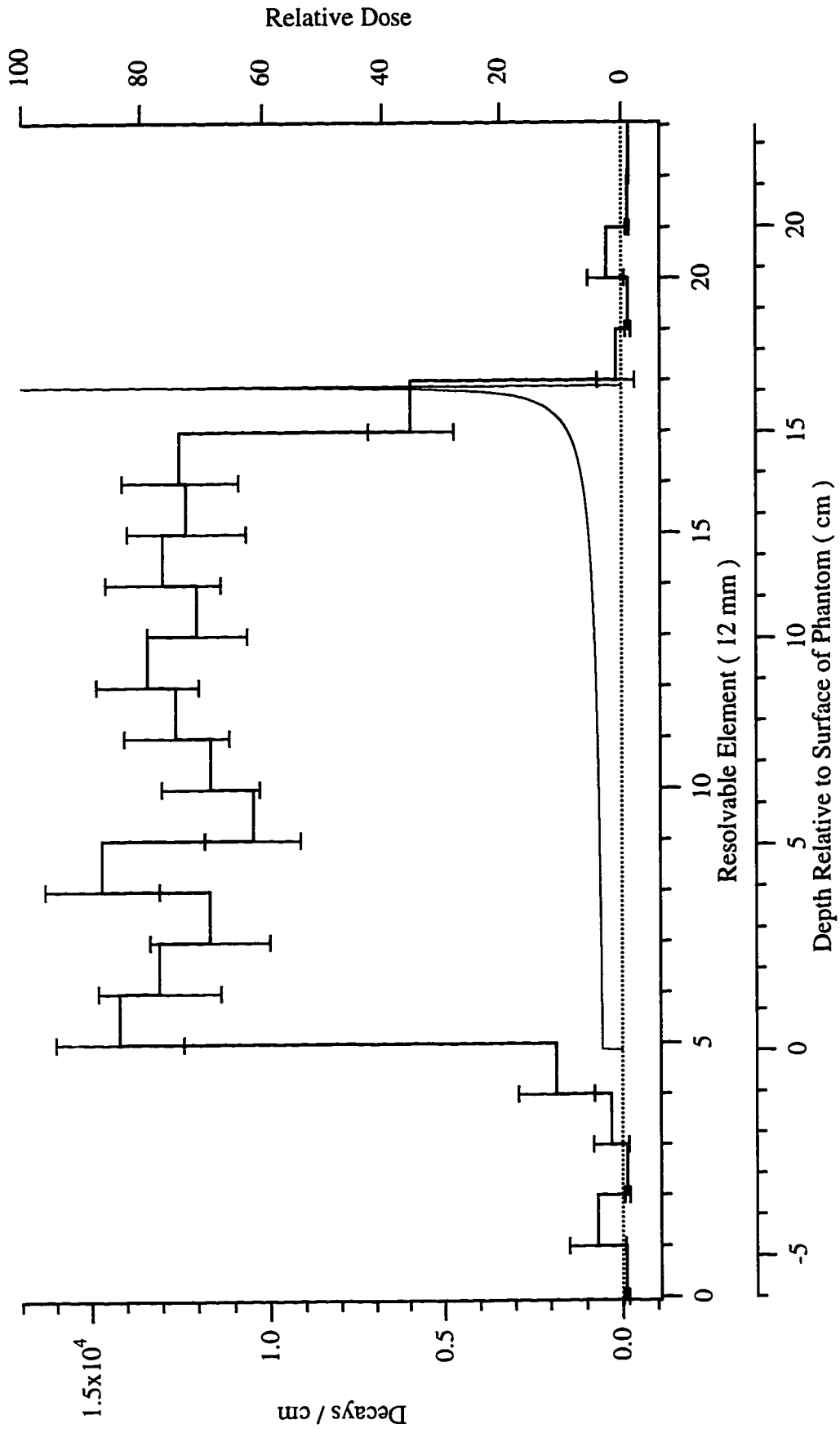

Figure 3.16. Range verification using the reconstructed decay distribution after one macro beam-pulse. This distribution was reconstructed from 1431 coincidence events. The expected dose distribution is shown for comparison.

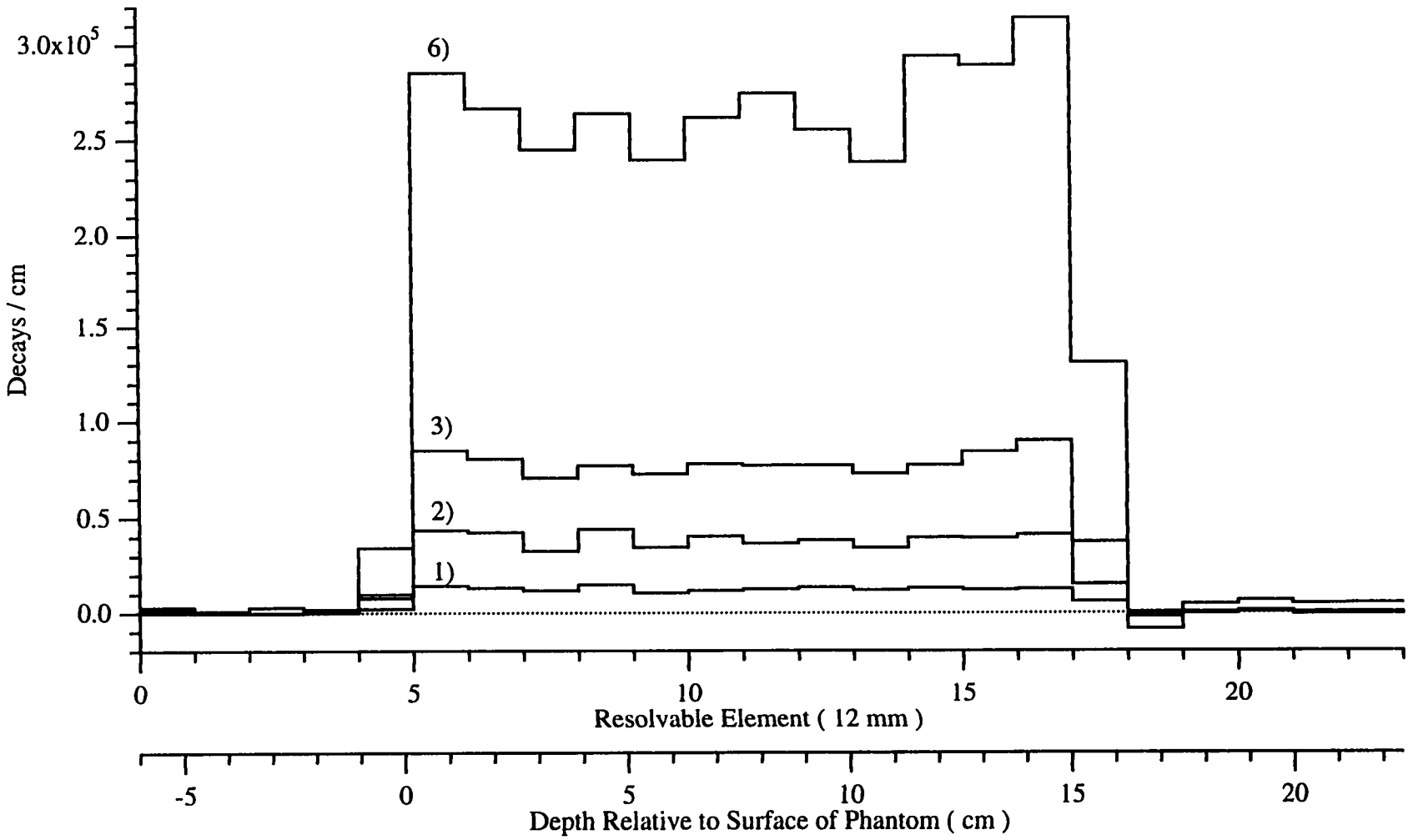

Figure 3.17. Decay distributions reconstructed after 1), 2), 3), and 6) macro-pulses.

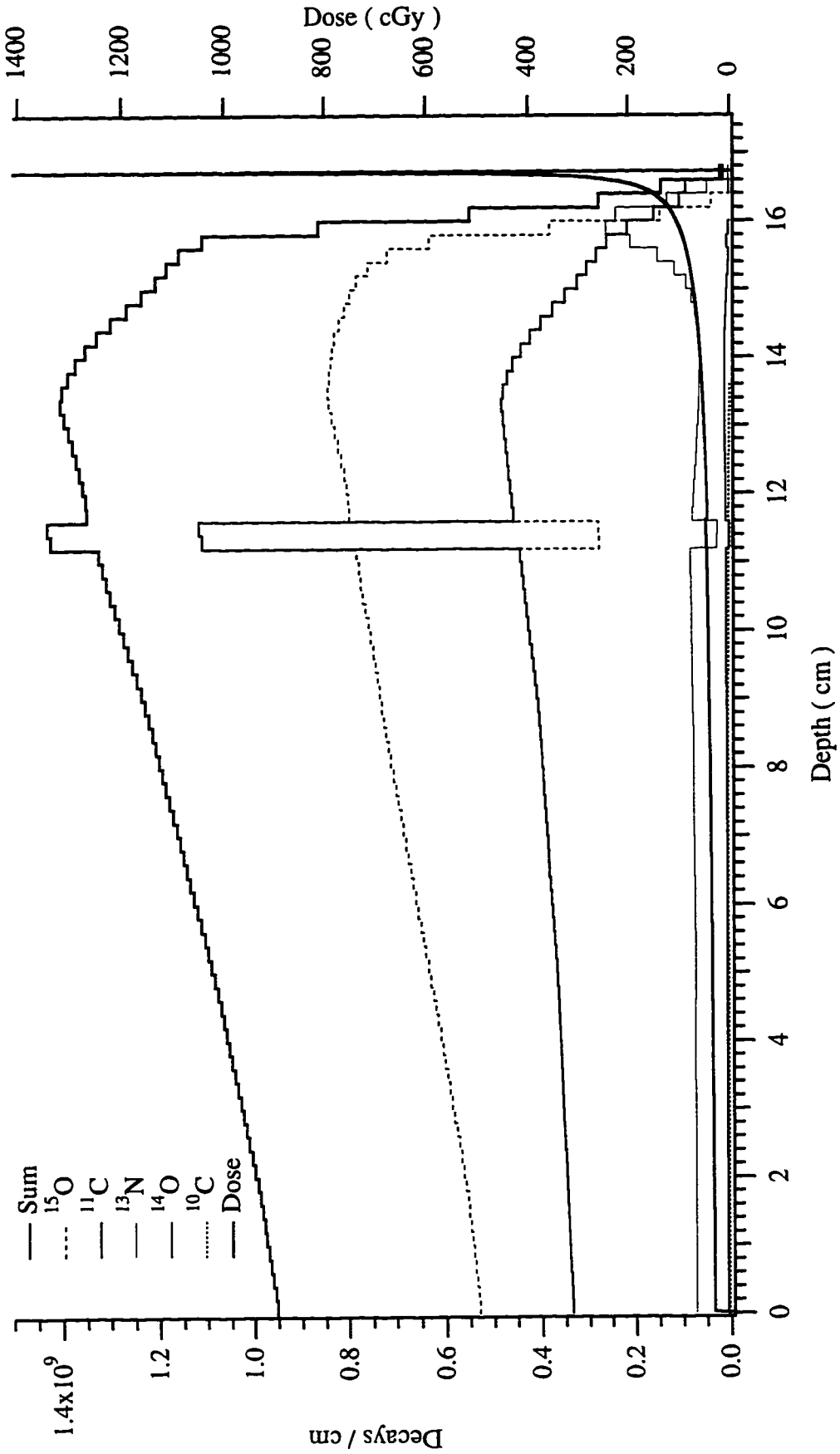

Figure 3.18. Expected isotopic decay distribution over 56 minutes for the activity created by a 1.75 nA, 150 MeV proton beam with a 10 second period which was implanted in a tissue phantom for 120 seconds. The dose distribution for a monoenergetic beam is shown for range comparison.

time. The initial amount of activity in this region is about half that in the regions containing muscle tissue due to the lack of oxygen to produce ^{15}O.

As in the experiments with continuous beams ^{15}O, ^{14}O, ^{13}N, ^{11}C, and ^{10}C are present in the summed decay data at the 99% confidence level. Radioisotopic response vectors were produced by first fitting the decay data to a decay model containing these radioisotopes for the individual pixels. Again, the validity of including the ^{10}C term in the decay model was tested for each set of decay data but was not justified at the 99% confidence level for any of the pixels. The isotopic images are shown in Figure 3.19. Note the dip in the ^{15}O distribution and the rise in the ^{11}C distribution due to the adipose deposit in the thirteenth resolvable element. Table 3.5 gives the total activity expected for each reaction, the expected total activity by radioisotope, and the expected and measured number of decays by radioisotope. The uncertainty in the expected activities given in Table 3.5 due to the uncertainty in the beam current is 20%. The amount of ^{15}O and ^{11}C agree well within these uncertainties. However, the amount of ^{13}N is 77% larger than expected and the amount of ^{14}O is 12.4 times larger than expected.

Activity Saturation with Macro-Pulsed Beams in Tissue

Another pulsed-beam experiment was conducted to investigate the maximum activity produced with pulsed beams for radioisotopes with half-lives comparable to or shorter than the treatment time. In (3.4), if the number of pulses, n, is very large the series converges so that if

$$\begin{aligned} \mathcal{A}_{ip}(\mathbf{r},t) &= \mathcal{A}_{ip}^{max}(\mathbf{r},t)\left(1-e^{-\lambda_i T_{on}}\right)\lim_{n\to\infty}\sum_{j=0}^{n-1}e^{-j\lambda_i T} \\ &= \mathcal{A}_{ip}^{max}(\mathbf{r}) \qquad\qquad for\ t >> T. \end{aligned} \tag{3.18}$$

Isotopes whose half-lives are short compared to the irradiation time will approach an equilibrium activity level as the decay rate approaches the production rate. In this experiment a 0.14 nA beam with a 20 second period was implanted into a tissue phantom

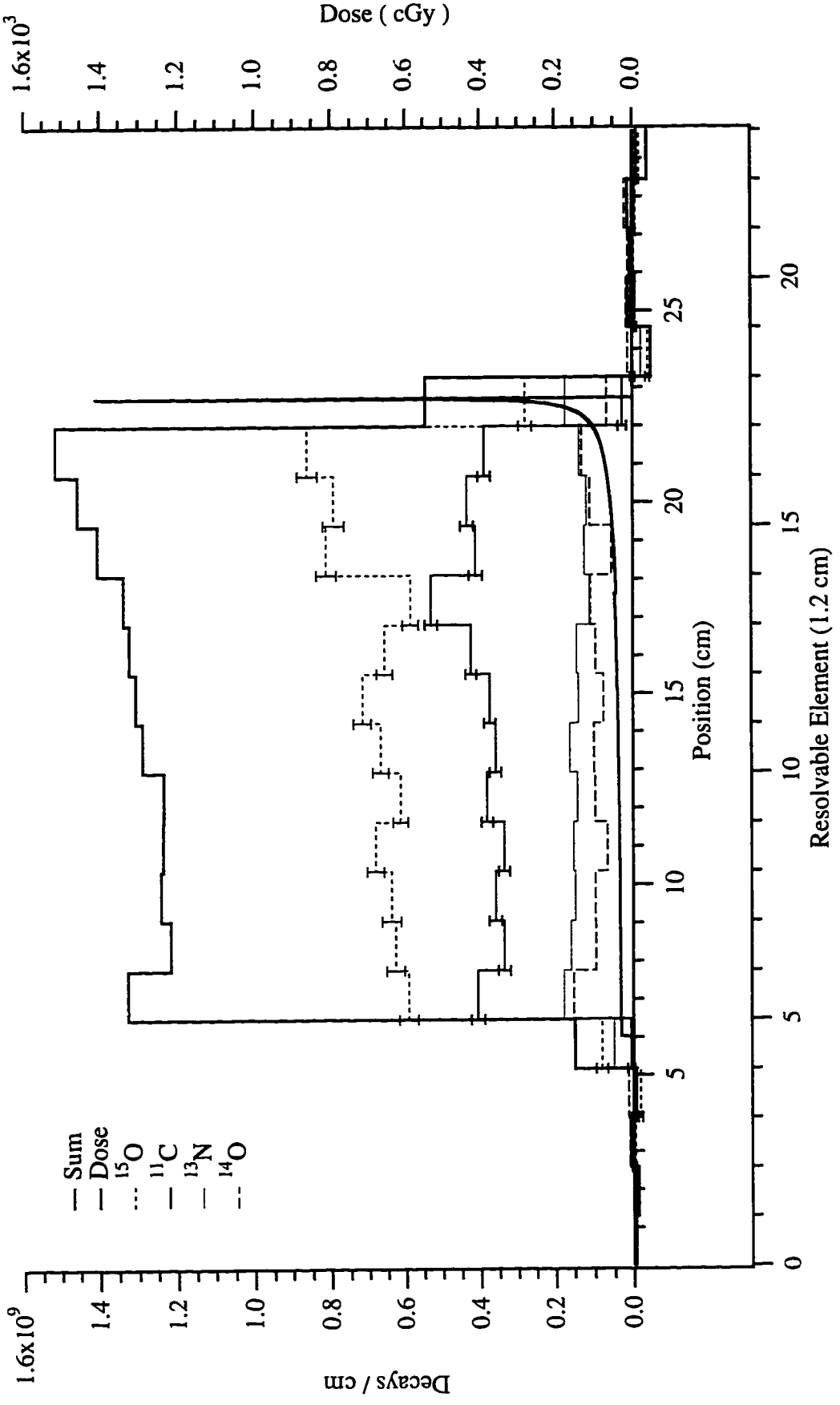

Figure 3.19. Radioisotopic images of the decay distributions of activity created by a 1.75 nA, 150 MeV proton beam with a 10 second period which was implanted in a tissue phantom for 120 seconds.

Reaction	Expected Activity (μCi) by Reaction	Expected Activity (μCi) by Isotope	Expected Counts ($x10^9$) by Isotope	Measured Counts ($x10^9$) by Isotope
$^{16}O(p,3p4n)^{10}C$	56.2	56.2	0.058	
$^{12}C(p,pn)^{11}C$	57.1			
$^{14}N(p,\alpha)^{11}C$	2.5	110.9	6.15	5.70±0.06
$^{16}O(p,\alpha pn)^{11}C$	51.3			
$^{14}N(p,pn)^{13}N$	4.2			
$^{16}O(p,\alpha)^{13}N$	37.1	41.3	1.29	2.28±0.07
$^{14}N(p,n)^{14}O$	0.85			
$^{16}O(p,p2n)^{14}O$	32.7	33.6	0.13	1.61±0.07
$^{16}O(p,pn)^{15}O$	1597.6	1597.6	10.42	10.19±0.09
$^{18}O(p,n)^{18}F$	0.00236	0.00236		
Totals		1910.1	18.05	19.78±0.15

Table 3.5. Summary of the isotopic activities produced and the expected and measured number of total coincidence events. This activity was produced by a 1.75 nA, 150 MeV proton beam which was pulsed with a 10 second period and implanted into a swine-tissue phantom for 120 seconds.

for 21 minutes. Data was acquired for ten seconds between beam pulses and continued for an additional 61 minutes after the beam ended. The front surface of the 27 cm x 5 cm x 5 cm swine-tissue phantom was placed 2.0±0.3 cm inside the front end of the imaging system.

The resulting production and decay of PET activity is shown in Figure 3.20. The production of activity is relatively constant over the first two to three minutes while the abundance of ^{15}O is still low. The sudden decrease in the number of counts between

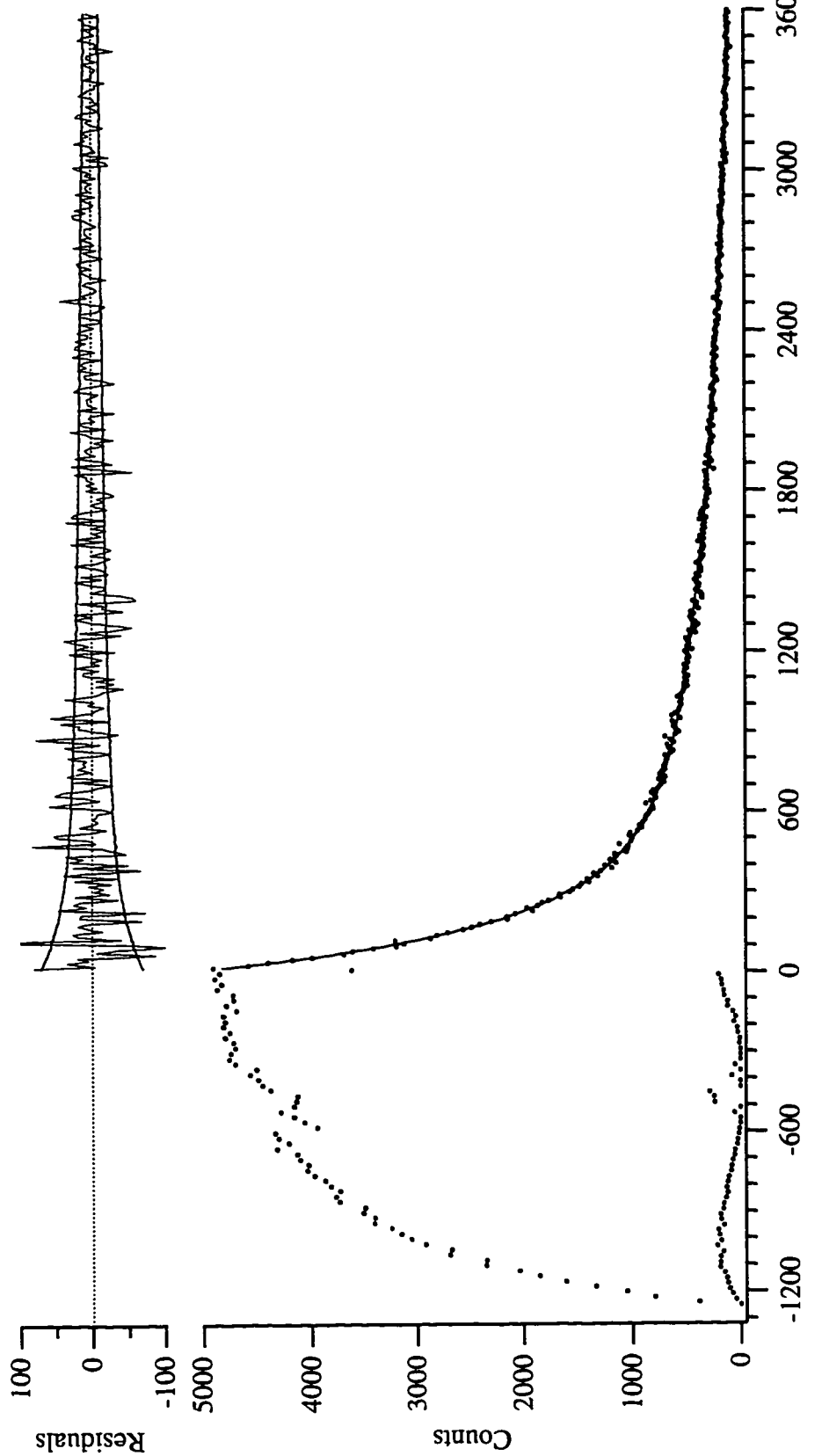

Figure 3.20. The total decay data collected while imaging after a 0.14 nA, 150 MeV proton beam with a 20 second pulse period was implanted for 21 minutes. Statistical tests of the decay model shows that ^{15}O, ^{14}O, ^{13}N, and ^{11}C are present at the 99% confidence level. The fit to the decay data using this model is shown by the solid line and the residuals of this fit are shown at the top with the Poisson uncertainty.

pulses which occurs about 7 minutes before the end of the beam is due to small variations in the response time of the shutter system relative to that of the data acquisition system. It can be seen that after 20 minutes the production rate has slowed considerably as all isotopes decay almost as quickly as they are produced. Since the beam duration is comparable to the half-life of ^{11}C, 20 minutes, and ^{13}N, 10 minutes, the activity of these isotopes will not be at their maximum levels. The activities of isotopes with half-lives shorter than roughly five minutes, such as ^{15}O and ^{14}O should be near their maximum levels. The decay data shown in Figure 3.20 was fit and found to contain primarily ^{15}O, ^{13}N, ^{11}C, and some ^{14}O. ^{10}C is not present at a the 95% confidence level in the summed decay data. Again, while ^{14}O is present at the 99% confidence level in the total decay data it was not found at this level in any of the individual positions. Fitting for ^{15}O, ^{13}N and ^{11}C and reconstructing their decay distributions gives the radioisotopic images shown in Figure 3.21. Figure 3.22 shows the expected activity distribution where different reactions leading to the same radioisotope have been added. Note that under the given beam and imaging parameters that the number of decays from ^{11}C is greater than from ^{15}O. This is due to the 21 minute beam duration. Table 3.6 gives the total activity expected for each reaction, the expected total activity by radioisotope, and the expected and measured number of decays while imaging by radioisotope. Again the uncertainty in the expected activity and expected counts by isotope is about 20% due to the uncertainty in the beam current. As before, the measured amounts of ^{11}C and ^{15}O agree with the expected amounts but the measured amount of ^{13}N is twice as high as expected.

Macro-Pulsed Beams with Energy Modulation

A typical proton treatment uses a macro-pulsed beam which is energy modulated to produce a spread-out Bragg peak(SOBP). The SOBP can be considered as the sum of several smaller raw Bragg peaks(RBP) occurring at different ranges. SOBP may be produced by passing the beam through a rapidly rotating energy modulation wheel

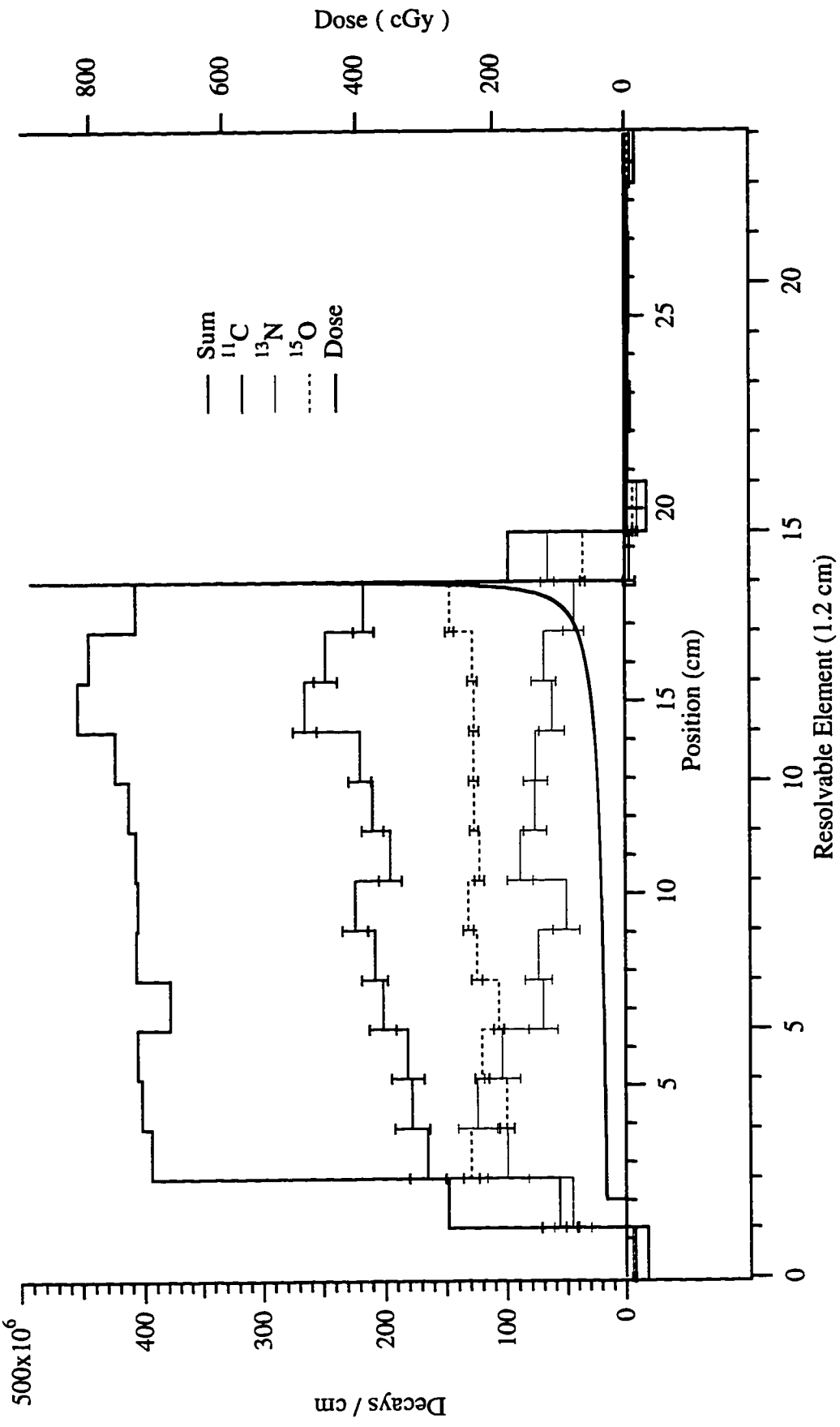

Figure 3.21. Radioisotopic images of the decay distributions of ^{15}O, ^{13}N, and ^{11}C. This activity was created by a 0.14 nA, 150 MeV proton beam with a 20 second period which was implanted in a tissue phantom for 21 minutes.

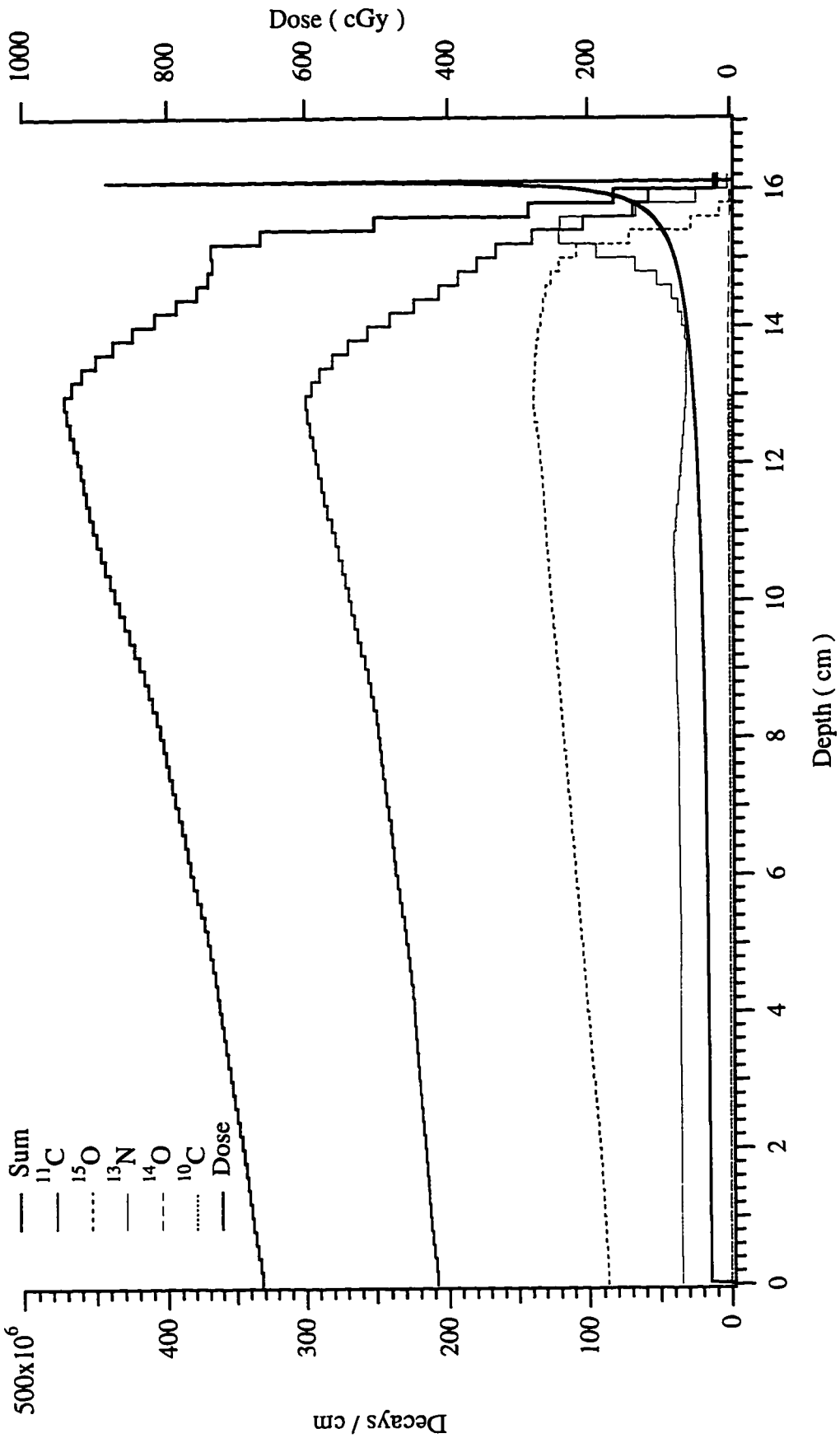

Figure 3.22. Expected isotopic decay distribution over 61 minutes for the activity created by a 0.14 nA, 150 MeV proton beam with a 20 second period which was implanted in a tissue phantom for 21 minutes. The dose distribution for a monoenergetic beam is shown for range comparison.

Reaction	Expected Activity (μCi) by Reaction	Expected Activity (μCi) by Isotope	Expected Counts ($x10^9$) by Isotope	Measured Counts ($x10^9$) by Isotope
$^{16}O(p,3p4n)^{10}C$	5.01	5.01	0.0052	
$^{12}C(p,pn)^{11}C$	31.83			
$^{14}N(p,\alpha)^{11}C$	1.57	65.97	3.75	3.08±0.04
$^{16}O(p,\alpha pn)^{11}C$	32.57			
$^{14}N(p,pn)^{13}N$	2.04			
$^{16}O(p,\alpha)^{13}N$	17.90	19.94	0.63	1.25±0.05
$^{14}N(p,n)^{14}O$	0.10			
$^{16}O(p,p2n)^{14}O$	3.95	4.05	0.015	
$^{16}O(p,pn)^{15}O$	267.65	267.65	1.75	1.88±0.02
$^{18}O(p,n)^{18}F$	0.0019	0.0019		
Totals		362.62	6.15	6.21±0.07

Table 3.6. Summary of the isotopic activities produced and the expected and measured number of total coincidence events. This activity was produced by a 0.14 nA, 150 MeV proton beam which was pulsed with a 20 second period and implanted into a swine-tissue phantom for 21 minutes.

consisting of varying thicknesses of absorber material. The energy lost in the absorber produces a distribution of energies incident upon the patient. The width of the distal end of the SOBP, having a uniform dose distribution, may be varied by using modulation wheels with different angular and thickness distributions of absorber material. Table 3.7 shows the distribution of thicknesses and area fractions for a Lucite modulation wheel used at Loma Linda to produce a 60 mm SOBP with a 150 MeV proton beam [55]. These distributions were empirically determined from measurements of the SOBP in a

Thickness (cm)	Area Fraction
0.0	0.376753
0.48927	0.128166
0.921888	0.091294
1.35794	0.075474
1.79743	0.062055
2.24033	0.056261
2.6867	0.049798
3.13648	0.045248
3.5897	0.041229
4.04635	0.037961
4.50644	0.035762

Table 3.7. Thickness and area fraction distributions for a 6.0 cm SOBP modulation wheel for use with 150 MeV protons.

water tank and therefore account for the loss of flux due to reactions, and the range straggling due to the momentum spread of the beam and energy straggling in the Lucite energy absorber and water.

While no experiments were conducted here using a SOBP, the expected distributions for this SOBP have been calculated for comparison to the distributions created by continuous and macro-pulsed, mono-energetic beams. From a computational perspective, the activity distribution is simply the superposition of the activity distributions produced by many beams of different currents and energies. This distribution is given by (3.19)

$$\mathcal{A}(\mathbf{r},t) = \sum_k w_k \mathcal{A}_k(\mathbf{r},t) \tag{3.19}$$

In (3.19), w_k, is the area fraction, of the k^{th} thickness of the modulation wheel. The SOBP described above freely passes the 150 MeV beam 37.7% of the time with no energy degradation. To compare the activity distribution created by this beam to those presented in the previous sections, similar parameters were chosen. A current of 1.75 nA was used, the pulse period was 10 seconds, and the total treatment time was two minutes. Figure 3.23 shows the predicted activity distributions for each of the weighted beams and their sum. Figure 3.24 shows the distribution of positron-emitting activity by radioisotope at the end of the treatment. These distributions have not been integrated over an imaging time like the earlier decay distributions. Table 3.8 lists the expected amount of activity, by radioisotope, created in the tissue and in the Lucite modulation wheel. The dose and activity distributions for the modulated and the unmodulated 150 MeV beams are shown in Figure 3.25. The dose distribution of the SOBP and its associated activity distribution have been convolved with a 0.5 cm FWHM gaussian to simulate the effects of the momentum spread in the treatment beam and the range straggling in the tissue. Due to the slowly varying nature of the reaction cross sections this convolution has little effect on the expected activity distribution. The decay distribution shown in Figure 3.18 was obtained by integrating the unmodulated activity distribution shown in Figure 3.25. Note that the initial activity in the adipose is rather low due to the lack of ^{15}O.

There are several interesting points to be made about the difference in the activity distributions created by a RBP and a SOBP with macro-pulsed beams. The most obvious difference in the distributions occurs at the distal end of the proton's range. The activity distribution associated with the SOBP starts decreasing just before the plateau region. The distance between the distal 90% and 10% activity levels gives a relatively good indication of the width of the plateau region of the SOBP. At the other end of the distribution the activity is slightly larger for the SOBP. This is predominately due to the

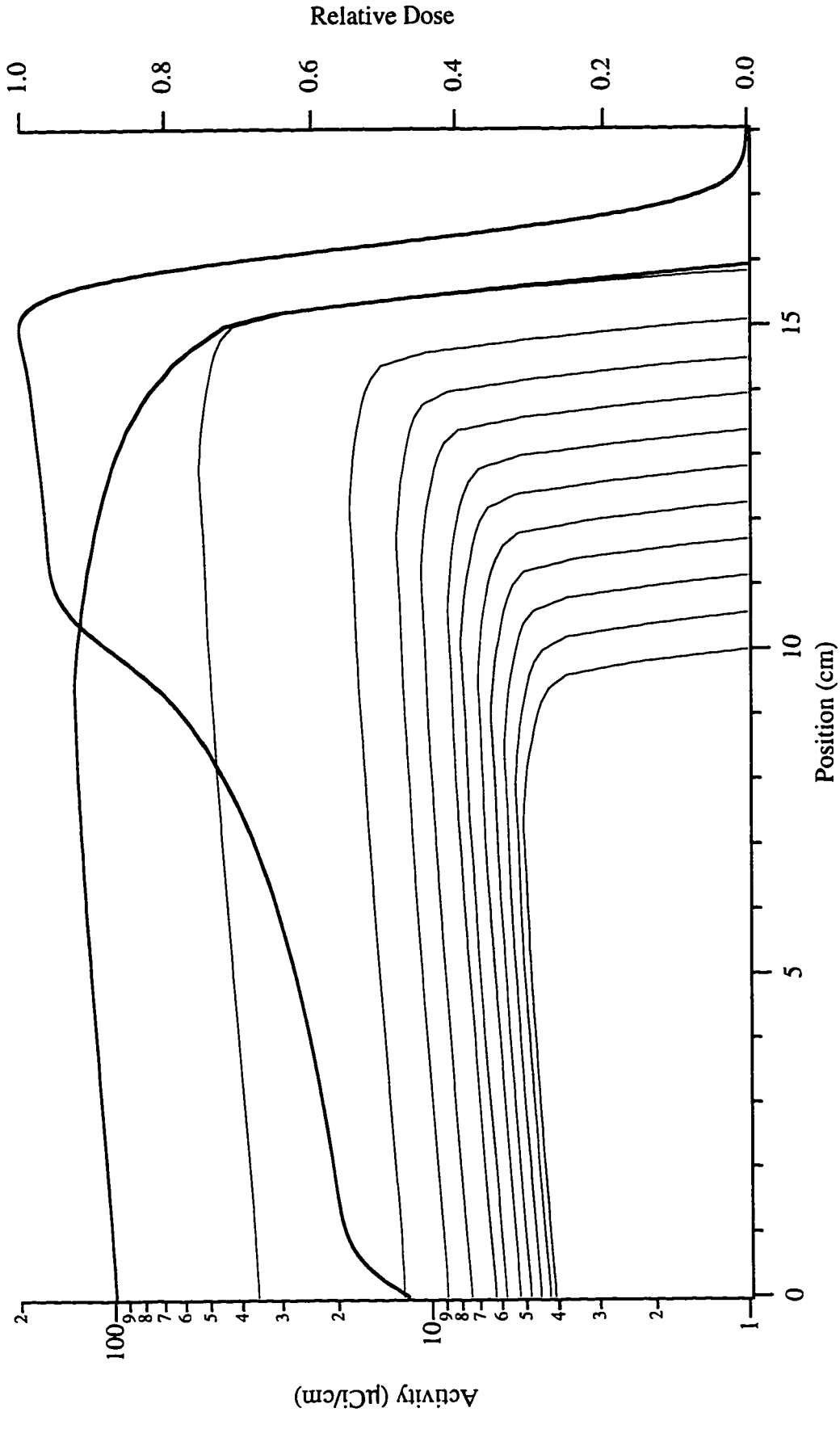

Figure 3.23. The activity distribution created by each energy of a pulsed, energy modulated beam by the end of a two minute treatment. The total activity distribution and calculated 6.0 cm SOBP are also shown.

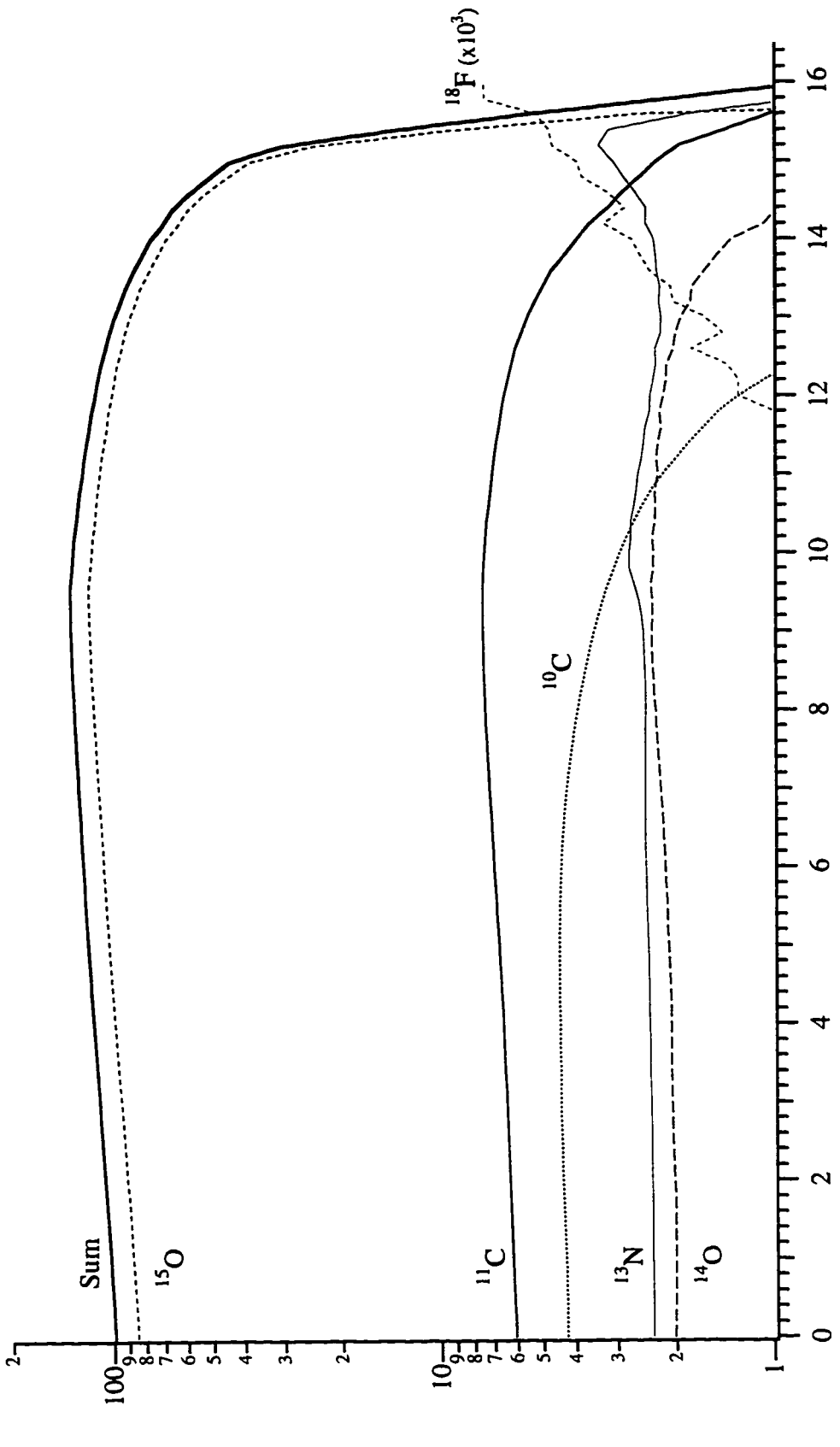

Figure 3.24. The radioisotopic activity distributions created by a pulsed, energy modulated beam by the end of a two minute treatment. The distribution of ^{18}F activity has been multiplied by 10^3 for illustrative purposes.

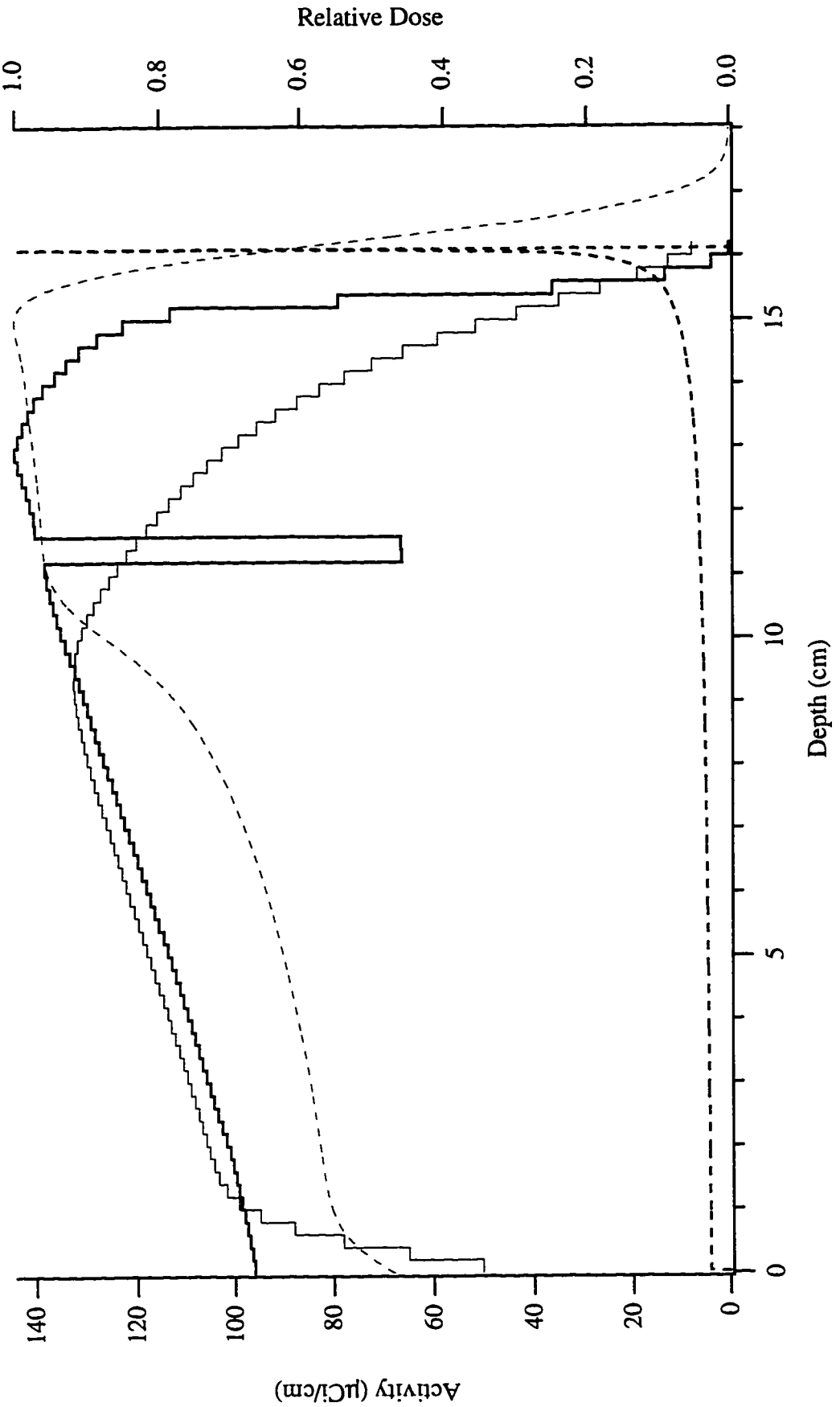

Figure 3.25. Comparison of the activity(solid lines) and dose distributions(dashed lines) for a RBP(dark lines) and a SOBP(light lines) with maximum energies of 150 MeV.

Isotope	Expected Activity (μCi) in Tissue	Expected Activity (μCi) in Lucite
^{10}C	47.00	2.1
^{11}C	97.60	18.7
^{13}N	38.75	1.1
^{14}O	30.80	1.0
^{15}O	1483.44	41.3
^{18}F	13.50	-
Totals	1711.09	64.2

Table 3.8. Summary of the isotopic activities which would be produced in a swine-tissue phantom and a Lucite modulation wheel by a 1.75 nA, 150 MeV proton beam, pulsed with a 10 second period and implanted for 120 seconds.

higher cross sections for the production of ^{15}O and ^{11}C at lower beam energies. This will always occur in tissue for energy-modulated beams whose greatest energy is higher than the peak production energy of ^{15}O and ^{11}C, or about 50 MeV as seen in Figure 3.1. Additionally, the macro-pulse period of the beam has little effect on the magnitude of the activity distribution. For example, the activity distribution shown in Figures 3.23 and 3.24, which were calculated by assuming a SOBP and a pulse period of 10 seconds, would only be about 1% smaller if the pulse period had been 2 seconds.

Due to the activity gradient at the distal end of the protons range created by SOBP, it may be difficult to ascertain the oxygen content of the tumor relative to the adjacent tissue. It would be preferable to have the energy-dependent reaction cross sections vary slowly across the width of the tumor. This situation occurs in proton radiography where a high-energy beam of roughly 400 MeV passes through the patient.

This transmission technique has been investigated for mapping the line integral of the density perpendicular to the treatment beam [40] and for patient alignment perpendicular to the beam [56] but it may also prove useful in monitoring the oxygen content in tumors to avoid the aforementioned problems with cross sections at low beam energies.

Discussion of Results

It has been shown that the range of the beam can be verified on-line within the resolution of the imaging system and some information on composition can be obtained. However, several issues must still be addressed. To be clinically useful the resolution of the imaging system must be reduced to the sub-centimeter range. In designing a detection system to accomplish this, consideration must be given to the average coincidence detection efficiency per unit length along the system axis. To maintain sufficient efficiency to obtain statistically significant images the detector height perpendicular to the plane of the detector array would have to increase if the width of each detector is decreased. This increase in detector volume would also increase the chance coincidence rate, especially if multiple crystals are optically coupled and fewer PMT's used for readout.

The effects of nuclear interactions on the dose distribution have been presented by other investigators [21, 22]. However, the effect of nuclear secondaries on the activity distribution has not been investigated in detail yet. The radioisotopic images suggest that a library of accurate cross sections needs to be developed for neutron- and proton-induced reactions on the elements in tissue [47, 57, 58]. The presence of activity beyond the proton beams range suggests that nuclear reactions induced by secondary neutrons and other charged particles may produce a significant amount of ^{14}O in the treatment volume. Since ^{10}C, ^{13}N, and ^{14}O are only produced in small quantities the uncertainties in their cross sections are of little consequence to on-line range verification. Most tissues are primarily composed of oxygen, carbon and hydrogen for which the cross sections for

producing positron-emitting radioisotopes are reasonably well known. Although the unexpected large production of ^{14}O may have a noticeable effect on the magnitude of images produced on short time scales, due to its short half-life, it is primarily produced from oxygen through the $^{16}O(p,p2n)^{14}O$ and $^{16}O(n,3n)^{14}O$ reactions. Thus the ^{14}O distribution primarily reflects the distribution of oxygen along the beam path.

Other more exotic reactions leading to the production of positron-emitting emitting are shown in Table 3.9. Many of these reactions occur with rare yet stable isotopes of elements commonly found in tissue, such as ^{13}C, ^{15}N, or ^{18}O. There has been much interest in many of these reactions as a more efficient means of producing PET radio-pharmaceuticals. Consequently, the cross sections for these reactions have been studied at energies primarily below 30 MeV. These reactions have been examined to determine the possibility of using them to more closely monitor proton radiotherapy treatments. The radiative capture reactions, (p,γ), may at first appear useful for range monitoring because they do not have a threshold energy. However, the cross sections for this class of reactions is typically microbarns, or three orders of magnitude smaller than competing reactions. Consequently, the amount of activity produced by these reactions is to small too be detected in the presence of other reactions. The other reactions listed are induced from heavy isotopes of carbon, nitrogen and oxygen. On-line verification requires an isotope that decays quickly such as ^{10}C, ^{14}O, ^{15}O, or ^{17}F. In this respect, the $^{15}N(p,n)^{15}O$ reaction may be useful. The proton beam has a range of 0.02 cm beyond the reaction's 3.8 MeV threshold energy making the reaction well suited as an end-of-range marker. In addition, the average cross section is roughly 150 millibarns between 4 MeV and 8 MeV where there are strong resonances. While this technique does have the disadvantage of requiring the placement of a sufficient quantity of the material at the end of the protons range, it may potentially be an effective end-of-range marker if the placement is possible.

Reaction	Threshold Energy, (MeV)	Q-value (MeV)	Range Below Threshold (cm)
$^{12}C(p,p2n)^{10}C$	34.5	-31.8	1.2
$^{14}N(p,n\alpha)^{10}C$	17.2	-16.0	0.3
$^{13}C(p,p2n)^{11}C$	25.5	-23.7	0.7
$^{15}N(p,n\alpha)^{11}C$	14.7	-13.8	0.3
$^{12}C(p,\gamma)^{13}N$	0.0	+1.9	0.00
$^{13}C(p,n)^{13}N$	3.24	-3.0	0.02
$^{15}N(p,nd)^{13}N$	20.4	-19.2	0.5
$^{15}N(p,t)^{13}N$	13.8	-12.9	0.2
$^{14}N(p,\gamma)^{15}O$	0.0	+7.3	0.00
$^{15}N(p,n)^{15}O$	3.8	-3.5	0.02
$^{16}O(p,\gamma)^{17}F$	0.0	0.6	0.00

Table 3.9. Uncommon reactions in tissue which produce positron-emitting isotopes.

The Effects of In Vivo Biological Washout and the Presence of ^{14}O on Total Dose Monitoring

As shown in earlier sections, the number of events detected between pulses n and $(n+1)$ varies nearly linearly on time scales less than about two minutes. While this is true in the experiments presented here additional complications will arise in living tissue. Much of the ^{15}O created will be bound in water which freely diffuses through cell membranes. This activity is consequently carried out of the field of view by the tumor's vasculature. In this situation the decay of ^{15}O must be modeled by two exponential terms [11]. The first term models the non-mobile fraction of the ^{15}O activity which disappears solely through radioactive decay. The second term models the mobile fraction of the ^{15}O

activity which disappears through radioactive decay and in vivo biological washout. The decay constant of the second term depends on the half-life of ^{15}O and the average rate of blood flow through the imaged volume [11]. The corresponding half-life for the washout term may vary greatly depending on the average blood flow rate. Reported values of the washout half-life range from roughly 40 seconds [10] to over 3 minutes [11]. If the treatment volume being imaged has a high blood flow then the activity will appear to decay on shorter time scales. The linear approximation of the number of counts detected between beam pulses will become less accurate making it a less reliable indicator of dose received in well-perfused treatment volumes.

It should be noted that using a standard water tank, typically used to verify the range and the dose distribution in many treatment facilities, is not suitable for calibrating this type of imaging system. The mechanisms which lead to the transport of activity within the tank are difficult to quantify accurately and may vary significantly from calibration to calibration. Typically, the amount of ^{15}O present is severely under-determined due to these processes and the amount of ^{14}O is over-estimated due to the difficulty in quantifying the transport mechanisms for the mobile component of the ^{15}O. In the presence of these transport phenomena the ^{15}O radioisotopic images was observed to be rather strongly peaked at the distal end of the protons range, much like the Bragg peak. This may be seen in Figure 2.7. While this seems to indicate that the activity created at higher energies has a higher macroscopic transport rate it more likely arises from conditions within the tank, such as currents induced by temperature gradients.

Correlation Between the Dose Distributions and the Induced Activity Distribution

The change in the total dose deposited in the treatment volume as a function of time may be monitored fairly reliably in treatment volumes with low blood flow rates. Figures 3.15b and 3.20 show that the number of 511 keV gamma-ray pairs detected between beam pulses increases nearly linearly with the number of beam pulses, and

consequently with the dose, for times less than about two minutes. However, it is difficult to infer the dose distribution from the activity distribution since the physical processes leading to the loss of energy and the creation of positron-emitting nuclei are not directly related. In the experimental results sections, the end of the dose distributions were found to coincide rather closely with the end of the activity distributions as seen in Figures 3.13a, 3.19, and 3.21. This is primarily due to the 1.2 cm resolution of the imaging system which is much larger than the 0.3 cm range of the treatment beam below the $^{16}O(p,n)^{15}O$ reactions threshold energy (Table 3.2). Since over 80% of the positron-emitting activity during and shortly after the treatment is due to the decay of ^{15}O this will be true for imaging systems with resolutions down to roughly 0.5 cm.

As noted previously, a correlation between the activity distribution and the dose distribution produced by a 6.0 cm SOBP does exist. Due to the successively shorter ranges of the portions of the beam passing through thicker regions of the modulation wheel, the distal end of the activity distribution steadily decreases over a distance the width of the SOBP plateau region. However, this effect may only be observed for SOBP with energy distributions which are large compared to the energy range over which the cross section drops from its maximum to near the reactions threshold. Additionally the minimum energy incident upon the patient when using a SOBP should be greater than the energy at which the maximum cross section occurs, which typically is between 35 MeV and 50 MeV. For the $^{16}O(p,pn)^{15}O$ reaction, the cross section drops from 90% of its maximum value to 10% of its maximum value in the energy range from 40 MeV to 20 MeV. In homogenous tissue the proton beam energy drops from 40 MeV to 20 MeV over a distance of about 0.9 cm. The range straggling of the beam will increase this width slightly and should be added in quadrature resulting in a distance of approximately one centimeter. The distance is slightly smaller for the $^{12}C(p,pn)^{11}C$ reaction. Consequently, this decrease in activity at the distal end of the distribution is barely observable for a SOBP with a two centimeter plateau produced by a 60 MeV treatment

beam [30] but should be readily observed at beam energies above 100 MeV in SOBP with plateau widths of several centimeters.

Figures 3.18 and 3.19 show that there are strong correlations between the radioisotopic activities and the composition of the tissue. While the extent of the adipose deposit along the beam path was only one-third the resolution of the imaging system, the correlations in the ^{15}O and ^{11}C radioisotopic vectors were still significant. Such correlations would be stronger with more extended inhomogeneities or with an imaging system with better resolution. While the dose deposited in various inhomogeneities may or may not vary significantly compared to the surrounding tissues these radioisotopic correlations may be used as reference points for range verification to anatomical features along the beam path.

The correlations observed in the radioisotopic images of Figures 3.18 and 3.19 are due to the oxygen content dropping from 75% by mass in tissue to 28% by mass in adipose, and the carbon content increasing from 11% to 60%, respectively. Equation (3.1) shows that the activity, and consequently the number of decays in any time interval, at any given depth varies linearly with the number density of target nuclei. Consequently, if the percent change in the density of a particular target nuclei is greater than the uncertainty in the reconstructed radioisotopic images, the compositional variation should be observable. This condition is common in tissues such as muscle, adipose and bone. However, the following argument suggests that this technique may not be sensitive enough to detect hypoxia in large tumors based upon variations in the number density of oxygen alone.

Tumor cells are said to be hypoxic if the amount of oxygen available to them for metabolic activity is low. If the only compositional differences between normal and hypoxic tumor cells originates from the amount of oxygen delivered in solution by the blood, then a rough estimate of the decrease in oxygen can be made. One gram of hemoglobin can carry roughly 1.34 mL of O_2 while the amount of hemoglobin in the

blood is about 340 g/L [59]. Capillary blood flow varies greatly in various tissues and values from 10 mL/min per 100 grams of tissue [11] to 90 mL/min per 100 grams of tissue [10] have been reported. If we assume a blood flow value of 50 mL/min per 100 grams of tissue is fairly representative then on the order of 5×10^{-4} g/sec/cm^3 of oxygen is delivered to non-hypoxic tumor cells which is not delivered to hypoxic cells. Assuming the hypoxic and non-hypoxic cells contain roughly 70% oxygen by mass and have a density of 1g/cm^3 we find that the composition varies by less than 0.1%, based on the amount of oxygen delivered to the cells by the blood. Consequently, the lack of oxygen in hypoxic cells would not be observable based on compositional variations alone. The blood flow gradient from the hypoxic center to the well-perfused outer layers of the tumor, however, may provide a mechanism by which the extent of hypoxia may be evaluated.

The mobile fraction of oxygen in well-perfused tissue may be significantly higher than in hypoxic tissue. In addition this mobile fraction will disappear from the FOV more quickly through biological washout. It has been shown that the volume averaged blood flow over the tumor is commonly 10% to 20% lower than the blood flow to the well-perfused region of the tumor at the surface [11]. Consequently, in most situations the hypoxic condition may be easily detected in tumors which are several times larger than the resolution of the imaging system.

Two- or Three-Dimensional Image Reconstruction

One of the more obvious ways to improve the present imaging system is to develop a two-dimensional reconstruction algorithm. This would allow planes of a typical treatment volume to be imaged and significantly lessen the blurring due to overlying activity which would be experienced with the present system. While there are many advantages to producing two-dimensional images of the activity created, there are also several disadvantages. Producing a statistically significant two-dimensional image

of would require roughly N^2 events compared to the N needed to produce a one-dimensional depth-distribution. The additional time required to collect this number of events would make reliable on-line range verification between macro-pulses much more difficult unless the number of detectors and associated electronics were greatly increased. Additionally, the algorithms for reconstructing incomplete tomographic datasets using a shift-variant point response function are iterative [60, 61]. Thus they requires more time to reconstruct an image before it can be evaluated. However, rapid advances in processor speeds will alleviate this problem in the near future.

Conclusions

Based on the results of these experiments it is seen that on-line range verification may be performed after a single typical macro beam-pulse. Calculations show that over 80% of the activity created in such a short times is ^{15}O, produced by the $^{16}O(p,pn)^{15}O$ reaction. The range of the proton beam below this reaction's 16.6 MeV threshold energy is 0.3 cm. Because the best practical resolution for this type of system is very similar to this residual beam range, the end of the dose distribution and the activity distribution will coincide to within the resolution of any foreseeable PET imaging system. The effects of energy straggling and the momentum spread of the treatment beam would only be observable by means of the activity distribution at the end of the range for proton beams with energies above 150 MeV using an imaging system with a resolution of two to three millimeters.

In general it is very difficult to infer the dose distribution from the induced activity distribution alone. However, some information on the width of the SOBP plateau region can be obtained from the fall of activity at the end of the range. This is only possible for treatment beams whose energy is about 100 MeV or greater and have a SOBP plateau width of roughly 4 centimeters or more. The total dose may be monitored more accurately by monitoring the increase in the total number of 511 keV gamma-ray

pairs detected between macro-pulses. The number of counts increases roughly linearly for treatment times less than about two minutes, at least in treatment volumes with low blood flow rates.

Variations in the elemental composition along the beam path are readily observed in layers of distinct tissue types. Variations as small as about 5% in a single element, averaged over a resolvable region, may be identified. The detectable size of these compositional variations will change based on the uncertainty in the reconstructed isotopic images, which is determined by the dose delivered and the imaging time. It may be possible to detect smaller variations if two isotopic image vectors exhibit strong positive or negative correlations in the same region. This phenomenon may be used to verify the range to various anatomical features along the beam path. It may also be particularly useful if used with high-energy, low intensity beams in conjunction with a proton-range telescope [56] for transverse patient alignment. In this situation, the beam would traverse the prescribed volume at higher energies where the PET isotope reaction cross sections vary slowly, resulting in more reliable compositional determination across and beyond the tumor volume.

Range verification capability will become increasingly important for improving dose localization. While it may be possible to reposition the patient and deliver the prescribed dose distributions with an uncertainty of just a few millimeters, it has been shown that internal organs, such as the prostate, may move one to three centimeters between treatments [62]. In such cases, the advantage of the high dose localization offered by protons may be compromised or even detrimental without proper alignment and range verification for the shifting anatomical features.

The prototype imaging system used for the experiments presented here was designed within a limited budget with the intention of investigating the feasibility of using PET imaging as a monitor for proton radiotherapy beams. It should by no means be considered an optimally-designed system for clinical use but rather as an experimental

system suitable for initial investigations. To be clinically useful the solid angle should be increased to compensate for attenuation of the 511 keV gamma-rays in the patient and the resolution should be improved to the sub-centimeter range. In addition, rectangular crystals should be used with no intercrystal shielding, especially if only one-dimensional decay distributions are being reconstructed. In this case, depth-of-interaction blurring is removed by the calibration procedure and the image reconstruction algorithm. However, blurring will occur if the treatment beam is more than a few centimeters wide [DWL1, 34]. Further design considerations and suggested improvements may be found in one of our earlier papers [DWL1, 34].

Acknowledgments

This work was supported by grants PHY 9512104 and PHY 9208468 from The National Science Foundation and by grants from the following groups within the University of Michigan: The Office of the Vice President for Research, The John Munn Foundation through The Comprehensive Cancer Center, The College of Literature, Science and Art, The Rackham School of Graduate Studies, and The Department of Physics. Additional acknowledgments are also due to the many students who made valuable contributions to this research while participating in the NSF's Research Experience for Undergraduates program. These people include: Armin Martin, Mary-Alice Abbott, Chris Hazard (two summers), Mark Chawla, and Chris Search.

References to Chapter 3

[1] M. S. Wagner, "Automated Range Compensation for Proton Therapy," *Med. Phys.* 9, pp. 749-752, 1982.

[2] P. L. Petti, Differential-Pencil-Beam Dose Calculations for Charged Particles," *Med. Phys.*, vol. 19, pp. 137-149, 1992.

[3] M. Goitein, "The Measurement of Tissue Heterodensity to Guide Charged Particle Radiotherapy," *Int. J. Rad. Oncol. Biol. Phys.*, vol. 3, pp. 27-33, 1977.

[4] M. Goitein, et al., vol. "The Influence of Thick Inhomogeneities on Charged Particle Beams," *Radiat. Res.*, vol. 74, pp. 217-230, 1978.

[5] M. Goitein, "Compensation for Inhomogeneities in Charged Particle Radiotherapy Using Computed Tomography," *Int. J. Oncol. Biol.*, vol. *Phys.*, vol. 4, pp. 499-508, 1978.

[6] A. A. Mustafa and D. F. Jackson, "The relation between X-ray CT numbers and charged particle stopping powers and its significance for radiotherapy treatment planning," *Phys. Med. Biol.*, vol. 28, no. 2 , pp. 169-176, 1983.

[7] E. L. Alpen, W. Saunders, A. Chatterjee, J. Llacer, G. T. Y. Chen and J. Scherer, "A comparison of water equivalent thickness measurements: CT method vs. heavy ion beam technique," *Brit. J. Rad.*, vol. 58, pp. 542-548, 1985.

[8] C.A. Tobias, "Analysis of Microcomposition of Biological Tissue by Means of Induced Radioactivity," *Science*, vol. 109, pp. 109-113, Feb. 1949.

[9] M. V. Mayneord, et al., "Production of Radioactivity in Animal Tissues by High-energy X-rays," *Nature,* vol. 164, pp. 728-730, 1949.

[10] W. L. Hughes, et al., "Tissue Perfusion Rate Determined from the Decay of Oxygen-15 Activity after Photon Activation *in Situ*," *Science*, vol. 204, pp. 1215-1216, 1979.

[11] R. K. Ten Haken, et al., "Photon activation-^{15}O decay studies of tumor blood flow," *Med. Phys.*, vol. 8, pp. 324-336, 1981.

[12] S. Graffman, et al., "^{11}C and ^{15}O Induced in the Mouse by 175 MeV Protons," *Acta Radio. Ther. Phys. Biol.*, vol. 14, pp. 113-126, 1975.

[13] G. W. Bennett, et al., "Visualization and Transport of Positron Emission from Proton Activation *in Vivo*," *Science,* vol. 200, pp. 1151-1152, 1978.

[14] R. K. Ten Haken, M. Awschalom, and I. Rosenberg, "Activation of the Major Constituents of Tissue and Air by a Fast Neutron Radiation Therapy Beam", *Med. Phys.*, vol. 10, no. 5, pp. 636-641, 1983.

[15] M. C. Taylor, "Pion Cancer Therapy: Positron Activity as an Indicator of Depth-Dose," *Science*, vol. 169, pp. 377-378, July, 1970.

[16] L. F. Mausner, et al., "*In Vivo* Beam Localization by Positron Activation in Pion Therapy," *Rad. Research,* vol. 80, pp. 10-23, 1979.

[17] H. Shirato, et al., "Detection of Pion-Induced Radioactivity by Autoradiography and Positron Emission Tomography," *Med. Phys.*, vol. 16, pp. 388-345, 1989.

[18] H. D. Maccabee, et al., "Tissue Activation Studies with Alpha-Particle Beams," *Phys. Med. Biol.*, vol. 14, pp. 213-224, 1969.

[19] J. Llacer, J. B. Schmidt, and C. A. Tobias, "Characterization of fragmented heavy-ion beams using a three-stage telescope detector: Measurements of 670-MeV/amu 20Ne beams," *Med. Phys.*, vol. 17, no. 2, pp. 151-157, 1990.

[20] W. Enghardt, W. D. Fromm, H. Geiss, G. Kraft, et al., "The spatial distribution of positron-emitting nuclei generated by relativistic light ion beams in organic matter," *Phys. Med. Biol.*, vol. 37, no. 11, pp. 2127-2131, 1992.

[21] S. M. Seltzer, "An assessment of the role of charged secondaries from nonelastic nuclear interactions by therapy proton beams in water," National Institute of Standards and Technology report NISTIR 5221, June, 1993.

[22] R. F. Laitano, M. Rosetti, M. Frisoni, "Effects of nuclear interactions on energy and stopping power in proton beam dosimetry," *Nucl. Instr. Meth. Phys. Res. A*, vol. 376, pp. 446-476, 1996.

[23] G. W. Bennett, et al., "Beam Localization Via ^{15}O Activation in Proton-Radiation Therapy," *Nucl. Inst. and Meth.*, vol. 125, pp. 333-338, 1975.

[24] R. Loevinger, et al., "A revised Schema for Calculating the Absorbed Dose From Biologically Distributed Radionuclides," *Soc. of Nucl. Med.* 1976.

[25] J. Llacer, A. Chatterjee, E. L. Alpen, W. Saunders, S. Andreae, and H. C. Jackson, "Imaging by Injection of Accelerated Radioactive Particle Beams," *IEEE Trans. Med. Imag.*, vol. 3, no. 2, pp. 80-90, June, 1984.

[26] D. W. Litzenberg, J. F. Bajema, F. D. Becchetti, et al., "On-Line Monitoring and P.E.T. Imaging of Proton Radiotherapy Beams," IEEE Med. Imag. Conf. Rec., 954-956, Orlando, FL, pp. 25-31, Oct. 1992.

[27] D. W. Litzenberg, J. F. Bajema, F. D. Becchetti, et al., "On-Line Monitoring and P.E.T. Imaging of Proton Radiotherapy Beams," IEEE Med. Imag. Conf. Rec., pp. 1672-1676, Norfolk, VA, Oct. 30-Nov. 5, 1994.

[28] S. Vynckier, S. Derreumaux, F. Richard, A. Bol, C. Michel, and A. Wambersie, "Is it possible to verify directly a proton-treatment plan using positron emission tomography," *Radiother. Oncol.*, vol. 26, pp. 275-277, 1993.

[29] A. M. J. Paans, and J. M. Schippers, "Proton Therapy in Combination with PET as Monitor: A Feasibility Study," *IEEE Trans. Nucl. Sci.*, vol. 40, no. 4, pp. 1041-1044, Aug. 1993.

[30] U. Oelfke, G. K. Y. Lam, and M. S. Atkins, "Proton dose monitoring with PET: quantitative studies in Lucite," *Phys. Med. Biol.*, vol. 41, pp. 177-196, 1996.

[31] J. Pawelke, L. Byars, W. enghardt, W. D. Fromm, et al. "The investigation of different cameras for in-beam PET imaging," *Phys. Med. Biol.*, vol. 41, pp. 279-296, 1996.

[32] A. Del Guerra, and G. Di Domenico, "Positron Emission Tomography as an aid to in "vivo" dosimetry for proton radiotherapy: a Monte Carlo simulation," TERA 93/10 TRA 9, Aug. 1993.

[33] M. G. Albouy, J.P. cohen, M. Gusakow, N. Poffe, H. Sergolle , and L. Valentine, "Spallation de L'Oxygene par bes Protons de 20 a 150 MeV," *Phys. Let.*, vol. 2, no. 7, pp. 306-307, Nov. 1962.

[34] D. W. Litzenberg, F. D. Becchetti, and D. A. Roberts, "On-Line PET Monitoring of Radiotherapy Beams: Image Reconstruction and Monte Carlo Simulations of Detector Geometries," *IEEE Trans. Nucl. Sci.*, vol. 44, no. 4, August, 1997.

[35] M. J. Berger, and S. M. Seltzer, Tables of energy loss and ranges of electrons and positrons, in Studies in Penetration of Charged Particles in Matter, U. Fano, Ed, Publ. No. 1133, National Academy of Sciences, National research Council, Washington D.C., pp. 1-30, 1956.

[36] J. F. Janni, "Proton Range-Energy Tables, 1 keV - 10 GeV," *Atomic Data and Nuclear Data Tables*, vol. 27, no. 2/3, March/May 1982.

[37] "Specifications for a Proton Therapy Research and Treatment Facility," Massachusetts General Hospital and Lawrence Berkeley Laboratory, NPTC-4, Oct. 1992.

[38] S. R. Cherry, Yiping Shao, S. Siegel, W. W. Silverman, et al., "Optical Fiber Readout of Scintillator Arrays using a Multi-Channel PMT: A High Resolution PET Detector for Animal Imaging," *IEEE Trans. Nucl. Sci.*, vol. 43, no. 3, pp. 1932-1937, June 1996.

[39] G. R. Lynch, and O. I. Dahl, "Approximations to multiple Coulomb scattering," *Nucl. Instr. Meth. Phys. Res. B*, vol. 58, pp. 6-10, 1991.

[40] U. Schneider and E. Pedroni, "Multiple Coulomb scattering and spatial resolution in proton radiography," *Med. Phys.*, vol. 21, no. 11, pp. 1657-1663, Nov. 1994.

[41] D. F. Measday, "The $^{12}C(p,pn)^{11}C$ Reaction from 50 to 160 MeV," Nucl. Phys., vol. 78, pp. 476-480, 1966.

[42] M. Epherre, and C. Seide, "Excitation Functions of ^{7}Be and ^{11}C Produced in Nitrogen by Low-Energy Protons," *Phys. Rev. C*, vol. 3, no. 6, pp. 2167-2171, June 1971.

[43] L. Valentin, G. Albouy, J. P. Cohen, and M. Gusakow, "Fonctions D'Excitation des Reactions (p,pn) et (p,2p2n) dans les Noyaux Legers Entre 15 et 155 MeV," *Jour. de Phys.*, vol. 25, pp. 704-706, June, 1964.

[44] S. W. Kitwanga, P. Leleux, P. Lipnik, and J. Vanhorenbeeck, "Production of ^{14}O, ^{15}O, ^{18}F, and ^{19}Ne radioactive nuclei from (p,n) reactions up to 30 MeV," *Phys. Rev. C*, vol. 42, no. 2, pp. 748-752, Aug. 1990.

[45] A. B. Clegg, "Gamma Radiation from Medium Energy Proton Bombardment of Lithium, Beryllium, Boron, Carbon and Nitrogen," *Proc. Phys. Soc.*, vol. 78, pp. 681, 1961.

[46] T. J. Ruth, and A. P. Wolf, "Absolute Cross Sections for the Production of ^{18}F via the $^{18}O(p,n)^{18}F$ Reaction," *Radiochim Acta*, vol. 26, pp. 21-24, 1979.

[47] M. B. Chadwick, and P. G. Young, "Proton nuclear interactions up to 250 MeV for radiation transport simulations of particle therapy," proceedings of the PTCOG conference to be published in Journal of Endocurietherapy / Hyperthermia Oncology, Detroit, 1996.

[48] D. W. Litzenberg, F. D. Becchetti, D. A. Roberts, A. M. Vander Molen, Ron Fox, "A Parallel, Transputer-Based Data Acquisition System for On-Line PET Imaging of Proton and Gamma-Ray Radiotherapy Beams," *IEEE Trans. Nucl. Sci.*, vol. 43, no. 1, pp. 154-158, Feb. 1996.

[49] H. Stark, and J. W. Woods, "Probability, random Processes, and Estimation Theory for Engineers. 2nd ed. New Jersey: Prentice Hall, 1994, pp. 251.

[50] P. R. Bevington, and D. K. Robinson, Data Reduction and Erroro Analysis for the Physical Sciences. 2nd ed. New York: McGraw-Hill, 1992, pp. 194-219.

[51] K. J. Kearfott, and L. R. Carroll, "Evaluation of the Performance Characteristics of the PC 4600 Positron Emission Tomograph," *J Comput Assist Tomogr*, vol. 8, no. 3, pp. 502-513, June, 1984.

[52] P. G. Young, E. D. Arthur, and M. B. Chadwick, "Comprehensive nuclear model calculations: introduction to the theory and use of the GNASH code," Los Alomos National Laboratory document LA-12343-MS, 1992.

[53] R. Eilbert, "Bone calcium determination in vivo by proton activation analysis," Ph. D. dissertation, Harvard University, 1975.

[54] ICRU, "Tissue Substitutes in Radiation Dosimetry and Measurement," Report 44 of the International Commission on Radiation Units and Measurements (Bethesda, MD), 1989)

[55] J. V. Siebers, private communication, March, 1997.

[56] J. J. Romero, J. H. Osborne, F. P. Brady, W. Caskey, et al., "Patient positioning for protontherapy using a proton range telescope," *Nucl. Instr. Meth. Phys. Res. A*, vol. 356, pp. 558-565, 1995.

[57] M. B. Chadwick, and P. G. Young, "Calculation and evaluation of cross sections and kerma factors for neutrons up to 100 MeV on ^{16}O and ^{14}N," *Nucl. Sci. Eng.*, vol. 123, pp. 1-16, 1996.

[58] M. B. Chadwick, and P. G. Young, "Calculation and evaluation of cross sections and kerma factors for neutrons up to 100 MeV on carbon," *Nucl. Sci. Eng.*, vol. 123, pp. 17, 1996.

[59] M. J. Inwood, S. Thomson, and N. J. Bryant, "Hematology," in Lynch's Medical laboratory Technology, S. S. Raphael, Ed., 4th ed. Philadelphia: W. B. Saunders Company, 1983, pp. 625-627.

[60] W. Enghardt, A noise suppressing iterative reconstruction technique for positron emission tomography," *Physica Medica*, VII N3, 1991.

[61] W. Enghardt, W. D. Fromm, P. Manfrass, and D. Schardt, "Limited-angle 3D reconstruction of PET images for dose localization in light ion tumour therapy," *Phys. Med. Biol.*, vol. 37, no. 3, pp. 791-798, 1992.

[62] J. M. Balter, K. L. Lam, H. M. Sandler, J. f. Littles, R. L. Bree, and R. K. Ten Haken, "Automated Localization of the Prostate at the Time of Treatment using Implanted Radiopaque Markers: Technical Feasibility," *Int. J. Radiation Oncology Biol. Phys.*, vol. 33, no. 5, pp. 1281-1286, 1995.

CONCLUSIONS

The goals of this research have been to evaluate the potential of using PET imaging as a monitor for proton radiotherapy treatments. Based on the results of these experiments it is seen that on-line range verification may be performed after a single typical macro beam-pulse. Calculations show that over 80% of the activity created in such a short times is ^{15}O, produced by the $^{16}O(p,pn)^{15}O$ reaction. The range of the proton beam below this reaction's 16.6 MeV threshold energy is 0.3 cm. Because the best practical resolution for this type of system is very similar to this residual beam range, the end of the dose distribution and the activity distribution will coincide to within the resolution of any foreseeable PET imaging system. The effects of energy straggling and the momentum spread of the treatment beam would only be observable by means of the activity distribution at the end of the range for proton beams with energies above 150 MeV using an imaging system with a resolution of two to three millimeters.

In general it is very difficult to infer the dose distribution from the induced activity distribution alone. However, some information on the width of the SOBP plateau region can be obtained from the fall of activity at the end of the range. This is only possible for treatment beams whose energy is about 100 MeV or greater and have a SOBP plateau width of roughly 4 centimeters or more. The total dose may be monitored more accurately by monitoring the increase in the total number of 511 keV gamma-ray pairs detected between macro-pulses. The number of counts increases roughly linearly for treatment times less than about two minutes, at least in treatment volumes with low blood flow rates.

Variations in the elemental composition along the beam path are readily observed in layers of distinct tissue types. Variations as small as about 5% in a single element, averaged over a resolvable region, may be identified. The detectable size of these compositional variations will change based on the uncertainty in the reconstructed isotopic images, which is determined by the dose delivered and the imaging time. It may be possible to detect smaller variations if two isotopic image vectors exhibit strong positive or negative correlations in the same region. This phenomenon may be used to verify the range to various anatomical features along the beam path. It may also be particularly useful if used with high-energy, low intensity beams in conjunction with a proton-range telescope for transverse patient alignment. In this situation, the beam would traverse the prescribed volume at higher energies where the PET isotope reaction cross sections vary slowly, resulting in more reliable compositional determination across and beyond the tumor volume.

Range verification capability will become increasingly important for improving dose localization. While it may be possible to reposition the patient and deliver the prescribed dose distributions with an uncertainty of just a few millimeters, it has been shown that internal organs, such as the prostate, may move one to three centimeters between treatments. In such cases, the advantage of the high dose localization offered by protons may be compromised or even detrimental without proper alignment and range verification for the shifting anatomical features.

The prototype imaging system used for the experiments presented here was designed within a limited budget with the intention of investigating the feasibility of using PET imaging as a monitor for proton radiotherapy beams. It should by no means be considered an optimally-designed system for clinical use but rather as an experimental system suitable for initial investigations. The design results presented in Chapter 1 may be used to help determine the best PET detection geometry based on the imaging conditions, the object being imaged, the desired resolution, the permissible image

acquisition time and budgetary considerations. The prototype system presented here may be further optimized for on-line imaging of radiotherapy beams. The highest detection efficiency may be achieved by removing the intercrystal shielding and minimizing the spacing between adjacent detection crystals. The detection efficiency may also be improved by minimizing the separation between the detector banks. However, the distance between the detector banks should not be less that given by (1.9) or blurring from outlying activity may degrade the resolution. Alternatively, the effective length may be reduced by omitting coincidences from oblique detector pairs. Thus the optimum configuration for on-line imaging is a compromise between detection efficiency and blurring due to extended activity distributions.

Based on these simulation results and experienced gained with this prototype imaging system several improvements may be suggested for next-generation systems. While planar detection arrays are an attractive improvement for providing 3D imaging of the treatment volume the iterative algorithms needed prohibit their use for fast, on-line image reconstruction. Possible improvements which retain the present imaging capabilities include the use of rectangular instead of cylindrical crystals and the omission of the intercrystal shielding. This would provide a significant increase in detection efficiency by increasing the solid angle and packing efficiency, and by allowing the detection of gammas which entered through adjacent crystal faces. Rectangular crystals having dimensions 0.5 cm along the system axis, 2 cm, perpendicular to the plane of the detectors, and 3 cm deep would provide a resolution along the system axis of about three millimeters, and increase the solid angle by 50% while using the same volume of scintillator used in the present system. Ideally each crystal would be readout by a single PMT. However, for the detector dimensions given above, individual crystal readout would quadruple the number of PMT's and electronic channels needed to process the signals. Alternatively, a block of scintillator may be partially cut perpendicular to its length every few millimeters producing an optically coupled block design which could be

readout with fewer PMT's or using fast position-sensitive PMT's . Depth-of-interaction blurring could still be prevented by using the same calibration technique with a point-like source or a line source perpendicular to the plane of the detectors.

Currently the best scintillator for use in PET applications is BGO due to its high stopping power and its adequate coincidence timing characteristics. It does however have the disadvantages of having a long decay constant, low light output, and hence poor energy resolution. The long time constant limits the count rate capabilities due to pulse pileup. The poor energy resolution makes the system susceptible to the detection of photons scattered by the overlying material in the object containing the activity. While not yet economical, the use of cerium-doped lutetium oxyorthosilicate (LSO) would significantly reduce these effects. LSO has a marginally lower stopping power and effective atomic number than BGO resulting in a photopeak efficiency 20% to 25% lower than that in BGO. However, LSO has better energy resolution since its light output is about five times larger than that of BGO. LSO is also capable of higher rates since it has decay constants of 12 ns (30%) and 42 ns (70%) compared to a 300 ns time constant for BGO.

While medical applications tend to require the best spatial resolution possible, other applications with less demanding needs may use larger spaces between the adjacent crystals. Simulations show that even with intercrystal shielding, spaces as large as half the detector width provide a reasonable detection efficiency at all points along the system axis. If the intercrystal shielding is removed the detection efficiency will likely increase by more than 50% and provide a more uniform *CDE* along the axis. In this case, detector separations of a detectors width would provide resolution of approximately the detector size with good efficiency and at a significantly lower cost.

APPENDICES

APPENDIX A

SCHEMATICS OF THE ELECTRONICS AND LOGIC CIRCUITS

The logic and electronics circuit is shown in a block diagram in Figure 2.1 for simplicity.

Figures A.1a, b, and c. The following three pages were photocopied from one of my lab manuals and show the logic and electronics circuits in more detail. The specific NIM and ECL electronics modules are identified along with the length of the lemo cables used to obtain the correct timing of signals among the modules.

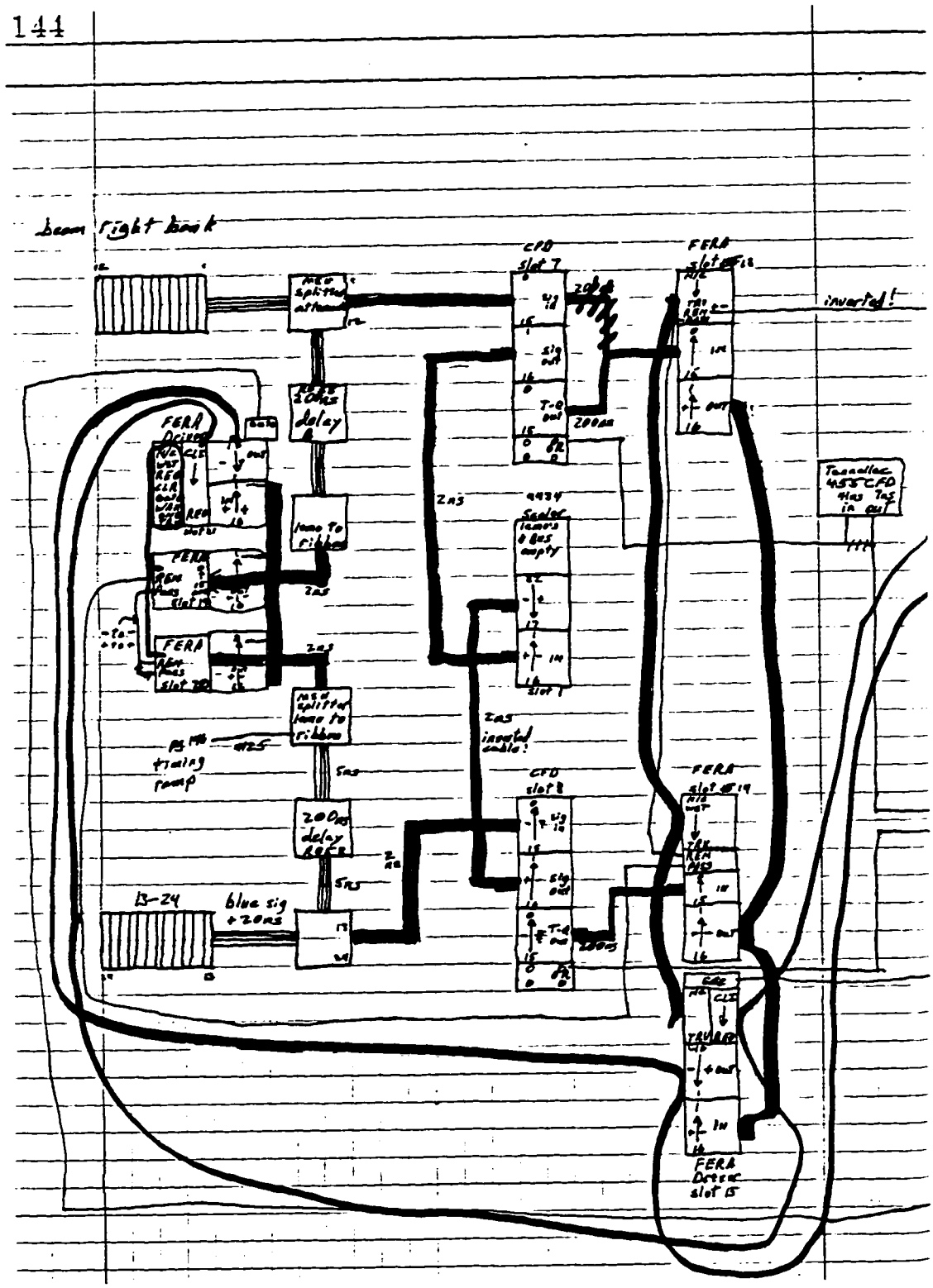
144
beam right back
CFD slot 7
FERA
inverted!
FERA Octet
delay
9934 Scaler
Tennelec 455 CFD
FERA slot 19
CFD slot 8
FERA Octet slot 15

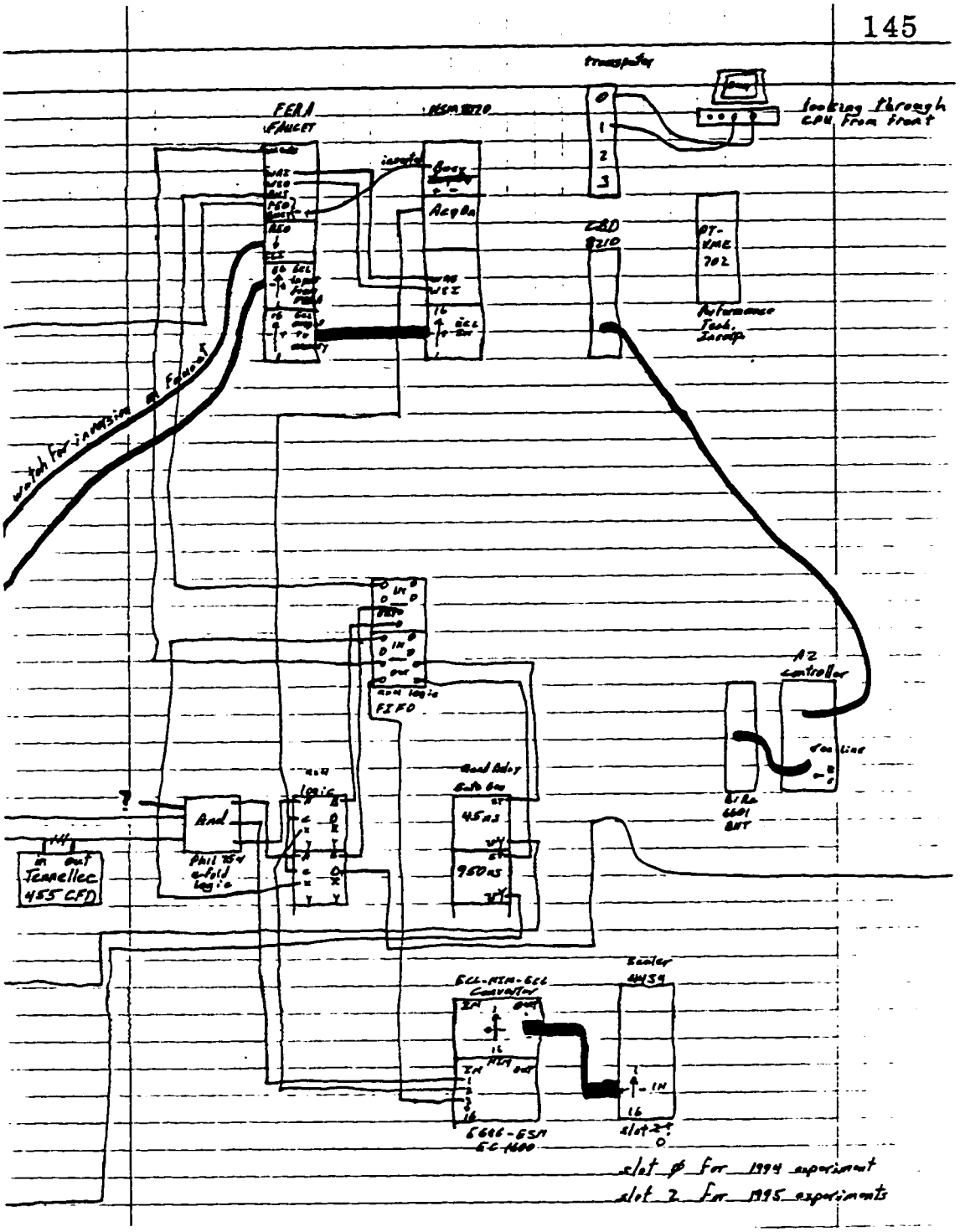
145
FERA
FASTBUS
Acq On
Transputer
looking through CPU from front
EXBD 9210
OT-VME 702
Performance Task Interrupt
watch for interrupt
FIFO
AZ controller
Tennelec 455 CFD
And
Phil 754 4-fold Logic
45 ns
950 ns
ECL-NIM-ECL Converter
6686-ESM
EC-1600
slot 0 for 1994 experiment
slot 2 for 1995 experiments

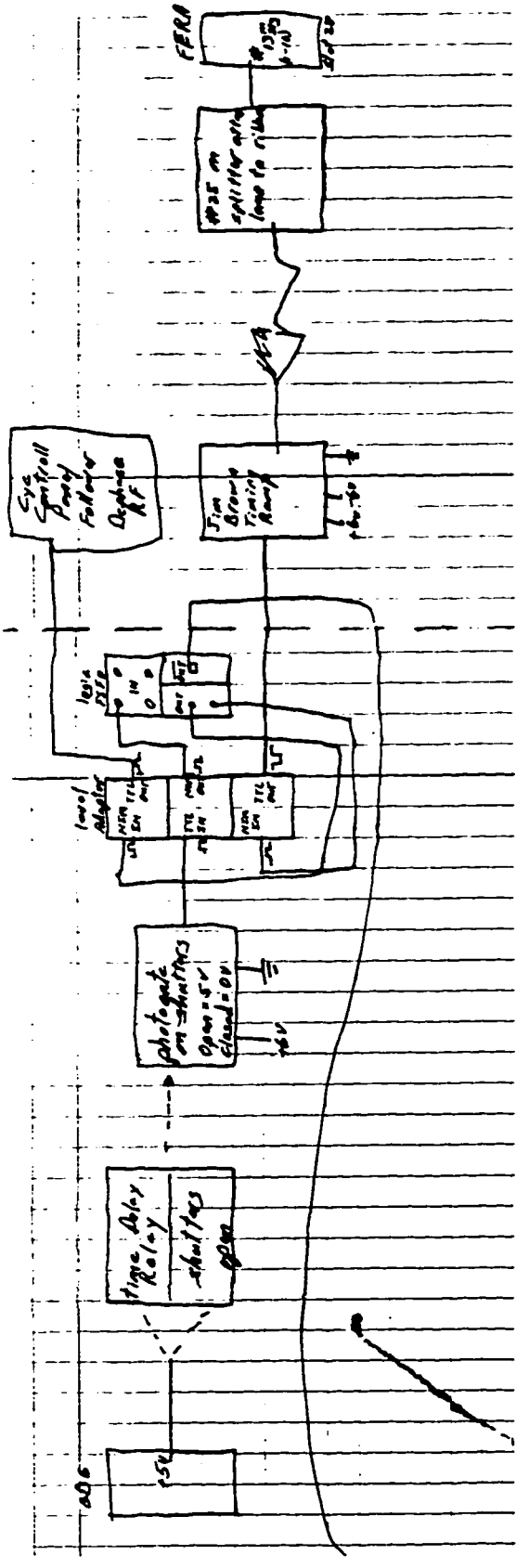
FERA
Eye Control Relay Software
Jim Brown Timing Relay
Level Adapter
Photogate on Shutters
Open = 5V
Closed = 0V
Time Delay Relay
Shutters
SW
506

APPENDIX B

FORMAT OF THE DATA BUFFERS

There are several types of buffers used which convey information about the status of the data acquisition system or contain various types of data. Each one of these buffers begins with a standardized 16 word header which contains the information given in Table B.1. The buffer types used during these experiments are listed in Table B.2.

Word Number	Words of Data	Contains
1	1	Number of useful words in buffer
2	1	Buffer type
3	1	Buffer checksum over used words
4	1	Run number
5	2	Buffer sequence number
7	1	1
8	1	Number of LAM registers in event stream
9	1	Number of CPU which generated buffer
10	1	Number of bit registers
11	1	Buffer revision level
12	5	Reserved for future use

Table B.1. Contents of NSCL's standard 16 word buffer header.

Value	Buffer contents
1	Physics buffer
2	Taped scaler data
11	Begin run buffer
12	End run buffer
13	Pause run buffer
12	Resume run buffer

Table B.2. Numerical values of NSCL buffer types.

The standard NSCL buffer headers were appended with a second 16 word header for use with the transputer-based data acquisition system for error checking. This header is appended by a VME based module designed at NSCL to control the flow of data from the FERA's. This module was named the FERA Faucet Maier(FFM). In addition to appending this header it places a unique separator, FFFF in hexadecimal, between each event read from the FERA's. The structure of a type one data buffer is shown in Table B.3. The data read out from each FERA are preceded by a one word FERA header. This header contains the CAMAC crate slot number in bits one through five, the CAMAC crate number in bits six through eight, and the number of data words read from that FERA, which follow the header, in bits twelve through fifteen. Each FERA contains sixteen channels of which the first 12 were used for the twelve detectors. Zero-suppression was enabled so that only energy channels which contained data were those containing a singles event over the energy threshold. Timing signals, constant current pulses which get integrated by the timing FERA's, are only generated by the CFD's when the signal from the PMT is over the energy threshold. The first block of a type one buffer is shown in Figure B.1. as an example.

Two 32 channel scalers were used to determine the number of singles events in each detector, the number of coincidences and the number of coincidences while the data acquisition system was not busy. Rates could then be determined using the time increment over which the data was acquired. During pulsed beam experiments this time interval was typically set to the macro-pulse period of the beam. This information was then used to correct for deadtime and to estimate the chance coincidences to be subtracted. The structure of the scaler buffers is shown in Table B.4. The first block of a type two buffer is shown in Figure B.2. as an example.

Number of Words	Contents
16	Standard NSCL buffer header
16	FFM error checking header
1	FFFF
1	First timing FERA header
1	data word one
1	...
1	data word n
1	FFFF
1	Second timing FERA header
1	data word one
1	...
1	data word n
1	FFFF
1	First energy FERA header
1	data word one
1	...
1	data word n
1	FFFF
1	Second energy FERA header
1	data word one
1	...
1	data word n
1	FFFF
1	First timing FERA header
1	...

Table B.3. Structure of a type one data buffer containing energy and timing information read from the FERA's.

```
Dump of file $1$DKA700:[LITZENBERG.BGO.BGO2]RUN000032.EVT;1

Virtual block number 3553 (00000DE1), 512 (0200) bytes

 0000 0000 0102 0304 0102 0004 0000 0003 0000 0001 0000 00DC 0020 0000 0001 023A
 001F 001E 001D 001C 001B 001A 0019 0018 0017 003A 0000 0000 0001 7591 0001 7484
 8833 4409 882E 1C00 882D FFFF 65B9 1FFF 9034 0BAB 8833 1BCC 882E 0BD0 882D FFFF
 FFFF 65AD 2450 9034 137F 8833 23D4 882E 1271 882D FFFF 65AF 4451 2899 9834 1CDB
 388B 9033 1BDE 882E 5413 882D FFFF 65AB 14CC 9034 0486 8833 13E0 882E 03E1 882D
 4547 348A 0302 A034 63FE 0C80 9033 3475 882E 0BBD 882D FFFF 65B2 1CE7 9034 543E
 2416 882E 3C4C 882D FFFF 65AB 1C33 9034 63A9 8833 1BE4 882E 2412 882D FFFF 65B1
 242D 9034 62BD 5019 9033 23F2 882E 23AB 882D FFFF 65B8 247A 9034 53B8 3C2A 9033
 5366 882E 1C24 882D FFFF 65B1 2D05 9034 144F 8833 2C1A 882E 13AD 882D FFFF 65AF
 2085 1BE7 A034 036F 8833 2BF4 882E 044F 882D FFFF 65AE 5463 9034 6442 1BEF 9033
 882E 5BEA 882D FFFF 65AE 12DB 9034 1B0B 8833 13CE 882E 1C7C 882D FFFF 65B0 2A14
 0C29 9034 4C9B 8833 0C2E 882E 4C06 882D FFFF 65B2 281D 14FF 9834 5B9F 8833 1458
 882E 0C3F 882D FFFF 65AB 2BF5 0452 9834 0C18 8833 03A6 882E 0BEE 882D FFFF 65B5
 08EA 9834 352F 2BA8 9033 23D8 882E 33B6 882D FFFF 65B5 1511 9034 0BAB 8833 13D0
 882E 2C44 882D FFFF 65B8 3556 9034 1BCE 8833 348F 882E 1BFD 882D FFFF 65B1 244C
 A034 4C52 8833 1C89 882E 4C00 882D FFFF 65AD 50C9 323E 9834 3006 2C11 9033 33EA
```

Figure B.1. Sample data from the first block(256 words) of a type 1 buffer(4096 words). These buffer types contain zero-suppressed data from the FERA's used to integrate energy and timing signals.

Contents of scaler buffers
16 word NSCL header
16 word FFM header
End time low word
End time high word
3 unused words
Start time low word
Start time high word
3 more unused words
First scaler channel
Second scaler channel
...

Table B.4. Structure of a type two data buffer containing scalers.

```
Dump of file $1$DKA700:[LITZENBERG.BGO.BGO2]RUN000032.EVT;1

Virtual block number 3569 (00000DF1), 512 (0200) bytes

 0000 0000 0102 0304 0102 0004 0000 0003 0000 0040 0000 0003 0020 0000 0002 00A4
 0001 33C7 0023 37E7 0023 6F3E 0DC8 9034 6064 0000 07D0 0C28 882E 13AD 0000 0BB8
 0000 0000 0000 0000 0000 0000 0000 0000 0000 0000 0000 0000 0000 0000 0000 0000
 0000 0000 0000 0000 0000 0000 0000 0000 0000 0000 0000 0000 0000 0000 0000 0000
 0000 0000 0000 0000 0000 0000 0000 0000 0000 0000 0000 0000 0000 0000 0000 0000
 0047 34E5 0041 E88E 0034 7B5F 0000 0000 0000 0000 0000 0000 0000 0000 0000 0000
 0062 FF2D 0065 C189 0066 8E2A 005F C58C 0063 66DB 004D 0784 0049 67AB 0068 989D
 0040 6BF6 003A 93B8 0030 DE1F 0000 0000 0000 0000 0000 0000 0000 0000 0067 43DF
 005C D1DC 004E 3605 005B B27C 0067 109A 0059 5CC1 0056 07D1 0047 D489 003F 43AC
 3DB3 8833 2466 882E 3C4B 882D 0000 0000 0000 0000 0000 0000 0000 0000 0050 80C6
 33A9 882D FFFF 65A8 2445 9034 0CAD 8833 2498 882E 0BBC 882D FFFF 65AD 23D2 9034
 0B23 9034 34F7 8833 0C54 882E 339D 882D FFFF 65B2 149D 9034 3525 8833 13E5 882E
 19F6 882D FFFF 65A7 2C6E 20BC 04B3 A034 150F 8833 2BDB 882E 1403 882D FFFF 65B4
 1C83 8833 2C21 882E 1BFE 882D FFFF 65AC 23CF 1C78 9834 19EB 0B7D 9033 1C5A 882E
 1BFE 882D FFFF 65A7 3CEA 9034 1B5D 8833 3C5B 882E 1BFD 882D FFFF 65B0 2CD9 9034
 65E9 492F 9033 1C55 882E 239A 882D FFFF 65BC 54E4 3915 9834 1C4E 8833 5360 882E
```


Figure B.2. Sample data from the first block(256 words) of a type 2 buffer(4096 words) containing 64 channels of scaler data.

APPENDIX C

SEMI-AUTOMATED DECAY DATA ANALYSIS AND RADIOISOTOPIC IMAGE RECONSTRUCTION

Radioisotopic imaging must be done off-line after the decay data has been collected. In these experiments the raw data from the data acquisition system were reduced on a VAX 4000/90 before being ported to a Macintosh for analysis of the decay data. The decay data were analyzed using a software analysis application called IGOR (WaveMetrics, Inc.). This package has an intuitive visual programming language built-in which may be used to build a graphical interface for complex automated data manipulations. Decay data from each of the 23 resolvable elements along the system axis are imported and summed to obtain the total detected decay data. The total decay data provides better statistics allowing trace radioisotopes to be detected more reliably. Figure C.1. shows the graphical interface for testing decay models to the decay data. Options are provided to fit only a portion of the decay data based on the position of cursors placed on the graph. The time scale of the decay data may be set relative to the placement of one of the cursors and the width of the time bins used during data acquisition. The radioisotopes included in the decay model are selected by removing the X in the box next to the desired isotopes. A background term and an isotope with an unknown half-life may also be included. Initial guesses for the activity coefficients of these isotopes are automatically calculated when the isotope is included. Another option allows biological washout to be modeled by including an additional term for each isotope the model. The half-life of each washout term is determined by fitting for a common blood flow coefficient which is added to the isotope half-life in each term. Residuals for each fit are automatically displayed on the accompanying graph. The decay data are fit using the non-linear Levenberg-Marquardt algorithm provided in the analysis application.

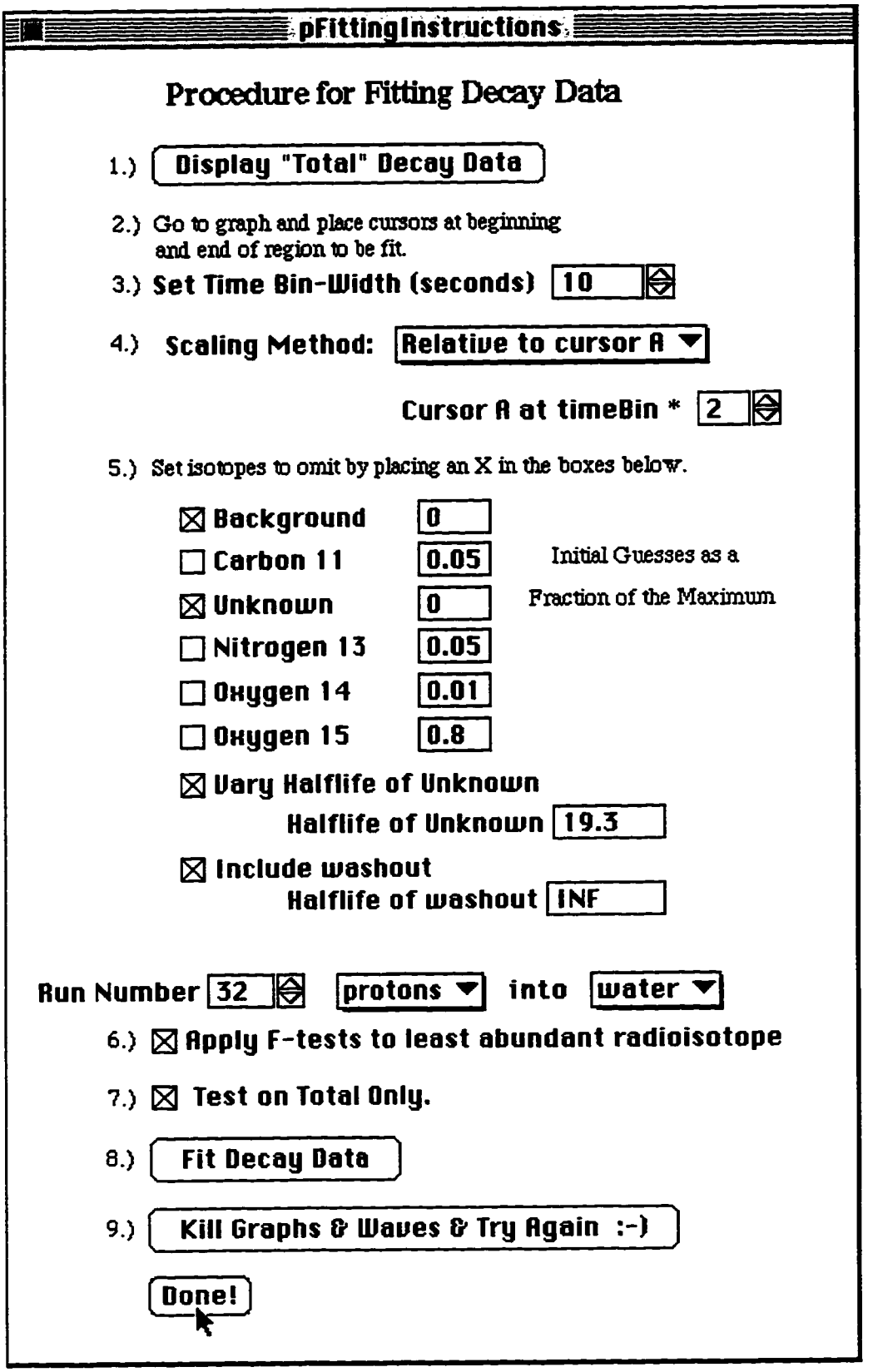

Figure C.1. Graphical interface for analyzing decay data and generating radioisotopic response vectors.

Once a suitable decay model has been found for the total decay data, the model may be applied to the decay data for each of the 23 resolvable elements. If desired, the *F* tests described in Chapter 3 may be automatically applied to each of the 23 decay datasets. This option more than doubles the analysis time and is typically used only for the final analysis.

After the decay model is applied to all 23 sets of decay data, radioisotopic response vectors are calculated by integrating the estimated decay curve, as shown in (3.14), for each isotope as determined by the activity coefficients found during the fit. The integration limits are determined by the location of cursors initially placed on a graph of the total decay data.

Once the radioisotopic response vectors have been found the image reconstruction interface shown in Figure C.2. may be selected from the menu bar. The radioisotopic reconstruction described by (3.15) is carried out through this interface. The images may be reconstructed using the appropriate system matrix. The inverses of the available system matrices may be preloaded into the analysis package after calibrations but before imaging experiments. The reconstruction algorithm returns image vectors whose magnitudes are calculated relative to the activity of the calibration source used during the calibration run. These may be converted to the absolute number of decays by essentially selecting the age of the ^{22}Na calibration source and its translation speed along the system axis during the calibration run.

Due to the simple rectangular phantom geometry used, attenuation corrections could be applied based on the phantom type and size. These corrections used a weighted sum over the number of detector pairs observing a given element along the axis. The were determined by the approximate solid angle of the detector pair and the phantom attenuation expected at the appropriate angle through the phantom.

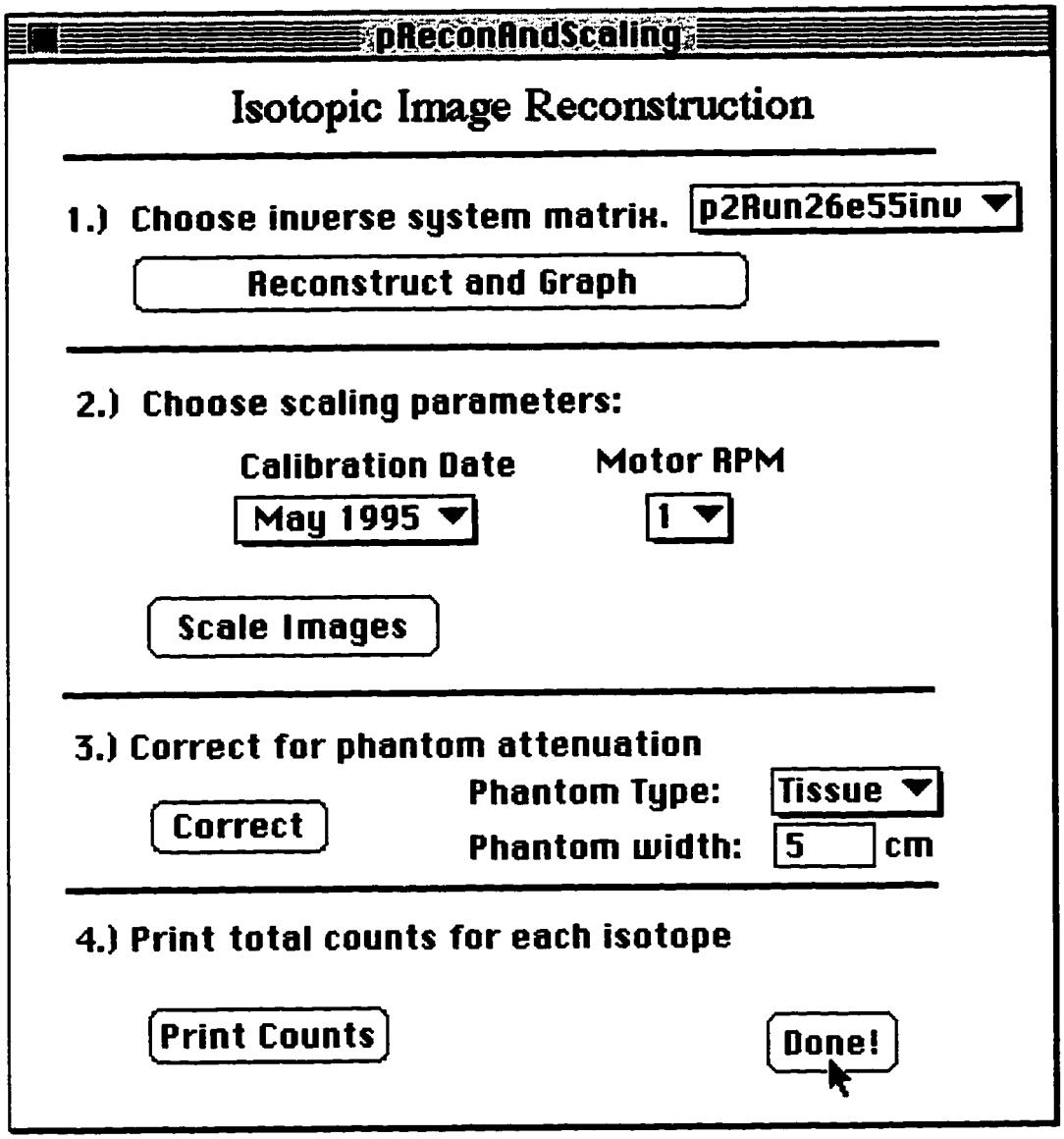

Figure C.2. Graphical interface for reconstructing and scaling radioisotopic image vectors.

APPENDIX D

GLOSSARY OF ACRONYMS

ADC .....Analog to Digital Converter

BGO .....Bismuth Germanate Oxide

CDE.....Coincidence Detection Efficiency

ECL .....Emitter Coupled Logic

CFD .....Constant Fraction Discriminator

CT.....Computed Tomography

DOI.....Depth of Interaction

FERA .....Fast Encoding Readout ADC

FFM.....FERA Faucet Meier

FOV.....Field of View

FWHM .....Full Width at Half of the Maximum

FWTM.....Full Width at one-Tenth of the Maximum

GNASH.....A preequilibrium, statistical nuclear model code for calculation of cross sections and emission spectra

LSO .....cerium-doped Lutetium Oxyorthosilicate

MSU NSCL..Michigan State University National Superconducting Cyclotron Laboratory

PET.....Positron Emission Tomography

PRF.....Point Response Function

PMT .....Photomultiplier Tube

RBP .....Raw Bragg Peak

SOBP.....Spread Out Bragg Peak

TAC.....Time to Amplitude Converter

APPENDIX E

EQUIPMENT PURCHASED TO CONSTRUCT THE PROTOTYPE IMAGING SYSTEM

Equipment for this project was purchased with funds provided by several groups within the University of Michigan. These groups include: The Office of the Vice President for Research, The John Munn Foundation through The Comprehensive Cancer Research Center, The College of Literature, Science and Art, The Rackham School of Graduate Studies, and The Department of Physics. The amount of the these grants are shown in Table D.1. The descriptions of the equipment purchased with these funds are shown in Table D.2. Items left justified in Table D.2. were purchased while the items at the bottom of the table which are right justified were priced but not purchased. The items not purchased for use during these experiments were borrowed from collaborators.

Organization	Contribution	Balance
OVPR	$25,000	$25,000
Cancer Research Center	$10,000	$35,000
LS&A	$12,125	$47,125
Rackham Graduate School	$2,500	$49,625
Physics Department	$2,500	$52,125

Table D.1. Funding provided by groups within the university of Michigam.

Item	Company	Unit Price	Qnty	Item Total	Account Balance
Init. Balance					$52,125
BGO	Rexon	$220.00	26	$5,720.00	$46,405.00
Shipping	Rexon	$42.50	1	$42.50	$46,362.50
Bases (E974-13)	Hamamatsu	$87.96	26	$2,286.96	$44,075.54
PMT's (R1166)	Hamamatsu	$295.52	26	$7,683.52	$36,392.02
FERA (4300B/610)	LeCroy	$2,502.60	4	$10,010.40	$26,381.62
FERA Driver (4301)	LeCroy	$1,815.00	2	$3,630.00	$22,751.62

CFD (3420)	LeCroy	$2,155.00	2	$4,310.00	$18,441.62
BBK-S4	Parsytec	$3,200.00	1	$3,200.00	$15,241.62
BBK-V2	Parsytec	$3,950.00	1	$3,950.00	$11,291.62
LNK-S (Cables)	Parsytec	$220.00	2	$440.00	$10,851.62
Shipping	Parsytec	$4.15	2	$8.30	$10,843.32
Hard Drive	Compet Comp Sys	$449.00	2	$898.00	$9,945.32
SHV Bulkheads	Oxford Instr	$9.00	26	$234.00	$9,711.32
Braided Cable	Purchase Radio	$48.00	1	$48.00	$9,663.32
BNC Bulkheads	Wedemeyer	$1.23	26	$31.98	$9,631.34
Bud Boxes	Wedemeyer	$4.50	26	$117.00	$9,514.34
Grommets	Wedemeyer	$4.87	1	$4.87	$9,509.47
UNIX book	B. Dalton	$31.75	1	$31.75	$9,477.72
Electrical tools	RadioShack	$15.02	1	$15.02	$9,462.70
Air cylinder	McMaster-Carr	$31.22	1	$31.22	$9,431.48
Cylinder Bracket Mount	McMaster-Carr	$3.40	1	$3.40	$9,428.08
Time Delay Relay	McMaster-Carr	$49.59	1	$49.59	$9,378.49
11 pin Relay Socket	McMaster-Carr	$4.77	1	$4.77	$9,373.72
Pillow Blocks	McMaster-Carr	$31.23	4	$124.92	$9,248.80
Stainless Eyebolts	McMaster-Carr	$10.30	4	$41.20	$9,207.60
Vibration Damping Pad	McMaster-Carr	$5.40	1	$5.40	$9,202.20
Synchronous Gearmotor	McMaster-Carr	$19.19	1	$19.19	$9,183.01
Ballscrew	McMaster-Carr	$37.92	1	$37.92	$9,145.09
Ball Nut	McMaster-Carr	$82.45	1	$82.45	$9,062.64
FAX charge	Purchasing	$10.00	1	$10.00	$9,052.64
VME Crate	OE Technologies	$375.00	1	$375.00	$8,677.64
Camac 811ADC	OE Technologies	$1,960.30	1	$1,960.30	$6,717.34
3 gigabyte disk drive	Transitional Tech	$1,695.00	1	$1,695.00	$5,022.34
Threaded Rod 1/2 x13	Schlenker	$2.76	1	$2.76	$5,019.58
Hex nuts 1/2 x 13		$0.08	50	$3.92	$5,015.66
Combination Square		$22.21	1	$22.21	$4,993.46
6" scale		$6.31	1	$6.31	$4,987.15
Black Felt (6'x8')	Jo-Ann Fabrics	$16.92	1	$16.92	$4,970.23
Wire Ties	Wedemeyer	$10.00	1	$10.00	$4,960.23
Biomed Particle Accel	AIP Press	$70.75	1	$70.75	$4,889.48
Cap screws (6-32x1/2)	Schlenkers	$0.14	150	$21.62	$4,867.85
Tap (6-32)	Schlenkers	$2.28	2	$4.56	$4,863.30
Tap Wrench	Jack's Hardware	$8.79	1	$8.79	$4,854.51
Tap (6-32)	Jack's Hardware	$2.43	1	$2.43	$4,852.08
Bubble Wrap	U-Haul	$4.05	1	$4.05	$4,848.03
Foam Cushion	U-Haul	$4.60	1	$4.60	$4,843.43
Packaging Tape	Ulrich's	$2.75	1	$2.75	$4,840.68
Aluminum Angle (2.5"x2.5")	Physics Shop	$4.00	10.008	$40.03	$4,800.65
Aluminum Angle (2"x3")	Physics Shop	$4.00	7.163	$28.65	$4,772.00

34 pin IDC connectors	Purchase Radio	$1.35	30	$40.50	$4,731.50
16 pin IDC connectors	Purchase Radio	$0.88	20	$17.60	$4,713.90
Elec. Tape (3M Super 88)	Purchase Radio	$4.00	4	$16.00	$4,697.90
Shipping	Purchase Radio	$16.50	1	$16.50	$4,681.40
Linear Bearing Pillow Blocks	McMaster-Carr	$41.74	4	$166.96	$4,514.44
Synchronous Gearmotor	McMaster-Carr	$19.92	1	$19.92	$4,494.52
Limit Switch	McMaster-Carr	$4.97	4	$19.88	$4,474.64
Roller Chain Breaking Tool	McMaster-Carr	$13.89	1	$13.89	$4,460.75
Heat Shrink Tubing	Purchase Radio	$7.40	1	$7.40	$4,453.35
Hex Cap Screw (1/4x20)	Schlenker's	$0.50	12	$5.98	$4,447.37
Flat Head Machine Screw(8-32)	Schlenker's	$0.20	20	$4.03	$4,443.34
Hex Hut (8-32)	Schlenker's	$0.05	20	$1.06	$4,442.28
Washers (#8)	Schlenker's	$0.05	20	$1.06	$4,441.22
Hammer	Sears	$13.77	1	$13.77	$4,427.45
Crescent Wrenchs (8" &10")	Sears	$26.49	1	$26.49	$4,400.96
Combination Wrench (1/2)	Sears	$6.14	2	$12.27	$4,388.69
Combination Wrench (7/16)	Sears	$6.35	2	$12.70	$4,375.99
Fasteners	Ace	$7.18	1	$7.18	$4,368.81
Socket Screws (6-32 x 1/2)	Schlenker's	$28.83	1	$28.83	$4,339.98
Hex Screws (1/4-20 x 3/2)		$2.04	1	$2.04	$4,337.94
Hex nuts (1/4 -20)		$1.59	1	$1.59	$4,336.35
Tool Box		$12.56	2	$25.12	$4,311.23
Ribbon Cable (16 conduc)	Purchase Radio	$7.50	1	$7.50	$4,303.73
Plastic target bottles	Meijer	$10.41	1	$10.41	$4,293.32
Lab notebooks	Mich Book & Supply	$23.03	1	$23.03	$4,270.29
Op Amps, ...	Radio Shack	$8.94	1	$8.94	$4,261.35
Relay, wire, ...	Radio Shack	$12.89	1	$12.89	$4,248.46
Solid State Relay	Grainger	$17.64	2	$35.28	$4,213.18
Travel Reimburs (Don Roberts)		$281.25	1	$281.25	$3,931.93
Travel Reimburs (Dale Litzenberg)	13 round trips	$439.40	1	$439.40	$3,492.53
MSU Housing Reimb (Dale Litz)		$85.00	1	$85.00	$3,407.53
IEEE MIC '94 (Norfolk, VA)		$979.28	1	$979.28	$2,428.25
Think C 6.0	Photo Services UM	$59.00	1	$59.00	$2,369.25
Graphic Services (poster prep)		$86.00	1	$86.00	$2,283.25
Igor Pro and XOP Toolkit	WaveMetrics	$484.00	1	$484.00	$1,799.25
Synchronous AC Gearmotor	McMaster-Carr	$38.43	2	$76.86	$1,722.39
Color Transparencies	Kinko's	$25.15	1	$25.15	$1,697.24

Poster Board	Ulrich's	$21.67	1	$21.67	$1,675.57
Blue pencils, razors, Poster Brd.	Ulrich's	$7.52	1	$7.52	$1,668.05
IEEE MIC Poster Title	Kolossos	$10.34	1	$10.34	$1,657.71
IEEE RT Poster Title	Kolossos	$4.10	1	$4.10	$1,653.61
Extension Cord	Jack's Hardware	$23.51	1	$23.51	$1,630.10
Felt, black	Jo-Ann Fabrics	$12.70	1	$12.70	$1,617.40
labbook, brushes, paint	MBS	$24.79	1	$24.79	$1,592.61
Ham, plastic bottles	Meijer	$109.78	1	$109.78	$1,482.83
Office Supplies	OfficeMax	$22.97	1	$22.97	$1,459.86
(On Hold!) VME Crate	Schroff	$2,100.00	1	$2,100.00	($640.14)
HMS 8170A	EG&G/CES	$4,636.00	1	$4,636.00	($5,276.14)
Camac/VME branch driver	EG&G/CES	$3,648.00	1	$3,648.00	($8,924.14)
4-way Solenoidal air valve	MSU	$0.00	1	$0.00	($8,924.14)
NIM Bin w/ supply		$1,200.00	1	$1,200.00	($10,124.14)
Co-axial ribbon cable		?	1	#VALUE!	#VALUE!
SHV Cables		?	1	#VALUE!	#VALUE!

Table D.2. Equipment purchased for the construction of the prototype imaging system.

APPENDIX F

COMPUTER PROGRAMS FOR REDUCING DATA , GENERATING SYSTEM MATRICES, AND PERFORMING ON-LINE ANALYSIS

There are three main programs used online data reduction and analysis. These include CAL.c, SYSMATRIX.c, and ONLINEFERA.c. The analysis code CAL.c is used after calibration runs to determine if the system is operating correctly and to determine the timing and energy cuts. The timing and energy cuts are used as the input for other analysis programs. These programs include SYSMATRIX.c which is used to generate a system matrix from the calibration data, and ONLINEFERA.C which is used for analysis during or after experiments. Most of the code in these three programs is very similar. The major differences involve how quantities are incremented, if cuts are made, and what is output for use by other programs.

Each of these programs can be run on VAX/VMS or SUN/UNIX platforms by uncommenting the appropriate preprocessor directives. The programs can accept data from file or directly from the router datastream for online analysis. While performing these experiments, results were displayed using a histogramming and graphing application called XAMINE which was written and maintained by Ron Fox at the NSCL. Preprocessor directives are included in the reduction and analysis code to allocate shared memory space for the quantities to be displayed.

The program SYSMATRIX.c is listed below and was chosen from the three programs due to its complexity. This program contains mainy more lines of code which are necessary to find the appropriate time cuts for binning the calibration data into the system matrix. This involves roughly finding the center of the CDE shown in Chapter 1 and placing cuts between the efficiency peaks. The cuts are then shifted to find the most symmetric weighting of the CDE about its center. Based on these cuts a system matrix is

generated which may be further improved by adjusting the cuts based upon symmetries of the matrix. These successive refinements to the binning of the system matrix rely upon the detectors having very similar efficiencies. The refinements are iterated until the system matrix is symmetric within the Poisson uncertainty. The CAL.c program simply increments various timing and energy histograms and makes cuts based on the characteristics of the peaks in each histogram. The ONLINEFERA.c program accepts or rejects event data based on these cuts and increments the appropriate quantities.

```
/* SysMatrix.C

        DALE LITZENBERG
        OCTOBER, 1994
        UNIVERSITY OF MICHIGAN

This program generates a system matrix from the data collected from the
Linear Positron Emission Imaging System.  It accepts as input three files.
The first input file, run##.cal, is generated by the program CALIBRATE.C
and contains statistical information about the raw data which is used to make
timing and energy cuts.  The second input file is the raw data file,
run0000##.evt, as generated by the imaging system.  The format of this
file is described in the MSU 4Pi Users Manual.  The third file contains
the system matrix.


JULY, 1994 NOTES
Since the calibration runs 45 - 51 had low statistics
the system matrices produces by these runs are added to improve the
statistics.  THE INITIAL VERSION DOES NOT HAVE TIMING CUTS DUE TO THE
LOW STATISTICS !!!

Spectra and statistical data generated by this program describe ONLY the
data which have not been cut by either timing or energy requirements.


APRIL/MAY, 1995 NOTES
A new 10uCi 22Na source has been obtained( 4 times stronger than last year )
and a slower motor has been installed on the calibrator( 5x slower ).
Statistics for a single calibration run should be about 20 times better.
However, a calibration run will now take approximately 110 minutes!

This program reads the energy and time cuts, length of calibration run,
and DAQ period from the calibration file, run##.cal.
The raw data is run through twice.  The first time is to determine the
hit distribution(unnormalized CDE) along the system axis.  This data is smoothed and
the maxima and minima found.  The location, in time, of the maxima and minima
determine the time cuts for incrementing position in the in the system
matrix.  The second pass through the data uses the time cuts to increment
position of the calibration source for generating the system matrix.
```

JULY, 1995 NOTES
Between runs 5 and 6 of the 1995 experiments we noticed that the scalers were not being read correctly. The problem was caused by a bad VME/CAMAC branch driver. While tracking down the problem the raw signals from detectors 1 and 13 got switched and efficitvely reduced the array to 11 detectors pairs for runs 6 through 24. Runs 6 - 24 will only be useful if calibration run 24 is good. It may be possible to use calibration runs 2 - 5 with runs >26 since detectors 1 and 13 hadn't been switched yet. After the VME/CAMAC branch driver was replaced the scaler dump period was accidentally set to 100 seconds instead of 10 seconds. This makes the position resolution for the hit distributions 10 times worse and makes it difficult to determine where to make time(position) cuts for incrementing the system matrix.

AUGUST, 1995 NOTES
Several improvements have been made to generate a better system matrix. Time cuts are found differently and an additional iteration has been added which makes small changes to the time cuts based on the matrices symmetry. As before the first pass through the data is used to generate the hit distribution. The locations of the timecuts are then CALCULATED based on the calibration motors speed, detector diameter, and detector spacing. The sum of the timecuts at these locations should be a minimum compared to timecuts which are slightly shifted. The timecuts are "wiggled around" and the minimum of the sampled positions is choosen as the best Minimum Weight Timecut. The second iteration though the data generates the system matrix bases on these timecuts. Additionally, when buffers are collected in two regions the counts are split between the regions(system matrix columns) bases on the percentage of time spent in each region. The matrix should be symmetric upon reflection about its center. So the elements to the left and right of the center element should be equal within counting error. If not, a theoretical shift is calculated and applied to the timecuts. The third iteration generates a new system matrix based on the symmetry corrected timecuts.

JANUARY, 1996 NOTES
Currently there are only two significant differences between this program and its companion program SYSMATGAM.c. The first is that the different motor speeds used are taken into account when calculating peak widths, finding the center of the hit distribution and when finding timecuts.
The second, doesn't exist anymore.
An error in finding the time shift for the symmetry correction was also corrected. See man#5, pg. 69.
Added column headings to hit distribution file (r##sm.hd) that IGOR reads in.

THINGS TO CORRECT AND CLEAN UP:

```
#include <stdio.h>
#include <stdlib.h>
#include <math.h>
#include <string.h>
#include <errno.h>

#ifdef unix
#include <mtaccess.h>
#endif unix
```

```
/*#define XAMINE*/          /* uncomment this line to use XAMINE */


#ifdef XAMINE
#define XAMINE_SPECBYTES 1024*1024  /* Set size of Xamine spectrum storage */
#include <Xamine.h>
#endif

#ifdef XAMINE
#ifdef VMS
#pragma nostandard
Xamine_shared _align(page) shared;
#pragma standard
#endif
#endif

/*#define Online */          /* Uncomment this statement to accept data */
                            /*  online from the router.            */


#define bfSiz 4096          /* input buffer size = 4096 words */

#define FE_K_DATA     1
#define FE_K_SCALER   2
#define FE_K_SCALER_PEEK 3
#define FE_K_START    11
#define FE_K_STOP     12
#define FE_K_PAUSE    13
#define FE_K_RESUME   14
#define ID_K_ERROR    8
#define ID_K_BEGIN    254
#define ID_K_HALT     255

#define file    1
#define tape    3
#define router  5

#define passes 4


/******************  Xamine Histogram Declarations  ***************/

#ifdef XAMINE

static void SetupSpectra( Xamine_shared *sp, short scalBf )
{

    int    i, j;

    strcpy(sp->dsp_titles[0], "Hit Distribution Along System Axis");
    sp->dsp_types[0]   = onedlong;
    sp->dsp_offsets[0] = 0;
    sp->dsp_xy[0].xchans = scalBf;

}

#endif


/******************  Global Struct Declarations ***************/

    typedef struct
    {
```

```
        short peak;             /* channel # of maximum in energy peak */
        short max;              /* maximum value in energy spectrum */
        short upper;            /* channel # of upper energy cut */
        short lower;            /* channel # of lower energy cut */
    } typeEnergyData;


    typedef struct
    {
        short backGrnd;                 /* average number of counts in background */
        short tPeak;            /* channel # of maximum in coincidence peak */
        short tMax;             /* maximum value in coincidence spectrum */
        short tUpper;           /* channel # of upper cut on time difference */
        short tLower;           /* channel # of lower cut on time difference */
        long rawSum;            /* total number of counts in uncut coinc spec */
        long cutSum;            /* number of counts in cut coinc spectra */
    } typeTimeData;


    typedef struct
    {
        short tPed;             /* time pedestal */
        short ePed;             /* energy pedestal */
        short time;             /* time data */
        short energy;           /* energy data */
    } typeEventData;


    typedef struct
    {
        long  tHits;            /* number of times detector fired CFD */
        long  eHits;            /* number of times energy recorded in detect */
        long  teHits;           /* number of detectors with time AND energy */
        short energy[2048];     /* energy spec, for dets with time AND energy */
        short time[2048];       /* timing spec, for dets with time AND energy */
    } typeDetectorData;

/*************** Global Function Declarations **************/

#ifdef unix
    volume *umtopen(char *VolLabel, char *Filename);
    void    umtclose(volume *vol, int dism);
    int     umtread(volume *vol, char *buf, int size, int dsize);
    int     SwapBytes( short **buffer );
#endif unix

/***************** Global Variables ****************/

#ifdef unix
        volume *volyoom;        /* volume control block for reading data  */
                                /*  from tape.                            */
#endif unix



/***************** Main Program *******************/

main()
{

/****************** Function Declarations ***************/

    int LoadSysMatrix( long SysMatrix[23][23], FILE **fPtrMat,
```

```
   char fileNameMat[] );

int LoadCal( typeEnergyData rEnergy[12], typeEnergyData lEnergy[12],
   typeTimeData coinc[12][12], long *lengthOfRun, short *DAQPeriod,
   short *offset );

int OpenIO( int *source, FILE **fptr, FILE **fptrOut, short **buffer,
          int *ichan, char notification[12], short incSysMat );

int CloseIO( int *source, FILE **fptr, FILE **fptrOut,
           char notification[12] );

int ReadBuffer( int *source, FILE **fptr, short *eof, short **buffer,
           int *ichan, char notification[12], short *numBf );

int AnalyzeEvent( typeEventData rDet[13], typeEventData lDet[13],
          typeEnergyData rEnergy[12], typeEnergyData lEnergy[12],
          typeDetectorData rBank[13], typeDetectorData lBank[13],
          long timeDiff[12][12][1000], float rTConv[12][2],
          float lTConv[12][2], long rNum511[12], long lNum511[12],
          long hitPat[23], long bufHitPat[23],
          typeTimeData coinc[12][12], long *numBfEvts,
          short *rCoinDet, short *lCoinDet, short *offset );

int FindTimeCuts( long smoothHD[], long timeCuts[], short scalBf,
                  short DAQPeriod );

int WriteSysMatrix( long SysMatrix[23][23], short *runNum,
          FILE **fPtrMat, char fileNameMat[] );

int CalcTimeCuts( short DAQPeriod, short runNum, long hitDist[],
          long timeCuts[], short scalBf, long lengthOfRun );

int SymmetryCorrection( short *incSysMat, short DAQPeriod, short runNum,
          long tempSysMatrix[23][23], long timeCuts[] );


/************** Struct Declarations ***************/

typeDetectorData
   rBank[13],           /* 12 dets in beam right bank, */
                        /*     declare 13 for convienience */
   lBank[13];           /* 12 dets + time stamp in beam left bank */


typeEventData
   rDet[13],            /* event data for detectors in right bank */
   lDet[13];            /* event data for detectors in left bank */


typeEnergyData
   rEnergy[12],         /* energy data for detectors in right bank */
   lEnergy[12];         /* energy data for detectors in left bank */


typeTimeData
   coinc[12][12];             /* coincidence data between detectors */
                        /* first index denotes right bank detectors */
                        /* last element contains array sum */


/******************** Array Declarations ******************/

long timeDiff[12][12][1000];/* time difference between 2 detectors */
```

```
                            /* first index denotes right bank detectors */
                            /* last element contains array sum */
    long rNum511[12];               /* num of 511's in an event in right bank */
    long lNum511[12];
/*
    long hitDist[6600];
*/
                            /* elements contain number of good events */
                            /*  in a buffer.  Buffer end time used as  */
                            /*  array index (longest run approx 6600sec */
                            /* arrays 0-22 correspond to positions 0-22 */
                            /* array 23 contains total of all arrays    */

    long timeCuts[24];              /* contains the time cuts for each of the 23 */
                            /* positions(24 boundaries) for calibration  */
                            /* data for approp run read in (runs 45-51)  */
                            /* Measured in units of tenths of seconds.   */

    long SysMatrix[23][23];  /* System Matrix - the first index specifies */
                            /* detector pair.  The second index specifies */
                            /* position                                  */

    long tempSysMatrix[23][23];/* temporary system matrix - All current      */
                            /* incrementing is performed on this matrix.  */
                            /* If a symmetry correction is necessary this */
                            /* matrix is zeroed and reincremented based   */
                            /* on the new timeCuts.  This matrix is then  */
                            /* added to any existing SysMatrix read form  */
                            /* a file.                                    */


/******  Xamine_shared Spectra and Declarations  ***********/

    long              *smoothHD;    /* smoothed hit distribution        */
                                    /* declared as short by Xamine      */


/************** Variable Declarations for Router Buffers *********/

    int     ichan;              /* pointer to "mailbox" containing buffer */
    char    notification[12];   /* 12 byte block for finding buffer in mailbox*/
    int     source;             /* source of data */


/*****************  Variable Declarations  ******************/


    register short wc;          /* contains word count from FERA header */
    register short wcMask;      /* word count mask */
    register short vsnMask;     /* virtual station number mask */
    register short saMask;      /* sub-address mask */
    register short dataMask;    /* data mask */
    register short i, j, k;     /* counter variables for loops */


    long       *hitDist;        /* ptr to arrays of decay data */
                                /*  array lengths are = (lengthOfRun/10) */
    long       *smooth;         /* holds intermediate results while smoothing */
    short      evsiz;           /* event size in words (data and FERA hdrs) */
    short      nBfWds;                  /* num useful words in bfr (incldg all hdrs) */
    long       hitPat[23];      /* hit pattern */
    long       bufHitPat[23];           /* hit pattern for events in one buffer */
    short      eof;             /* end of file marker */
```

```
    short       endOfRun;       /* end of run */
    short       runNum;             /* gets run number from fourth word in Begin */
                                /* of Run Buffer                          */
    short       numBf;          /* total number of buffers read in */
    short       physBf;             /* number of physics buffers read in */
    short       scalBf;             /* number of scaler buffers dumped */
    short       *buffer;        /* contains the buffer being analyzed */
    short       iBfTyp;             /* identify buffer type */
    short       lastBfTyp;      /* keeps track of the previous buffer type */
    short       wcTR,wcTL;      /* word count for time FERA, right and left */
    short       wcER, wcEL;     /* word count for energy FERA, right & left */
    short       sa;             /* sub-address */
    short       rCoinDet;       /* det in right bank involved in a coinc */
    short       lCoinDet;       /* det in left bank involved in a coinc */
    short       goodEvt;        /* test variable for a good event */
    long        numGoodEvts;    /* total number of events with proper format */
    long          numCoinc;         /* total number of events which pass the     */
                                    /*  timing and energy cuts                   */
    long        numBfEvts;      /* number of events after time and energy */
                                /*  cuts in a buffer                  */
    short       incSysMat;      /* counter variable to record 1st( =0 )    */
                                /*  or 2nd( =1 ) pass through data           */

    float       rTConv[12][2];      /* Channel to time conversion factors */
                                /*  [][0] for runs 1-9, [][1] for 10-end */
    float       lTConv[12][2];      /* Channel to time conversion factors */


/********* All Times are measured in tenths (0.1) of a second **********/

    unsigned short  endTimeLowWd;    /* end time low wd from scaler */
    unsigned short  endTimeHighWd;   /* end time high wd from scaler buffer */
    unsigned short  startTimeLowWd;  /* start time low wd from scaler buffer */
    unsigned short  startTimeHighWd; /* start time high wd from scaler buffer */

    long          bufEndTime;     /* end of acquisition time for that buffer */
    long          bufStartTime;   /* start of acquisition time for that buffer */

    double        timeFrac1;      /* fraction of scaler dump acquisition time  */
                                  /*  before or after a time cuts              */
    double        timeFrac2;      /* fraction of scaler dump acquisition time  */
                                  /*  before or after a time cuts              */

    short       offset;             /* time offset for deltaT histograms */
    short       DAQPeriod;      /* acquisition time between buffer dumps */
    long        lengthOfRun;    /* end time of last buffer dump */
    long        lengthOfRun2;   /* end time of last buffer dump */

    FILE        *fptr;
    FILE        *fPtrOut;
    FILE        *fPtrMat;

    char        fileNameMat[255];     /* I/O system matrix file */


/**************** Initialize Masks **********/
/* bits numbered 1 - 16 below              */
/* word shifted first then masked          */

/*** FERA header masks ***/
    wcMask      = 0x000F;       /* word count in bits 12 - 15 inclusive      */
    vsnMask     = 0x00FF;       /* virtual station number in 1 - 8 inclusive */
```

```
/*** data word masks *****/
    saMask      = 0x000F;       /* sub-address in bits 12 - 15 inclusive     */
    dataMask    = 0x07FF;       /* data in bits 1 - 11 inclusive             */



/**************** Load or Create System Matrix ******************/

    LoadSysMatrix( SysMatrix, &fPtrMat, fileNameMat );


/**************** Load Energy and Time Calibrations **************/

    LoadCal( rEnergy, lEnergy, coinc, &lengthOfRun, &DAQPeriod, &offset );
    scalBf = (short)( floor( lengthOfRun/DAQPeriod ) ) + 1;

/************** Allocate Memory for Large Arrays *****************/

    hitDist  = (long *)malloc(sizeof(long) * scalBf );
    smooth   = (long *)malloc(sizeof(long) * scalBf );

#ifdef XAMINE
    smoothHD = (long *)shared.dsp_spectra.XAMINE_1;
#else
    smoothHD   = (long *)malloc(sizeof(long) * scalBf );
#endif



printf("\nlength of run = %d/10 sec\n", lengthOfRun );
printf("DAQ Period    = %d/10 sec\n", DAQPeriod );
    lengthOfRun2 = lengthOfRun;
printf("Time Offset   = %d channels\n", offset );


    incSysMat = 9999;

    printf("\n");
    printf("OpenIO\n");
    OpenIO( &source, &fptr, &fPtrOut, &buffer, &ichan, notification, incSysMat);



/*****************************************************************/
/*****************************************************************/

/**************  Begin  Passes  Through  Data  *****************/

/*****************************************************************/
/*****************************************************************/


for( incSysMat=0; incSysMat<passes; incSysMat++ )  {



/******************** Initialize Hit Patterns *****************/

    for( i=0; i<23; i++ )  {
       hitPat[i] = 0;
```

```
        bufHitPat[i] = 0;
    }

/***************** Initialize arrays **********************/

    for( i=0; i<scalBf; i++)  { /***** Initialize hit distributions *****/
        hitDist[i]  = 0;
        smooth[i]   = 0;
        smoothHD[i] = 0;
    }


    for( i=0; i<13; i++ ) {

        rDet[i].tPed = 0;       /***** Initialize typeEventData *****/
        rDet[i].ePed = 0;
        rDet[i].time = 0;
        rDet[i].energy = 0;

        lDet[i].tPed = 0;
        lDet[i].ePed = 0;
        lDet[i].time = 0;
        lDet[i].energy = 0;


        rBank[i].tHits = 0;     /****** Initialize typeDetectorData *****/
        rBank[i].eHits = 0;
        rBank[i].teHits = 0;

        lBank[i].tHits = 0;
        lBank[i].eHits = 0;
        lBank[i].teHits = 0;

        for( j=0; j<2048; j++ ) {

            rBank[i].energy[j] = 0;
            rBank[i].time[j] = 0;

            lBank[i].energy[j] = 0;
            lBank[i].time[j] = 0;
        }
    }


    for( i=0; i<12; i++ ) {     /***** Initialize time information *****/
        for( j=0; j<12; j++ ) {
            coinc[i][j].cutSum = 0;
            for( k=0; k<1000; k++ ) timeDiff[i][j][k] = 0;
        }
    }


    for( i=0; i<12; i++ ) {     /***** Initialize num 511's *****/
        rNum511[i] = 0;
        lNum511[i] = 0;
    }


    numGoodEvts = 0;
    numBfEvts = 0;


/*************** Get first buffer ***************/
```

```
    numBf = 0;
    lastBfTyp = 0;
    iBfTyp = 0;


    ReadBuffer( &source, &fptr, &eof, &buffer, &ichan, notification, &numBf );
    numBf++;

#ifdef unix
    SwapBytes( &buffer );
#endif unix


    runNum = buffer[3];                              /* Get run number */
    if( incSysMat == 0 ) printf("\nRun Number %d\n", runNum );

    if( incSysMat == 0 ) printf("Generating Hit Distribution ... \n");
    if( incSysMat == 1 ) printf("\t...Done\n\nGenerating System Matrix using Minimum
Weight Timecuts...\n ");
    if( incSysMat >= 2 ) printf("\t...Done\n\nGenerating Symmetry Corrected System
Matrix ...\n" );


    endOfRun = 0;

/**************** Loop over buffer till eof is reached *************/

    while( !endOfRun ) {

        j = 0;

/*
       printf("reading in buffer %d\n", numBf);
*/

       lastBfTyp = iBfTyp;          /* save last buffer type */

       /* Get buffer type from header information */
       iBfTyp = buffer[1];
       if( iBfTyp<0 ) iBfTyp = (-iBfTyp);


       if( iBfTyp == FE_K_DATA ) {          /* Event buffer */
           nBfWds = buffer[0];                    /* get # words in this buffer */
           j = 32;                          /* move ptr past 32 wd hdr */
           nBfWds -= 32;                    /* subtr 32 wd hdr from */
                                            /*  remaining nBfWds */

           while( nBfWds > 0 ) {

/*             printf("\tpointing to FFFF at j = %d\n", j);
*/
               j++;                         /* move past FFFF */
               nBfWds--;

               while( (buffer[j] != -1) && (nBfWds > 0) ) {

                   goodEvt = 0;

                    if( (*(buffer+j) & vsnMask ) == 0x002D ) {

                        wc = ( buffer[j] >> 11 ) & wcMask;
                        wcTR = ( wc ) ? wc : 16;
```

```
                /*printf("wcTR = %d (%x)\n", wcTR, buffer[j]);
                fflush(stdout);*/
                        evsiz = 1 + wcTR;

                        if( (*(buffer+j+evsiz) & vsnMask ) == 0x002E ) {

                            wc = ( buffer[j + evsiz] >> 11) & wcMask;
                            wcTL = ( wc ) ? wc : 16;
                    /*printf("wcTL = %d (%x)\n", wcTL, buffer[j+evsiz]);
                    fflush(stdout);*/
                            evsiz += 1 + wcTL;

                            if( (*(buffer+j+evsiz) & vsnMask ) == 0x0033 ) {

                                wc = ( buffer[j + evsiz] >> 11) & wcMask;
                                wcER = ( wc ) ? wc : 16;
                    /*printf("wcER = %d (%x)\n", wcER, buffer[j+evsiz]);
                    fflush(stdout);*/
                                evsiz += 1 + wcER;

                                if( (*(buffer+j+evsiz) & vsnMask ) == 0x0034 ) {

                                    wc = ( buffer[j + evsiz] >> 11 ) & wcMask;
                                    wcEL = ( wc ) ? wc : 16;
                    /*printf("wcEL = %d (%x)\n", wcEL, buffer[j+evsiz] );
                    fflush(stdout);*/
                                    evsiz += 1 + wcEL;

                                    if( (*(buffer+j+evsiz) == -1) ||
                                        ((nBfWds-evsiz) <= 0) )  {


/*
        printf("\t\tevent size = %d\n", evsiz);
        printf("\t\tnumber of words remaining in buffer = %d\n",(nBfWds-evsiz));
*/

                    goodEvt = 1;
                    numGoodEvts++;

/********************** Initialize event data to zero *****/

                    for( i=0; i<13; i++ ) {
                       rDet[i].time = 0;
                       lDet[i].time = 0;
                       rDet[i].energy = 0;
                       lDet[i].energy = 0;
                    }




/********************** Load event data and inc total hits ******/
                                        /* loop over 1st time FERA data */
                     for( i=0; i<wcTR; i++ ) {
                         j++;           /* move past 1st time FERA hdr */
                         nBfWds--;      /* then get next data word */

                         sa = ( *(buffer+j) >> 11 ) & saMask;
                         rDet[sa].time = ( *(buffer+j) & dataMask );
                     }
                     j++;               /* move to 2nd time FERA hdr */
                     nBfWds--;
```

```
                                /* loop over 2nd time FERA data */
                for( i=0; i<wcTL; i++ ) {
                    j++;            /* move past 2nd time FERA hdr */
                    nBfWds--;

                    sa = ( *(buffer+j) >> 11 ) & saMask;
                    lDet[sa].time = ( *(buffer+j) & dataMask );
                }
                j++;                /* move to 1st energy FERA hdr */
                nBfWds--;

                                /* loop over 1st energy FERA data */
                for( i=0; i<wcER; i++ ) {
                    j++;            /* move past 1st energy FERA hdr */
                    nBfWds--;

                    sa = ( *(buffer+j) >> 11 ) & saMask;
                    if( sa == 12 ) sa = 4;  /* Bad FERA channel */
                    rDet[sa].energy = ( *(buffer+j) & dataMask );
                }
                j++;                /* move to 2nd energy FERA hdr */
                nBfWds--;

                                /* loop over 2nd energy FERA data */
                for( i=0; i<wcEL; i++ ) {
                    j++;            /* move past 2nd energy FERA hdr */
                    nBfWds--;

                    sa = ( *(buffer+j) >> 11 ) & saMask;
                    lDet[sa].energy = ( *(buffer+j) & dataMask );
                }
                j++;                /* move to next 0xFFFF hdr */
                nBfWds--;


/****************** Inc time stamp spectra *************/

                if( lDet[12].energy ) {
                    lBank[12].energy[ (lDet[12].energy) ]++;
                }


/****************** Analyze Event **********************/

              AnalyzeEvent( rDet, lDet, rEnergy, lEnergy,
                        rBank, lBank, timeDiff, rTConv, lTConv,
                        rNum511, lNum511, hitPat, bufHitPat,
                        coinc, &numBfEvts, &rCoinDet, &lCoinDet,
                        &offset );



                            }  /* end of -1 if */
                        }      /* end of vsn = 52 if */
                    }          /* end of vsn = 51 if */
                }      /* end of vsn = 46 if */
            }          /* end of vsn = 45 if */

            if( !goodEvt ) {
               while( (buffer[j] != -1)  && (nBfWds > 0) ) {
                    j++;
                    nBfWds--;
```

```
                }
            }


        }             /* end of WHILE loop over events */
    }          /* end of while loop over useful data */
}              /* end of DATA if */


if( iBfTyp == FE_K_SCALER ) {

    endTimeLowWd = buffer[(0+16)];
    endTimeHighWd = buffer[(1+16)];
    startTimeLowWd = buffer[(5+16)];
    startTimeHighWd = buffer[(6+16)];

    bufEndTime = (endTimeHighWd << 16) + endTimeLowWd;
    bufStartTime = (startTimeHighWd << 16) + startTimeLowWd;

}


/********** Record total good events per buffer(i.e. time) *********/

if( (lastBfTyp == 1) && (iBfTyp == 2)
    /* (rCoinDet != 99) && (lCoinDet != 99) */  )  {

    hitDist[ (bufEndTime/DAQPeriod) - 1 ] = numBfEvts;

    if( incSysMat >= 1 ) {

        /*** Increment System Matrix from buffer hit pattern *****/
        /***  Incrementing starts in lower right corner and  *****/
        /***  and works diagonally to upper left corner.     *****/

        i = 23;
        while(         (bufStartTime >= timeCuts[i]) && (i>0) ) i--;

        if( (i == 23) && (bufEndTime > timeCuts[23]) )  {
            timeFrac1 = ((double)(bufEndTime) - (double)(timeCuts[i])) /
                        (double)(DAQPeriod);
            for( j=0; j<23; j++ ) {
                tempSysMatrix[j][i-1] += (long)
                    (floor(((double)(bufHitPat[j])) * timeFrac1 +0.5) );
            }
        }

        if( (bufEndTime >= timeCuts[i]) && ( i != 0 ) && ( i != 23 )  ) {

            timeFrac1 = ((double)(bufEndTime) - (double)(timeCuts[i])) /
                        (double)(DAQPeriod);
            timeFrac2 = ((double)(timeCuts[i])-(double)(bufStartTime)) /
                        (double)(DAQPeriod);
            for( j=0; j<23; j++ ) {
                tempSysMatrix[j][i] += (long)
                    (floor(((double)(bufHitPat[j]) * timeFrac2 +0.5)));
                tempSysMatrix[j][(i-1)] += (long)
                    (floor(((double)(bufHitPat[j]) *timeFrac1 +0.5)));
            }
        }

        if( (bufEndTime <= timeCuts[i]) && ( i != 0 ) && ( i != 23 )  ) {
            for( j=0; j<23; j++ ) tempSysMatrix[j][i] += bufHitPat[j];
```

```
            }

              if( (i == 0) && (bufStartTime < timeCuts[0]) &&
                              (bufEndTime >= timeCuts[0]) )    {
                  timeFrac2 = ((double)(timeCuts[i]) -
                              (double)(bufStartTime)) / (double)(DAQPeriod);
                  for( j=0; j<23; j++ ) {
                      tempSysMatrix[j][i] += (long)
                          (floor(((double)(bufHitPat[j]) * timeFrac2 +0.5)));
                  }
            }

              if( (i == 0) && (bufStartTime < timeCuts[0]) &&
                           (bufEndTime < timeCuts[0])   ) {
                  for( j=0; j<23; j++ ) tempSysMatrix[j][i] += bufHitPat[j];
              }



        }          /* end if incSysMat */
    }



    if( (lastBfTyp != 1) && (iBfTyp == 2)
        /* (rCoinDet != 99) && (lCoinDet != 99) */  )  {

        hitDist[ (bufEndTime/DAQPeriod) - 1 ] = 0;
    }


/**** Zero variables if current buffer is not a physics buffer **********/

    if( iBfTyp != 1 )  {
        numBfEvts = 0;

        for( i=0; i<23; i++ )  {
           bufHitPat[i] = 0;
        }
    }



/*************** Read in next Buffer ************************/

#ifdef Online
                                        /* give pointer back to router */
     if( source == router ) ReleaseBuffer(notification);
#endif Online

     ReadBuffer( &source, &fptr, &eof, &buffer, &ichan,
                notification,&numBf );
     numBf++;

#ifdef unix
     SwapBytes( &buffer );
#endif unix


     if(  eof ||
         (abs(buffer[1]) == FE_K_STOP) ||
         (abs(buffer[1]) == ID_K_HALT)    ) endOfRun = 1;
```

```
    }                /* end of file while loop */


    if( incSysMat == 0 )  {

       CalcTimeCuts( DAQPeriod, runNum, hitDist, timeCuts, scalBf,
                     lengthOfRun );

#ifdef unix
       if( source = tape ) {
           printf("rewinding tape\n" );
           /***** Go to end of tape and rewind ******/
           OpenIO( &source, &fptr, &fPtrOut, &buffer, &ichan, notification,
                  incSysMat);
           /***** Find file and open again *********/
            OpenIO( &source, &fptr, &fPtrOut, &buffer, &ichan, notification,
                   incSysMat);
       }
#endif unix


    }


    if( incSysMat >= 1 )  {

       SymmetryCorrection( &incSysMat, DAQPeriod, runNum, tempSysMatrix,
                           timeCuts );

#ifdef unix
        if( source = tape ) {
            printf("rewinding tape\n" );
            /***** Go to end of tape and rewind ******/
            OpenIO( &source, &fptr, &fPtrOut, &buffer, &ichan, notification,
                   incSysMat);
            /***** Find file and open again *********/
            OpenIO( &source, &fptr, &fPtrOut, &buffer, &ichan, notification,
                   incSysMat);
        }
#endif unix


    }

}       /* end of for loop controlling passes over data file */

printf("\t...Done\n");

/*************** Add existing and new system matrices ****************/

    for( i=0; i<23; i++ ) {
       for( j=0; j<23; j++ ) {
           SysMatrix[i][j] += tempSysMatrix[i][j];
       }
    }


/*************** Write System Matrix to file *************/

    WriteSysMatrix( SysMatrix, &runNum, &fPtrMat, fileNameMat );
```

```
/****************** print hit pattern array to file ****************/

    printf("\n");
    printf("Writing hit pattern to file\n");

    fprintf(fPtrOut,"\n");
    fprintf(fPtrOut,"\tHit Pattern\n\n");
    fprintf(fPtrOut,"Position Index\tHit Count\n" );
    fprintf(fPtrOut,"-------------------------\n" );
    for( i=0; i<23; i++ ) {
        fprintf(fPtrOut,"       %2d \t%6d\n", i, hitPat[i] );
    }



/****************** print number of timing hits in each detector to file *****/
/*
    fprintf(fPtrOut,"\n\n");
    fprintf(fPtrOut,"\tNumber of timing hits in each detector\n\n");
    fprintf(fPtrOut,"Right Bank\t\tLeft Bank\n");
    for( i=0; i<13; i++ ) {
       fprintf(fPtrOut,"%d\t%d\t\t%d\t%d\n",(i+1),rBank[i].tHits,
              lBank[i].tHits,(i+13));
    }
    fprintf(fPtrOut,"\t%d\t\t%d\ttime stamp\n",rBank[12].tHits, lBank[12].tHits);
*/


/****************** print number of energy hits in each detector to file *****/
/*
    fprintf(fPtrOut,"\n\n");
    fprintf(fPtrOut,"\tNumber of energy hits in each detector\n\n");
    fprintf(fPtrOut,"Right Bank\t\tLeft Bank\n");
    for( i=0; i<12; i++ ) {
       fprintf(fPtrOut,"%d\t%d\t\t%d\t%d\n",(i+1),rBank[i].eHits,
              lBank[i].eHits,(i+13));
    }
    fprintf(fPtrOut,"13\t\t\t%d\ttime stamp(25)\n", lBank[12].eHits);
*/

/* print number of hits in each detector with time and energy words to file */
/*
    fprintf(fPtrOut,"\n\n");
    fprintf(fPtrOut,"\tNumber of Hits in Detectors with Time and Energy Words\n\n");
    fprintf(fPtrOut,"Right Bank\t\tLeft Bank\n");
    for( i=0; i<12; i++ ) {
        fprintf(fPtrOut,"%d\t%d\t\t%d\t%d\n",(i+1),rBank[i].teHits,
               lBank[i].teHits,(i+13));
    }
*/


/********************* Print energy spectra *********************/
/*
    fprintf(fPtrOut,"\n");
    fprintf(fPtrOut,"\tEnergy Spectra - Right Detectors\n");
    for( i=0; i<2048; i++ ) {
        fprintf(fPtrOut,"%d\t", i );
        for( j=0; j<13; j++ ) {
            fprintf(fPtrOut,"%d\t",  rBank[j].energy[i]);
```

```
        }
        fprintf(fPtrOut,"\n");
    }

    fprintf(fPtrOut,"\tEnergy and time Stamp Spectra - Left Detectors\n");
    for( i=0; i<2048; i++ ) {
        fprintf(fPtrOut,"%d\t", i );
        for( j=0; j<13; j++ ) {
            fprintf(fPtrOut,"%d\t",  lBank[j].energy[i]);
        }
        fprintf(fPtrOut,"\n");
    }
*/


/************** Print Decay data to file ****************/

printf("Writing hit distribution to file\n");

    fprintf(fPtrOut,"\n\n");
    fprintf(fPtrOut,"\tNumber of Coincidences per DAQ Period\n\n");
    fprintf(fPtrOut,"End Time    Total\n");
    fprintf(fPtrOut,"(0.1 sec)   Counts \n");
    fprintf(fPtrOut,"-----------------\n");

    for( i=0; i<scalBf; i++ ) {
       fprintf(fPtrOut,"  %4d       %4d \n", i, hitDist[i] );
    }


/************** print histogram of # of 511's in event to file *****/

printf("Writing 511 stats to file\n");


    fprintf(fPtrOut,"\n\n");
    fprintf(fPtrOut,"\tNumber of 511's per bank in an event\n\n");
    fprintf(fPtrOut,"Num 511\t Right\t Left\n");
    for( i=0; i<12; i++ ) {
       fprintf(fPtrOut,"  %2d\t%7d\t%7d\n",i,rNum511[i],lNum511[i] );
    }


/******************* print number of good events **************/

    fprintf(fPtrOut,"\n\n");
    fprintf(fPtrOut,"%7d = Number of Events with Proper Format\n", numGoodEvts);

    numCoinc = 0;
    for( i=0; i<23; i++ ) numCoinc += hitPat[i];
    fprintf(fPtrOut,"%7d = Number of 511 Coincidences\n", numCoinc );


/************** print cut time difference array sums to file *************/

printf("Writing cut time differences to file\n");


    fprintf(fPtrOut,"\n\n");
    fprintf(fPtrOut,"\t\t\tTime Difference Array Sums After Timing Cuts\n\n");
    fprintf(fPtrOut,"\t\t\t      Left Detector\n");
    fprintf(fPtrOut,"     ");
    for( i=0; i<12; i++ )  fprintf(fPtrOut,"%5d ", i);
    fprintf(fPtrOut,"\n");
```

```
    fprintf(fPtrOut,"    ");
    for( i=0; i<12; i++ )  fprintf(fPtrOut,"------");
    fprintf(fPtrOut,"\n");

    for( i=0; i<12; i++ ) {
       fprintf(fPtrOut,"%5d ", i);
       for( j=0; j<12; j++ ) {
           fprintf(fPtrOut,"%5d ", coinc[i][j].cutSum );
       }
       fprintf(fPtrOut,"\n");
    }


/**** Print Coinc Timing Backgrnd, Lower, Peak, Upper, Max, & Num Hits ******/

printf("Writing coinc timing info to file\n");


    fprintf(fPtrOut,"\n\n");
    fprintf(fPtrOut,"\tCoincidence Timing Information\n");
    fprintf(fPtrOut,"Right\tLeft\tBackGnd\tLower\tPeak\tUpper\t Max\t# Hits\n");

    for( i=0; i<12; i++ ) {
        for( j=0; j<12; j++ ) {
            fprintf(fPtrOut,"%3d\t%3d\t  %3d\t %3d\t%3d\t %3d\t%4d\t %5d\n",
                i, j, coinc[i][j].backGrnd, coinc[i][j].tLower,
                coinc[i][j].tPeak, coinc[i][j].tUpper,
                coinc[i][j].tMax, coinc[i][j].rawSum );
        }
    }



/************** print time difference spectra to file *****/
/*
    fprintf(fPtrOut,"\n\n");
    fprintf(fPtrOut,"\tTime Difference + offset\n\n");
    fprintf(fPtrOut,"index\tR%1dL%1d\tR%1dL%1d\tR%1dL%1d\n", 7,8,8,7,11,3);
    for( i=0; i<1000; i++ ) {
       fprintf(fPtrOut,"%4d\t%4d\t%4d\t%4d\n", i, timeDiff[7][8][i],
                     timeDiff[8][7][i],timeDiff[11][3][i]);
    }
*/


CloseIO( &source, &fptr, &fPtrOut, notification );

}




LoadSysMatrix( long SysMatrix[23][23], FILE **fPtrMat, char fileNameMat[] )
{
/*
    char filename[255];
*/
    char temp_string[80];
```

```
    int fileExists;
    int i, j;
    int temp_int;
    int pos;


/*************** Open System Matrix File **************/


    printf("\n");
printf("Name of file containing system matrix to be augmented or created?\n");
printf("WARNING - Don't enter a file that contains a matrix you don't want altered.");
    printf("\n?");
    scanf("%s", fileNameMat);


    *fPtrMat = fopen( (char*)fileNameMat, "r" );

    fileExists = ( *fPtrMat == NULL ) ? 0 : 1;

    if( fileExists )  {
       printf("Opening %s.\n", fileNameMat );
    }else{
/*
       *fPtrMat = fopen( (char*)fileNameMat, "w" );
       if( *fPtrMat == NULL )  {
           printf("ERROR CREATING NEW FILE!\n");
       }else{
            printf("%s created.\n", fileNameMat );
       }
*/
    }
/*
printf("fPtrMat = %d\n", *fPtrMat );
*/


    if( fileExists )  {

       /************* Read first text line and discard ******************/

       fgets ( temp_string, 80, *fPtrMat );
       fscanf(*fPtrMat,"%d", &temp_int );
       fgets ( temp_string, 80, *fPtrMat );
       printf( "%d   Last Run Number\n", temp_int);

       /************* Read in Matrix if there is one in the file *********/

       printf( "\nLoading System Matrix\n" );
       for( i=0; i<23; i++ )  {
           for( j=0; j<23; j++ )  {
                fscanf(*fPtrMat,"%d", &temp_int );
              SysMatrix[i][j] = temp_int;
              printf( " %3d", SysMatrix[i][j] );
           }
           printf( "\n" );
              }

       fclose(*fPtrMat);

    } else {

       /*************  Initialize System Matrix  ******************/
```

```
        printf( "Initializing System Matrix\n" );
        for( i=0; i<23; i++ )  {
            for( j=0; j<23; j++ )  {
               SysMatrix[i][j] = 0;
            }
               }
    }


/*
    if( fileExists )  {
       pos = fseek(*fPtrMat, 0, 0 );
       printf("file pointer position = %d\n", pos );
    }
*/                              /* move 0 bytes from, beginning */

/*** System matrix file is closed in WriteSysMatrix subroutine ***/

}




WriteSysMatrix( long SysMatrix[23][23], short *runNum, FILE **fPtrMat,
                char fileNameMat[] )
{
/*
    char filename[255];
*/
    char header[] = "Detector Pair (Down)   SYSTEM MATRIX (23x23)     Position -->";
    char temp_string[80];

    int i, j;
    int temp_int;

/*
printf("fPtrMat = %d\n", *fPtrMat );
*/

/*************** Open System Matrix file **************/
/*
    strcpy( fileNameMat, "SysMat45_51.dat" );
*/
    *fPtrMat = fopen( (char*)fileNameMat, "w" );
    if( (*fPtrMat) == NULL ) printf( "ERROR OPENING SYSTEM MATRIX FILE" );

/************* Write header to file ******************/

    fputs( header, *fPtrMat );
    fputs( "\n", *fPtrMat );
    fprintf( *fPtrMat, "%d   Latest Run Number\n", (*runNum) );

/************* Write System Matrix to file *****************/

    printf("\n");
    printf( "Writing System Matrix\n" );
    for( i=0; i<23; i++ )  {
        for( j=0; j<23; j++ )  {
            fprintf( *fPtrMat, " %5d", SysMatrix[i][j] );
           printf( " %5d", SysMatrix[i][j] );
       }
       fprintf( *fPtrMat, "\n" );
       printf( "\n" );
```

```
    }

/*************** Write row sums of system matrix to file ***************/

    printf("\n");
    printf("Row sums of System Matrix\n" );
    fprintf( *fPtrMat, "\n" );
    fprintf( *fPtrMat, "Row sums of System Matrix\n" );
    for( i=0; i<23; i++ )  {
        temp_int = 0;
        for( j=0; j<23; j++ ) temp_int += SysMatrix[i][j];
        fprintf( *fPtrMat, " %5d\n", temp_int );
        printf( " %5d\n", temp_int );
    }


    fclose(*fPtrMat);

}




LoadCal( typeEnergyData rEnergy[12], typeEnergyData lEnergy[12],
       typeTimeData coinc[12][12], long *lengthOfRun, short *DAQPeriod,
       short *offset )
{

    char filename[255];
    char temp_string[80];

    int i, j, k;
    int temp_int;

    float enRes;                    /* Energy Resolution */
    float timeRes;                  /* % height of the coincidence timing */
                                    /* peak to make cuts between */

    FILE *fPtr;


/*************** get and open calibration file **************/

    printf("\n");
    printf("Name of calibration file? (run##.cal) ");
    scanf("%s",filename);
    fPtr = fopen( (char*)filename, "r" );


/****** Read first text lines and discard ******/

    for( i=0; i<3; i++ ) fgets (temp_string, 80, fPtr);


/*** Read in det #, peak, and max for detectors in right bank ***/

    for( i=0; i<12; i++) {
        fscanf(fPtr,"%d%d%d", &temp_int, &rEnergy[i].peak, &rEnergy[i].max);
    }


/***** Read text lines and discard ******/
```

```
    for( i=0; i<4; i++ ) fgets (temp_string, 80, fPtr);


/*** Read in det #, peak, and max for detectors in left bank ***/

    for( i=0; i<12; i++) {
        fscanf(fPtr,"%d%d%d", &temp_int, &lEnergy[i].peak, &lEnergy[i].max);
    }


/*************** Print channel #, and max to screen ************/

    printf("\n\n");
    printf("\t\t\tEnergy Calibrations\n");
    printf("Det #    Peak\t   Max\t\t   Max\t  Peak  Det #\n");
    for( i=0; i<12; i++ ) {
       printf("%3d\t %4d\t%6d\t\t%6d\t  %4d\t  %2d\n", i, rEnergy[i].peak,
              rEnergy[i].max, lEnergy[i].max, lEnergy[i].peak, (i+12) );
    }



/************** Get Energy Resolution *****************/


    printf("\n");
    printf("Enter the Energy Resolution (.20): ");


    scanf("%f", &enRes);


/************* Calculate Upper and Lower Energy Cuts *************/

    for( i=0; i<12; i++ ) {
       rEnergy[i].lower = (short)( floor(rEnergy[i].peak * (1.0 - enRes)) );
       rEnergy[i].upper = (short)( floor(rEnergy[i].peak * (1.0 + enRes)) );

       lEnergy[i].lower = (short)( floor(lEnergy[i].peak * (1.0 - enRes)) );
       lEnergy[i].upper = (short)( floor(lEnergy[i].peak * (1.0 + enRes)) );
    }


/*************** Print energy cuts to screen ************/

    printf("\n\n");
    printf("\t\t\tEnergy Cuts\n");
    printf("Det #    Lower\t Peak\tUpper\tUpper\tPeak\tLower    Det #\n");
    for( i=0; i<12; i++ ) {
        printf("%3d\t %4d\t%4d\t%4d\t%4d\t%4d\t%4d\t  %2d\n",
              i, rEnergy[i].lower, rEnergy[i].peak, rEnergy[i].upper,
              lEnergy[i].upper, lEnergy[i].peak, lEnergy[i].lower, (i+12) );
    }


/***** Read text lines and discard ******/

    for( i=0; i<2; i++ ) fgets (temp_string, 80, fPtr);


/*********** Read in Length of Run *************/

    fscanf(fPtr,"%d", lengthOfRun );
```

```
/***** Read text lines and discard ******/

    for( i=0; i<4; i++ ) fgets (temp_string, 80, fPtr);


/*********** Read in DAQPeriod *************/

    fscanf(fPtr,"%d", DAQPeriod );


/***** Read text lines and discard ******/

    for( i=0; i<3; i++ ) fgets (temp_string, 80, fPtr);


/*********** Read in offset *************/

    fscanf(fPtr,"%d", offset );


/***** Read text lines and discard ******/

    for( i=0; i<4; i++ ) fgets (temp_string, 80, fPtr);


/******************** Read Coincidence Timing data ********************/


    printf("\n\n");
    printf("\tCoincidence Timing Information\n");
    printf("Right\tLeft\tBackGnd\tLower\tPeak\tUpper\t Max\t# Hits\n");

    for( i=0; i<12; i++ ) {
       for( j=0; j<12; j++ ) {


                    /* Can't put all these in one statement because
                       coinc[i][j].tLower and coinc[i][j].tUpper
                       get zeroed 2 fscanf's after being read.
                       Seems to be a glitch in fscanf or Mem. Man. */
            fscanf(fPtr,"%d", &temp_int );
            fscanf(fPtr,"%d", &temp_int );
            fscanf(fPtr,"%d", &coinc[i][j].backGrnd );
            fscanf(fPtr,"%d", &temp_int );
              coinc[i][j].tLower = temp_int;
            fscanf(fPtr,"%d", &coinc[i][j].tPeak );
            fscanf(fPtr,"%d", &temp_int );
            fscanf(fPtr,"%d", &coinc[i][j].tMax );
            fscanf(fPtr,"%d", &coinc[i][j].rawSum );
              coinc[i][j].tUpper = temp_int;


                    printf("%d\t%d\t%d\t%d\t%d\t%d\t%d\t%d\n", i, j,
                      coinc[i][j].backGrnd, coinc[i][j].tLower,
                      coinc[i][j].tPeak, coinc[i][j].tUpper,
                      coinc[i][j].tMax, coinc[i][j].rawSum );

       }
    }


/************** print coincidence raw sums to screen *************/
```

```
    printf("\n\n");
    printf("\t\t\tRaw Timing Coincidence Sums\n\n");
    printf("\t\t\t      Left Detector\n");
    printf("    ");
    for( i=0; i<12; i++ )  printf("%5d ", i);
    printf("\n");

    printf("    ");
    for( i=0; i<12; i++ )  printf("------");
    printf("\n");

    for( i=0; i<12; i++ ) {
       printf("%5d ", i);
       for( j=0; j<12; j++ ) {
           printf("%5d ", coinc[i][j].rawSum);
       }
       printf("\n");
    }



    fclose(fPtr);

}



AnalyzeEvent( typeEventData rDet[13], typeEventData lDet[13],
                typeEnergyData rEnergy[12], typeEnergyData lEnergy[12],
                typeDetectorData rBank[13], typeDetectorData lBank[13],
                long timeDiff[12][12][1000], float rTConv[12][2],
                float lTConv[12][2], long rNum511[12], long lNum511[12],
                long hitPat[23], long bufHitPat[23],
                typeTimeData coinc[12][12], long *numBfEvts,
                short *rCoinDet, short *lCoinDet, short *offset )
{

    short i, j, k;          /* counter */
    short rNumHits;         /* # dets in right bank with time & 511 */
    short lNumHits;
    short rEvent[12];               /* list of det # which were hit */
    short lEvent[12];
    short deltaT;
    short minDeltaT;


    lNumHits = 0;
    rNumHits = 0;


    for( i=0; i<12; i++ ) {
       rEvent[i] = 0;
       lEvent[i] = 0;
    }


/*************** Pick out Detectors With 511's and Time **************/
/*
if( lDet[9].time && lDet[9].energy && rDet[4].time && rDet[4].energy ){
        printf("\n");
        printf("\t%d  %d  %d    %d  %d  %d\n",
                lEnergy[9].lower,lDet[9].energy,lEnergy[9].upper,
                rEnergy[4].upper,rDet[4].energy,rEnergy[4].lower);
```

```
        printf("\t%d   %d   %d   %d   %d\n",lDet[9].time,coinc[4][9].tLower,
                (lDet[9].time-rDet[4].time+500),coinc[4][9].tUpper,
                rDet[4].time);

}
*/

    for( i=0; i<12; i++ ) {
       if( lDet[i].time && lDet[i].energy ) {
           if( (lDet[i].energy > lEnergy[i].lower) &&
              (lDet[i].energy < lEnergy[i].upper)    )  {

              lEvent[lNumHits] = i;
              lNumHits++;

           }
       }
    }


    for( i=0; i<12; i++ ) {
       if( rDet[i].time && rDet[i].energy ) {
           if( (rDet[i].energy > rEnergy[i].lower) &&
              (rDet[i].energy < rEnergy[i].upper)    )  {

              rEvent[rNumHits] = i;
              rNumHits++;
           }
       }
    }

    rNum511[rNumHits]++;
    lNum511[lNumHits]++;

/*     printf("rNumHits = %d,  lNumHits = %d\n", rNumHits,lNumHits);
*/

/****************** Compare Time ******************/


    minDeltaT = 9999;
    *rCoinDet = 99;
    *lCoinDet = 99;


    for( i=0; i<rNumHits; i++ ) {
       for( j=0; j<lNumHits; j++ ) {

           deltaT = ( rDet[(rEvent[i])].time - lDet[(lEvent[j])].time );


            if( (abs(deltaT)) < abs(minDeltaT) ) {
               minDeltaT = deltaT;
              *rCoinDet = rEvent[i];
              *lCoinDet = lEvent[j];

           }
       }
    }

/*
printf("right detector = %d,  left detector = %d\n", *rCoinDet, *lCoinDet );
printf("\tright time = %d, left time = %d, minDeltaT = %d\n",
       rDet[(*rCoinDet)].time,lDet[(*lCoinDet)].time, minDeltaT );
```

```
*/

    if( (minDeltaT != 9999 ) &&
       ( (minDeltaT + (*offset)) >= coinc[(*rCoinDet)][(*lCoinDet)].tLower) &&
       ( (minDeltaT + (*offset)) <= coinc[(*rCoinDet)][(*lCoinDet)].tUpper) ) {

/*    printf("%d\t%d\t%d\n", *rCoinDet, *lCoinDet, minDeltaT );
*/
        if( (minDeltaT + (*offset)) > 999 )
              timeDiff[(*rCoinDet)][(*lCoinDet)][999]++;

        if( (minDeltaT + (*offset)) < 0 ) timeDiff[(*rCoinDet)][(*lCoinDet)][0]++;

        if( ((minDeltaT + (*offset)) >= 0) && ((minDeltaT + (*offset)) <= 999) ) {
           timeDiff[(*rCoinDet)][(*lCoinDet)][(minDeltaT+(*offset))]++;
        }


    }



    if( ((minDeltaT + (*offset)) >= coinc[(*rCoinDet)][(*lCoinDet)].tLower) &&
       ((minDeltaT + (*offset)) <= coinc[(*rCoinDet)][(*lCoinDet)].tUpper) &&
       (rDet[(*rCoinDet)].energy > rEnergy[(*rCoinDet)].lower) &&
       (rDet[(*rCoinDet)].energy < rEnergy[(*rCoinDet)].upper) &&
       (lDet[(*lCoinDet)].energy > lEnergy[(*lCoinDet)].lower) &&
       (lDet[(*lCoinDet)].energy < lEnergy[(*lCoinDet)].upper)    ) {


       coinc[(*rCoinDet)][(*lCoinDet)].cutSum++;  /* increment array sum */

       rBank[(*rCoinDet)].time[ (rDet[(*rCoinDet)].time) ]++;
       rBank[(*rCoinDet)].energy[ (rDet[(*rCoinDet)].energy) ]++;
        rBank[(*rCoinDet)].teHits++;

       lBank[(*lCoinDet)].time[ (lDet[(*lCoinDet)].time) ]++;
       lBank[(*lCoinDet)].energy[ (lDet[(*lCoinDet)].energy) ]++;
        lBank[(*lCoinDet)].teHits++;

       hitPat[ ((*rCoinDet) + (*lCoinDet)) ]++;
       bufHitPat[ ((*rCoinDet) + (*lCoinDet)) ]++;
       (*numBfEvts)++;

    }
}




CalcTimeCuts( short DAQPeriod, short runNum,
       long hitDist[], long timeCuts[], short scalBf, long lengthOfRun )
{

    short      cars;          /* number of values used for summing       */
                              /*  on either side of a given value in     */
                              /*  Box car summing algorithm              */
    short      arrayCenter;   /* Center of array by maximum weight       */
    short      arrayCenterTC;       /* Center of array by min weight timecuts */
    short      peakQuartWidth;      /* number of dumps in one quarter of a  */
                              /*  peak width                             */
```

```
    register short i, j;
    register long weight, weight1;
    register short train;

    long       maxWeight;     /* used for finding center of array */
    long       minWeight;     /* used for finding optimum time cuts       */

    float      motorRPM;      /* RPM of calibration motor */
    float      numDetPairs;   /* number of detector pairs */
    float      numDpsInAry;   /* number of times scalers are dumped while */
                              /* calibration source is between detectors  */
    float      peakTimeWidth;       /* Width of hit distribution efficiency peak */
                              /*  in tenths of seconds                  */
    float       arrayTimeWidth; /* Width of array hit distribution           */
                                /*  in tenths of a second                    */


    FILE       *fPtrOut3;

    char        fileNameOut3[255];      /* output file name for smoothed HD */
    char       waveName[255];              /* name of hit distribution used in */
                                 /*  IGOR                                */

    motorRPM = ( runNum <= 23 ) ? 2.0 : 1.0;
    numDetPairs = ( /*!runNum*/ (6 <= runNum) && (runNum <= 24)  ) ? 11 : 12;
    peakTimeWidth = 0.95 / 2                        /* peak width in inches */
                  * 8                               /* revolutions/inch */
                  / motorRPM * 60                   /* seconds/revolution */
                  * 10;                             /* tenths of seconds */

    arrayTimeWidth = 11.2                          /* array width in inches */
                  * 8                              /* revolutions/inch */
                  / motorRPM * 60                  /* seconds/revolution */
                  * 10;                            /* tenths of seconds */

    peakQuartWidth = (short) ( floor(
                   0.95 / 2                      /* peak width in inches */
                  / 4                               /* divided by 4              */
                   * 8                             /* revolutions/inch     */
                   / motorRPM * 60                 /* seconds/revolution   */
                   * 10                            /* tenths of seconds    */
                  / DAQPeriod ) );          /* dumps/tenths of sec  */

printf("\tpeakQuartWidth = %d\n", peakQuartWidth);


    cars = (short)( floor( arrayTimeWidth/DAQPeriod / 2 ) + 2 );


    weight = 0;                                 /* sum of cars in train      */
    maxWeight = 0;
    train = 2*cars + 1;


                    /* get and open file */
    printf("\tName of file for array center? (r##sm.hd) ");
    scanf( "%s", fileNameOut3 );
    fPtrOut3 = fopen( (char*)fileNameOut3, "w" );
    if( fPtrOut3 == NULL ) printf("ERROR OPENING FILE\n");

    i = 0;
    while( (fileNameOut3[i] != '.') && (i<strlen(fileNameOut3)) ) {
        waveName[i] = fileNameOut3[i];
        i++;
```

```
    }
    waveName[i] = '\0';
    strcat( waveName, "hd" );


        fprintf( fPtrOut3, "Number of Cars = %d\n\n", cars );
       fprintf( fPtrOut3, "%s\tweight\tmaxWeight\n", waveName );


       /************** Weight(sum) of first, cars+1, data points  ********/

       for( i=0; i<cars; i++ ) weight += hitDist[i];
       for( i=0; i<=cars; i++ )  {
           weight += hitDist[(i+cars)];
           if( weight > maxWeight )  {
              arrayCenter = i;
              maxWeight = weight;
           }
           fprintf( fPtrOut3, "%d\t%d\t%d\n", hitDist[i], weight, maxWeight );
       }


       /************** Weight of Intermediate data points  **************/

       for( i=(cars+1); i<=(scalBf-cars); i++ )  {
           weight = weight - hitDist[ (i-(cars+1)) ] + hitDist[ (i+cars) ] ;
            if( weight > maxWeight )  {
              arrayCenter = i;
              maxWeight = weight;
           }
           fprintf( fPtrOut3, "%d\t%d\t%d\n", hitDist[i], weight, maxWeight );
       }


       /************** Weight of last, cars+1, data points *************/

       for( i=(scalBf-cars+1); i<scalBf; i++ )  {
           weight -= hitDist[ (i-(cars+1)) ];
            if( weight > maxWeight )  {
              arrayCenter = i;
              maxWeight = weight;
           }
           fprintf( fPtrOut3, "%d\t%d\t%d\n", hitDist[i], weight, maxWeight );
       }



       fprintf( fPtrOut3, "Center of Array = %d (by weight)\n", arrayCenter );



/************** Calculate timecuts from center *******************/

/* Assume arrayCenter is at the center of the array and work outward    */
/*  from center to assign timecuts on either side of efficiency peaks.  */
/*  Each peak is half the distance between detector centers.            */
/*                                                                      */
/* Because detectors 0/11 and 12/23 only have neighboring detectors     */
/*  on one side the first and last time cuts are in slightly different  */
/*  locations.  Instead of being at the center of the axis segment      */
/*  common to adjacent detector pairs, it is located at the beginning   */
/*  or end of the array.
/* timeCuts[0] is located at the beginning of the detector array        */
```

```
/*  on the upbeam side of detector pair 0/12 (1/13).  Since the          */
/*  calibration source is started at the other end of the array it       */
/*  is necessary to number the timeCuts backwards so that the first      */
/*  time cut is timeCuts[23].                                            */

/********* Calculate timecuts 0 - 11 to find timecut weight *********/

       minWeight = 1000000;
       arrayCenterTC = arrayCenter;

       if( peakQuartWidth != 0 )  {
       for( j=arrayCenter-peakQuartWidth; j<=arrayCenter+peakQuartWidth; j++) {
           weight = 0;
           for( i=11; i>=1; i-- )  {
               timeCuts[i] = (long)( floor( j * DAQPeriod +
                             (11-i+0.5) * peakTimeWidth ) );
              weight += hitDist[ (timeCuts[i]/DAQPeriod) ];
           }
            timeCuts[0] = (long)( floor( j * DAQPeriod +
                       0.5 * arrayTimeWidth ) );
            weight += hitDist[ (timeCuts[0]/DAQPeriod) ];

/********* Calculate timecuts 12 - 23 to find timecut weight *********/

            for( i=12; i<=22; i++ )  {
                timeCuts[i] = (long)( floor( j * DAQPeriod -
                              (i-12+0.5) * peakTimeWidth ) );
              weight += hitDist[ (timeCuts[i]/DAQPeriod) ];
            }
            timeCuts[23] = (long)( floor( j * DAQPeriod -
                       0.5 * arrayTimeWidth ) );
            weight += hitDist[ (timeCuts[23]/DAQPeriod) ];


           if( weight< minWeight ) {
              minWeight = weight;
              arrayCenterTC = j;
           }

       }
       }


        fprintf( fPtrOut3, "Center of Array = %d (by min TC weight)\n",
              arrayCenterTC );



/********* Calculate timeCuts bases on minimum timeCut weight *************/
/********* Calculate timecuts 0 - 11 to closest tenth of a second *********/

       for( i=11; i>=1; i-- )  {
           timeCuts[i] = (long)( floor( arrayCenterTC * DAQPeriod +
                             (11-i+0.5) * peakTimeWidth ) );
       }
        timeCuts[0] = (long)( floor( arrayCenterTC * DAQPeriod +
                       0.5 * arrayTimeWidth ) );
        weight += hitDist[ (timeCuts[0]/DAQPeriod) ];


/********* Calculate timecuts 12 - 23 to closest tenth of a second ********/

        for( i=12; i<=22; i++ )  {
            timeCuts[i] = (long)( floor( arrayCenterTC * DAQPeriod -
```

```
                                (i-12+0.5) * peakTimeWidth ) );
        }
        timeCuts[23] = (long)( floor( arrayCenterTC * DAQPeriod -
                        0.5 * arrayTimeWidth ) );
        weight += hitDist[ (timeCuts[23]/DAQPeriod) ];


/*********** Print timeCuts to file ***************/

        fprintf( fPtrOut3, "\n" );
        fprintf( fPtrOut3, "peakTimeWidth = %f\n", peakTimeWidth );
        fprintf( fPtrOut3, "TimeCuts\n" );
       for( i=23; i>=0; i-- )    fprintf( fPtrOut3, "%d\n", timeCuts[i] );



    fclose( fPtrOut3 );

}



SymmetryCorrection( short *incSysMat, short DAQPeriod, short runNum,
                    long tempSysMatrix[23][23], long timeCuts[] )
{

    short     i, j;          /* loop counter                              */
    short     errorSM10;     /* statistical counting error in     */
                             /*  tempSysMatrix[11][10]            */
    short     errorSM12;     /* statistical counting error in     */
                             /*  tempSysMatrix[11][12]            */
    long      peakTotal;     /* total counts in the 5 elements containing  */
                             /*  the central peak of the system matrix     */
    float     shiftTC;       /* Amount to shift timeCuts by as determined  */
                             /*  by Matrix Symmetry Correction         */
    float     motorRPM;      /* RPM of calibration motor                      */
    float     detWidth;      /* diameter of BGO in inches                     */
    float     peakWidth;     /* half of the distance between BGO centers   */


       motorRPM = ( runNum <= 23 ) ? 2.0 : 1.0;

       errorSM10 = (short)( sqrt((double)(tempSysMatrix[11][10])) );
       errorSM12 = (short)( sqrt((double)(tempSysMatrix[11][12])) );
       if( ( ((tempSysMatrix[11][10] + errorSM10) > tempSysMatrix[11][12]) &&
             ((tempSysMatrix[11][10] - errorSM10) < tempSysMatrix[11][12]) ) ||
           ( ((tempSysMatrix[11][12] + errorSM12) > tempSysMatrix[11][10]) &&
             ((tempSysMatrix[11][12] - errorSM12) < tempSysMatrix[11][10]) )   )  {

           *incSysMat = passes;/* elements on left and right of center   */
                               /* are equal within statistical error.    */
                               /* Increment incSysMat to prevent another */
                               /* iteration through the data.               */
           printf("\tSystem Matrix is symmetric about center using minimum time cuts
method.\n");

           printf("\t%d\t%d\t%d\n", tempSysMatrix[11][10],
                     tempSysMatrix[11][11], tempSysMatrix[11][12]);

       }else{

           printf("\tCalculating Symmetry Correction to System Matrix\n");
```

```
            shiftTC = 0.0;
            peakTotal = 0;
            for( i=9; i<14; i++ ) peakTotal += tempSysMatrix[11][i];
            detWidth = 0.75;          /* inches */
            peakWidth = 0.95 / 2;     /* inches */

            shiftTC = detWidth*detWidth *
                      (tempSysMatrix[11][10]-tempSysMatrix[11][12])/
                      (4*peakTotal * (peakWidth-detWidth) );      /* in inches */

                      /* See pages 58 - 68 in manual #5 for derivation      */
                      /*  of correctional shift for time cuts.         */
                      /* If tempSysMatrix[11][10](lower diag) < [11][12]    */
                      /* (upper diag) then shiftTC > 0.  Since calibration */
                      /* source goes through the array backwards, starting */
                      /* at detector pair 11/23, timeCuts[23] < timeCuts[0]*/
                      /* shiftTC must be subtracted to move the timecuts    */
                      /* toward the back of the detector array.        */


            shiftTC = (float)( floor(
                      shiftTC               /* shift in inches    */
                      * 8                   /* revolutions / inch        */
                      / motorRPM * 60             /* seconds / revolution */
                      * 10 ) );                   /* tenths of seconds         */

            for( i=0; i<24; i++ ) timeCuts[i] -= (long)( shiftTC ) ;

            printf("\tSymmetry Correction Time Shift = %4.0f/10 seconds\n", shiftTC );

             printf("\t%d\t%d\t%d\n", tempSysMatrix[11][10],
                         tempSysMatrix[11][11], tempSysMatrix[11][12]);


/******* Zero tempSysMatrix before generating symmetry corrected version ******/

           if( *incSysMat < (passes-1) ) {            /* passes is #defined at beg */
               for( i=0; i<23; i++ ) {
                   for( j=0; j<23; j++ ) {
                      tempSysMatrix[i][j] = 0;
                   }
               }
           }


           }      /* end if{ }else{ } */

}




OpenIO( int *source, FILE **fptr, FILE **fPtrOut, short **buffer, int *ichan,
       char notification[12], short incSysMat )
{

/*                              These are globally defined at the
                                beginning of the program.
    #define     router  1
    #define     file    3
    #define     tape    5
*/
```

```
    char        filename[255];  /* name of input data files        */
    char        fileNameOut[255];       /* output file name                */
    char        volLabel[255];          /* label assigned to data tape     */

    short       i;

    (*source) = 0;


/***************** Get Data Source ******************/

    if( incSysMat == 9999 )  {

       printf("Data Source:\n");    /* get and open input data file */
       printf("\tFile    (1)\n");
       printf("\tTape    (3) (UNIX only)\n");

#ifdef Online
        printf("\tRouter  (5)\n");
#endif Online

       printf("? ");
       scanf("%d", source);

       while( (*source) != 1 && (*source) != 3 && (*source) != 5 )    {
            printf("Try again( 1,3 or 5 ): ");
            scanf("%d", source);
       }

    }          /* end if( incSysMat == 9999 ) */


    switch( (*source) ) {

        case file:

           /********* Open Input and Output Files ******************/
           printf("\n");            /* get and open input data file */
           printf("Name of event file? (run0000##.evt) ");
           scanf("%s",filename);
           *fptr = fopen((char*)filename,"r");
           if( (*fptr) == NULL ) printf( "ERROR OPENING EVENT FILE" );
           else printf("IO Opened\n");


            /***************** Allocate Memory for Buffer ********/
            (*buffer) = (short *)malloc( sizeof(short) * 4096 );
            for( i=0; i<4096; i++) (*buffer)[i]=0;      /* initialize buffer */
            break;

#ifdef unix
        case tape:
                    /* incSysMat is initialized to 9999 before OpenIO */
                    /* is called the first time                       */
           if( incSysMat == 9999 )  {
              /***************** Open input file ******************/
              printf("Enter volume label? " );
              scanf("%s", volLabel );
              printf("\n");         /* get and open data file */
              printf("Name of input file? (RUN0000##.EVT) ");
              printf("\n");
              scanf("%s", filename);
           }
```

```
            volyoom = umtopen( volLabel, filename );

            /***************** Allocate Memory for Buffer ********/
            if( incSysMat == 9999 )  {
              (*buffer) = (short *)malloc( sizeof(short) * 4096 );
              for( i=0; i<4096; i++) (*buffer)[i]=0;  /* initialize buffer */
            }
            break;
#endif unix

#ifdef Online
        case router:
            OpenDataStream( ichan );            /* see buffers.for for code */
            printf("Opening Data Stream from Router\n");
            break;
#endif Online


    }


/****************** Open output files ********************/

    i = 0;
    while( (filename[i] != '.') && (i<strlen(filename)) ) {
        if( i < 3 ) fileNameOut[i] = filename[i];
        i++;
    }
    fileNameOut[3] = filename[(i-2)];
    fileNameOut[4] = filename[(i-1)];
    fileNameOut[5] = '\0';
    strcat( fileNameOut, ".sm" );
    *fPtrOut = fopen((char*)fileNameOut, "w");
    if( (*fPtrOut) == NULL ) printf("\n\tERROR OPENING OUTPUT FILE.\n" );

}




ReadBuffer( int *source, FILE **fptr, short *eof, short **buffer,
            int *ichan, char notification[12], short *numBf )
{
/*                              These are globally defined at the
                                beginning of the program.
    #define     file    1
    #define     tape    3
    #define     router  5
*/


    short       i;
    short     goodRead;


    switch( (*source) ) {

        case file:

            /********** Read buffer ***********/
            for( i=0; i<4096; i++ )  (*buffer)[i]=0;
                     /* locate next buffer to read */
```

```
            *eof = fseek( *fptr, 8192*(*numBf), 0 );
                    /* read in a buffer*/
            goodRead = fread( (*buffer), sizeof(short), 4096, *fptr);
           if( !goodRead ) printf( "ERROR READING BUFFER" );
            break;

#ifdef unix
        case tape:
            /* read 4096*2 bytes into buffer from volume */
            *eof = umtread( volyoom, (char *) (*buffer), 4096, 2 );
            break;
#endif unix

#ifdef Online
        case router:            /* get a pointer to a buffer */
            GetBuffer( ichan, notification, buffer );
            break;
#endif Online

    }

}



CloseIO( int *source, FILE **fptr, FILE **fPtrOut, char notification[12] )
{
/*
    #define     router  1
    #define     file    3
    #define     tape    5
*/


    short       i;
    short       dismount;


    switch( (*source) ) {

        case file:
            fclose(*fptr);
            break;

#ifdef unix
        case tape:
            printf( "Dismount tape? (0 or 1)" );
            scanf( "%d", &dismount );
            printf( "\n" );
            umtclose( volyoom, dismount );
            break;
#endif unix

#ifdef Online
        case router:
            ReleaseBuffer(notification);    /* give pointer back to router */
            break;
#endif Online


    }

}
```

```
#ifdef unix
SwapBytes( short **buffer )
{
/*
    short               highMask = 0xFF00;
    short               lowMask  = 0x00FF;
*/
    register int        i;


    for( i=0; i<4096; i++ )
        (*buffer)[i] = ( ((*buffer)[i] & 0x00FF) << 8 ) |
                                            ( ((*buffer)[i] & 0xFF00) >> 8 );


}
#endif unix
```